University of Southampton

Faculty of Engineering, Science and Mathematics

School of Chemistry & Institute of Sound
and Vibration Research

A Comparison of Measurement Techniques for Acoustic Cavitation

by

Christopher James Bradshaw Vian

A thesis submitted for degree of Doctor of Philosophy

September 2007

UNIVERSITY OF SOUTHAMPTON

ABSTRACT

Faculty of Engineering, Science and Mathematics
School of Chemistry & Institute of Sound and Vibration Research

Doctor of Philosophy

A COMPARISON OF MEASUREMENT TECHNIQUES FOR ACOUSTIC CAVITATION

by Christopher James Bradshaw Vian

Light emission, acoustic pressure, surface erosion/corrosion and sonochemical rates are compared in a number of different ultrasonic systems representing "idealised" and "real world" scenarios. The spatial correlation between the measurements is shown.

An electrochemical sensor based on surface erosion/corrosion of a passive metallic solution/metal interface is developed and shown to be applicable to a number of environments. Counting of discrete surface erosion/corrosion events on either an aluminium or titanium electrode is used to investigate cavitation activity as a function of position within an ultrasonic reactor with up to 4×10^5 events being recorded in 30 s. The technique represents a 4 orders of magnitude increase in sensitivity compared to similar weight loss techniques. To conduct measurements in the "real world" environment (e.g. an ultrasonic cleaning vessel) a new unipolar linear optocoupled current follower is described and its performance analysed. The application of this current follower reduces the noise signal recorded from > 100 μA to < 0.1 μA. This allows measurement of erosion/corrosion events in situations that would otherwise be precluded. The processes that lead to erosion/corrosion on the surface of an electrode are investigated using high-speed photography with particular reference to the difference between sharp "primary" and rounded "secondary" peaks.

A stable and reproducible electrochemical flow cell is used to make sonochemical measurements as a function of position. It is found that mass transfer within ultrasonic vessels made spatial resolved measurements unrealistic with this system. A bi-polar optocoupled current follower is constructed to allow the electrochemical measurement of sonochemical activity under adverse conditions and used to show a rate of I_3^- generation of 1.3 nM s^{-1} in an ultrasonic cleaning bath.

A systematic study of a single transducer ultrasonic reactor at different drive frequencies is made using all available techniques. This shows an excellent correlation between pressure and light measurements at 92 kHz and pressure, light and surface measurements at 23 kHz. The relationship between the frequency and the light, surface and sonochemical measurements is investigated revealing that light emission and sonochemical activity occur at different frequencies.

The light emission, acoustic pressure and surface activity are measured as a function of position in three ultrasonic cleaning baths demonstrating the inhomogeneous nature of the inertial cavitation generated. The placing of items within a cleaning bath is shown to reduce cavitation activity.

Measurements made in the NPL reference vessel reveal a close spatial correlation between light emission, acoustic pressure, surface erosion/corrosion activity and broadband acoustic emission. The invasive nature of sensors is shown using light emission measurements.

Contents

Acknowledgements

I would like to extend my thanks and gratitude to many people for their help and assistance throughout the course of my Phd. In particular I would like to thank:

Dr Peter Birkin, my supervisor, for all his boundless enthusiasm and assistance throughout my Phd. I have come to dread the words "I've had a brilliant idea" but have also found that most problems can be overcome with enough solder and some epoxy resin. My particular thanks go for his assistance in the writing of this thesis and managing to remove the majority of my spelling mistakes.

Prof. Timothy Leighton, my co supervisor, for his insight into acoustics and cavitation and his ability to find solutions that no one else has thought of.

To Bajram Zeqiri, Mark Hodnett and Min Joo Choi at NPL for there assistance with measurements in the reference vessel and letting me use their hydrophone and broadband sensor data.

The rest of the Birkin research group; Doug, Hanne, Jyo, Katie and Raya for their help and putting up with me borrowing their equipment, taking it to the dark room and forgetting to bring it back. Particular thanks to Doug for his assistance in writing Visual Basic programs.

Ken, Matt, Steve, Rich, Steve, Nefelli, Matt, Jason, Laura and everyone else on the seventh floor of the chemistry department. As well as Dave, Duncan, Simon and Emily, Kate, Rina for the endless games of pool and pub quizzes. Matt and Pam for being good friends

Mum and Dad for there help and support throughout my university career and for feeding me whilst I wrote up

Finaly thanks to Hurfo, Louise, Mike, Sleepy, Steve, Toby and the rest of the canoe club without whom this would have been submitted a lot earlier but the process would have been far less entertaining.

I acknowledge the funding of the University of Southampton and NPL

Symbols and Abbreviations

Symbols

A	Electrode area (cm^2)
c	Concentration (mol^{-1} dm^3 or mol^{-1} cm^3)
F	Faradays constant (96,480 C mol^{-1})
f_p	Drive frequency (Hz)
I_l	Mass transfer limited current (A)
k_m	Mass transfer coefficient (typically cm s^{-1})
n	Number of electrons
P	Pressure (kPa)
P_0	Hydrostatic liquid liquid pressure (kPa)
P_B	Blake pressure (kPa)
P_g	Gas pressure (kPa)
R	Bubble radius (m)
R_0	Initial bubble radius (m)
R_B	Blake radius - the threshold value for R_0 in the Blake equation (m)
R_{crit}	The critical radius below which no interaction between a bubble and the sound field will be seen (m)
R_{max}	The maximum radius of the bubble (m)
R_{min}	The minimum bubble radius (m)
R_r	The resonant bubble radius (m)
t	Time (s)
t_1	The time after the pressure exceeds the Blake pressure that a bubble responds (s)
t_2	The time at which the liquid ceases to be under tension (s)
ε	Extinction coefficient (mol dm^{-3} cm^{-1})
σ	Surface tension

Abbreviations

ADC	Analogue to Digital Converter
COMORAC	Characterisation Of Measurements Of Reference Acoustic Cavitation
CV	Cyclic Voltammogram
EDTA	Ethylene Diamine Tetraacetic Acid
ESR	Electron Spin Resonance spectroscopy
HIFU	High Intensity Focused Ultrasound
MBS(C)L	Multi Bubble Sono(Chemi)Luminescence
MBSL	Multi Bubble SonoLuminescence
MCA	Multi Channel Analyser
MTLP	Mass Transfer Limited Potential
NPL	Nation Physical Laboratory (UK)
PMMA	PolyMethylMethAcrylate
PMT	Photon Multiplier Tube
PZT	Piezoelectric
RMS	Root Mean Squared
SBSL	Single Bubble SonoLuminescence
SCE	Standard Calomel reference Electrode
UV/VIS	Ultraviolet and Visible spectroscopy
XRF	X-Ray Fluorescence

1. Introduction

Cavitation of a liquid is the phenomenon where a pressure change or action of an appropriate energy influx causes the generation and activity of bubbles (or cavities) (*1, 2*). In turn the action of the cavities can cause a number of effects from acoustic pressure shocks (*3-5*) to light emission (*6-23*). The effects can be both beneficial and detrimental depending on the situation and location of the bubble centre. Interestingly it was the detrimental effect of cavitation on the action of propellers that first lead to its discovery. While this is an interesting process, with a variety of unusual effects produced within a liquid which is at room temperature, the generation and characterisation of this phenomenon is far from trivial. In addition the methods available for the generation of cavitation are varied. Young (*2*) describes how there are four ways in which cavitation can be produced:

1. Hydrodynamic cavitation produced by pressure variations in a flowing liquid.
2. Acoustic cavitation produced by the pressure variations within a sound field.
3. Optical cavitation produced by photons from a laser beam causing local heating, liquid breakdown and bubble formation.
4. Particle cavitation produced by elementary particles creating local heating in the liquid.

However, Lauterborn (*24*) splits the methods of creating cavitation into two different groups; those brought about as a result of mechanical tension in the liquid (here we are able to classify hydrodynamic (*25, 26*) and acoustic cavitation as part of this group) and those created by an energy deposit (for example optical (*27-37*) and particle (*38*) cavitation). While these areas are of general interest, this thesis investigates the characterisation and monitoring of acoustic cavitation and specifically that generated by ultrasound.

1.1. Ultrasound and cavitation

Ultrasound is defined as the frequency above the range of human hearing (>16 kHz) and is widely used in research, medicine and industry for process where the generation of cavitation can have either positive (e.g. cleaning or organic destruction

(*39, 40*)) or detrimental (e.g. erosion of surfaces (*5, 27, 38, 41-47*)) consequences. In medical fields ultrasound is used as a diagnostic tool, for therapy and through the use of HIFU (high intensity focused ultrasound) the possible treatment of cancer (*48*). In biology it is used to destroy cells and in the pharmaceutical industry it is used to extract bioactives from plant materials. In sonochemistry ultrasound is used to destroy organic pollutants and the formation of nanoparticles. In addition to these applications ultrasonic baths are used for critical cleaning in many situations.

Acoustic cavitation can be divided into two forms; inertial and non-inertial cavitation (*49, 50*). Inertial cavitation was previously described as 'transient cavitation' and non-inertial as 'stable cavitation', this was after the duration that the cavitating bubbles were thought to exist for (transient cavitation was thought to last approximately one pressure cycle). After the discovery by Gaitan and Crum (*11*) that it was possible for a single bubble to undergo repeated light emission (indicative of the presence of inertial (*51, 52*) cavitation) over many thousands of pressure cycles the current appellations were considered more appropriate.

For cavitation to take place, be it inertial or non-inertial, then the tension in the liquid must exceed the Blake pressure (*53*) in order that the bubbles within the liquid can grow (*1*). The Blake pressure can be calculated from equation 1.1

$$P_B = P_o + \frac{8\sigma}{9}\sqrt{\frac{3\sigma}{2R_B^3\left(P_o + \left(2\sigma / R_B\right)\right)}} \qquad \text{(valid for } R_0 << R_r\text{)} \qquad (1.1)$$

where R_0 is the equilibrium bubble radius which is termed R_B the Blake radius in equation 1.1; R_r, the radius of a bubble that would be in pulsation resonance with the incident sound field; P_B (the Blake pressure) is the minimum acoustic pressure at which a gas bubble of radius R_B will rapidly grow; P_o is the hydrostatic liquid pressure outside the bubble and σ is the surface tension of the liquid. As the pressure within the liquid reduces below the Blake pressure for a given bubble the bubble begins to rapidly expand. Due to the inertia of the system this expansion continues beyond the point in time where the pressure is above the Blake threshold until the bubble wall is stationary. Here it can no longer be maintained and it begins to reduce

in size. If the cavitation is to be inertial then the motion of the bubble will be more violent; an explosive isothermal growth will be followed by a rapid adiabatic collapse leading to the possible breaking up of the bubble. This has the effect of concentration the energy in the liquid to a tiny point. Figure 1.1 shows a schematic of the bubble radius as a function of time during a bubble rebound (left) and inertial cavitation collapse (right).

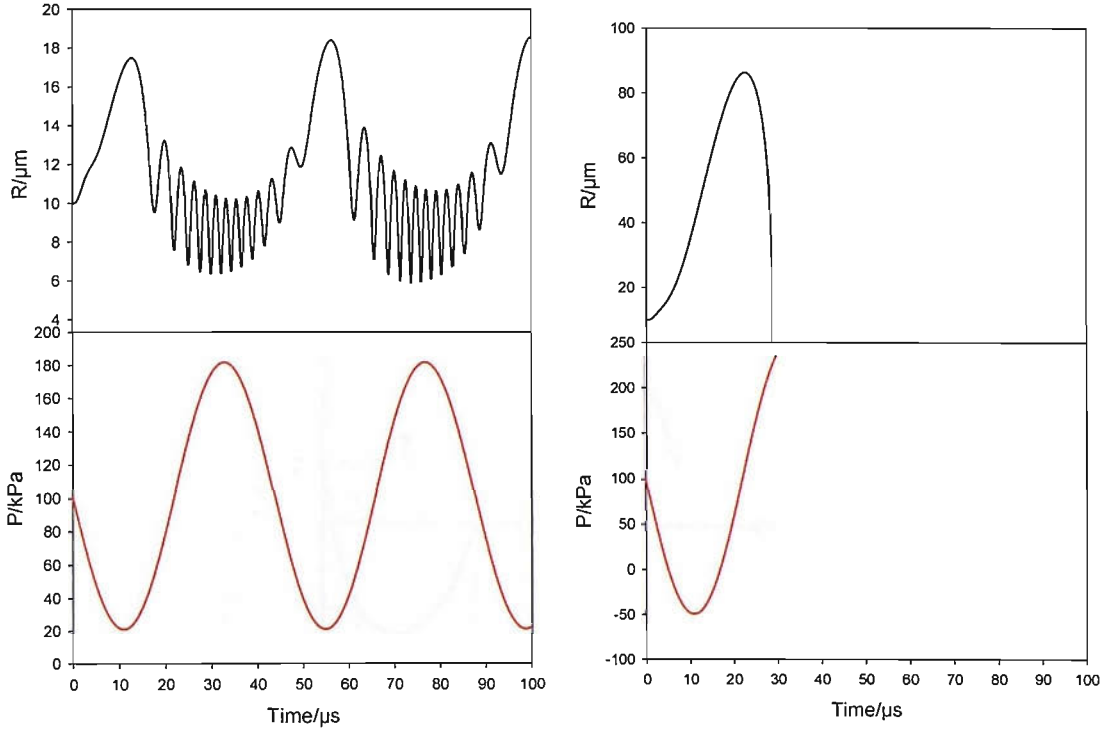

Figure 1.1: Plots showing the radius of a bubble as a function of time under the action of a pressure wave. The bubble has an initial radius of 10 μm and is subjected to a sound field of 160 kPa peak to peak (left) or 300 kPa peak to peak (right). The right hand bubble undergoes a inertial collapse where as the right hand bubble is an interesting repetitive oscillation. Developed from (*1*) by (*54*).

The concentration of energy during the collapse of the bubbles leads to extreme conditions at the point of collapse. It has been calculated that at the point of bubble collapse the temperature within the bubble reaches in excess of 5000 K (*55-57*) and the pressure over 50 MPa. The collapse of the bubble and the conditions within it generate acoustic pressure shocks, chemical radicals (*58-60*), light emission and, if the collapse happens near enough to a surface, surface erosion/corrosion (*1, 5, 38, 41-47*).

The conditions that precipitate the initiation of cavitation are not reliant only on the presence of acoustic pressure in excess of the Blake pressure. The Blake pressure only requires that the radius of the bubble that is to be the nucleation point for the cavitation be greater than R_{crit} which is defined as the critical dimension below which any change in hydrostatic pressure will have no effect. Therefore if the acoustic pressure is above the Blake pressure then bubbles within the liquid whose radius is greater than R_{crit} ($R > R_{crit}$) will be active and undergo cavitation. This does not explain whether the cavitation will be inertial or non-inertial. To determine this Holland and Apfel (*61*) introduced an analytical function that incorporated both upper and lower radius thresholds. Figure 1.2 shows how the variation in the pressure field leads to change in the radius of the bubble. This model is discussed in detail beyond the scope of this thesis in Leighton (*1*).

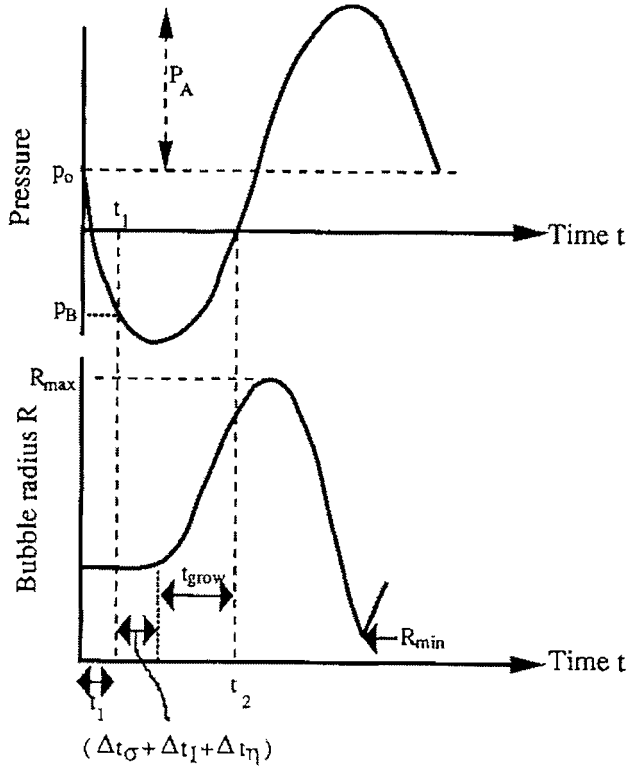

Figure 1.2: The model response of a bubble undergoing inertial cavitation to the pressure field. Further explanation of the model can be found in (*1, 61, 62*). (Figure taken from Leighton's (*1*) redrawing of Holland and Apfel (*61*).)

Figure 1.2 shows how as the negative phase of the sound field increases the liquid initially goes into tension. After $t = t_1$ the negative pressure amplitude reaches the Blake pressure (P_B) which is followed by a lag time before the bubble responds and begins to grow. At $t = t_2$ the liquid ceases to be under tension but the inertia, surface

tension and viscosity of the bubble cause the bubble to continue expanding until it reaches its maximum size (R_{max}). The forces acting on the bubbles then cause the bubble to rapidly collapse to R_{min}.

Power (*62*) incorporated the model and equations of Holland and Apfel (*61*) and Leighton (*1*) into a Microsoft Visual Basic program that allowed the pressure threshold as a function of bubble size to be calculated. Figure 1.3 shows the output from this model at 25 kHz with the Blake (——) and expansive (— —) pressure thresholds. This model relies upon a number of approximations. These include:

- The Holland and Afel model (*61*) requires that the temperature inside the bubble reach at least 5000 K. This is not unreasonable given that the temperature inside a bubble has been measured to be well in excess of this (*55-57*).
- The model also assumes that the bubbles (nuclei) will undergo prompt cavitation; that is to say they will cavitate after one acoustic cycle.

Throughout this thesis the Visual Basic program developed by Power is used for the calculation of pressure thresholds; specifically the expansive pressure threshold is used.

The threshold plots seen in figure 1.3 show that bubbles of different sizes have different pressure thresholds. At a pressure amplitude of 150 kPa a bubble with a rest radius of 10 μm will undergo inertial cavitation at 25 kHz; whereas under the same conditions a bubble of initial radius 50 μm will undergo non-inertial cavitation. However, bubbles that are not of suitable size to undergo inertial cavitation are not precluded from interaction with the sound field. Those which are either too small or too large to initiate inertial cavitation will still be subjected to the action of the pressure field and undergo non-inertial cavitation. Instead of the explosive growth seen for bubbles undergoing inertial cavitation the growth of the bubble is more measured as the pressure decreases. During this period the amount of gas within the bubble increases as further dissolved gas from the liquid surrounding the bubble is drawn into the bubble through 'rectified diffusion'(*63-68*). Figure 1.4 shows a schematic representation of the processes involved in this phenomenon. Rectified diffusion, under the appropriate physical conditions, can increase the size of bubble.

Consequently it may either now be big enough to undergo inertial cavitation or be so big that it collapses and forms a number of smaller bubbles that can undergo rectified diffusion in order to grow to a suitable size to undergo inertial cavitation.

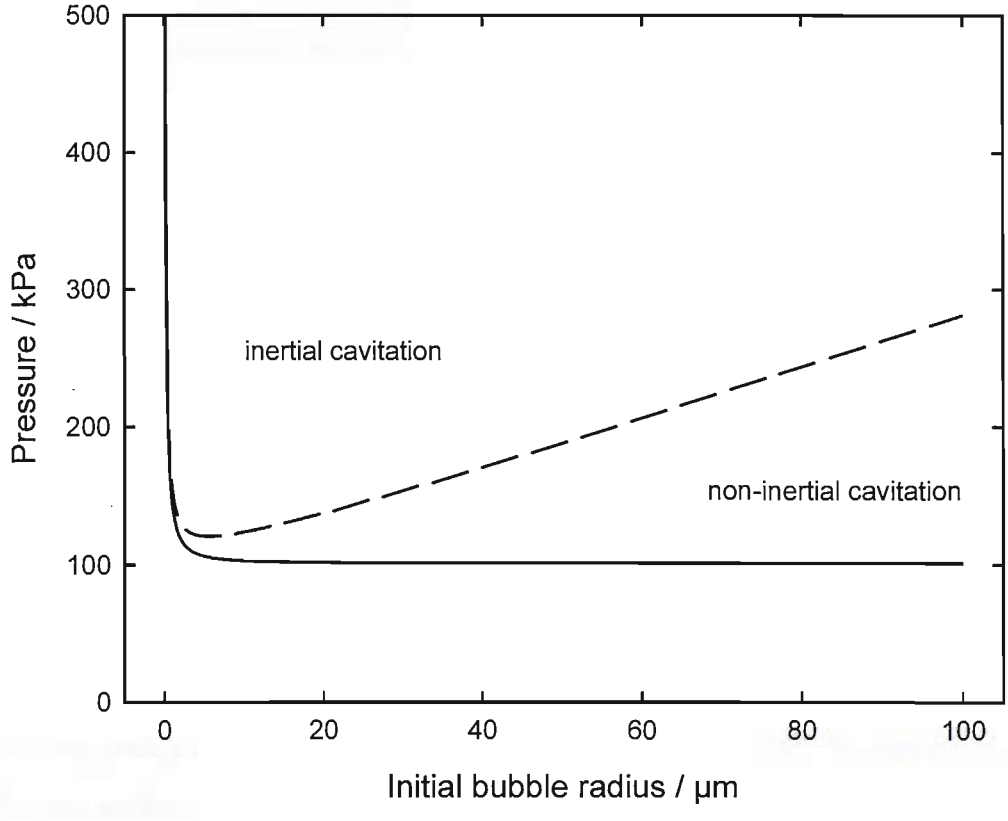

Figure 1.3: Plot showing the theoretical pressure threshold for inertial cavitation (— —) and the Blake pressure (——) as a function of bubble radius at 25 kHz. Calculated using the Visual Basic program developed in (*62*).

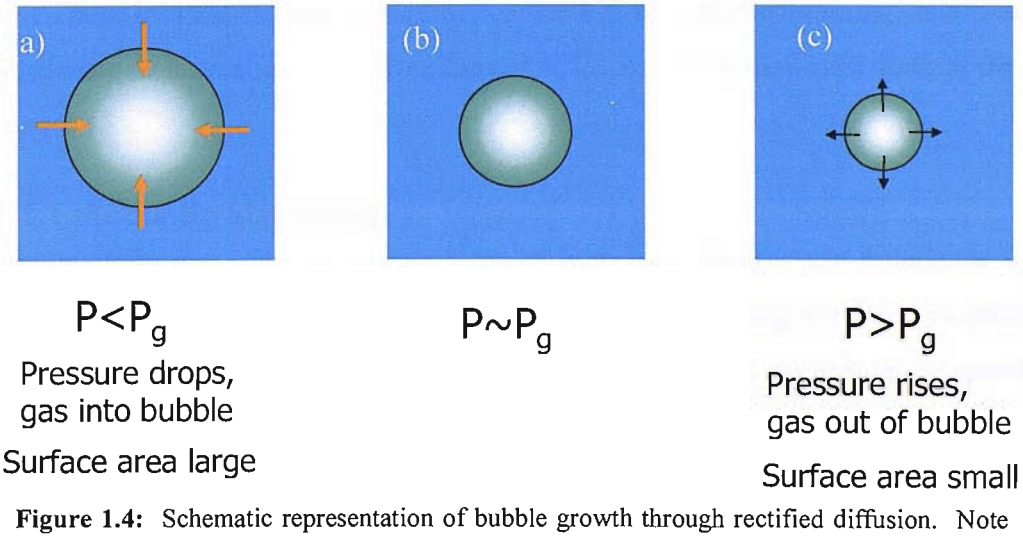

Figure 1.4: Schematic representation of bubble growth through rectified diffusion. Note in (a) the bubble is large and the flux of gas into the bubble exceeds (c) where the bubble is small.

The extreme conditions found at the point of bubble collapse are not restricted to the action of an acoustic pressure field within a liquid; the same explosive isothermal growth followed by rapid adiabatic collapse is seen with other forms of cavitation generation. Such are the pressures and temperatures experienced at bubble collapse that it has been postulated that it is possible to initiate nuclear fusion within them (*69, 70*). Evidence for fusion in deuterated acetone has been reported using acoustic cavitation with and without neutron seeding (*71*). The veracity of these results is disputed and the subject lies outside the purview of this thesis but is of interest to note.

1.2. Effects of cavitation

Cavitation has effects that can be seen in the bulk of the liquid in which it is taking place in addition to the localised activity seen at the point of bubble collapse (*1*). These effects include acoustic pressure shocks, light emission, chemical change (from radical formation), increase in temperature (*72*) and if the cavitation is taking place in vicinity of a surface, surface erosion/corrosion. It is these effects that can make cavitation both a useful and detrimental effect. These effects will be discussed in the following sections.

1.2.1. Physical effects

A number of physical effects within the liquid surrounding cavitation activity can be seen. These include acoustic streaming (or bulk flow), microstreaming, microjetting, acoustic shock waves and cluster collapse (*5, 73, 74*). We shall now look at these in turn:

1.2.1.1. Acoustic streaming

Acoustic streaming (*53, 75*) is bulk flow of liquid due to pressure imbalance in the liquid caused by the attenuation of the pressure field. Using sonoelectrochemistry (*76*) it has been suggested that at the tip of an ultrasonic horn the streaming speed can be up to 10 cm s^{-1} (*77*).

1.2.1.2. Microstreaming

Microstreaming (*65, 78-81*), as the name suggests, takes place on a smaller scale than acoustic streaming. When small obstacles, such as bubbles, are placed in a sound

field the frictional forces at the boundary layer lead to circulation of the solution in a small (often microscopic) layer. This is termed microscopic streaming. The way in which the solution circulates around the obstacle was investigated by Elder (*82*) who utilised aluminium powder to visualise the flow. This lead to four distinct patterns being observed. They are summarised below and shown in figure 1.5.

Type a: Seen in a low viscosity liquid at low pressure if the surface of the bubble is contaminated.

Type b: Seen over a wide range of viscosities and pressure amplitudes

Type c: Seen at the same time as the onset of surface wave modes. Normally seen in low viscosity liquids but can be seen on those of higher viscosity if the pressure is great enough.

Type d: Seen in low viscosity liquids with high pressure amplitude; allowing more than one surface mode to be excited.

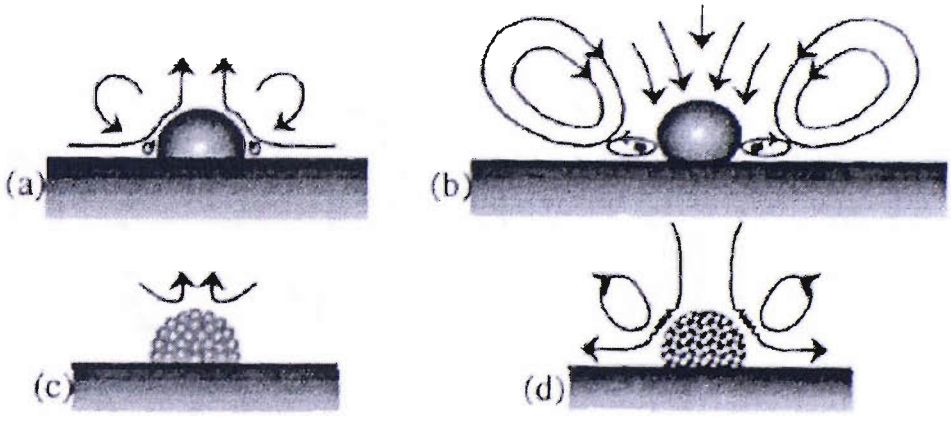

Figure 1.5: Schematic representation of the four types of microstreaming identified by Elder(*82*). Taken from a re-drawing of the original by Leighton(*1*).

It is also possible to use electrochemical methods to detect microstreaming (*63, 64, 68, 83-91*). Here the motion of the gas/liquid interface of a tethered bubble using a novel electrochemistry approach. (*84, 85, 88*) In this technique a microelectrode (*92*) (25 μm diameter platinum) was positioned, using a micrometer and stage, close (~ 5 - 10 μm) to the gas/liquid interface of a large gas bubble (bubble equilibrium radius, R_0 ~ 2 mm). The position of the microelectrode with respect to the gas/liquid interface was determined by employing standard scanning electrochemical microscopy theory to analyse the negative feedback (*93, 94*) approach curves measured as the

microelectrode approached the insulating bubble wall (employing $Fe(CN)_6^{3-}$ as a redox agent). The motion of the gas liquid interface could then be followed as additional current resulting from the ensuing enhanced mass transfer due to forced convection (*84*). This forced convection was produced by bubble oscillation as the result of acoustic irradiation of the liquid at the appropriate frequency and pressure ranges required to excite at the bubble wall either Faraday wave motion (a surface wave at $f_p/2$ where f_p represents the drive frequency) or the excitation of bubble pulsation (*88*) at f_p.

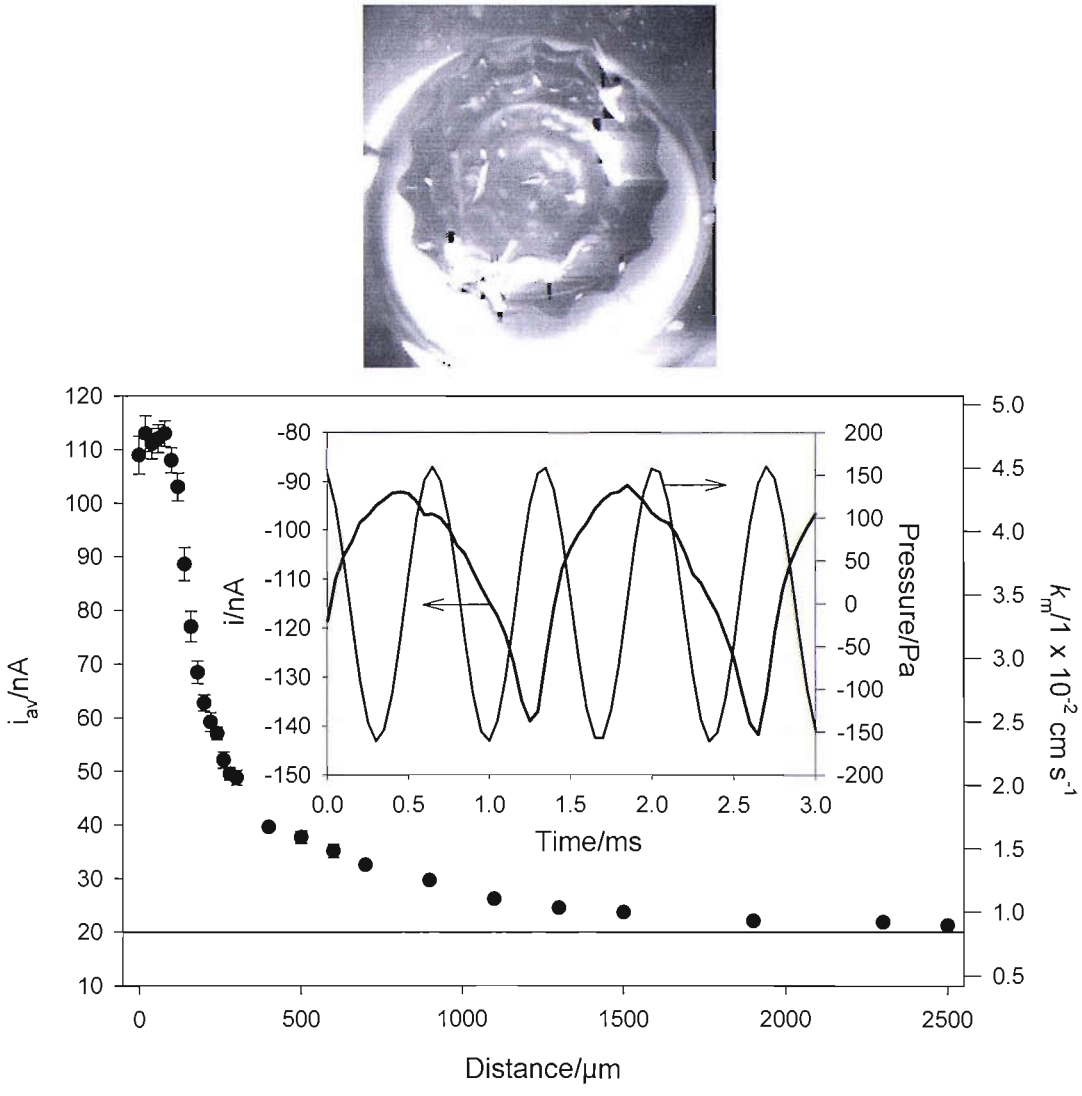

Figure 1.6: Image (scale bar = 2 mm) and plots taken from refs (*84, 88*) showing the average current (•) and associated mass transfer coefficient for a single air bubble driven into oscillation by a sound field operating at 1.46 kHz. The solution contained 5 mmol dm^{-3} $[Fe(CN)_6]^{3-}$ in 0.2 mol dm^{-3} $Sr(NO_3)_2$. The insert shows the oscillation in the current (——) and pressure ( ) as a function of time employing high temporal resolution equipment. The experiment was performed at *ca.* 20-23 °C under aerobic conditions. The solid horizontal line represents the steady state current or mass transfer coefficient for the microelectrode in a stagnant solution.

These studies have shown that this electrochemical technique is able to monitor the motion of the gas/liquid interface with high sensitivity. Motion below the μm scale could easily be detected by the microelectrode as enhancements in mass transfer. Figure 1.6 shows a surface wave on a tethered bubble and the current time history recorded for a microelectrode positioned next to the gas/liquid interface of an oscillating bubble.

Clearly this acoustoelectrochemical (*95*) approach to the study of bubble dynamics is useful.

1.2.1.3. Microjetting

If a bubble is close to a surface when it collapses then the surface can inhibit the flow of solution and lead to an asymmetrical collapse. This creates a jet towards the centre of the bubble which can continue through the bubble and impinge onto the surface. This is thought to be a major mechanism in the surface erosion/corrosion associated with cavitation. The impact of the jets on the surface leaves characteristic pits that are approximately one-tenth of the radius of the original cavity (*96-98*). Through laser induced cavitation and high-speed photography the study of microjets is extensive (*34, 37, 99-102*). Lauterborn *et al.* observed jets with velocities of 120 m s^{-1}. Their work enabled the theoretical work of Plesset and Chapman (*102*) to be confirmed. Figure 1.7 shows the agreement between the theoretical (—) and experimental (o) measurements.

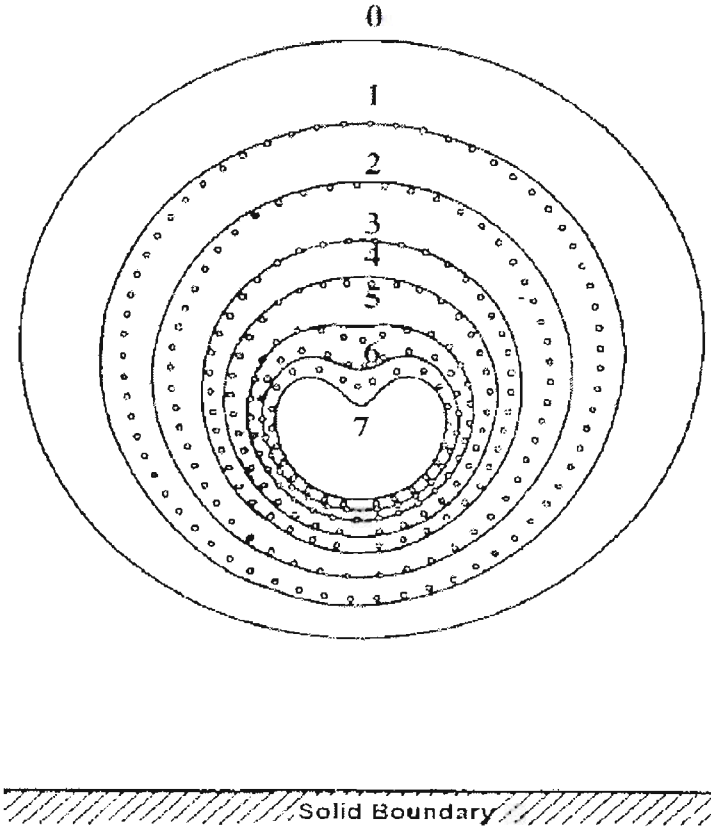

Figure 1.7: Plot showing the comparison of the theoretical (—) and experimentally (o) derived shapes of a bubble collapsing near to a surface. Taken from Lautherborn and Bolle(*101*) with the theoretical work of Plesset and Chapman(*102*). Experimental work conducted at 300,000 fps, initial bubble radius was 2.6 mm and the bubble centre 3.9 mm from the surface.

Under certain conditions the wall of the bubble furthest from the surface may traverse the bubble interior and penetrate the bubble wall nearest the surface. An excellent example of such an effect, taken by Crum, is shown in figure 1.8.

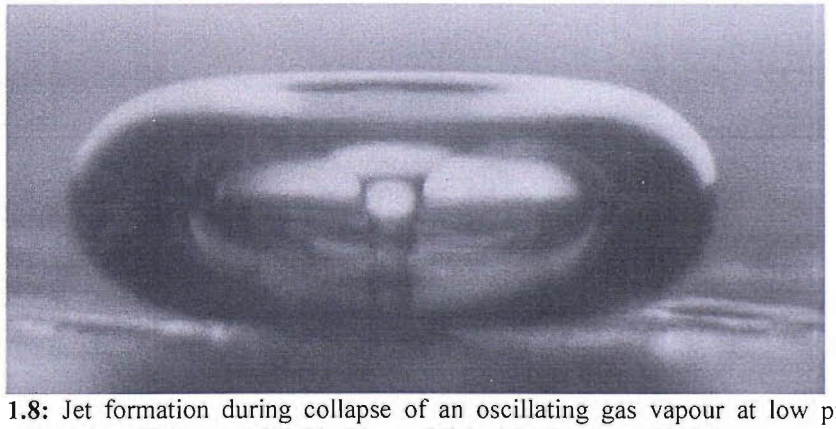

Figure 1.8: Jet formation during collapse of an oscillating gas vapour at low pressure (0.04-0.05 bar) in a 60 Hz sound field. First published by Prosperetti(*103*).

1.2.1.4. Acoustic pressure shocks

The collapse of a bubble emits a pressure pulse back into the surrounding liquid in the form of a shock wave. It has been shown that the shock generated at the point of collapse of a laser generated bubble can have an amplitude up to 1 GPa. These shocks are thought to damage adjacent surfaces (*99*). Hirsimäki (*37*) has suggested, through the use of simultaneous high-speed imagery and electrochemical surface erosion/corrosion measurements, that the shock has as important role in the damage to local surfaces as microjetting. In the isolated case of the single bubble generated by a laser bubble the shock is rapidly attenuated only a surface within close proximity will be affected. This is not the case when the collapsing bubble is part of a cluster.

1.2.1.5. Cluster collapse

Hansson (*4, 5*) *et al.* have described the concept of cluster collapse where the collapse of a cloud of bubbles causes damage to a surface remote from initial bubble collapse. The energy associated with the collapse of a bubble (or shell of bubbles in a cloud) at the edge of a cluster is transferred to its neighbours. This inward transfer of collapse energy, concentrating into the centre of the cluster, can result in very energetic collapses at the centre. This is seen in the presence of violent microjetting and high amplitude shock waves. The damage done to surfaces through a cluster collapse is still attributable to individual bubbles, but the magnitude of the effects are magnified by the cluster collapse.

1.2.2. Increase in temperature

The energy being introduced to the cavitating liquid from the sound energy will lead to an increase in temperature of the liquid. This can be seen to be significant in magnitude in chapter 8 of this thesis. The heating of the liquid has been used as a measure of cavitation (*104*). It is though a poor method for doing so with it being difficult to separate the heating effect of the cavitation from that caused by other factors. For example over prolonged usage ultrasonic transducers are liable to heat up and, given that for good acoustical transmission they have to be in close contact with the cavitating liquid, this heat can be transferred to the liquid causing heating above that seen from cavitation alone.

1.2.3. Light emission

Light emission as a side effect from cavitation was first observed by Frenzel and Schultes in 1934 (*105-107*) when they tried to speed up the photographic developing process by agitating the solution with ultrasound. Upon finishing their developing the effect of specks of light was found on their images. Further investigation revealed that the light was being generated from the cavitation. Similar light emission can be seen from many situations where cavitation exists (*106, 107*). In sonoluminescence only a single flash of light is seen for each pressure cycle. It is assumed that the bubble responsible for the luminescence is then destroyed by the bubble collapse and subsequent luminescence is as a result of different bubbles. This is not always the case. Under certain well controlled conditions it is possible to trap a single bubble at a pressure anti-node that will luminesce every pressure cycle for many tens of thousands of cycles. This is known as single bubble sonoluminescence (SBSL) and the more common form of sonoluminescence, where light emission is seen from a large number of bubbles throughout the cavitating vessel, multi-bubble sonoluminescence (MBSL).

1.2.3.1. Mechanism of sonoluminescence

The mechanism that leads to the emission from light at bubble collapse is much debated and no single theory is universally accepted. A number of theories have been proposed including thermal, mechanochemical, electric, opacity and a quantum theory. The majority of these theories were developed for MBSL light emission before being adapted to suit SBSL light emission as well. Each is discussed briefly in turn below.

1.2.3.2. Thermal mechanism

The thermal mechanism for light emission was proposed by Griffing (*108*). The theory proposes that heat is generated by the compression of the gas and vapour within a bubble collapse. The heat generated within the bubble cannot be dissipated to the surrounding liquid because the thermal transport is slower than the bubble collapse. Consequently there is a concentration of energy into the confines of the bubble such that the conditions are extreme enough that molecular excited states and radicals are formed. The recombination of the radicals and relaxation of the excited

states dissipates the excess energy in the form of light, giving rise to light emission. The theory is supported by emission spectra from the sonoluminescence of hydrocarbons which show vibrationally resolved bands attributed to the emission from the excited states of diatomic molecules (*109*). The theory though does not explain the short duration of the flashes of light seen.

1.2.3.3. Electrical mechanism

The electrical mechanism for light emission was first proposed by Frenkel (*110*) and is as a consequence of work which reveals that a single argon bubble can be characterised as a spark like plasma. Lepoint *et al.* (*111*) assume that the bubble expansion and a major part of its collapse is governed by Rayliegh-Plesset dynamics. The mechanism speculates that just prior to the collapse of the bubble needle like jets invade the bubble and deposit a minute spray of droplets (radius 150 nm) into the bubble. The distortion of the electrical double layer surrounding the bubble results in the jets and the droplets they deposit being oppositely charged. The shockwave electric field creates a plasma which releases energy as the form of light in a very short burst. An overpressure is associated with the plasma formation and this is believed to induce a deceleration in the bubble collapse. This theory does not explain why light emission is observed in liquid mercury (*1*).

1.2.3.4. Mechanochemical mechanism

The mechanochemical mechanism is based upon spherical microshock waves propagating within the bubble was proposed by Jarman (*112*) and has been supported by Barber and Putterman (*113*) and Lofstedt *et al.* (*114*). The shock waves reach supersonic speeds and induce the super heating of the gas at the centre of the bubble. The gas then emits light according to Bremsstrahlung radiation. By coupling the Rayleigh-Plesset and Euler equations Wu and Roberts and Moss *et al.* predicted that the temperature within the bubble could reach 10^5-10^6 K.

1.2.3.5. Quantum vacuum radiation

Eberlein (*115, 116*) uses quantum vacuum radiation theory to explain the light emission from a collapsing bubble. This is supported by the absence of UV radiation from the emission.

The level of light emission seen from MBSL is very low (of the order of a few hundred counts per second at a single photon counter module) and as such requires very dark conditions and specialised equipment for a meaningful measurement to be made. It is possible, through the addition of chemicals such as luminol (*62, 83, 117-122*) to the cavitating liquid, to increase the level of light emission to the point where it can be clearly seen with the naked eye. We shall now look at this process in more detail.

1.2.3.6. Multi-bubble sono(chemi)luminescence

Multi-bubble sono(chemi)luminescence (MBS(C)L) is the augmentation of the multi-bubble sonoluminescence with light emission from excited chemical states created by cavitation. It is well known that an alkaline solution containing luminol will generate light if subjected ultrasound of sufficient intensity. The mechanism has been investigated and determined by a number of authors (*123, 124*). The luminescence is as a result of an oxidative chemiluminescent process involving sonochemically generated $OH^{\bullet}$ (*118*). The proposed mechanism (*125*) by McMurray *et al.* for luminescence from luminol is shown in figure 1.9. Various studies have shown that the process is more efficient at higher pH and that the H_2O_2 concentration has a significant effect on the level of light emission (*123, 126, 127*). The addition of EDTA as a chelating agent to remove any metal ions from the luminol containing solution reduces any the possibility of an artificial signal being created by H_2O_2 being catalysed to $OH^{\bullet}$.

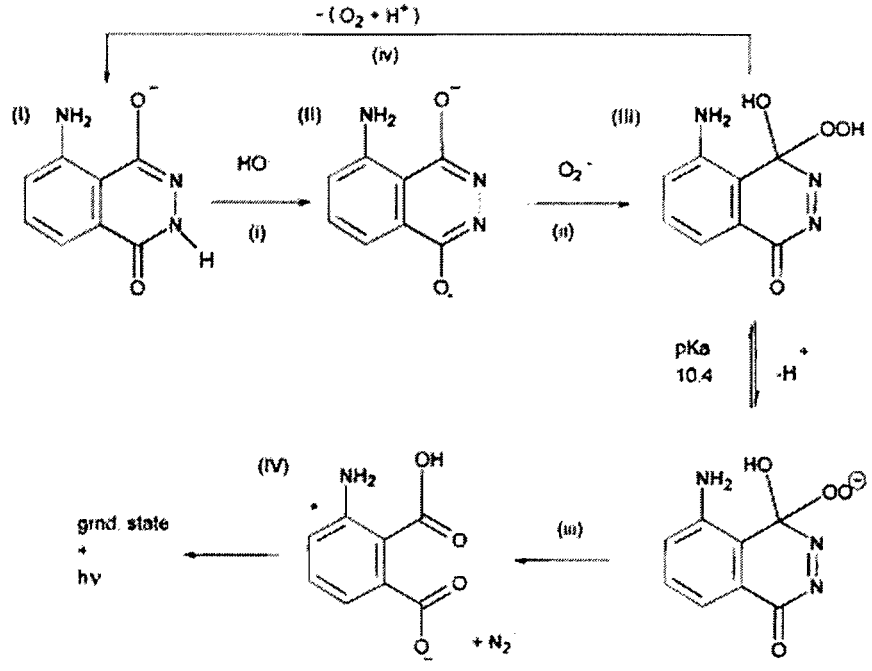

Figure 1.9: Proposed mechanism of sono(chemi)luminescence taken from McMurray(*123*)

The level of light emission recorded from MBS(C)L is significantly greater than that recorded for MBSL in isolation. As part of a high resolution study into the effect of frequency on the level of light emission from a single transducer ultrasonic reactor Birkin *et al.* (*128*) demonstrated that, despite the increased level of light emission seen from a solution containing luminol, there was an excellent correlation between the relative level of MBSL and MBS(C)L at a given frequency, see figure 1.10.

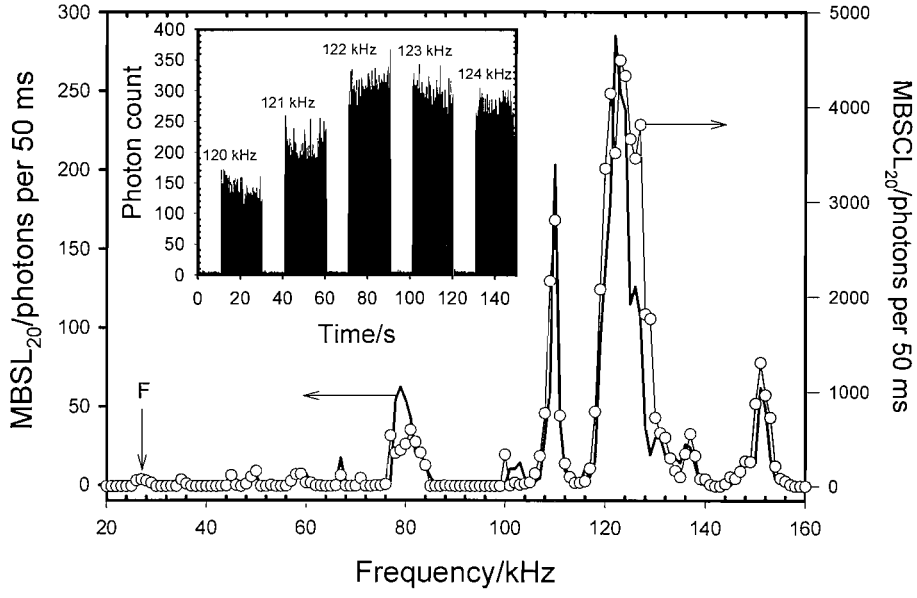

Figure 1.10: Plot showing the MBSL20 (——) and MBSCL20 (—○—) output of the sonochemical cell as a function of drive frequency. Taken from Birkin *et al*(*128*)

1.2.4. Radical chemical formation

In the preceding section we have seen how radicals (*60, 129-135*) formed in the process of inertial cavitation can be utilised to increase the level of light emission seen from a cavitating liquid. The presence of $OH^{\bullet}$ and $H^{\bullet}$ (*136*) radicals and the effect that they have on the chemistry of the bulk of the cavitating liquid can also be measured.

The formation of hydroxyl radicals ($OH^{\bullet}$) by cavitation was established by Weissler through the detection of H_2O_2, it being the geminate recombination product of the hydroxyl radicals. The presence of both hydroxyl radicals and hydrogen atoms ($H^{\bullet}$) was shown by Riesz *et al.* who used spin traps to convert the short lived radicals into more stable nitroxyl radicals that it was possible to detect using ESR (electron spin resonance) (*137*). The spin traps were chosen such that the $OH^{\bullet}$ product would form a doublet in the ESR spectrum whereas the $H^{\bullet}$ product would form a triplet allowing the two to be differentiated and confirming the presence of both $OH^{\bullet}$ and $H^{\bullet}$ radicals.

The bulk concentration of radicals with an ultrasonic reactor is quite low (*138, 139*). It has been proposed that the local concentration of radicals generated around a single cavitation event can reach 4 mmol dm^{-3} (*130*). This despite that it is thought that only 10% of the radicals generated in the vapour phase within the bubble reach the solution (*140*).

1.2.4.1. Chemical dosimetry

Numerous dosimeters have been used by sonochemists to determine the rate of $OH^{\bullet}$ radical formation as a result of cavitation (*141, 142*). In dosimetery the radiation dose is determined from the chemical change of a well known and characterised chemical reaction. Fricke and Hart (*143*) outlined the properties of the ideal dosimeter but no single reaction is likely to be ideal and fulfil all the requirements. The principle properties hoped to be found in a dosimeter as outlined by Fricke and Hart are:

- It must sensitivity enough; aqueous chemical dosimeters can measure doses between $10 - 10^{10}$ rads with an absolute accuracy of 1-2 %. This is limited by the value of the absorption coefficient.
- It must be stable before and after irradiation.
- The dosimeter should show an independence of product yield on the dose rate, quality of radiation and temperature.
- Ideally the relationship between the dose and amount of reaction product would be linear.

In sonochemistry many dosimeters have been utilised(*62*); principle amongst these are the Fricke (*141*), terephthalate (*139*) and Iodide (*144*) (or Weissler) systems. The Fricke dosimeter uses an acidified solution of Fe^{2+} which, when subjected to conditions that generate $OH^{\bullet}$ forms Fe^{3+}. Initially developed for work on ionising radiation it has also seen use in sonochemical measurements (*139, 141, 143*). The terephthalate dosimeter is specific to only the measurement of $OH^{\bullet}$ formation. The terephthalate ion undergoes a hydroxylation which makes it possible to detect using fluorescence spectroscopy. Further details of the mechanism and its use in sonochemical measurements can be found elsewhere (*144*).

The generation of free radicals as a by-product of cavitation was first confirmed by Weissler in 1959 *(60)*. Previously to this he had recorded the oxidation of I^- to I_3^- in a solution of potassium iodide when subjected to ultrasonic cavitation (*145*). Reactions 1.1 to 1.4 show the cascade of reactions involving the $OH^{\bullet}$ radical and iodide to form the I_3^- ion.

$$I^- + {}^{\bullet}OH \longrightarrow {}^-OH + I^{\bullet} \quad (1.1)$$

$$I^{\bullet} + I^- \longrightarrow I_2^{\bullet -} \quad (1.2)$$

$$2I_2^{\bullet -} \longrightarrow 2I^- + I_2 \quad (1.3)$$

$$I_2 + I^- \longleftrightarrow I_3^- \quad (1.4)$$

The Weissler reaction is a particularly powerful dosimeter as it is possible to measure the formation of I_3^- using both electrochemical and UV/Vis absorption spectroscopy.

1.3. Electrochemical measurements

Electrochemistry offers a very powerful method for measuring the effects of cavitation. Through the use of a redox couple it is possible to record bulk flow within a reactor through increased mass transfer (*54, 146-148*). The use of a suitable chemical dosimeter enables the formation of radicals by the action of cavitation to be recorded (*62*). The reformation of passivated films on an electrode surface makes it possible to monitor surface erosion/corrosion in real time and at a specific location (*37, 54, 149*). Of particular interest to this work is the use of electrochemistry to monitor the chemical change taking place within a cavitating liquid and to monitor the reformation of passive films (*150-153*) destroyed after surface erosion corrosion. In this section we shall look at a number of previous studies where electrochemistry has been used to measure cavitation. First, we shall look at the measurement of chemical change as a result of radical species formation before second, looking at the use of passivated electrodes to study surface erosion corrosion.

1.3.1. Chemical measurements

Compton and co-workers (*154*) reported the direct measurement of $OH^{\bullet}$ radicals using electrochemistry through an increased current beyond that which would be associated with purely mass transfer enhancement. Power *et al.* reported the detection of $H^{\bullet}$ radicals using a Cu^{2+} system (*136*). Though both are impressive achievements they do not give an indication as to the overall level of radical generation within the bulk of the cavitating liquid. Such electrochemical measurements were made, also by Power *et al.* (*62, 128, 155, 156*) whilst investigating the frequency dependence of both light emission (through MBSL and MBS(C)L) and chemistry and the correlation between them (*157*). By making use of a flow cell it was possible to make a measurement without having to consider the mass transfer enhancement effect of acoustic streaming within the liquid and make accurate measurements as to the concentration of I_3^- produced by radicals. The study showed that there was a general trend that both the light emission and rate of chemical change (radical formation) increased as a function of drive frequency, (see figure 1.9).

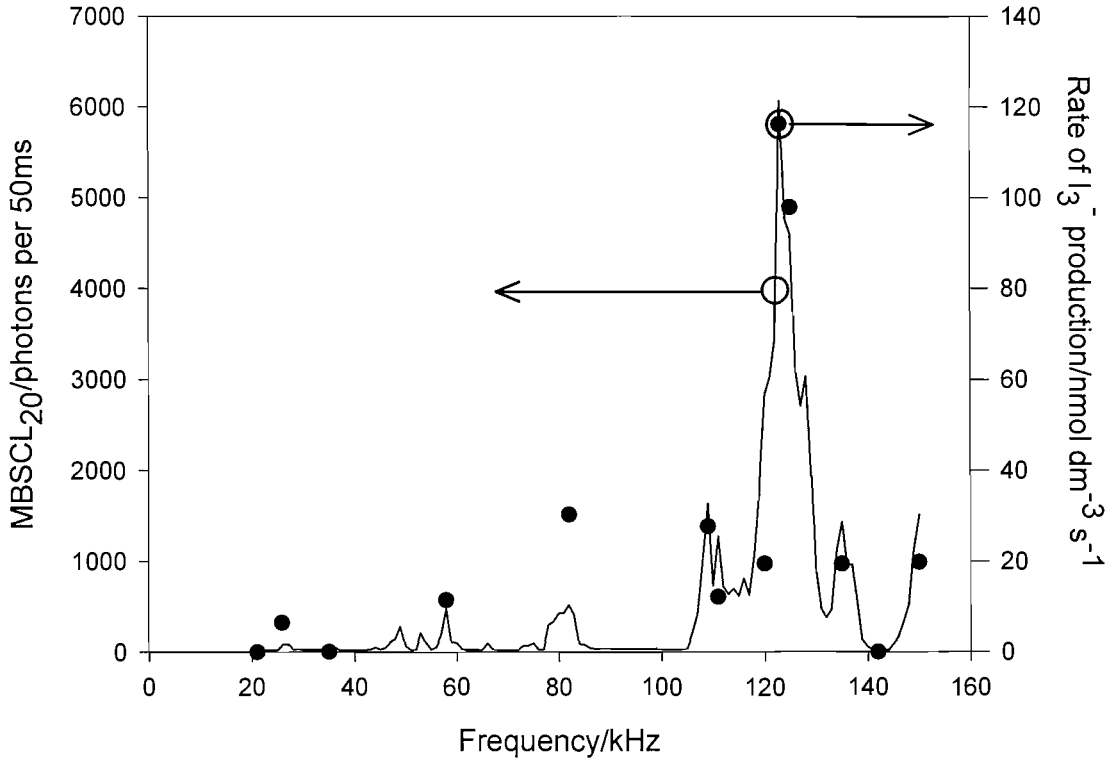

Figure 1.11: Plot showing the frequency dependemce of both MBS(C)L light emission and the production of I_3^- (indicative of radical production) in a single transducer cylindrical reactor. Taken from Power (*62*).

Further analysis of the frequency range around 124 kHz also showed that there is a strong correlation between the MBSL output and sonochemical yield of a variety of reactions. Figure 1.12, taken from reference (*121*) shows this correlation.

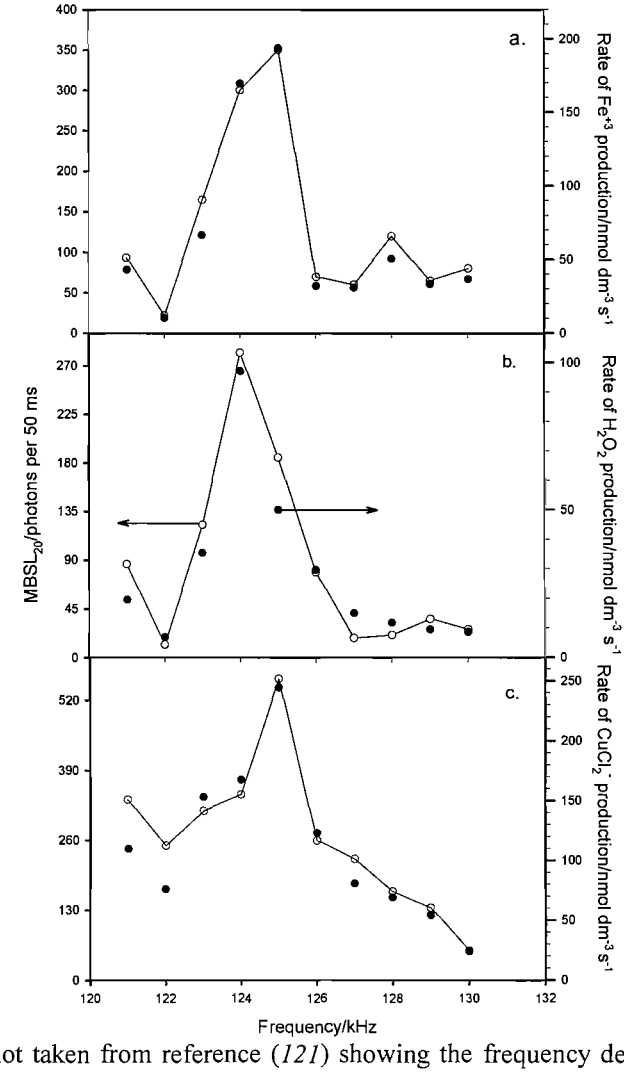

Figure 1.12: Plot taken from reference (*121*) showing the frequency dependence of both MBSL output of the cell (—○—) and three sonochemical reactions (●).

1.3.2. Surface erosion/corrosion measurements

In section 1.2.1 we have seen that the action of a collapsing bubble or the associated shock can cause the pitting and damage of a surface local to it. If the surface local to the collapse is an electrode covered by a passive layer then it is possible to identify the presence of surface events electrochemically (*54, 149, 158*). When the passive layer is damaged it reveals the active electrode underneath; this causes a current to flow as the passive layer is reformed. Figure 1.14 shows the sequence of events associated with this process. This procedure has been reported for a number of metals (*158, 159*). Offin *et al.* made use of a novel dual electrode where a platinum microelectrode was set in close proximity to a lead electrode that was passivated with a lead sulphate layer (*42*). This allowed the simultaneous investigation of the mass

transfer and erosive/corrosive effects of cavitation. The electrode was used to map the cavitation activity at the surface of an ultrasonic horn, see figure 1.13.

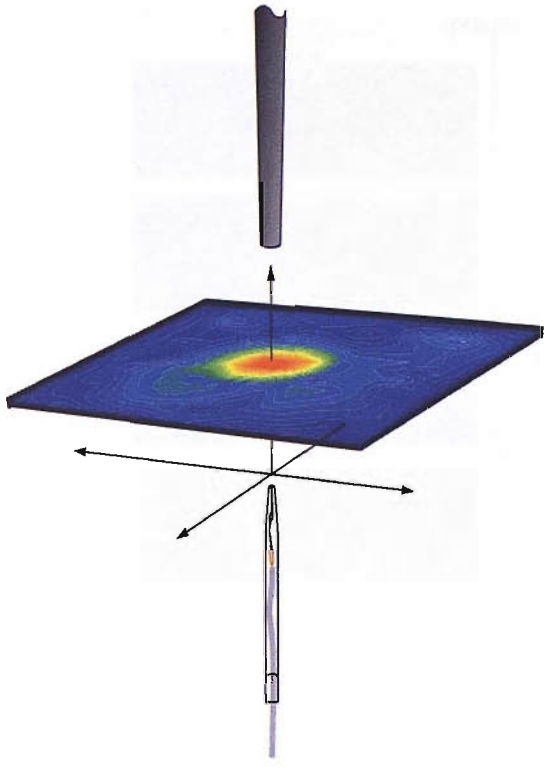

Figure 1.13: Taken from reference (*74*) showing the mapping procedure used to analyse the cavitation field from an operating ultrasonic horn.

Hirsimäki (*37*) made use of the same methodology in accompaniment of high-speed imaging to investigate the processes that lead to surface erosion as a result of single bubble laser induced cavitation. The time resolved real-time measurement that the use of electrochemistry allows enabled the process by which bubbles collapse causes damage to be investigated in a way not previously possible. This suggested that the pressure shock at the collapse of a bubble had a more significant role in the erosive process (*37*).

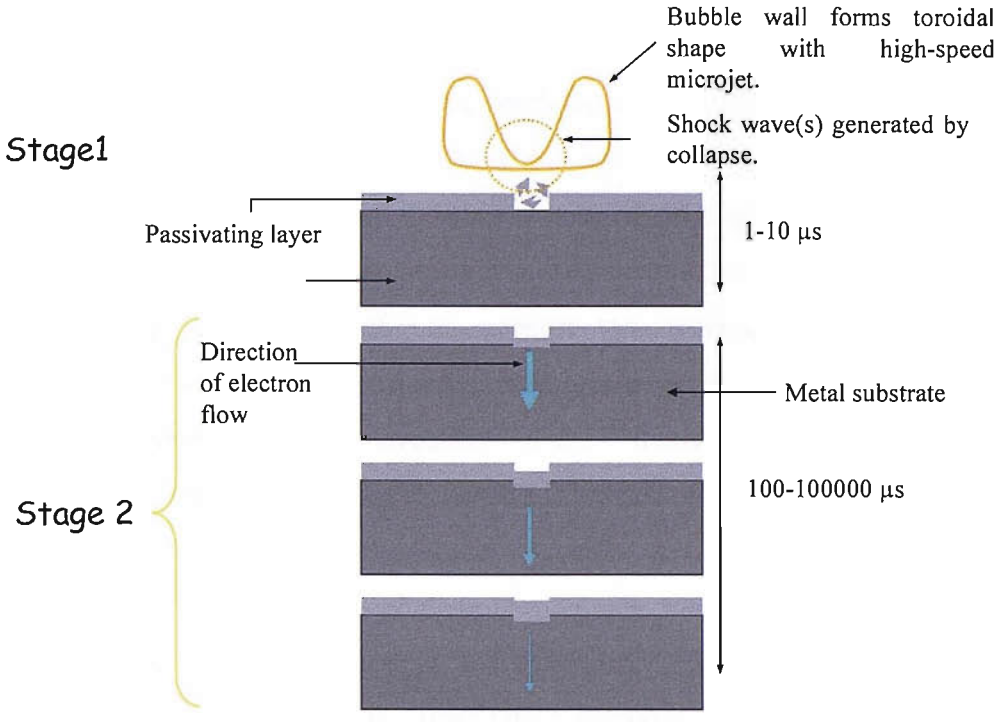

Figure 1.14: Schematic representing the sequence of events expected for an erosion corrosion event produced by cavitation.

This section has shown that clearly the use of electrochemistry is a powerful measurement technique for the study of cavitation.

1.4. Measurement of acoustic cavitation

Despite wide use of devices that make use of acoustic inertial cavitation there is no recognised and agreed method by which it is measured. Consequently comparison between different experimental and industrial setups is problematic and the exploitation of the phenomena is thus curtailed. Apfel identified three "golden rules" that should govern the measurement and investigation of cavitation. These were:

Know thy sound field (including the vessel containing the liquid)

Know thy liquid (including all it contains)

Know when something happens (a measure of the effects of cavitation)

As Walton (*107*) also notes that,

"Physicists may, for example, take some care over setting up a known sound field yet be content with "tap water". Chemists, by contrast, may go to great pains to characterise the liquid yet be content with a commercial sonicator producing an essentially unknown sound field"

This inconsistency makes it difficult to compare results between different studies.

1.4.1. COMORAC (*104*)

With this in mind the UK Department of Trade and Industry commissioned the UK National Physical Laboratory (NPL) and Southampton Universities Institute of Sound and Vibration Research (ISVR) to look at this area. The result was an exhaustive technical report (*160*) that detailed the current state of measurement techniques within the field and demonstrated the need for a standardised method of measurement. For a detailed description of the different measurement techniques used to measure cavitation the reader is directed towards this technical report (*160*). The publishing of the technical report led to the formation of the Characterisation Of Measures Of Reference Acoustic Cavitation or COMORAC project where a number of different measurement techniques were tested under the same conditions at NPL (*104, 161*).

The experiments were conducted in a standardised reference vessel at NPL and reported that it was possible to differentiate between "hot" and "cold" spots of cavitation (*62*). The COMORAC project was continued in two ways by NPL: first a large cylindrical reference vessel was developed and then extensively characterised using a hydrophone (*162*). Second a new, novel, broadband acoustic sensor was developed (*163, 164*).

1.4.2. NPL reference vessel

The reference vessel is based on a model P1800-25 Ultrasonic Processing Cell produced by Sonic Systems with a volume of 30 dm^3. The stainless steel vessel has thirty 25 kHz PZT transducers bonded to it and is controlled by a computer. To facilitate measurement an XYZ positioning system is mounted above the vessel. The facility is sighted at Teddington, London and allows the accurate comparison of different measurement protocols. The reference vessel has been characterised using a hydrophone (*162*) and with the NPL cavitation sensor (unpublished). Within this thesis light emissive and surface erosion/corrosion measurements will be presented.

1.4.3. NPL cavitation sensor

The NPL cavitation sensor measures the broadband acoustic emissions seen from bubble collapse. Neppiras (*165*) identified that hydrophones need a high frequency

response in order to measure the sharp edges of cavitation shocks. Figure 1.15 shows a schematic of the sensor. The sensor is a hollow cylinder of 4mm thick polyurethane onto the inside of which is mounted a 110 μm thick piezoelectric film which responds to sound waves in the MHz range. The polyurethane acts as a shield, attenuating the MHz noise from outside sensor but leaving the drive signals below 120 kHz unaffected (*166*). This makes the sensor spatially specific to the volume within it. In order to minimise the effect that the sensor has on the conditions within the liquid to be measured, the fabric of the sensor is acoustically matched to water. The invasiveness of the sensor will be looked at in chapter 9.

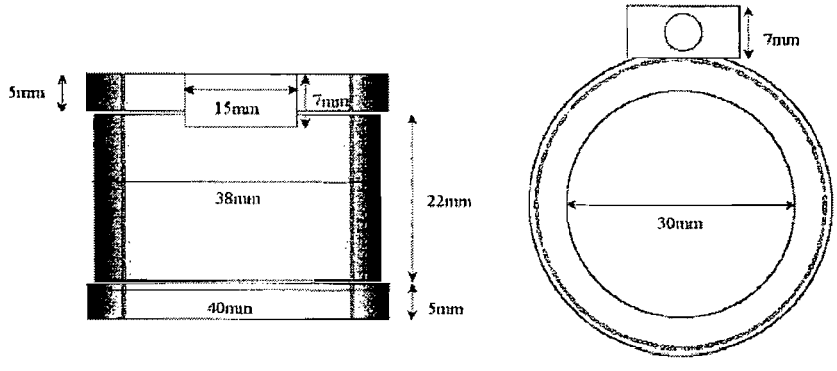

Figure 1.15: Schematic of the cavitation sensor developed by NPL. Taken from Zeqiri *et al.(163)*

The NPL are developing associated electronics to allow the operation of the device without attendant specialist equipment and training. The sensor has already been used in a number of studies (*167-169*) and results from use of the sensor will be compared to other methods for measuring cavitation in chapter 9.

1.5. Summary of work presented

The primary aim of the work presented in this thesis is characterisation of cavitation through the concurrent measurement of a number of the resultant effects of the presence of inertial cavitation. Specifically the light emission (through either the action of MBSL or MBS(C) L), acoustic pressure, chemical change and rate of surface erosion/corrosion events on a passivated electrode will be examined. In order that the research obeys Apfels three golden rules (*170*) certain measures are followed. To comply with "know thy liquid" the content of solutions used through out the work are recorded. The pressure measurements made fulfil the second rule of "know thy

sound field" and the light emissive, sonochemical and surface erosion/corrosion measurements fulfil the third criteria of "know when something happens".

Measurements were conducted in a number of different environments from the idealised conditions of a single transducer ultrasonic reactor (chapters 3 to 6) through to the chaotic conditions found in commercial cleaning baths and the NPL reference vessel (chapter 9). As such the work in this thesis is split into two parts; in the first part encompassing chapters 3 - 6 the work is conducted in idealised conditions; in the second part consisting of chapters 7, 8 and 9 the work is conducted in the more realistic earthed confines of ultrasonic cleaning baths and the NPL reference vessel. We shall now look briefly at the work presented in each chapter.

Chapter 2 covers the broad experimental techniques used to conduct the experiments in the following chapters.

Part A

Chapter 3 deals with the measurement of chemical change through both electrochemical and spectroscopic means. A measurement protocol will be discussed that allows repeatable, accurate electrochemical measurements to be made with a limited degree of spatial resolution.

Chapter 4 covers the action of near surface bubble collapses on aluminium and titanium electrodes. A new method for counting the number of events taking place in a given time will be introduced and the method compared to existing techniques. The new method will then be used to measure the variation in activity at the surface of a horn and in a single transducer reactor.

Chapter 5 investigates further the mechanism through which current time events are formed on the surface of a passivated electrode by the means of concurrent high speed imaging and electrochemistry. Investigations were conducted under the repeatable conditions found at the tip of an ultrasonic horn as well as the different conditions found with an electrode placed in a single transducer ultrasonic reactor.

Chapter 6 brings together the techniques demonstrated in chapters 2 and 3 along with low light and pressure measurements to investigate the level of cavitation taking place in a relatively large single transducer ultrasonic reactor at a number of different frequencies as a function of position within the reactor.

Part B

Chapter 7 deals with the problems associated with conducting sensitive electrochemical measurements in the earthed conditions found in commercial ultrasonic reactors. Various methods are considered to isolate the electrochemical cell from the surrounding environment and the development of two novel optically isolated current followers for fast surface erosion/corrosion events and slow chemical change measurements are discussed and tested.

Chapter 8 sees a series of experiments conducted on three ultrasonic cleaning baths with low light, pressure, chemical and surface erosion/corrosion event measurements conducted to give a rounded view as to the level of cavitation taking place within the baths. In addition to this a number of objects are introduced into one of the baths to simulate the effect that items to be cleaned will have on the level and distribution of areas of high cavitation activity within the bath.

Chapter 9 concentrates on measurements within the NPL reference vessel; bringing together measurements made by staff at the NPL with the NPL broad band cavitation sensor with measurements conducted as part of this project using low light imagery and photon counting, surface event measurements and chemical change measurements.

Chapter 10 brings together the results in chapters 3 to 9 and draws final conclusions from the work before suggesting possible directions for further work.

2. Experimental

2.1. Lab based ultrasonic equipment

Three different methods were used to generate ultrasonic cavitation in the laboratory at Southampton: an ultrasonic horn, single transducer ultrasonic reactors and commercial ultrasonic baths. Each of these devices has differing characteristics. The ultrasonic horn provides an intense and repeatable localised volume, the reactors provided a repeatable larger active volume and the ultrasonic baths provided an example of the industrial world situation. Each system will now be discussed in turn.

2.1.1. Ultrasonic Horn

The ultrasonic horn used was an Adaptive Biosystems ultrasonic horn transducer with a 3 mm diameter titanium tip (also by Adaptive Biosystems) operating at ~ 23 kHz. The horn provided a localised and repeatable volume containing inertial cavitation, in a region close to the face of the emitting surface. This extent of the area of inertial cavitation can be seen from the MBSL emission in image B in Figure 2.1.

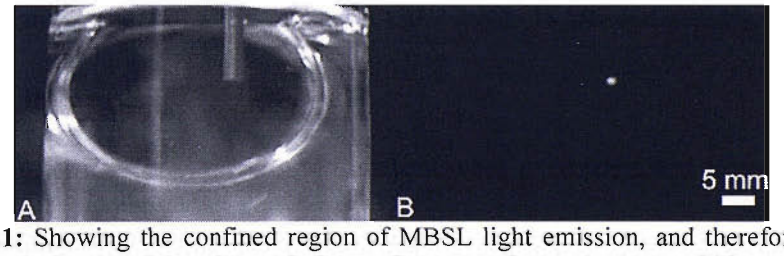

Figure 2.1: Showing the confined region of MBSL light emission, and therefore inertial cavitation, at the tip of the ultrasonic horn. Image A shows the horn within a cell under ambient light condition, image B is an intensified image of the same area with the horn operating. The horn is being driven at 120 V and 23.18 kHz in distilled water.

2.1.2. Ultrasonic Reactors

Four single transducer ultrasonic reactors were used; denoted from this point on as 1, 2, 3 & 4. Reactors 1&4 have been employed in previous studies (*62, 128, 155*) whereas reactors 2&3 were constructed as part of this project. It was found that the transducer driving reactor 1 had degraded and therefore was no longer able to generate the pressures amplitudes required for the generation of inertial cavitation (described in more detail in chapter 3). This necessitated the construction of reactors 2 & 3. Reactors 1, 2 & 3 were all water jacketed allowing the temperature control of the solution within the reactor.

Figure 2.2 shows a schematic of reactor 1 including the dimensions of the cell. The glass water jacketed cell was bonded to a Morgan Electro Ceramics Ltd. transducer with resonance frequency of 27 kHz using slow set epoxy resin (Streurs Epofix).

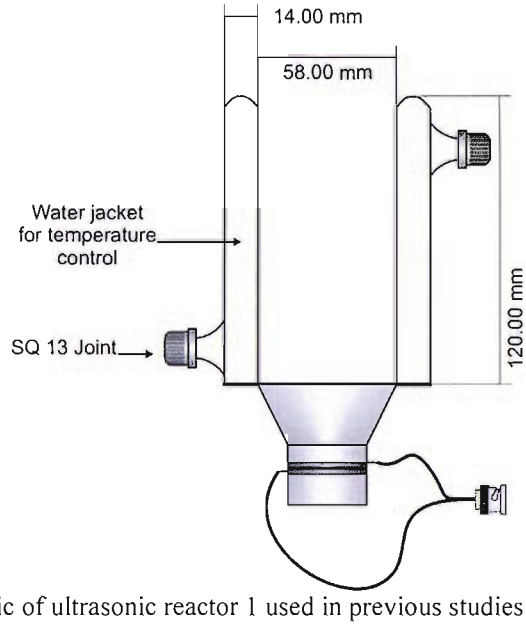

Figure 2.2: Schematic of ultrasonic reactor 1 used in previous studies (*62, 128, 155*).

After the failure of reactor 1 the construction of replacement reactors of a similar design became imperative. Initially replacement reactors were constructed in the same manner as that used for reactor 1 (e.g. a glass base). However, it was found that after a sustained period of use the bases of the reactors became cracked. This was found to be due to the epoxy within the thread of the transducer being extruded from the transducer through the base of the reactor. An image of the transducer complete with the extruded epoxy can be seen in figure 2.3.

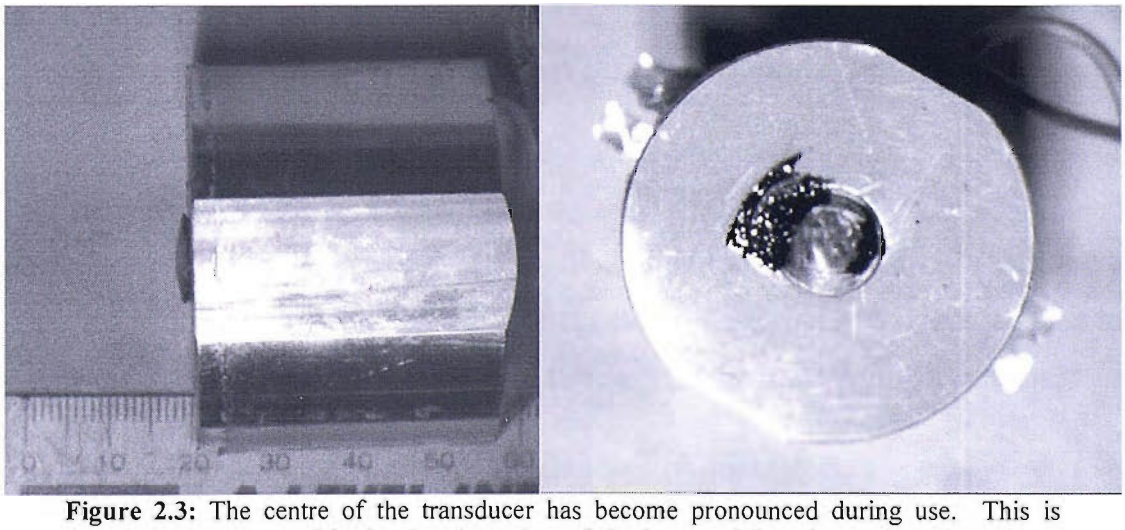

Figure 2.3: The centre of the transducer has become pronounced during use. This is thought to be responsible for the shattering of the bases of the glass cells. Transducer shown a MPI-C-28.

In order to overcome this problem, reactors 2 and 3 differed in construction from reactor 1 in two important ways. First, the glass base of the reactors were replaced by a plastic sheet (from the front of a CD case) and second, fast set epoxy resin (RS) was used to bond the transducer to the base. This prevented ingress of the resin into the threaded hole of the transducer. These two alterations in the construction of the reactor enabled reactors 2 and 3 to be used for prolonged periods without damage.

Reactor 2 was driven by an MPInterconsulting MPI-C-40 transducer with resonant a frequency of 40 kHz and had internal dimensions of 60 mm diameter and 106 mm height. Reactor 3 was driven by an MPInterconsulting MPI-C-28 transducer with a resonant frequency of 28 kHz. Figure 2.4 images A and B show schematics of the reactors 2 and 3 respectively.

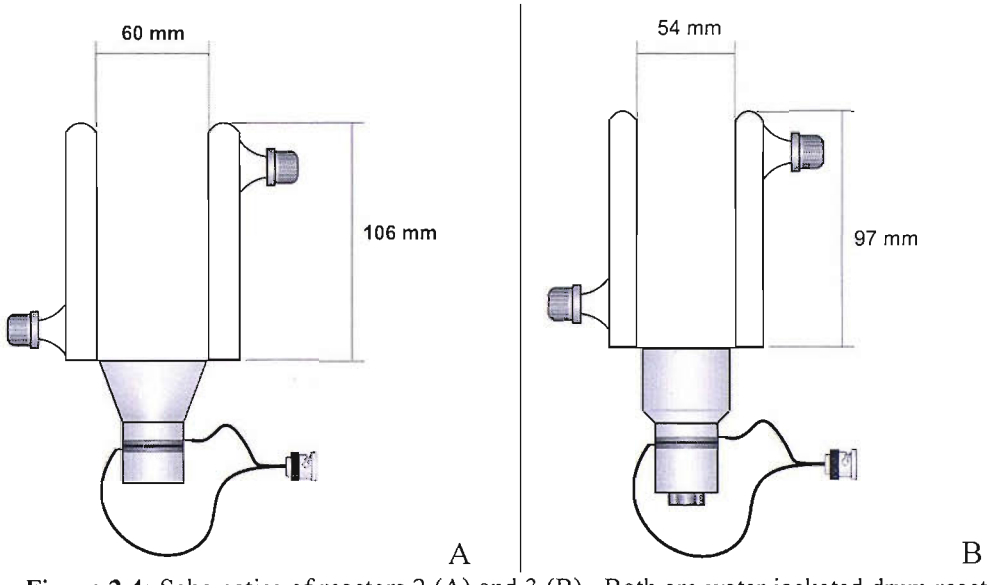

Figure 2.4: Schematics of reactors 2 (A) and 3 (B). Both are water jacketed drum reactors with plastic bases.

In contrast to reactors 1-3 which had double walled glass sides reactor 4 consisted of a single walled cylinder of 1 mm polymethylmethacrylate (PMMA) with a machined metal base sealed in the cylinder with a rubber o-ring and Teflon tape. The driving transducer (Morgan Matroc Ltd, 33 kHz resonance frequency(*171*)) was bonded to the metal base using Epofix epoxy resin (Streurs). Figure 2.5 shows a schematic of reactor 4 and its construction.

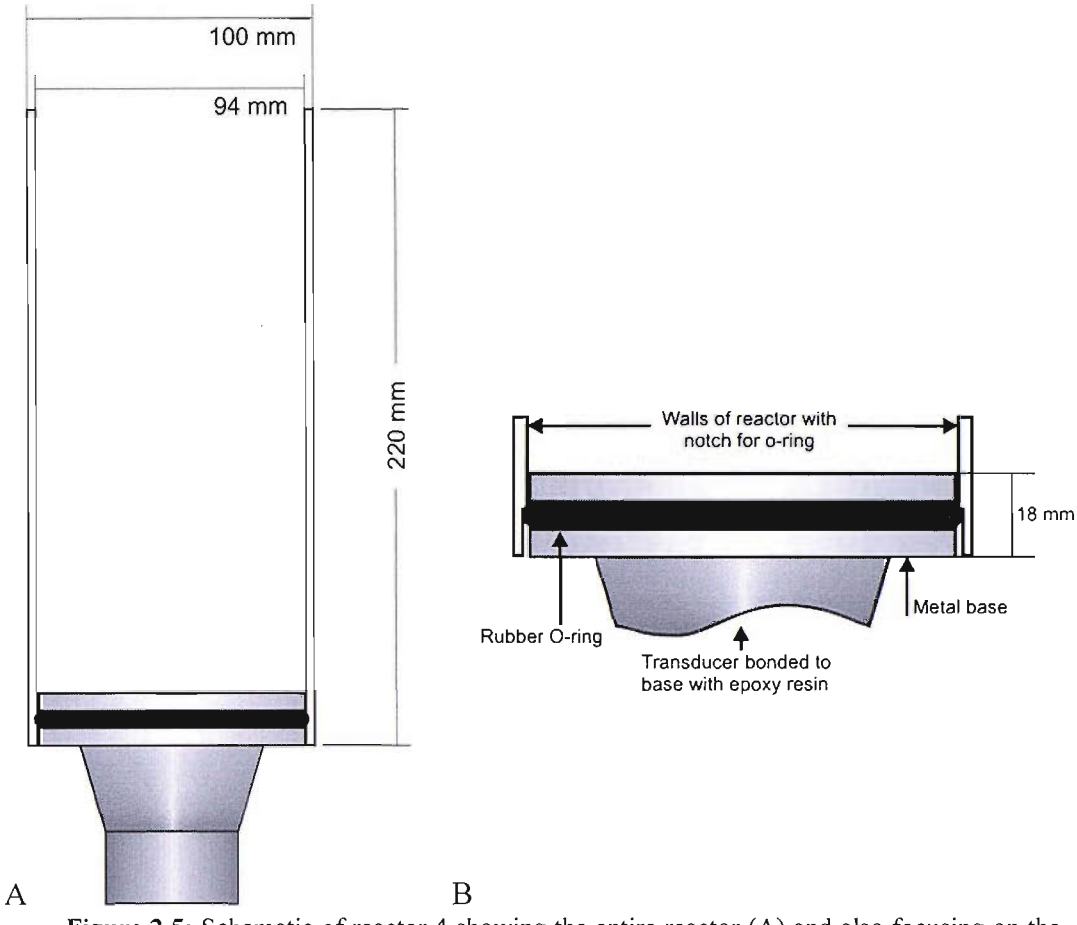

Figure 2.5: Schematic of reactor 4 showing the entire reactor (A) and also focusing on the base of the reactor and how the metal base was attached to the body of the reactor (B).

2.1.3. Commercial ultrasonic baths

Three commercial ultrasonic cleaning baths were used to conduct experiments: an Ultrawave U50 bath, a Branson B1210E-MT bath and a Semat ultrasonic bath named A, B and C respectively. All three were standard ultrasonic baths with timers allowing the variation of the period of sonication. All three baths were used without modification except for thorough cleaning prior to use.

2.1.4. Electrical signal generation

The electrical signal required to drive the ultrasonic horn and reactors 1-4 was generated using a Thurlby Thandar TG1010 function generator and amplified by a Brüel & Kjear 2713 Power amplifier. This setup had a maximum zero to peak voltage amplitude of 150 V. The signal was monitored using an oscilloscope. The drive voltage was recorded separately for each experiment and can be found in the relevant figure legend.

2.2. Surface event measurement

A major component of this thesis involved the counting of erosion/corrosion events on a passive electrode under potential control. The measurements were conducted using aluminium and titanium electrodes.

2.2.1. Electrode construction

Aluminium electrodes were constructed by sealing aluminium wire (various thicknesses, Advent) in Epofix epoxy resin (Streurs) inside glass Pasteur pipettes (figure 2.6). The electrodes were connected to shielded coaxial cable (RS 7/0.2 mm) by soldering. Titanium (Advent) electrodes were constructed in two different supporting materials; Epofix epoxy resin and glass. The epoxy supported electrodes were constructed in a similar manner to those for aluminium. The titanium wire was sealed within a glass Pasteur pipette using Epofix epoxy resin, but due to difficulties in soldering the titanium wire to the coaxial cable the connection between the two was made using conductive silver paint (RS) coated with lacquer.

Due to its low melting point (660 ^{o}C) aluminium is unsuitable for sealing in glass as it was found to become molten when glass was sealed around the electrode wire. Titanium though has a high enough melting point (1660 ^{o}C) to be sealed in glass. The glass electrodes were constructed by first sealing a short section of wire (ca 5 cm) at the end of a soda glass support with a blow torch. The glass support was then placed in an electrode fabricator and the glass collapsed around the electrode wire using a heating element whilst keeping the electrode under reduced pressure (figure 2.6). To form an electrical connection between the electrode wire and the coaxial cable was made by melting indium wire (Aldrich, 1 mm diameter 99.99% purity).

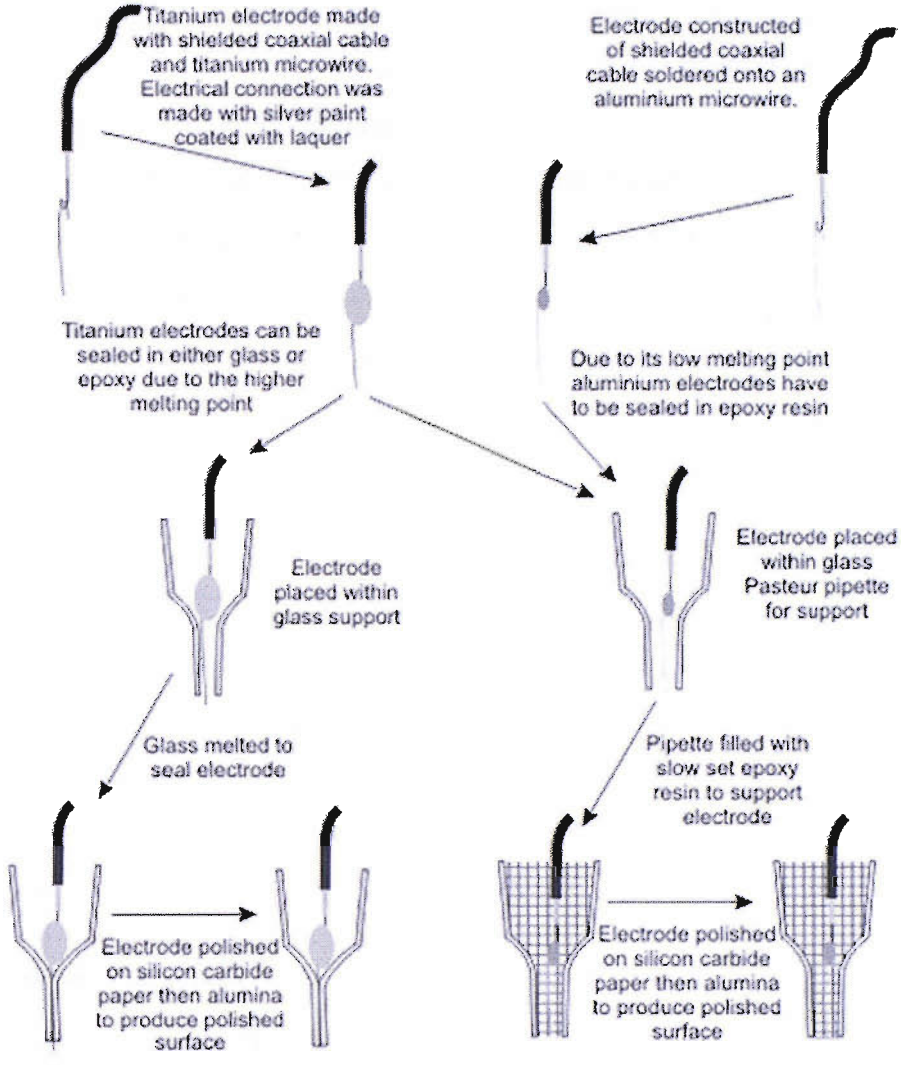

Figure 2.6: Showing the method by which aluminium and titanium electrodes were constructed

The electrodes produced using both methods were polished to produce a smooth reproducible surface with successive grades of silicon carbide paper (400, 600 and 1200 Deer) and an alumina slurry (1 μm and 0.3 μm Buehler) supported on Microcloth (Buehler). The electrodes were polished back to a smooth mirror like surface before each experiment unless stated otherwise.

2.2.2. Electrochemical instrumentation for surface events

2.2.2.1. Under normal conditions

The time scale of the current time transients produced by the cavitation surface erosion/corrosion events on the electrodes necessitated that a relatively simple

instrumental setup was employed. To this end, a current follower was connected at 0 V verses a counter/reference electrode consisting of either a silver wire or a stainless steel needle (see figure 2.7). Two current followers were used in this project, both constructed in house. One was battery powered and the other mains powered. In order to cope with the fast current time events generated by the erosion/corrosion events the operational amplifiers in the current followers were OPA121KP with a bandwidth of 2 MHz. Current time transients were then recorded using either a Tektronix TDS 224, a LeCroy 9310AM oscilloscope or a TiePie Engineering Handyscope HS3 (100 MHz) USB oscilloscope. All the data was stored on a PC.

2.2.2.2. Under earthed conditions

The earthed metal tanks used in commercial ultrasonic cleaning baths and the NPL reference vessel introduced a large amount of electrical noise and interference into the signal recorded from the electrodes. Consequently a novel optically isolated fast unipolar current follower was developed that enabled measurements in such conditions to be made. The construction of this current follower, its' testing and an examination of alternative methods of isolating the electrochemistry from the surrounding environment is discussed in chapter 7.

2.2.2.3. Peak Counting

In previous studies (*54, 74, 172*) a computer with a fast data acquisition system has been used to count the number of surface events taking place within a certain period. These studies have concentrated on events on the surfaces of lead or stainless steel electrodes which are longer in period then those seen for both aluminium and titanium (lead electrodes take 60 μs to return to 10% of the maximum value (*54*), aluminium 15 μs). This, coupled with the necessity of the system being portable for use with the NPL test rig, requires an alternative way of counting and analysing the events taking place. To accomplish this, an Amptek Pocket MCA 8000A Multi Channel Analyser (MCA) was employed to analyse the signal from the electrodes. The MCA records the number of peaks as a function of the magnitude of the peak. The ability of the MCA to collect worthwhile data will be discussed in greater detail in chapter 4 section 4.5.1.

2.2.3. Experimental setup for ultrasonic horn

To conduct surface event measurements in a repeatable environment the Adaptive Biosystems ultrasonic horn was mounted vertically above a cell into which a working electrode could be introduced from the base and into which a counter/reference electrode could also be placed. The horn could be positioned vertically using a Newport micrometer stage (25 mm travel 10 μm resolution). In addition a Photon Control XY stage (25 mm travel and 10 μm resolution in both directions) was employed so that the electrode could be positioned accurately in the area of intense cavitation near the horn tip. A schematic of the setup can be seen in figure 2.7. For line scans one of the micrometer screws could be removed from the XY stage and replaced by a Parker L25i positioner to allow automation of the process.

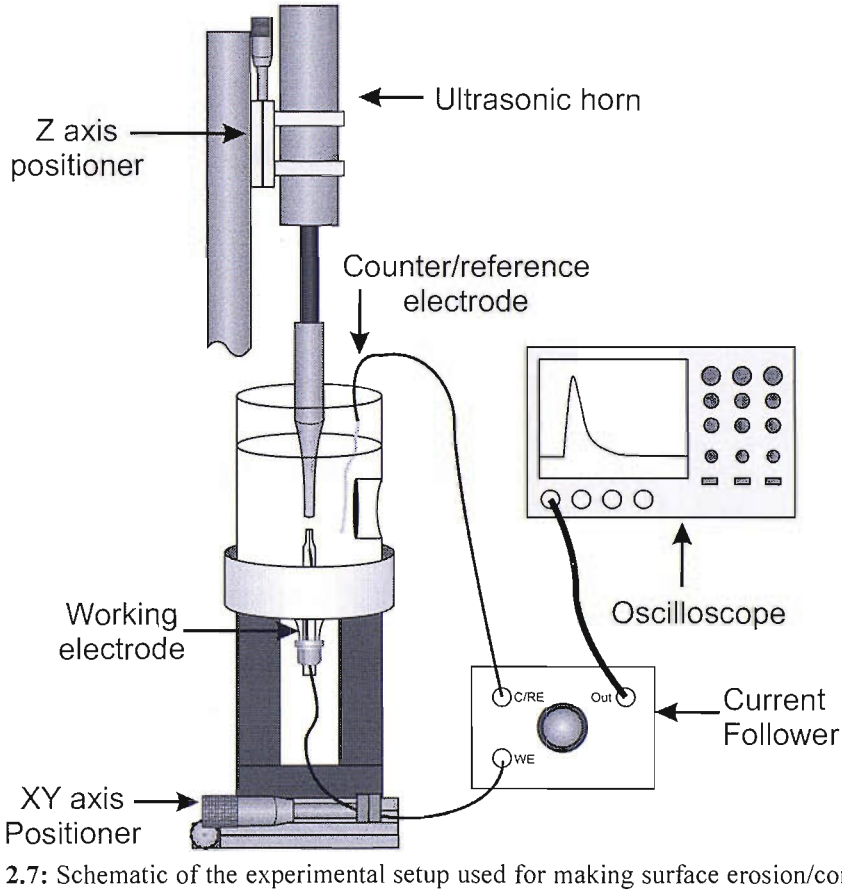

Figure 2.7: Schematic of the experimental setup used for making surface erosion/corrosion measurements at the tip of an ultrasonic horn.

2.2.4. Experimental setup for reactors

For surface measurements within either reactors 1-4 or the ultrasonic cleaning baths the working electrode and counter reference electrode were mounted vertically within the vessel. A schematic of the setup can be seen in figure 2.8.

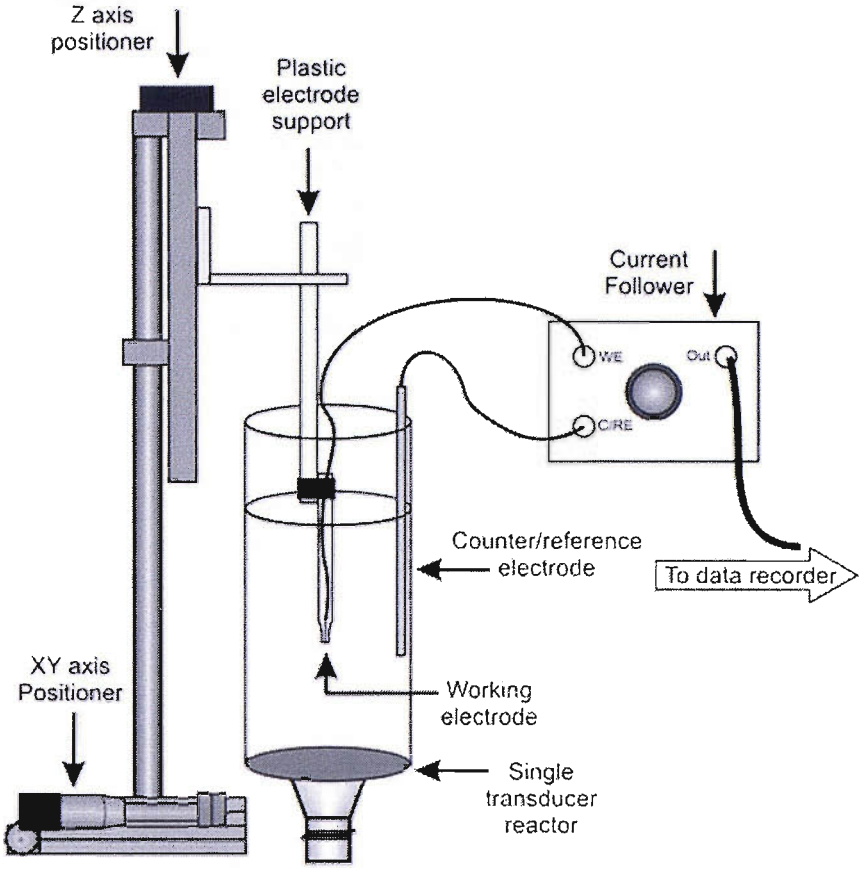

Figure 2.8: Schematic of the experimental setup for making surface erosion/corrosion in single transducer reactors.

2.3. Chemical change measurements

Two different methods were utilised in this work to conduct the chemical change measurements; electrochemical and UV/VIS detection. For both measurements the level of chemical change was determined using flow cells as direct assay within the ultrasonic environment was not possible.

2.3.1. Electrochemical measurements

2.3.1.1. 3 electrode flow cell

The three-electrode cell, a schematic of which can be seen in figure 2.9, had been used in previous studies (*62, 128, 173*). In this work the flow cell was employed as both a 2 and 3 electrode system. For both set-ups a 0.5 mm platinum working electrode sealed in glass was used. In the 3 electrode system a stainless steel counter electrode and an in house manufactured saturated calomel reference electrode (SCE)

were used. When used as a 2 electrode set-up the SCE electrode was used as a counter/reference electrode. Two configurations were used for the inlet to the flow cell; a 1.6 mm diameter Teflon tube and a 1 mm diameter, 18 gauge needle.

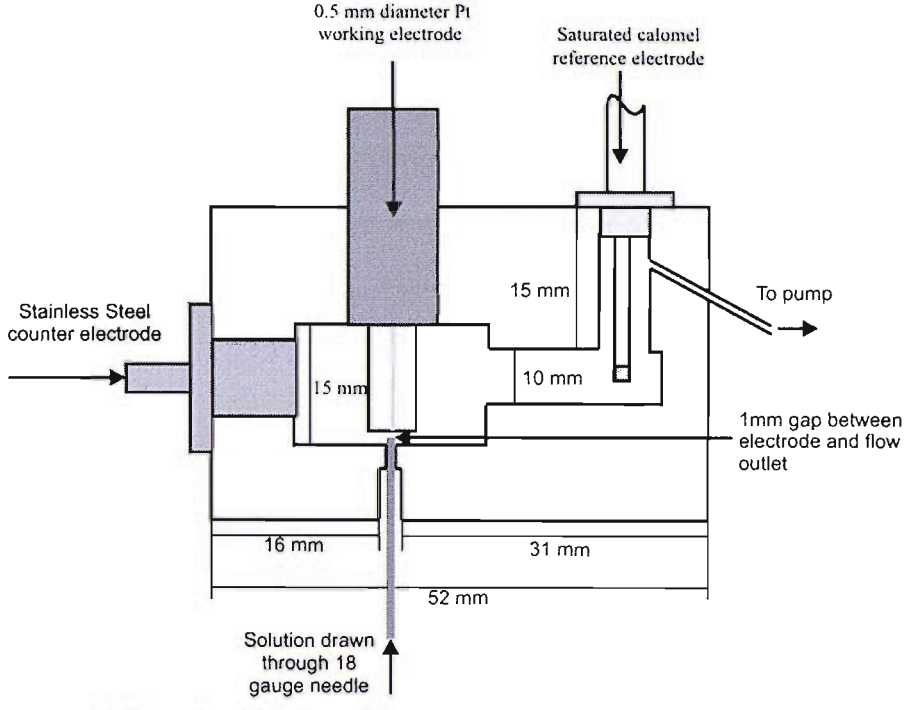

Figure 2.9: Schematic of the three electrode flow cell (adapted from (*62*)).

2.3.1.2. Acquisition under normal conditions

Depending on the requirements of the experiment and the number of electrodes used different measurement protocols were used. For the majority of measurements only two electrodes were used. In this case where a varying potential was required an in-house USB 2 electrode potentiostat was used. When a single potential difference between the working and reference electrodes was required either the USB potentiostat was used or a separate potential source and current follower was employed. When experiments were conducted at which the potential between the working and counter/reference electrodes was maintained at 0 V, a current follower alone was used. When three electrodes were used an in-house three electrode potentiostat was used. With the exception of the measurements conducted using the USB potentiostat the output from the current follower (whether in a potentiostat or a stand alone device) was interfaced with a PC using an ADC card (either a National instruments PCI-6025E or a Measurement Computing CIO – DA5802/16) and the data recorded by an in-house Visual Basic based software.

2.3.1.3. Bi-polar optocoupled measurements

In order to conduct measurements in the environments found in the ultrasonic cleaning baths and the NPL reference vessels it was necessary to use a bipolar optically isolated current follower. In addition to being a current follower the device also encompassed a rudimentary voltage source making it possible to vary the potential between the working and counter/reference electrodes. The necessity of this device, construction, testing, as well as alternative methods of isolating the electrochemistry from the earthed environment, is discussed in chapter 7. The signal from the current follower was recorded using either a National Instruments PCI-6025E ADC card or a Tie Pie Engineering Handyscope HS3 USB oscilloscope.

2.3.2. UV/VIS Spectroscopy

A PC based Avantes UV100-2 spectrometer with an Avantes Mini-D2 UV-VIS-NIR Light source (both Anglia instruments) was used to record the absorbance and spectrum of solutions irradiated by ultrasound. The light source was connected directly to a cuvette holder and onto the spectrometer by means of a fibre optic cable. A Hellma Precision quartz cuvette with a 1 cm path length was used for each measurement.

In addition an optical flow cell with a 1cm path length was constructed. A schematic of the flow cell is shown in Figure 2.10. The flow cell was used to measure the absorbance of the solution within the reactor as a function of time, therefore allowing any change as a function of position or power to be studied. Flow cells used in previous work (*39*) had a short path length (~1 mm) which wasn't sufficient to pick up the low concentrations of I_3^- generated. A peristaltic pump (detailed in section 2.3.31) was used to draw solution through the system. Solution was either drawn from the reactor directly or passed through an electrochemical flow cell prior to arrival in the optical cell. This enabled simultaneous UV/VIS absorbance and electrochemical measurements to be made.

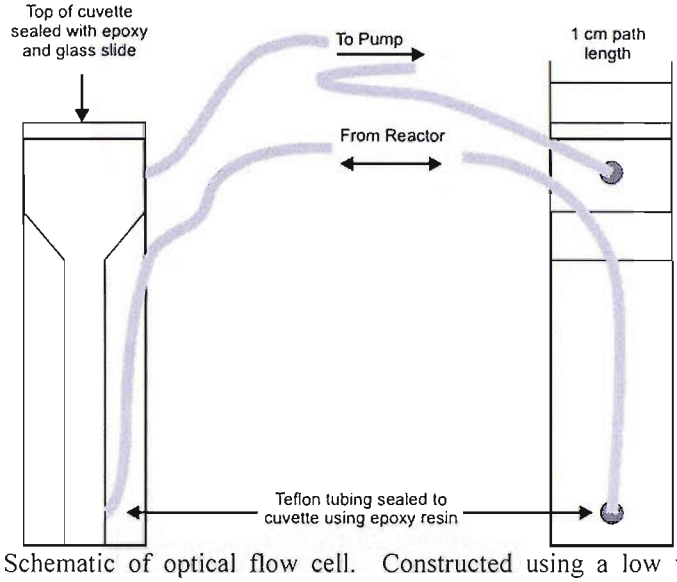

Figure 2.10: Schematic of optical flow cell. Constructed using a low volume plastic cuvette.

2.3.3. Pumping system

The pumping system by which solution is removed from the reactor is almost as important as the flow cell in which the measurement is made. For the electrochemical measurements, a constant stable flow is required. In this work a peristaltic pump (Pharmacia Fine Chemicals, P-1) was used for this purpose.

2.3.3.1. Peristaltic pump

The peristaltic pump produced significant fluctuation in the rate of flow. To reduce this fluctuation, two different "damping systems" were employed: the first (for high flow rates) consisted of a syringe with the plunger pulled fully back attached to a T joint in the piping just before entering the pump (figure 2.11 B_1). The second (for low flow rates) consisted of a syringe with the plunger fully removed and the end sealed with latex from a glove and insulating tape (figure 2.11 B_2).

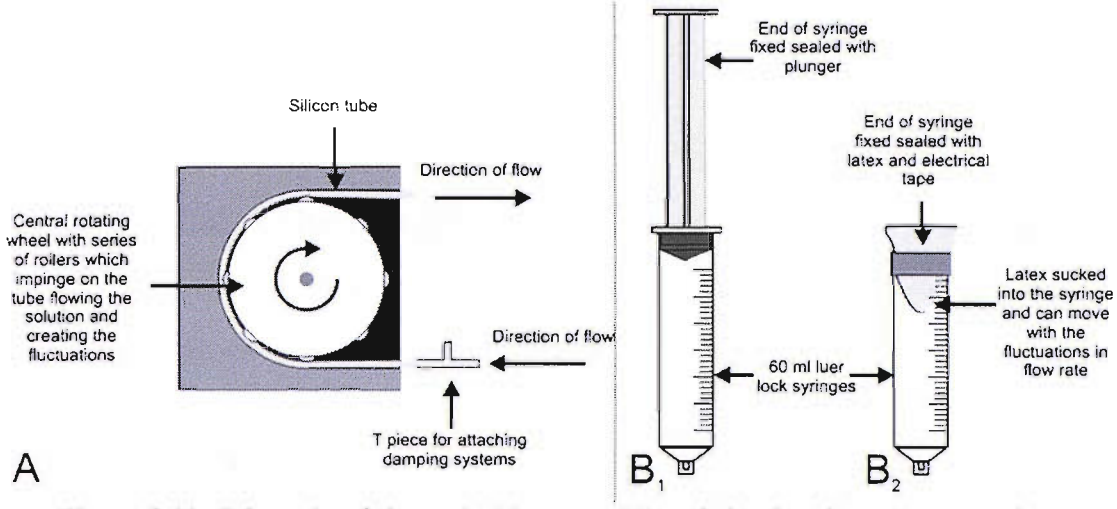

Figure 2.11: Schematic of the peristaltic pump (A) and the damping systems used to smooth the flow (B_1 & B_2).

2.4. Pressure measurement

Pressure measurements were conducted with either a Brüel & Kjaer 8103 hydrophone or a Gras Type 10 CT hydrophone attached to a Brüel & Kjaer 2635 charge amplifier and recorded using either a fast PC based ADC card (Measurement Computing PCI-DAS 4020/12) or a LeCroy 9310AM oscilloscope attached to a PC in order to save the data.

2.5. Low light measurement

The level of light emitted from a solution undergoing intense multibubble sonoluminescence (MBSL) within an ultrasonic reactor can be measured as being of the order of 60 photons per second (see figure 6.1 in chapter 6). The addition of a chemical additive such as luminol (3-Aminophthalhydrazide) can boost the light output by means of sonochemiluminescence to around 5000 photons per second. Even with the addition of chemical additives the level of light recorded is still significantly less than the level of ambient light found in a laboratory. Consequently in order for accurate and repeatable results to be made it was imperative that all measurements were conducted in black out conditions, ideally in a dark room. Working in a dark room it was possible to reduce the level of light recorded with the single photon counter module to ~3 counts s^{-1}. The only exception to this was the

measurements conducted on the NPL reference vessel the reasons for which are dealt with in chapter 9.

2.5.1. Imaging of the reactor

The low intensity of light generated by cavitation makes the use of standard photographic equipment impractical. Consequently two low light camera systems were employed so that immediate images could be made. The two cameras were a Darkstar intensified CCD video camera from Photonics Science and a unit constructed in-house from a separate image intensifier and video camera. The in-house constructed unit consisted of a c-mount lens (25 mm Schneider f0.95 or 25 mm Fujinon f1.4) focusing the image onto the three stage phosphor intensifier (Photek MCP325 intensifier controlled by a Photek MCPU - 2.3 control unit) the image from which was recorded using a JAI CV-A50 CCD camera connected to a Cyberoptics imagenation PXC200A capture card in a PC. The images were recorded using in house software based on the manufacturer supplied software and adapted in Visual Basic. The Photek intensifier setup was capable of producing a luminous gain of the order of 2×10^7 compared to a normal CCD camera. The arrangement of the system can be seen in figure 2.12.

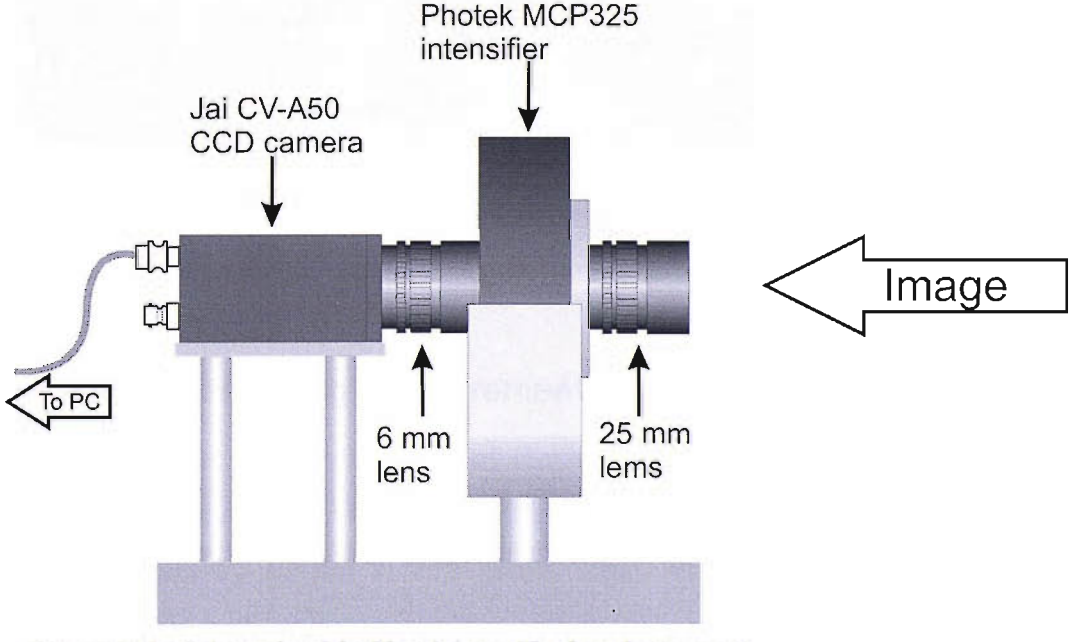

Figure 2.12: Schematic of the Photek intensifier based camera system.

The Photonics Science Darkstar camera was not capable of the same level of light amplification as the Photek intensifier based system but was more portable and easier

to position. The image from the Darkstar camera was recorded using either the same Cyberoptics capture card as for the Photek system or by a Hauppage USB WIN-TV capture device and software.

2.5.2. Stacking Software

To remove random noise from the images, multiple images were stacked and/ or averaged using Tambaware Software Image Stacker V 1.03. The effect of this software can be seen in figure 2.13. Figure 2.13 (a) shows an original image; while figure 2.13 (b) is the result of stacking and averaging 93 other images recorded at the same time leading to a considerably clearer image.

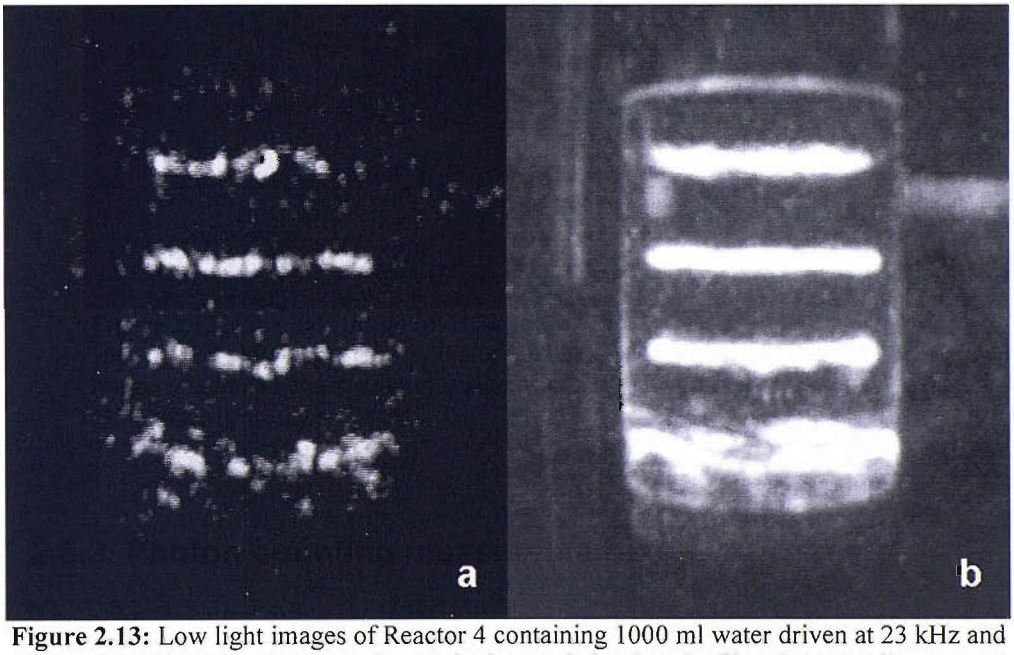

Figure 2.13: Low light images of Reactor 4 containing 1000 ml water driven at 23 kHz and 150 V (~250 kPa). Image a is the original recorded using the Photek intensifier system. Image b is the amalgamation of image a with 93 other images recorded at the same time using image stacking software.

2.5.3. Photon counting measurements

To make quantitative measurements of the light output two photon counters were used. A prototype SensL PCM SN 10 prototype photon counter with an active detector 150 μm by 10 μm in size and a SensL PCMPlus-20 intelligent photon counting module with an active detector 150 by 20 μm. The prototype PCM SN 10 was a standard photon counter module generating a pulsed output that required external measurement. The signal from the photon counter was analysed using an EG

& G Multi-channel scaler connected to a PC. The dwell time was set to 50 ms for all experiments and readings recorded for either 10 or 8 sec at a time. In contrast the PCMPlus-20 counting module had an on board counting device and was controlled from a computer by means of a USB connection and data recorded using SensL integrated environment software. The PCMPlus-20 photon counting module was used for all experiments except for those in chapter 3 for which the PCM SN 10 module was used.

2.5.4. Use of luminol

The addition of a solution containing luminol to a cavitating environment can greatly increase the level of light emission through the process of sonochemiluminescence. An example is shown in figure 2.14 which shows the luminescence from a Guinness Surger device. The elevated level of light emission from Luminol also permits the use of long time scale standard photography of a particularly active reactor such as the image of reactor 4 in figure 2.14.

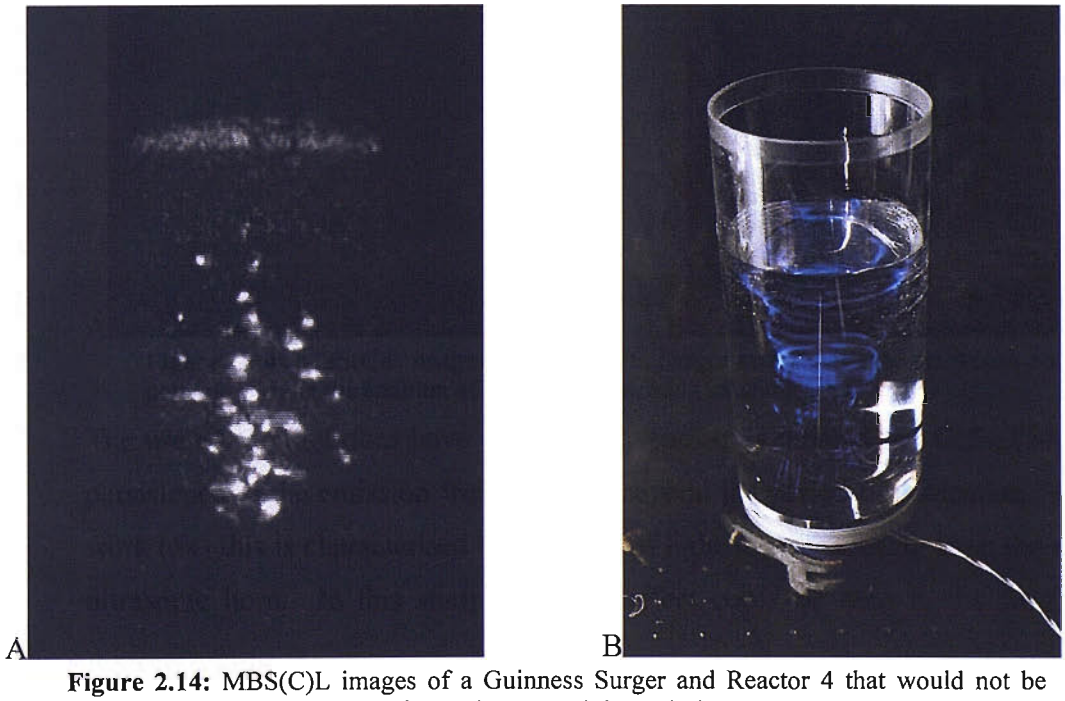

Figure 2.14: MBS(C)L images of a Guinness Surger and Reactor 4 that would not be possible without the addition of a luminol containing solution.

The use of luminol does have certain draw backs; as reported by Offin (*54*) there is persistence in the emission from luminol beyond the period of sonication. In Offins work (*54*) this is characterised by a stream of light seen emanating from the end of an ultrasonic horn. In this study a similar effect could be seen in the forming of a

"glowing cup" in a reactor after a prolonged period of sonication. The presence of this phenomenon was not restricted to the single transducer reactors but could be observed in all environments tested. Figure 2.15 show an example in reactor 3.

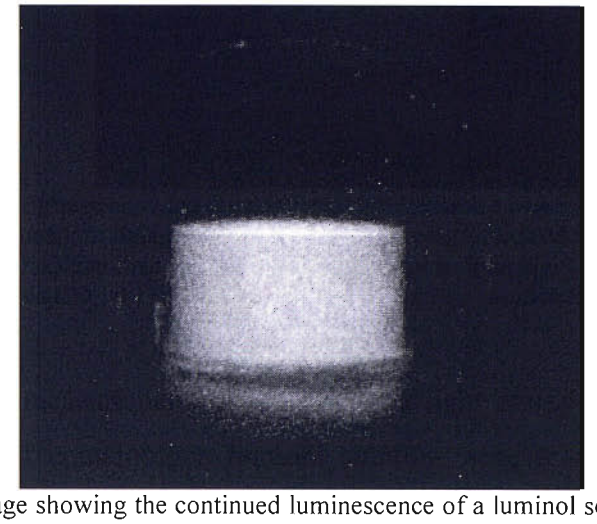

Figure 2.15: Image showing the continued luminescence of a luminol solution beyond the period of sonication. Image is of reactor 3 after being sonicated for 30 s at 143 kHz and 80 V (zero to peak) and then left for one minute prior to imaging. The reactor contained 100 ml 100 mM Na_2CO_3, 0.1 mM EDTA and 5 μM luminol solution held maintained at 25 C.

If quantitative measurements of the level of light emission from an ultrasonically cavitated vessel containing a lumionl solution were made using a single photon counter or photo multiplier tube then the persistence of the luminol could be seen more clearly. The graph in figure 2.16 shows that the luminescence from the vessel containing luminol extends beyond the period of sonication. Light emission in figure 2.16 recorded using a EMI-Gencon Inc. RFI/B-293 photo multiplier tube (PMT) powered by a 2 kV power supply (Brandenburg 475R).

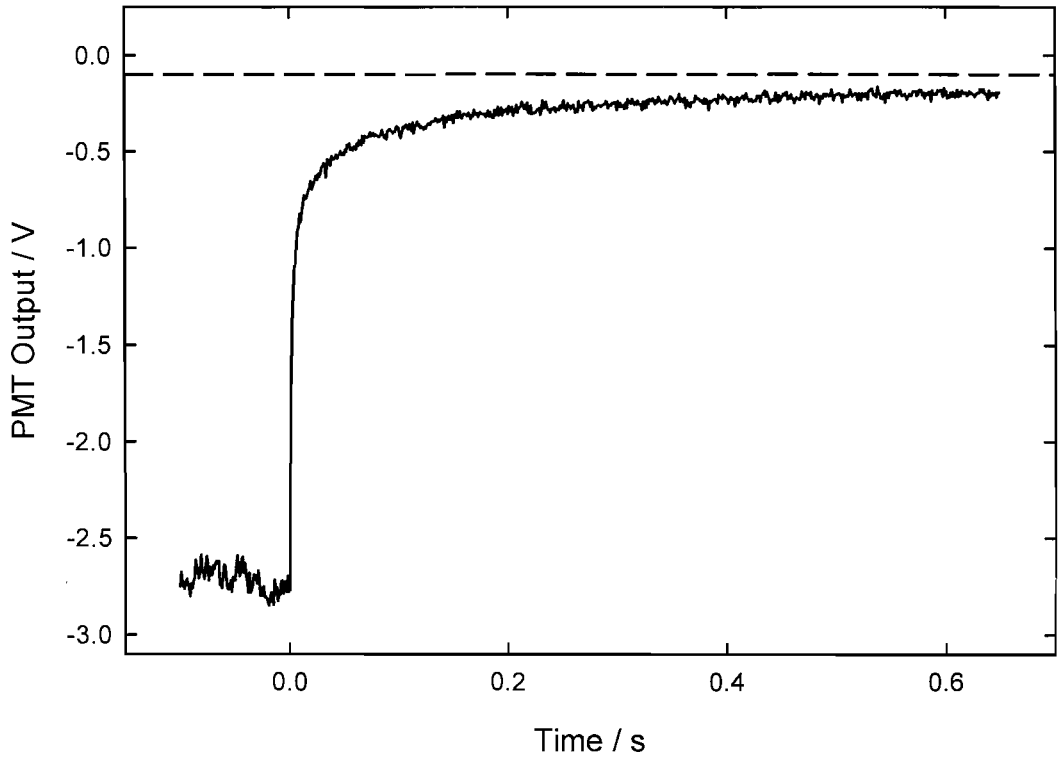

Figure 2.16: PMT trace showing the persistence of the luminescence from a solution of luminol beyond the point at which sonication ended (0 s). The initial signal from the PMT tube prior to sonication is represented by (- - -). Reactor 3 was driven for 30 s at 143 kHz and 80 V (zero to peak) with 100 ml 100 mM Na_2CO_2, 0.1 mM EDTA and 5 μM luminol solution held maintained at 25 C. The PMT tube was driven at 1600 V.

The persistence in the luminescence from solutions containing luminol beyond the period in time during which they are subjected to cavitation presents certain problems. The continuation in the luminance precludes the use of luminol to amplify the light output of images acquired of an ultrasonic horn or any similar situation where a high degree of flow takes place due to the location of the luminescence being extended to locations in which no cavitation is found. For the majority of situations where there is no substantial flow (e.g. single transducer reactors) the region of light emission is not significantly increased by the persistence of the luminol light emission; the emission having subsided before the solution moves away from the point of cavitation.

2.6. High-speed imaging

High-speed imaging was used to further understand the processes involved in the removal and then reformation of passivated oxide layers on electrodes. Experiments were conducted at the tip of the ultrasonic horn and in the centre of a single transducer ultrasonic reactor (reactor 4). Imaging was conducted using a Photron APX-RS camera and a Navitar 12 x Zoom c-mount lens connected to a fast PC by means of a firewire (IEEE 1394) cable. The camera was mounted on an XY stage enabling the easy positioning of the camera and ensuring an accurate focus could be attained. The images were analysed using Photron Fastcam Viewer software version 2.4.3.8. Illumination was provided by a Fostec DCR 150W Light Source positioned such that the image reaching the camera was a silhouette. Electrochemical information was collected using a 250 μm diameter aluminium working electrode and a silver wire counter/reference electrode with the signal amplified by a battery current follower and recorded on a Le Croy 9310 digital oscilloscope connected to a PC using a GPIB port. To ensure simultaneous recording of the high-speed imagery and the electrochemistry the signal from the electrochemistry was monitored by a PC based ADC card (National Instruments PCI-6025E) and when the magnitude of the current from the electrochemistry exceeded a trigger value (signifying the presence of an event) a TTL pulse was sent to the camera and oscilloscope to trigger them. Despite both the camera and the oscilloscope being triggered simultaneously there is an uncertainty in the exact position of the actual trigger relative to the zero time stamp on the high-speed image frames of up to three quarters of a frame. Both the camera and the oscilloscope were configured such that the trigger would fall in the centre of the data recorded. A schematic of the set up with the ultrasonic horn is in figure 2.17.

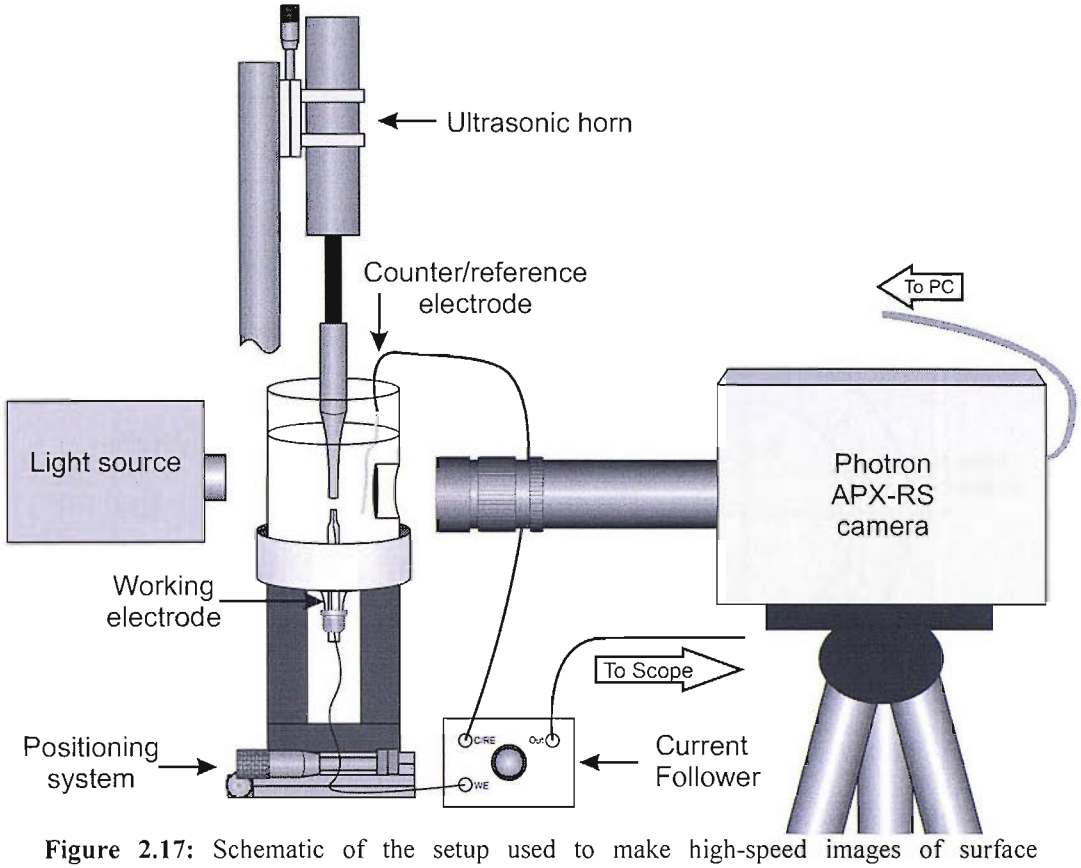

Figure 2.17: Schematic of the setup used to make high-speed images of surface erosion/corrosion events.

2.7. NPL Sensor

An NPL broadband acoustic sensor was used to compare the broadband high frequency acoustic emission with light, pressure and surface erosion/corrosion measurements. The sensor is described in detail in literature (*163, 164*) and is hoped to be the basis of a standardised unit of cavitation. The output from the sensor was recorded using an NPL cavimeter which showed the level of activity in terms of volts. Prior to use the sensor was soaked in distilled water for at least 24 hrs to ensure that the surface was fully wetted to give consistent results.

2.8. NPL Reference vessel

NPL have developed an acoustic cavitation reference vessel in order that different measurement methods can be compared. The reference vessel is based on a model P1800-25 Ultrasonic Processing Cell produced by Sonic Systems with a volume of 30 dm^3. The vessel is positioned within an enclosure below a 3-axis positioning system

(Time and Precision) allowing the positioning of sensors within the vessel. Control of the vessel and the positioning system is conducted by a LabView based program on a PC.

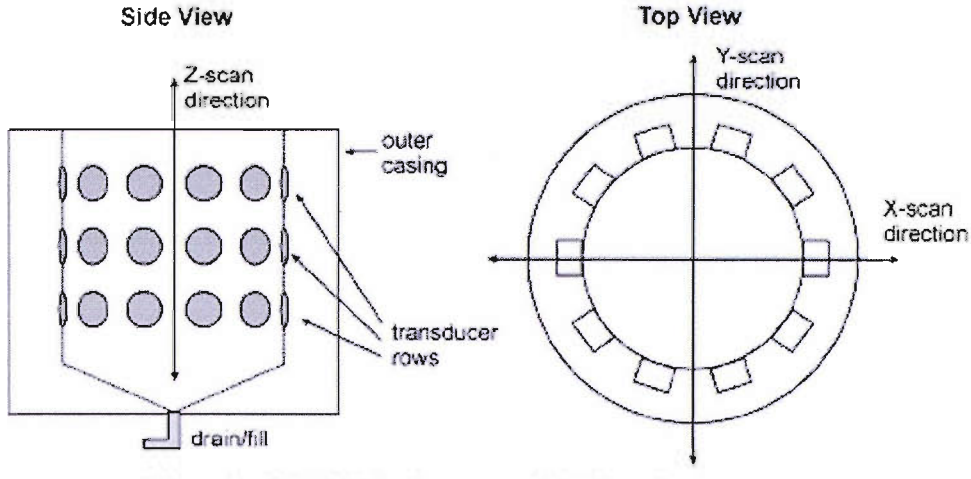

Figure 2.18: Schematic of the NPL reference vessel. Taken from Hodnett (*162*).

Figure 2.18 shows a schematic of the reference vessel taken from (*162*). The vessel is made of a stainless steel with a hard-chromed inner surface and is 330 mm high with a diameter of 312 mm giving a volume of approximately 30 dm^3. Bonded in three rows of ten are thirty identical 25 kHz PZT transducers; in the work conducted in this thesis only the middle set of transducers were utilised these being at the "half height" of the vessel. The controlling computiong program allowed the variation of the drive power transmitted to the transducers from 10 to 600 W. The water within the vessel was provided by a Elga Option 10 water system.

2.9. Chemicals

All solutions, except those for use in the NPL reference vessel, were made up using water from an USF Elga Purelab Option E10 water purification system. Water purified in this manner had a conductivity of below 0.01 $\mu S\ cm^{-1}$ and a low organic content (manufacture quoted TOC < 30 ppb). All chemicals were used without further purification; their suppliers and purity can be found in table 2.1.

Name	Formula	Supplier	Purity
Potassium Chloride	KCl	Fisher	99.7 %
Potassium Iodide	KI	Timstar	AR
Sodium Sulphate	Na_2SO_4	Fisher	LRG
Potassium Ferricyanide	$K_3FE(CN)_6$	Sigma	99+ %
Sodium Nitrate	$NaNO_3$	Fisher	99+ %
Stontium Nitrate	$Sr(NO_3)_2$	Sigma	99+ %
3-Aminophthalhydrazide	$C_8H_7N_3O_2$	Aldrich	97 %
Hydrogen peroxide	H_2O_2	BDH	29-31 %
Sodium Carbonate	Na_2CO_3	BDH	99 %
EDTA		Lancaster	-

Table 2.1: Table of chemicals

3. Sonochemical measurements

It is well known and understood that the action of inertial cavitation can lead to the formation of radicals in the high temperatures and pressures found at the point of bubble collapse (*1*). The measurement of the concentration of these radicals or their bi-products provides a good method for ascertaining the level of sonochemical activity.

Previous studies have shown that it is possible to detect radicals generated by the action of inertial cavitation (be they $H^{\bullet}$ or $OH^{\bullet}$) either directly using electrochemistry (*174*) or indirectly by the use of various radical trapping methods (*141-143*). Though these methods are effective they are often difficult and intricate in their deployment. The simplest method available is the use of a dosimeter that enables the generation of the $OH^{\bullet}$ radicals to be monitored using either electrochemistry or UV/VIS absorbance spectroscopy.

3.1. Use of dosimeter

The dosimeter chosen for this work was KI which works through the oxidation of I^- to I_3^- by $HO^{\cdot}$ radicals according to the Weissler reaction (*60, 145*). The advantage of this dosimeter is that it can be detected using both electrochemical and spectrochemical measurements(*62*). Figure 3.1 shows a cyclic voltamogram of a solution of 10 mM KI and 90 mM KCl. The solution has been subjected to sonication for 600 s which resulted in a concentration of 17 μM I_3^- ions being present; the current associated with which is too small to be observed when compared to the I^- oxidation and oxygen reduction signals. In figure 3.1 it can be seen that at above +0.4 V *vs.* SCE the iodide (I^-) ions are oxidised to I_2, some of which is plated onto the electrode surface and some forms I_3^-. On the reverse scan the iodine can be seen to be stripped from the electrode surface as well as I_2/I_3^- being reduced at the electrode surface. Reaction (1.4) has shown that I_2 and I_3^- are in equilibrium in solution and therefore if one species is reduced so will the other species. In homogeneous conditions (i.e. when I_2 is not plated on the surface of the electrode) I_3^-/I_2 can be reduced at 0 V *vs.* SCE and from the current the concentration of sonochemically generated I_3^- can be ascertained.

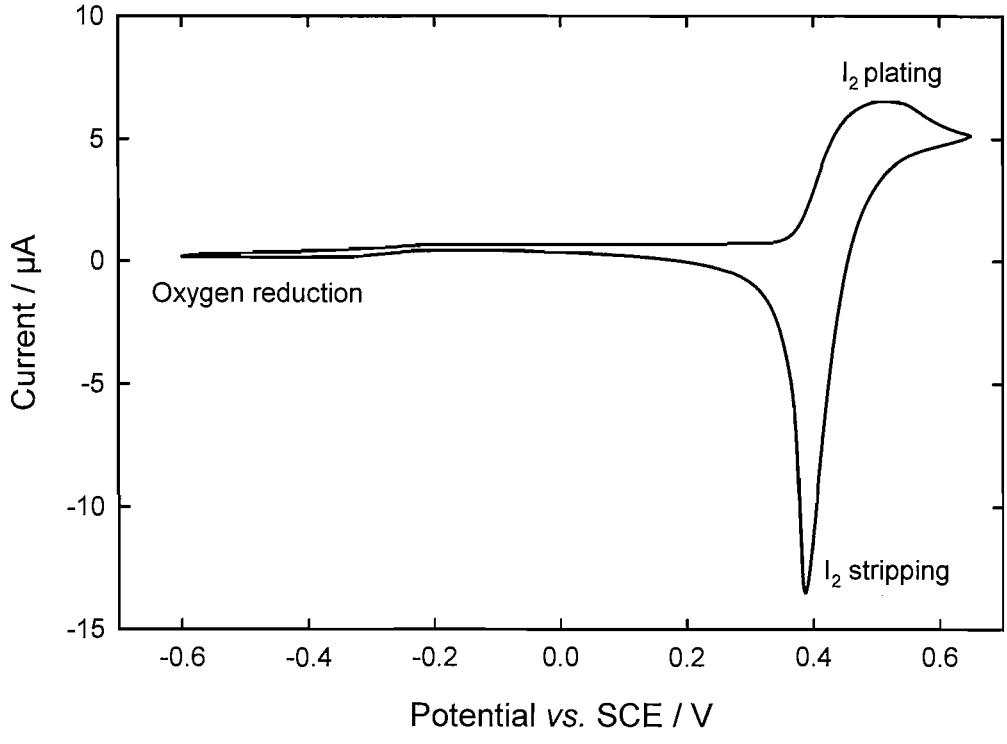

Figure 3.1: Cyclic voltamogram of a solution of 10 mM KI and 90 mM KCl after exposure to ultrasound. Solution now contains 17 µM I_3^- which cannot be observed on the CV. The solution was irradiated at 143 kHz and 220 kPa (zero to peak) in reactor 3. CV conducted on a 0.5 diameter Pt electrode with a SCE reference electrode and Pt gauze counter electrode. I_3^- concentration calculated using UV/Visable absorbance.

One of the main constraints of measuring chemical change is that both electrochemical and spectrometric measurements are only feasible *ex-situ* from the reactor. It is theoretically possible to make spectrometric measurements utilising the reactor as the absorbance cell; measuring the absorbance across the entire width of the reactor. In reality this is impractical; apart from the cell having to be constructed of quartz any bubbles in the reactor, be they large individual bubbles or part of cavitation bubble cloud, will alter the absorbance (through scattering (*54*)) of the solution and therefore adversely affecting the result. Even if this could be applied to a small scale lab based reactor it would be impossible and impractical in a commercial ultrasonic bath with metal sides impervious to light.

There are also a number of complications associated with *in situ* electrochemical measurements within a cavitating environment. Acoustic streaming and other localised flow induced by the primary pressure field and cavitation, affects the mass transfer of analyte to the electrode surface. This variation leads to a variable current recorded at the electrode that is not solely dependent on the concentration of the

analyte within the solution (*175*). Consequently for both spectrometric and electrochemical measurements flow cells were employed where a small proportion of the solution is removed from the reactor, analysed and then returned to the reactor in a closed loop system.

We will now look at the flow cells used and then apply them to make measurements within single transducer ultrasonic reactors.

3.2. Flow cells

Previous studies (*62, 128*) utilised a 3 electrode flow cell system in which the solution to be analysed was drawn from the base of the sonochemical reactor by means of a 1.6 mm diameter Teflon tube, passed through a peristaltic pump and then driven into the flow cell. Though this system works well it is only capable of giving an overall or global measurement for the reactor; providing poor spatial and time resolution within the reactor as a result of the inlet to the system being easily moved by the action of the activity within the reactor. In an effort to improve the spatial resolution of the measurements two approaches were used; changing the conformation of the inlet system for the three electrode flow cell and a new needle based flow cell.

The needle flow cell was discarded as it was found that the narrow outlet from the needle leading to the electrode lead to the surface of the electrode becoming blocked by bubbles; out gassed from the solution. The conformation of the system with the electrode being in close proximity to the glass support prevented the bubbles being removed from the surface of the electrode making measurements impossible. The pressure within the reactor and capillary flow through the needle exacerbates these problems. Consequently work concentrated on the use of the three electrode flow cell.

3.2.1. Three electrode cell

The spatial resolution of the three electrode cell was constrained by the manner that solution was transferred from the reactor to the flow cell; the flexibility of the Teflon tubing resulted in the position of the inlet moving within the reactor. To improve the

resolution the conformation of the inlet system was altered such that the solution was drawn directly from the reactor through a 19 gauge needle and onto the electrode surface. In addition to improving the spatial specificity of the measurement the use of the needle changed the jet profile onto the surface of the electrode compared to that from the Teflon tube. Figure 3.2 shows that the needle moved the outlet 1mm closer to the electrode; effectively moving the electrode further up the flow region of the of the wall jet electrode flow*. In addition the outlet from the needle was approximately three quarters the diameter of that from the Teflon tube; therefore for a given pump rate the velocity of solution within and exiting the needle will be greater than that from the Teflon tube. The greater flow reduces the size of the diffusion layer and increases the mass transfer rate to the electrode; leading to an increase in current. Typical mass transfer rates for ferricyanide of 1.94 x 10^{-2} cm s^{-1} (see figure 3.3) were produced by this experimental arrangement.

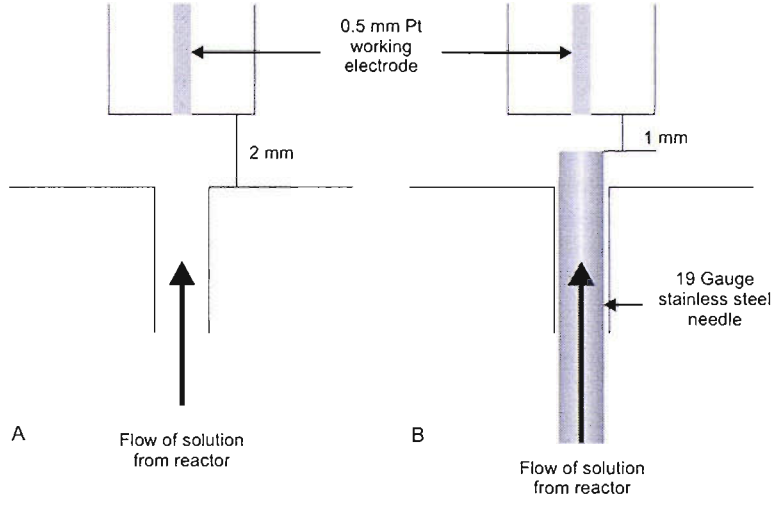

Figure 3.2: Comparison of the geometry of the Teflon tubing and needle inlets two the three electrode flow cell.

Figure 3.3 shows the effect of the change in conformation on the current with the current recorded (and therefore mass transfer) with the needle inlet (—) being significantly larger than that with the Teflon tube (—).

* For both the needle and Teflon tubing inlets the jet onto the electrode is within the potential core region as described in (*176*). The moving of the electrode further up this region increases the velocity of the solution.

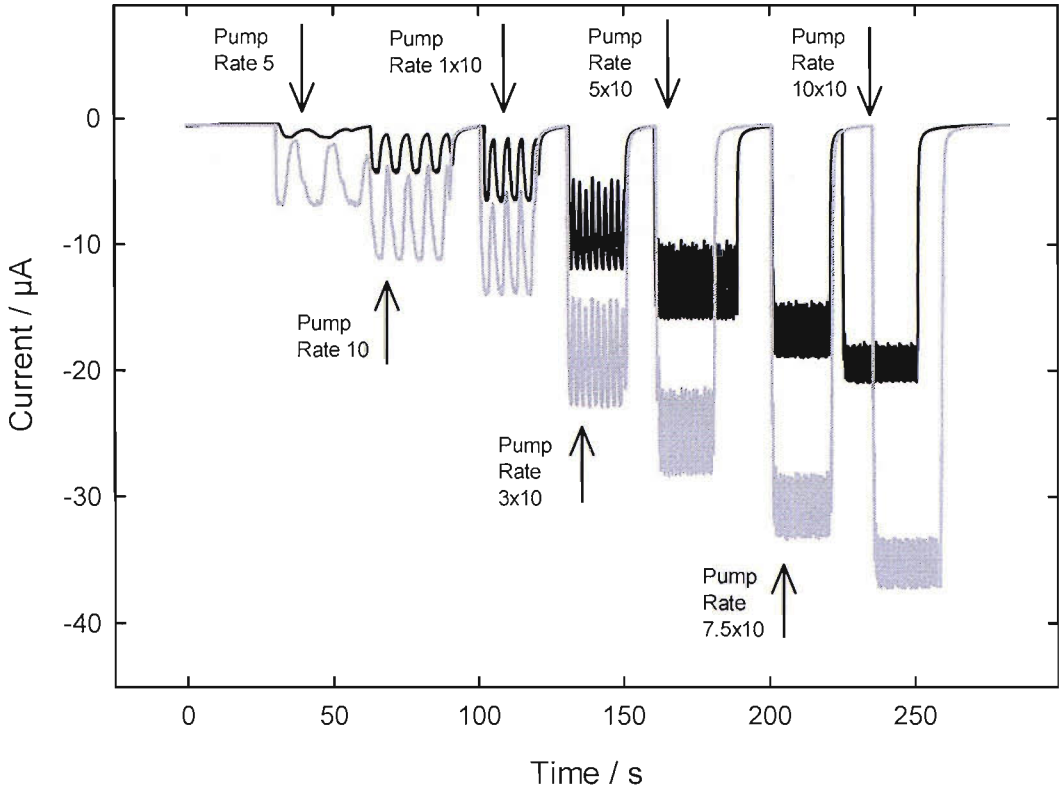

Figure 3.3: Comparison of mass transfer for different flow settings and inlet systems; 1.6 mm Teflon tubing (——) and a needle (- - -). Recorded using a 3 electrode cell with a 0.5 mm diameter Pt working electrode held at –0.2 V (the MTLP) *vs.* a SCE reference electrode with a stainless steel counter electrode. The aqueous solution employed consisted of 5 mM $K_3Fe(CN)_6$ in 0.1 M $Sr(NO_3)_2$ supporting electrolyte.

Figure 3.3 shows a large fluctuation in current caused by a variation in the flow rate over time. The peristaltic pump used pulses solution as the wheels used to force the solution through the pump rotate. The resultant variation in i can be as great as 25 % (flow setting 3x10: lowest k_m= 1.5 x 10^{-2} cm s^{-1}, average k_m= 1.94 x 10^{-2} cm s^{-1}, highest k_m=2.41 x 10^{-2} cm s^{-1}). Such instability is undesirable and consequently other pumping systems were investigated.

3.2.2. Pumping systems

Clearly variation in the flow of analyte to the electrode surface will result in a variation in the current recorded at the electrode due to changes in mass transfer. Therefore the ideal situation for a pumping system is one that provides a constant flow of solution, enabling variations in the chemistry to be accurately recorded. Figure 3.3 shows that the peristaltic pumping system initially employed (an un-

damped system) was non-ideal, causing large periodic variations in the flow and consequently current. Two different pumping systems were looked at; a continuous flow pump and a syringe pump; neither of which were found to be suitable. The continuous flow pump was found to not be physically robust enough for the task and the syringe pump was found to have a non-continuous rate of flow.

Other pumping methods having been found not to be suitable alternatives to the peristaltic pump, the possibility of "damping" the flow from the peristaltic pump was looked at such that the fluctuations in the rate, and therefore the current recorded at the electrode, were minimised. In attempts to mitigate this effect, and reduce the magnitude of the surges, a reservoir of air was inserted into the system between the pump and the flow cell. This air pocket acted as a damping component in the system and creating a more stable flow.

The damping reservoirs used were the body of a 60 ml syringe attached to a T piece situated on the inlet of the peristaltic pump. Varying the seal at the open end of the syringe allowed that the flow rate at which the damping was effective could be adjusted from low flow rate (latex glove) to high flow rate (fixed syringe plunger). The two damping systems can be seen in figure 2.11. The effect of these 2 systems on the current at various pump rates can be seen in figures 3.4 and 3.5.

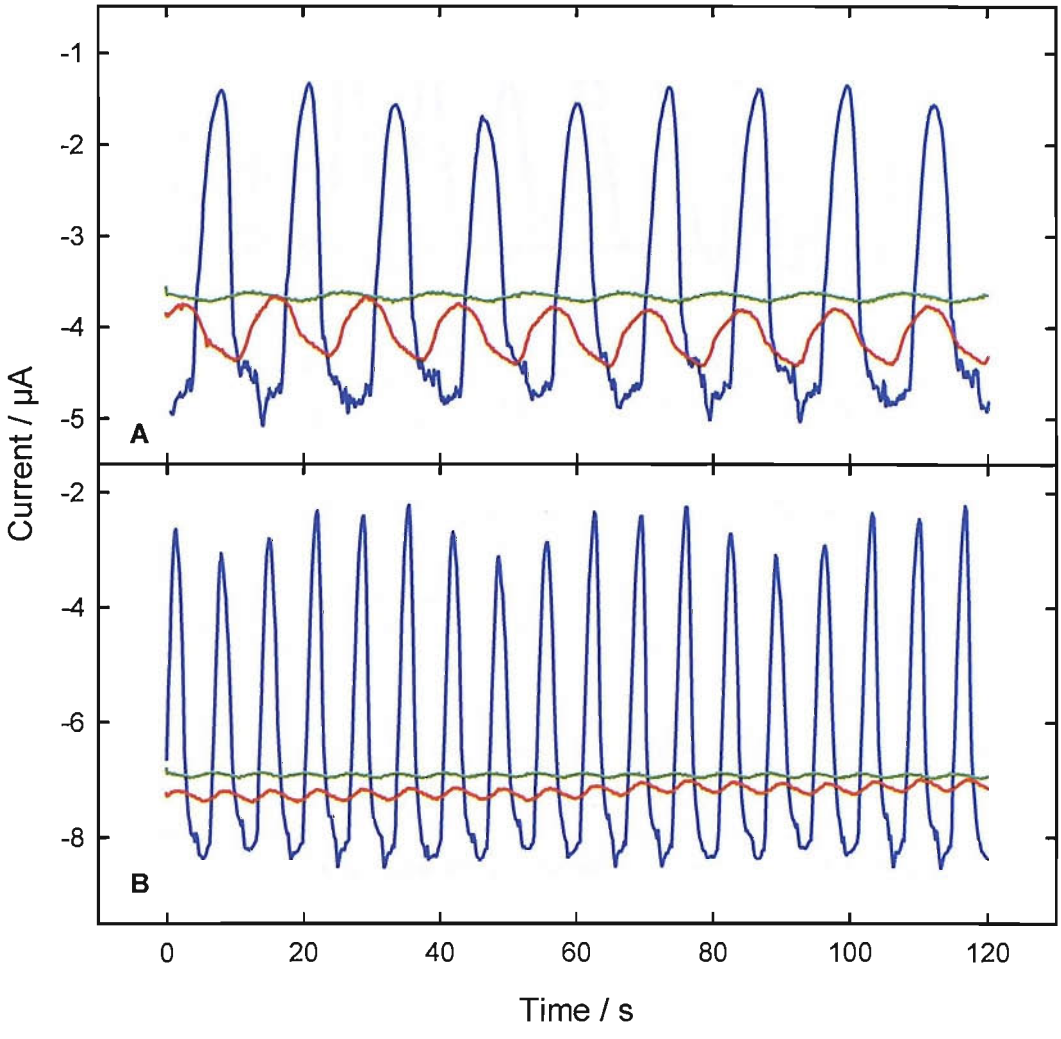

Figure 3.4: Comparison of different methods of damping; (—) un-damped, (—) soft damping and (—) hard damping; of a peristaltic pump at lower flow rates. A corresponds to a flow rate of 40 ml hr^{-1} and B to a flow rate of 80 ml hr^{-1}. Recorded using the three electrode flow cell with a 0.5 mm diameter Pt working electrode held at 0 V *vs.* a SCE counter/reference electrode. Aqueous solution of 0.1 M $Sr(NO_3)_2$ and 5 mM $K_3Fe(CN)_6$.

As can be seen in figure 3.4 at both flow rates both damping systems significantly reduce the fluctuations in current caused by variation in the flow from the pump. The improvement is even more significant in figure 3.5. Here it can be seen that the addition of the "soft damping" has the greatest effect at slow and medium flow rates (40, 80 and 388 ml hr^{-1}) where as the addition of hard damping has the greatest affect at high flow rates (697 ml hr^{-1}). Specifically at a flow rate of 388 ml hr^{-1} the addition of the soft damping reduces the peak to peak amplitude of the signal from the electrode from 8.2 μA to 0.12 μA; a reduction of over 60 times.

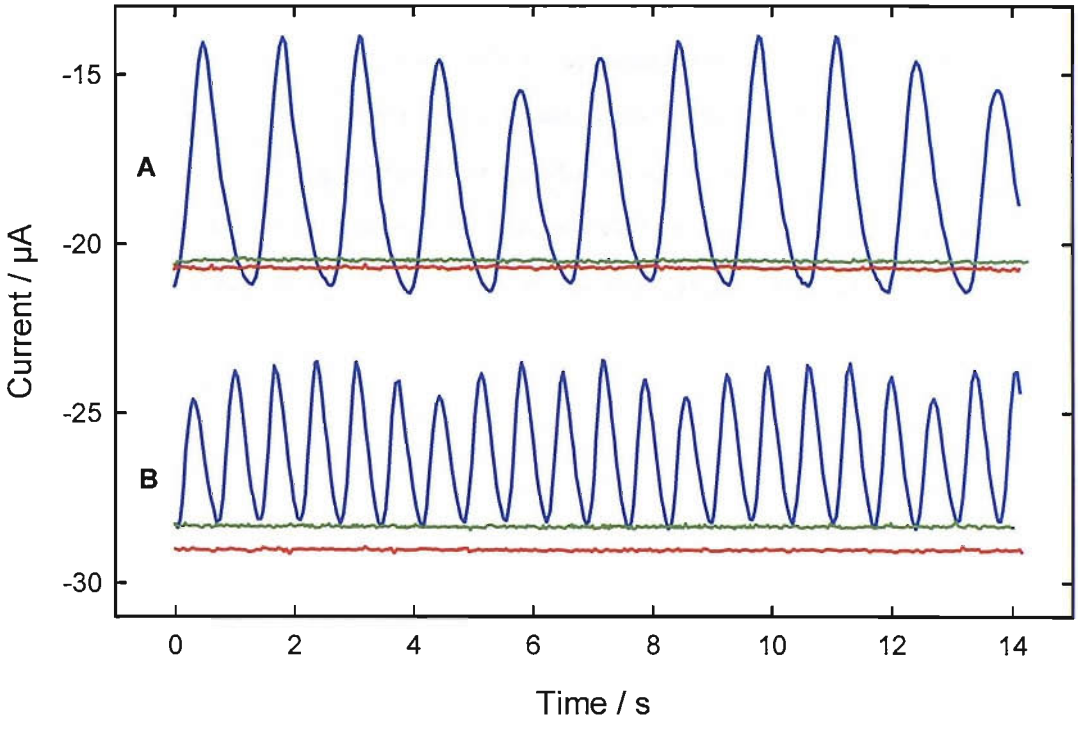

Figure 3.5: Comparison of different methods of damping; (—) un-damped, (—) soft damping and (—) hard damping; of a peristaltic pump at high flow rates. A corresponds to a flow rate of 388 ml hr^{-1} and B to a flow rate of 697 ml hr^{-1}. Recorded using the three electrode flow cell with a 0.5 mm diameter Pt working electrode held at 0 V *vs.* a SCE counter/reference electrode. Aqueous solution of 0.1 M $Sr(NO_3)_2$ and 5 mM $K_3Fe(CN)_6$.

The addition of damping to the peristaltic produces a constant stable flow of solution from the reactor to the flow cell allowing accurate amperometric measurements to be made.

3.2.3. Optical flow cells

UV/Vis adsorption measurements were conducted in two ways. Both involved the removal of solution from the reactor to make the measurements *ex-situ.* For continuous, time correlated measurements the optical flow cell described in figure 2.10 was introduced between the electrochemical flow cell and the pump. When the time dependence of the concentration of the I_3^- was not of interest, instead of using the flow cell, aliquots of solution were removed from the reactor and analysed in a quartz cell.

3.3. Repeatability measurements

The ease with which the electrochemical measurement procedure can be adapted in order to make scans of a reactor and to make measurements in different environments makes it a more appealing method for measuring the level of chemical change within a cavitating environment than UV/Visible spectroscopy. The main concern with the technique is its repeatability. It was found that slight variations in the flow rate through an electrochemical flow cell can result in fluctuations in the current leading to inaccuracies in the measured chemical change. Of particular concern is what effect the damping of the flow system has on the repeatability of measurements; the use of "slow damping" required a period of priming before a stable flow is reached.

To ascertain the repeatability of the system the three electrode flow cell with a needle inlet was mounted so as to draw solution from the centre of reactor 3. The reactor was filled with 100 ml of a solution containing 10 mM potassium iodide and 90 mM potassium chloride so that an identifiable chemical change would take place after a period of exposure to sonication. The peristaltic pump with "soft damping" (see figure 2.11 in chapter 2) was primed and the level of solution within the reactor topped up to the level pre-priming. The solution was then irradiated, the current recorded and a sample of the final solution collected for analysis with a UV/Vis spectrometer to determine the exact concentration of I_3^- produced over this period. Figure 3.6 shows an example current time trace from the flow cell and figure 3.6 (a) the absorbance spectrum recorded for the corresponding final sample.

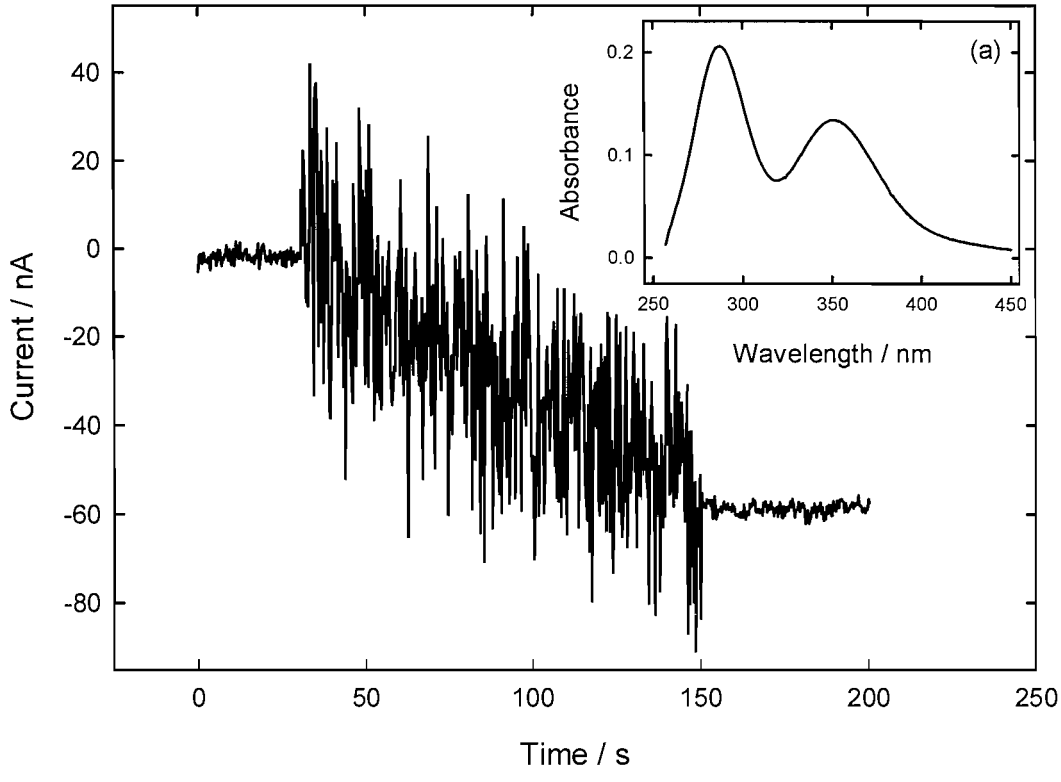

Figure 3.6: Plot of a current time trace showing the formation of I_3^- and the final steady state current. Insert (a) shows the UV/Vis absorbance spectrum of the final solution with an absorbance of 0.134 at 350 nm corresponding to an I_3^- concentration of 5.7 μM. Reactor 3 containing an aqueous solution of 90 mM KCl and 10 mM KI irradiated for 120 s at 143 kHz driven at 75 V and thermostated at 25 °C. Electrochemical signal recorded using the three electrode flow cell with a 0.5 mm diameter Pt working electrode held at 0 V *vs.* a SCE counter/reference electrode and a flow rate of 388 ml hr^{-1} provided by peristaltic pump with "soft damping".

As can be seen in figure 3.6 the current proceeds cathodically during the sonication. Interference from the ultrasound generation equipment dominates the signal during sonication. Once the drive signal is removed a steady state current is established which was measured to be 59 nA. The absorbance spectrum of the final solution in figure 3.6 (a) shows that the absorbance as a result of I_3^- concentration within the solution was 0.134 corresponding to a concentration of 5.1 μM. The experiment was repeated a total of seven times with varying periods of sonication to give a spread of concentrations of I_3^- produced. The results of these experiments are plotted in figure 3.7.

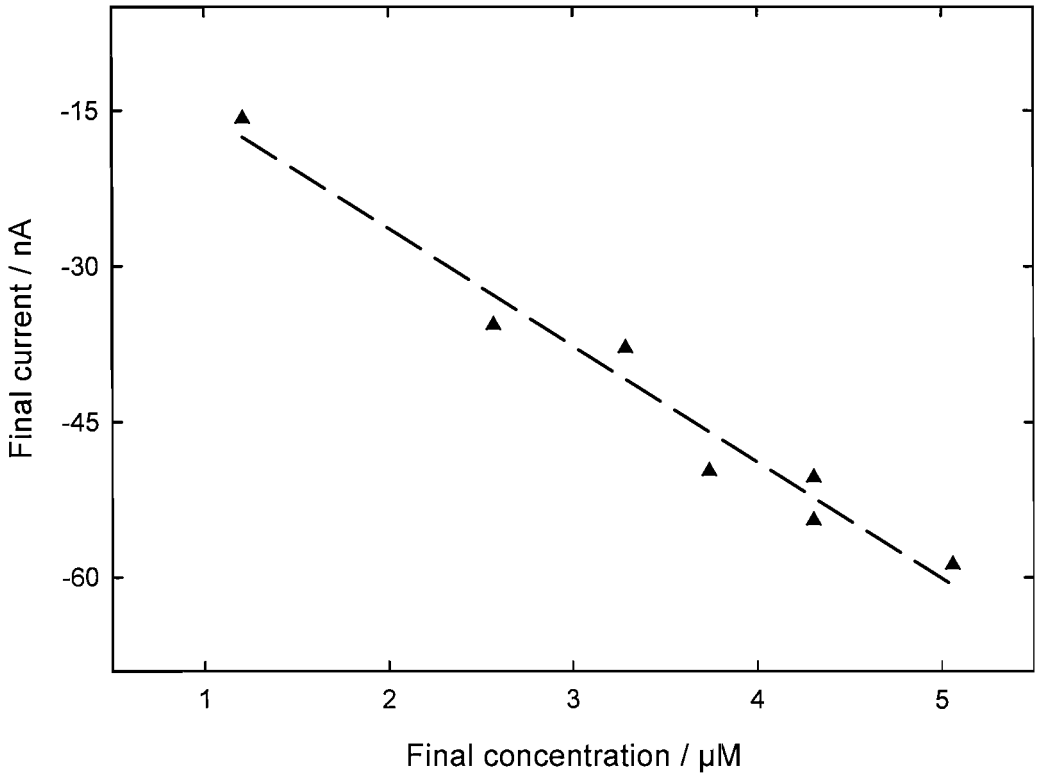

Figure 3.7: Calibration plot of steady state current vs. final concentration with line of best fit (- - - -) generated using Sigma plot. Line of best fit has a gradient of 0.012 A M^{-1} with an R^2 value of 0.99.

Figure 3.7 shows, as would be expected, that there is a close correlation between the final current and I_3^- concentration from the experiments. The line of best fit through the assembled points in figure 3.7 has a gradient of 0.012 A M^{-1}. This value can be used directly to interpolate currents recorded from the flow cell to the concentration of I_3^- in solution at that point of time. Working from the measurements in figure 3.7 it is also possible to calculate the effective mass transfer constant of I_3^-.

The limiting current at the working electrode is related to the other variables in the system by equation (3.1).

$$I_l = nFAk_mc \qquad (3.1)$$

where I_l is the limiting current at the working electrode, n is the number of electrons involved in the process, F is Faradays constant, A is the area of the electrode, k_m is the mass transfer constant for the system and c is the concentration of the ion under investigation. The reaction taking place at the electrode involves 2 electrons as can be seen in reaction 3.1.

$$I_3^- + 2e^- \rightarrow 3\ I^- \qquad (3.1)$$

The gradient of the line of best fit in figure 3.7 corresponds to I_l/c and by substituting in the values of the other known parameters for the experimental conditions used it is possible to calculate the effective mass transfer constant (k_m). The values of the known parameters are listed in table 3.1.

Parameter	Value
n	2
F	96,480 C mol^{-1}
A	Electrode of radius 0.25 mm $\therefore$ $A = \left(\pi \cdot 0.25 \times 10^{-1}\right)^2$ cm^2 $A = 1.96 \times 10^{-3}$ cm^2
$\frac{I_l}{c}$	Gradient from figure 3.7: -0.0112 A mol^{-1} dm^3 -11.2 A mol^{-1} cm^3
k_m	Unknown

Table 3.1: Table of parameters referring to figure 3.7 and equation (3.1).

Inserting these values into equation (3.1) gives the effective mass transfer coefficient to be 0.029 cm s^{-1} the calculations for which can be seen in equation 3.2.

$$I_l = nFAk_m c$$

$$\frac{I_l}{c} = nFAk_m$$

$$k_m = \frac{\left(\frac{I_l}{c}\right)}{nFA}$$

$$k_m = \frac{11.2 \text{ A mol}^{-1} \text{ cm}^3}{\left(2 \cdot 96480 \text{ C mol}^{-1} \cdot 1.96 \times 10^{-3} \text{ cm}^2\right)}$$

$$k_m = \frac{11.2 \text{ C s}^{-1} \text{ mol}^{-1} \text{ cm}^3}{378 \text{ C mol}^{-1} \text{ cm}^2}$$

$$k_m = 0.029 \text{ cm s}^{-1}$$

Equation 3.2: Calculation of effective mass transfer coefficient of three electrode flow cell at flow rate of 388 ml hr^{-1}.

The reproducibility of the current from the flow cell system here demonstrated means that for the examined conformation of the flow cell and solution conveyance mechanism it is possible to interpolate the concentration from the current measured. For measurements where it was not possible to use the exact same conformation as

has been examined here, the effective mass transfer coefficient of the experimental setup was calculated independently. This was achieved by measuring the final I_3^- concentration using UV/Visible spectroscopy and equating this to the steady state current recorded at the electrode.

3.4. Reactor 1 Measurements

The reactor designated reactor 1 in this work has been used extensively in previous studies(*39, 62, 155, 177*). In these studies it had been shown to be generating both high pressures and a large rate of chemical change (*62, 128*). In order to check the performance of reactor 1, a number of analytical tests where performed. In particular it was believed that the transducer powering the reactor had degraded over time. The tests performed included measuring the rate of a standard sonochemical reaction (specifically the Weissler reaction) and the acoustic pressure amplitude recorded using a calibrated hydrophone. The sonochemical reaction was monitored using the 3 electrode flow cell as well as the optical flow cell. In this case the two measurements were performed in series with the output from the electrochemical cell flowing directly into the inlet for the optical flow cell. This gave a dual conformation of the rate of production of I_3^- production as can be seen in figure 3.8. In the Weissler reaction, I^- reacts with oxidising species (associated with the production of $OH^\bullet$) according to the Weissler reaction (*145*) to give I_3^-. This is an ideal system as the I_3^- is both electrochemically active and can be detected UV/VIS spectroscopy (I_3^- adsorbs strongly at 350 nm, $\varepsilon = 26{,}500\ M^{-1}\ cm^{-1}$).

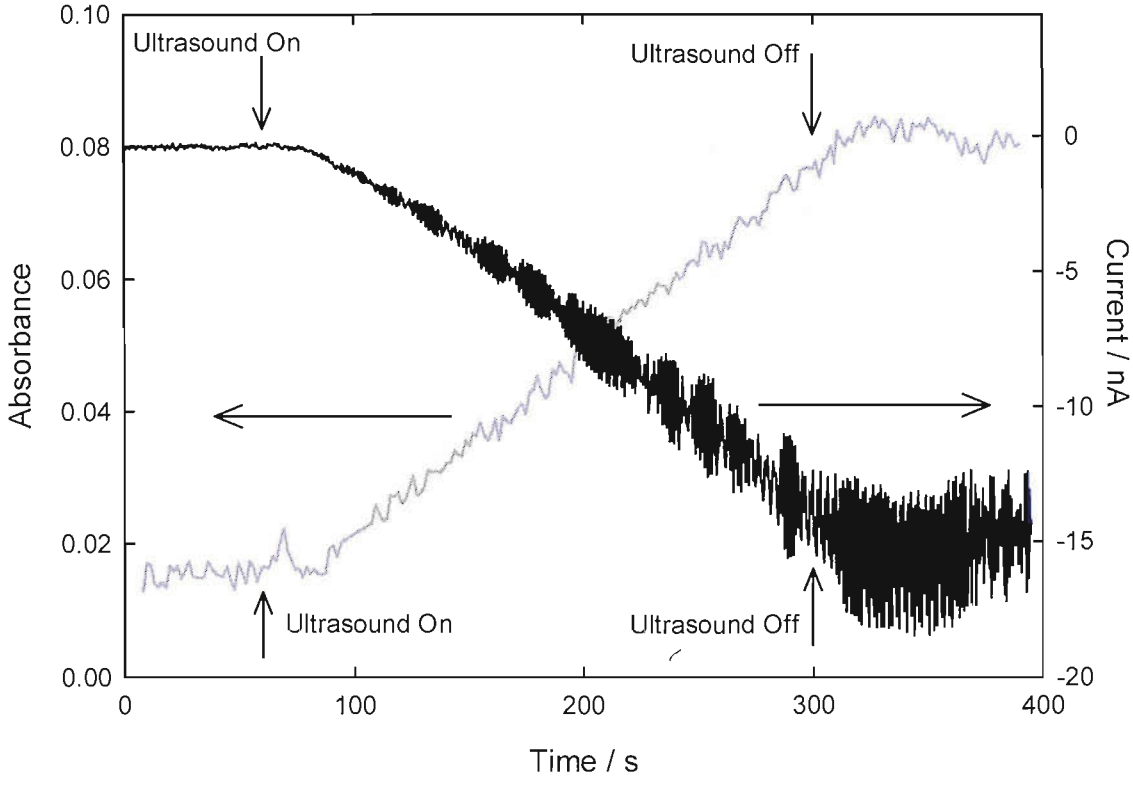

Figure 3.8: Graph of current (—) and Absorbance at 350 nm ( ) against time. An aqueous solution of 90 mM KCl and 10 mM KI irradiated for 300 s after 60 s at 124 kHz with a drive voltage of 100 V. Potential of a 0.5 mm Pt working electrode held at + 0.2 V *vs.* a SCE reference electrode with a stainless steel counter electrode. Absorbance measured at 350 nm.

Figure 3.8 shows that the current proceeds cathodically as the concentration of I_3^- builds up in the solution. At the same time the absorbance at 350 nm increases as expected. The rate of I_3^- production was calculated independently for the two methods and found to be 10.2 nM s^{-1} for the absorption and 9.8 nM s^{-1} for the electrochemical measurement. The rates were calculated by working out the gradient of a line of best fit through the relevant trace as can be seen in figure 3.9.

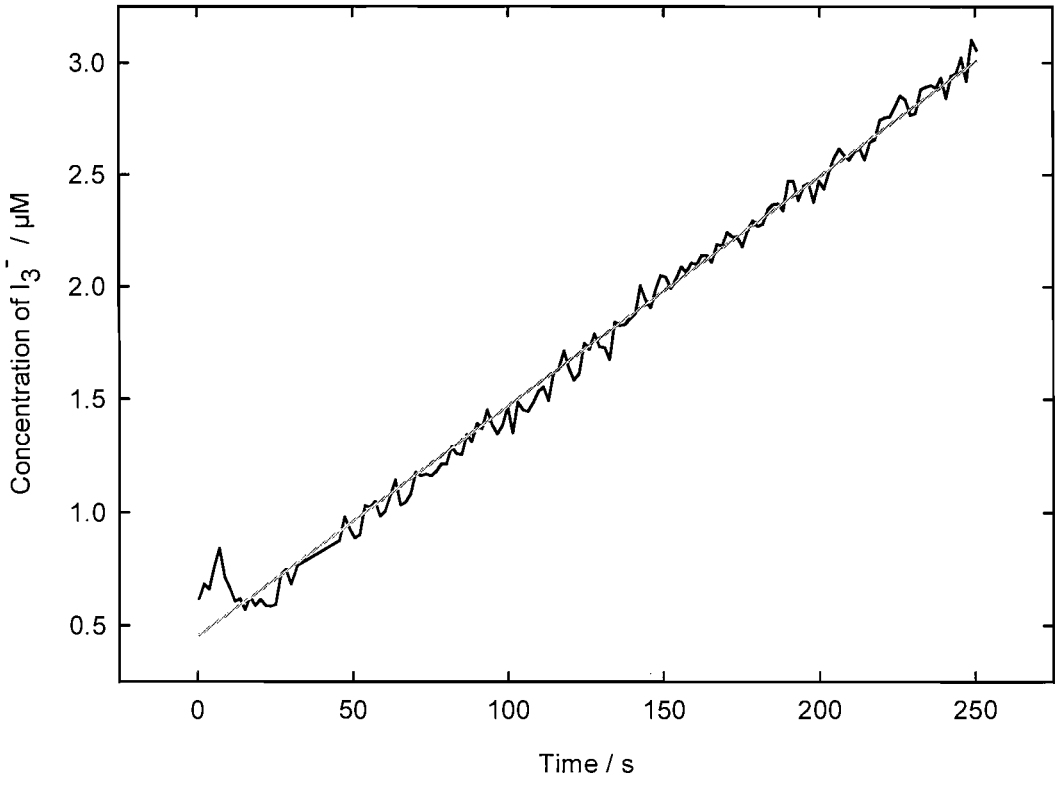

Figure 3.9: Plot showing the concentration of I_3^- (—) as a function of time during the period of irradiation. Concentration of I_3^- calculated from the plot of UV/VIS absorbance at 350 nm from figure 3.8. Line of best fit calculated using Sigma Plot (—) giving the rate of I^{3-} production as 10.2 nM s^{-1}.

The rates recorded were substantially below that seen in previous studies(*62*). The acoustic pressure amplitude (zero to peak) within the reactor was found to be 150 kPa at 124 kHz with drive voltage amplitude of 100 V. This is over 100 kPa less than the pressure reported previously(*62*). Table 3.2 shows a comparison of the rate of I_3^- at similar pressures. It can be seen that the figures are in excellent agreement. This indicates that there has been a reduction in the pressure amplitude, and therefore level of cavitation, that reactor 1 is capable of producing.

	Pressure / kPa	Rate of $OH^\bullet$ production / nM s^{-1}
Power's Thesis (*62*)	258	40
Power's Thesis (*62*)	150	10
Dual Experiment	150	10.2

Table 3.2: Comparison of pressures and consequent production of $OH^\bullet$ at each pressure.

3.5. Variation within a Reactor

Having established that the electrochemical flow cell system was capable of accurately measuring the concentration of I_3^- we shall now examine the variations in the rate of chemical change in a cavitating environment. We shall demonstrate the flow cells ability to detect variations in chemical rate at different reactor drive voltages before attempting to detect variations in the rate of chemical change as a function of position

3.5.1. Rate of I_3^- production as a function of pressure amplitude

Increasing the drive voltage to a reactor will increase the acoustic pressure it generates (see chapter 6). Consequently changing the drive voltage is an easy method to confirm that an electrochemical flow cell is capable of detecting variations in the rate of chemical change. Reactor 3 was driven at two pressures (125 and 220 kPa, drive voltages of 50 and 75 V) at a frequency that was known to generate high rates of chemical change (143 kHz) whilst the current passed at the working electrode was recorded. The variation in the rate of change of current (and therefore I_3^- production) can be seen in figure 3.10.

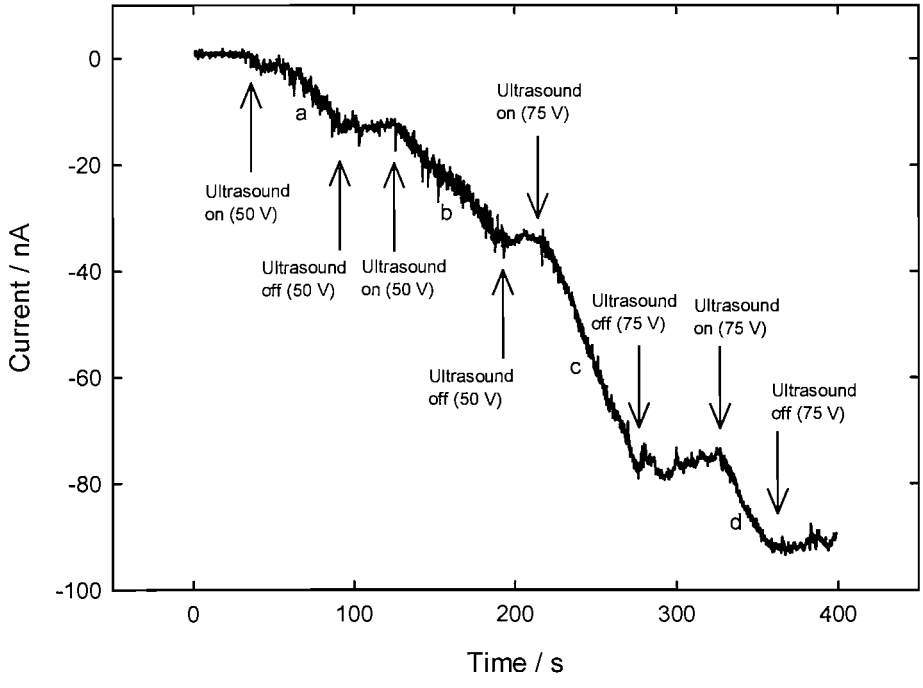

Figure 3.10: Comparison of two different pressures 220 kPa & 125 kPa (50 & 75 V) for reactor 3 at 143 kHz. Reactor contained 100 ml of 10 mM KI, 90 mM KCl solution, kept at 25 °C. Recorded using a 3 electrode cell with a 0.5 mm Pt working electrode held at +0.2 V *vs.* a SCE reference electrode with a stainless steel counter electrode and needle inlet pumped using peristaltic pump with syringe + plunger damping. Final absorbance of 0.258 at 350 nm giving I^{3-} concentration of 9.7 μM.

By measuring the gradient of the current time trace during sonication the rate of production of I_3^- was calculated to be 79 nM s^{-1} at 220 kPa and 31.6 nM s^{-1} at 125 kPa. More significantly figure 3.10 demonstrates that it was possible to identify differences in the rate of chemical change using the electrochemical flow cell setup.

3.5.2. Variation of I_3^- production by position

Having established that the electrochemical flow cell was capable of detecting variations in the rate of chemical change caused by different drive voltages (and therefore pressure amplitudes), its ability to identify spatial variation in the chemistry within a reactor was investigated. The movement and acquisition of data from the electrochemistry was automated by means of a Visual Basic control program. In order to control the movement of the inlet, the flow cell was mounted on a single axis positioner such that the end of the needle was positioned within the central axis of the reactor. Measurements were taken at 17 points within reactor 2 with a resolution of 2 mm starting 2 mm from the base. The drive signal of 150 kHz and 85 V was maintained throughout the experiment and the current time signal from the flow cell recorded for 30 s at each point; the gradients of the resulting slopes were elucidated by means of a Microsoft Excel Macro. The flow cell and solution transport regime were the same as for the repeated experiment and calibration seen in figure 3.6 therefore the currents were converted to rates of chemical change and plotted in figure 3.11.

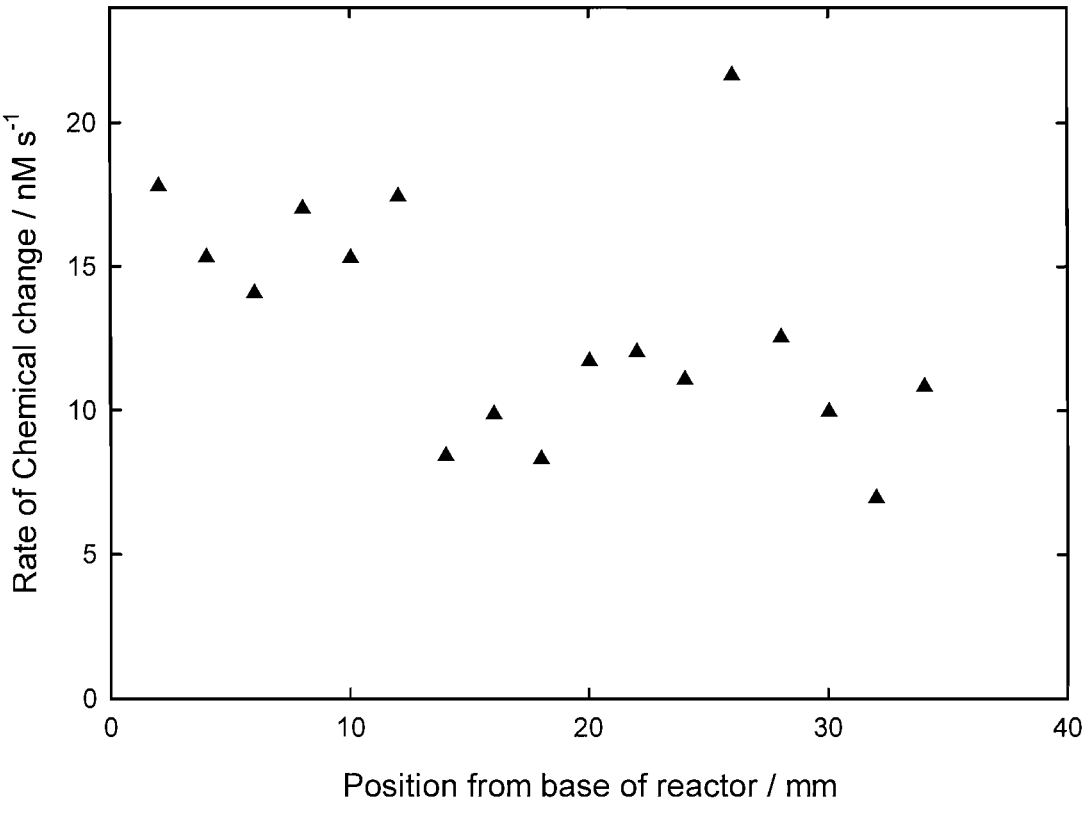

Figure 3.11: Plot of the rate of chemical change as a function of displacement of sampling volume from the base of reactor 2. Each point calculated from the rate of change of current with respect to time over 30 s. Three electrode flow cell with 0.5 mm Pt working electrode held at 0 V *vs.* a SCE counter/reference electrode with a flow rate of 388 ml hr^{-1} provided by a soft damped peristaltic pump. Reactor 2 with 115 ml of aqueous solution containing 90 mM KCl and 10 mM KI irradiated at 150 kHz and driven at 85 V.

Figure 3.11 shows that there is a large degree of variation in the rate of chemical change recorded within the reactor ranging from 7 nM s^{-1} to 22 nM s^{-1}. In general greater rates were recorded towards the base of the cell with a significant discontinuity seen at 14 mm from the base of the cell. To show that the different rates seen in figure 3.11 were not as a result of a change in the global rate of chemical change within the reactor the average of the first 1 s of data recorded at each position was taken and plotted versus the position in the reactor in figure 3.12. The plot is linear, confirming that the variation is as a result of localised effects. The data in figure 3.11 is taken from only a single experiment and therefore does not represent a definitive view of the sonochemical rate within the reactor.

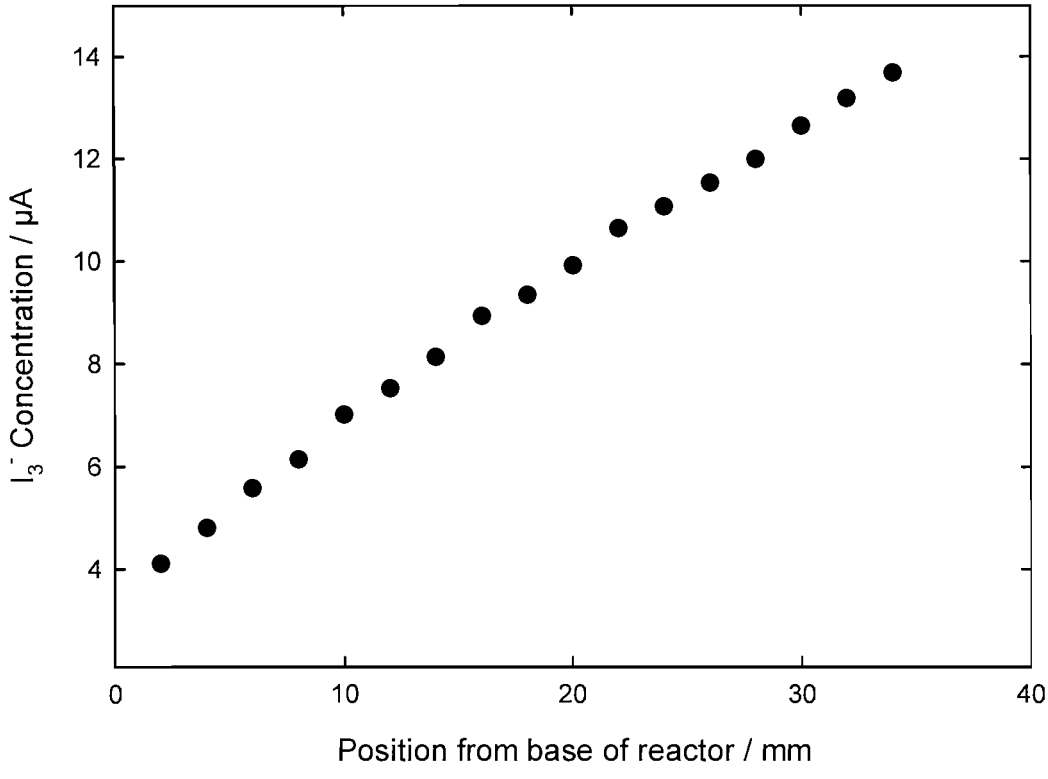

Figure 3.12: Plot of initial concentration of I_3^- at each point of a vertical scan through reactor 2. Aqueous solution of 90 mM KCl and 10 mM KI irradiated for 30 s at each point at 150 kHz and a drive voltage of 85 V. Three electrode flow cell with 0.5 mm Pt working electrode held at 0 V *vs.* a SCE counter/reference electrode with a flow rate of 388 ml hr^{-1} provided by a soft damped peristaltic pump.

The combination of the spread of rates seen in figure 3.11 and the conformity of global rates recorded in figure 3.12 confirms that it may be possible to see changes in the rate of chemical change as a function of distance. Given the relatively large volume which the flow cell is sampling for each measurement and the mixing of solution caused by flow within the reactor it is unsurprising that no fine structure is elucidated from the scan.

3.6. Conclusions

In this chapter we have discussed the construction of a repeatable electrochemical flow cell and pumping system and utilised this to identify an ultrasonic reactor that had ceased to function properly. The flow cell has also been used to detect changes in the electrochemical rate as a function of reactor pressure and position within the reactor. The detection of spatial variation in the rate at which sonochemical products of cavitation are formed is not proven. Some variation between points is seen but as to whether this is genuine variation or experimental error is unclear. Definitive conclusions should not be formed from the single scan conducted in this reactor. Regardless of whether it is possible to see spatial variation in the measurements, making repeated measurements within the reactor and averaging provides a more accurate measure of the rate of sonochemical change.

4. Transient Events

4.1. Introduction

A commonly used method to measure the effectiveness of cavitation within an ultrasonic reactor is the monitoring of the degradation of aluminium foil by surface transient events (*104, 160*). In this process the foil is mounted within the reactor and subjected to the cavitation field. After a predetermined time the foil is removed and examined for signs of degradation which are then held to correspond to the areas at which high levels of cavitation are taking place. Though simple and cheap this is not the most scientifically rigorous method available and difficult to compare to results garnered from other measuring techniques. Though the measurement of the degradation of a foil may not in its self be a usable measurement technique; the premise of measuring the relative rate at which a surface is damaged within a cavitating body is a useful one. If the surface onto which the cavitation acts is an electrode held under conditions such that the surface is a passivated layer; then the reformation of this passive layer after damage by a surface erosion/corrosion cavitation event can be followed electrochemically (see figure 4.1) (*42, 54, 158*). After the removal of the protective passive layer through the action of a cavitation bubble collapse (stage 1) the exposed material becomes electrochemically active. As the passive layer reforms (stage 2) current passes through the electrode to oxidise the material at the surface to reform the passive layer. Before the passive layer is reformed the exposed material will also undergo corrosion of the surface in accompaniment to the erosion from the action of the cavitation event.

The use of electrodes in such ways has been the subject of previous research; specifically on the use of lead electrodes passivated with lead sulphate (*42, 54*). This work has shown that it is possible to map the presence of inertial cavitation taking place at the tip of an ultrasonic horn by monitoring the number of distinct passive layer reformation events recorded on an electrode (*54*). In a similar manner cavitation events have previously been detected on the surface of aluminium (*158*) and stainless steel electrodes (*149, 158*) by monitoring the reformation of an oxide layer. In this chapter we shall look at the behaviour of aluminium electrodes in a cavitating environment and examine their suitability as a method of gauging the

presence of inertial cavitation. We shall also for the first time look at the use of titanium electrodes in the same manner.

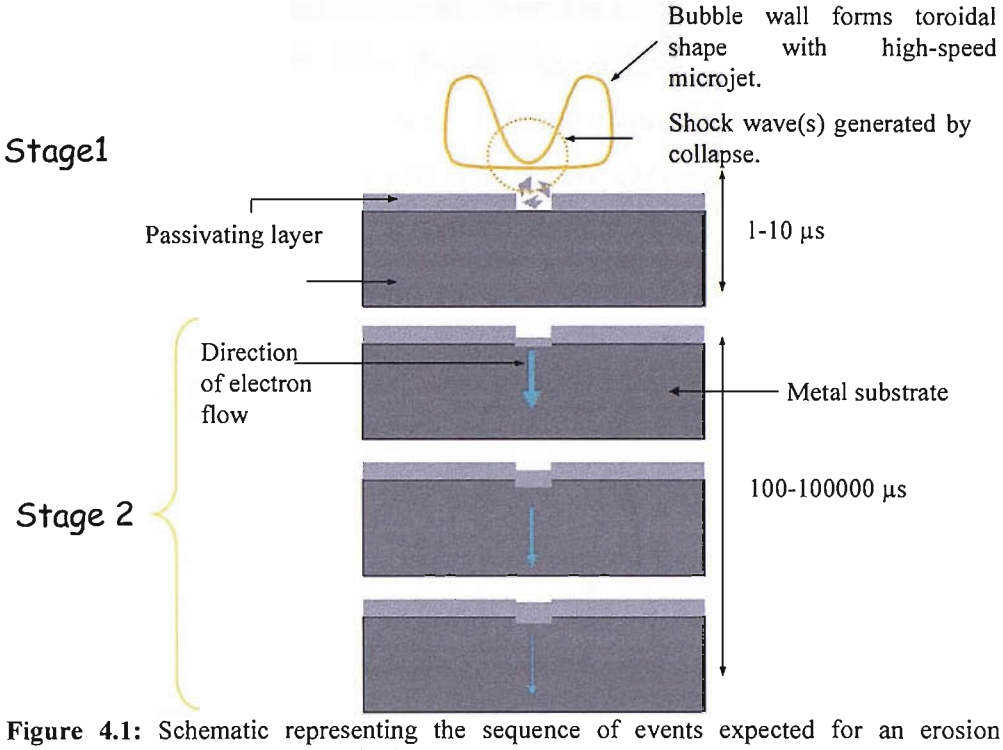

Figure 4.1: Schematic representing the sequence of events expected for an erosion corrosion event produced by cavitation.

4.2. Transients on Aluminium electrodes

It is well known that aluminium is a reactive metal that rapidly forms an inert oxide on surface exposed to oxidising conditions. As mentioned previously the reformation of the protective aluminium oxide layer after it has been destroyed by a surface erosion/corrosion cavitation event can be detected and monitored electrochemically.

4.2.1. Size and shape of transients

In order to study the effect of inertial cavitation on the surface of the aluminium, electrodes were positioned within an inertial cavitation cloud produced by an ultrasonic horn using micropositioners (described in chapter 2 and elsewhere (*159, 175*)). The inertial cavitation produced by this device has been shown to be within ~2 mm of the surface of the emitter (*74*). Hence the electrode was typically positioned to within ~ 1.5 mm from the emitter surface. These conditions are thought to be suitable for the investigation of inertial cavitation events; generating both

luminescence and surface erosion/corrosion events (*54, 159*). The extent of the luminescence can be seen in the lowlight image of a cavitating horn in figure 2.1.

The localised area of inertial cavitation allows the effects of inertial cavitation events on the surface of an electrode to be studied. When an event occurs near to the electrode surface it can remove some of the protecting layer of oxide, exposing the metal underneath to the solution and to the electrochemical environment. The oxide layer quickly reforms producing an anodic current spike. Such an erosion/corrosion event is shown in figure 4.2 peak 1.

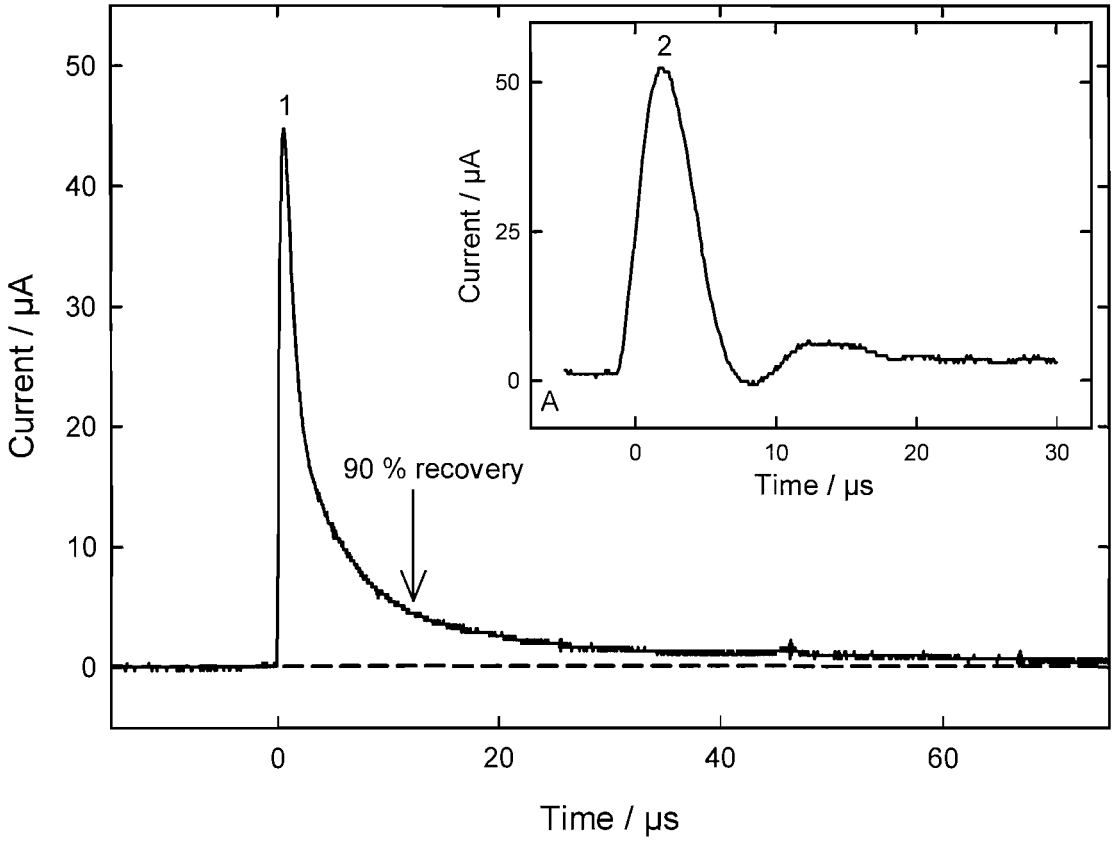

Figure 4.2: Plot showing a typical current time transient recorded for a surface event on an aluminium electrode (diameter 250 μm). The ultrasonic drive frequency was 23.17 kHz, voltage amplitude to the transducer was 100 V (zero to peak) corresponding to a power of 56 ± 5 W cm^{-2} (calculated by Offin (*54*). The electrode was positioned 0.5 mm from the tip of the ultrasonic horn and held at 0 V *vs.* a Stainless Steel reference electrode in an aqueous 0.25 M Na_2SO_4 solution. Insert A is recorded under the same conditions except for a different current follower.

The rapid nature of events such as figure 4.2 peak 1 imparted significant strain on the equipment used; for a large transient from an aluminium electrode the rise time of the transient is around 0.66 μs for ~ 45 μA; with the current follower set to a gain of 10^4

A V^{-1} this corresponds to a slew rate of over 650,000 V s^{-1} required of the operational amplifier within the current follower. If a standard operational amplifier, as used for passivated lead electrodes, was used then the elevated slew rate can result in the signal bouncing as in figure 4.2 (insert A), peak 2.

The erosion/corrosion transients recorded on aluminium were found to be of considerably shorter period compared to those recorded on lead electrodes. A lead electrode takes approximately 60 μs (*54*) for the current to return to 10 % of the maximum current in the transient compared to ~15 μs seen for the aluminium electrode in peak 1 in figure 4.2.

4.2.2. Process of reformation

The process by which a passivated layer reforms at the surface of an electrode has been studied elsewhere (*54, 152*). Two methods of passive film growth have been identified; ion migration and place exchange. Burstein and Davenport described an analysis that allowed the process taking place to be ascertained by plotting the current time data from a reformation transient in a particular manner. Their analysis suggests that if the method by which the passive layer is reformed is due to ion migration then the tail of a log(I) *vs.* $(I\ t)^{-1/2}$ should be vertical and that the slope of log(I) *vs.* log(t) at long t should be linear. Figure 4.3 shows the transient from figure 4.2 in such a way.

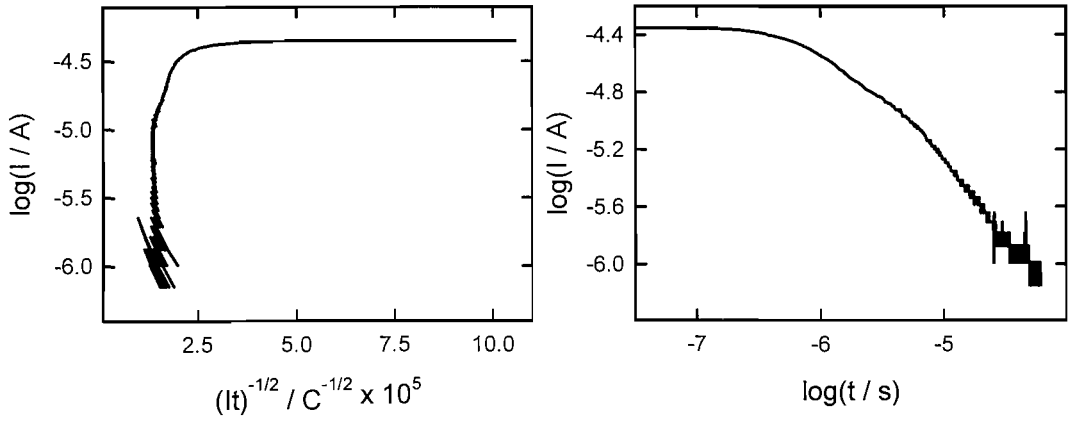

Figure 4.3: Plots of log(i/A) vs. $(it)^{-1/2}$ and log(i/A) *vs.* log(t/s) for the erosion/corrosion transient in figure 4.2.

Figure 4.3 suggests that the reformation of the passive layer is predominantly ion migration in character. Offin (*54*) used the same analysis to investigate a large

number of surface erosion/corrosion events on stainless steel electrode passivated with an oxide layer. Though the materials involved are different the analysis is instructive. In (*54*) four different scenarios are presented and the two most realistic (2 and 3) identified. These are:

> **Scenario 2:** A large amount of material is removed from the electrode surface resulting in bared metal (physically reasonable)
> **Scenario 3:** A small amount of material removed, not resulting in freshly bared metal (physically reasonable)

Pertinent to this work it is identified that though there may be events such as that in figures 4.2 and 4.3 that are predominately formed through ion exchange the majority of events are a mixture of the two processes.

4.2.3. Secondary events

After an electrode had been subjected to prolonged exposure to intense inertial cavitation (~120 s with the electrode positioned 0.5 mm away from a horn operating at 23 kHz and 100 V zero to peak), an alteration in the shape of some of the transients recorded at the electrode could be seen. In addition to the sharp, saw tooth peak seen in figure 4.2 peak 1, other more symmetric peaks would appear interspersed between the saw tooth peaks. These "secondary" peaks were generally smaller in amplitude than the saw tooth or "primary" peaks, with longer rise times and a more rounded apex. A good example of this can be seen in figure 4.4 where the sharp primary peak (labelled 'a') is followed by a more rounded secondary peak (labelled 'b') 55 μs later.

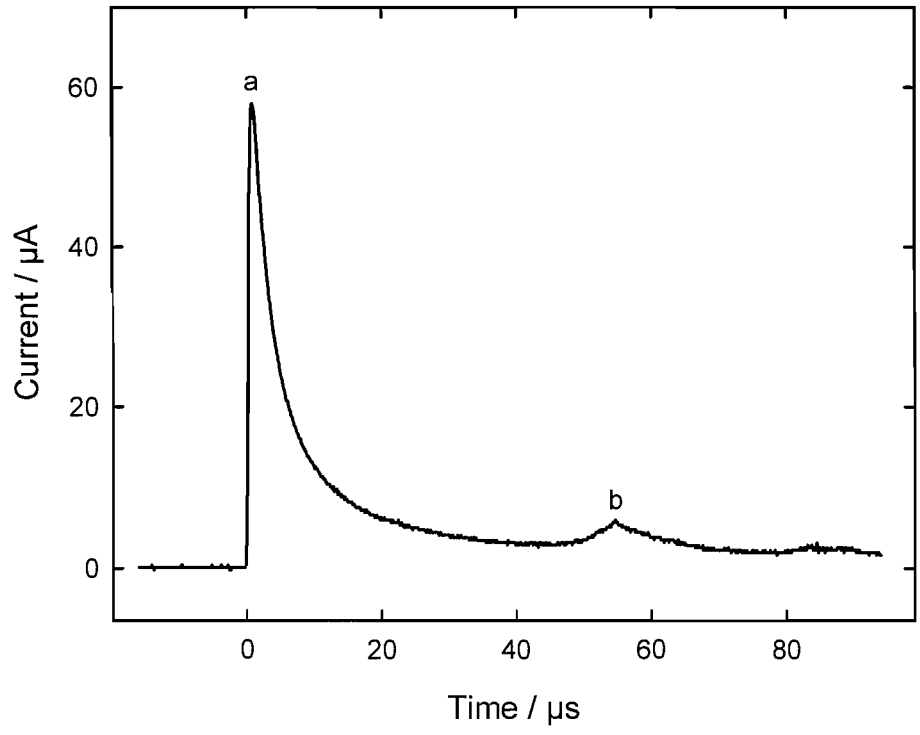

Figure 4.4: Current time plot showing a saw tooth "primary" peak (a) followed by a smaller "secondary" peak (b). Recorded on a 250 μm aluminium working electrode held at 0 V *vs.* an Ag counter/reference electrode. Electrode held 1.5 mm from the tip of the ultrasonic horn operating at 23.16 kHz and 100 V zero to peak drive voltage in 0.25 M Na_2SO_4.

The event labelled 'b' in figure 4.4 is substantially smaller in magnitude in comparison to the primary peak that precedes it, making discrimination between the two easier. Such disparity was not always the case as the current time trace (—) in figure 4.5 shows. Here the secondary peak, labelled b_2, is of comparable size to the preceding primary peak (a_2) and is larger than the first primary peak recorded (a_1). Also included in figure 4.5 is the differential of the current time signal with respect to time (┈). This emphasises the differences with the event 'a_1' having a higher differential signal (11.875 A s^{-1}) compared to 'b_2' (10.625 A s^{-1}) even though the current time trace for 'a_1' gives a smaller maximum when compared to 'b_2'.

It is also instructive to note that the separation between the primary and secondary peaks is not constant. In figure 4.5 the two normal "spike" transients (marked a_1 and a_2 respectively) are separated by 87.5 μs which corresponds to two pressure cycles at the drive frequency of 23.16 kHz. In contrast the gaps between the primary and secondary transients are 54 and 58 μs for a_1 to b_1 and a_2 to b_2 respectively. Overall

the period of separation between the primary events and secondary events was found to vary from as little as 20 μs to over 100 μs.

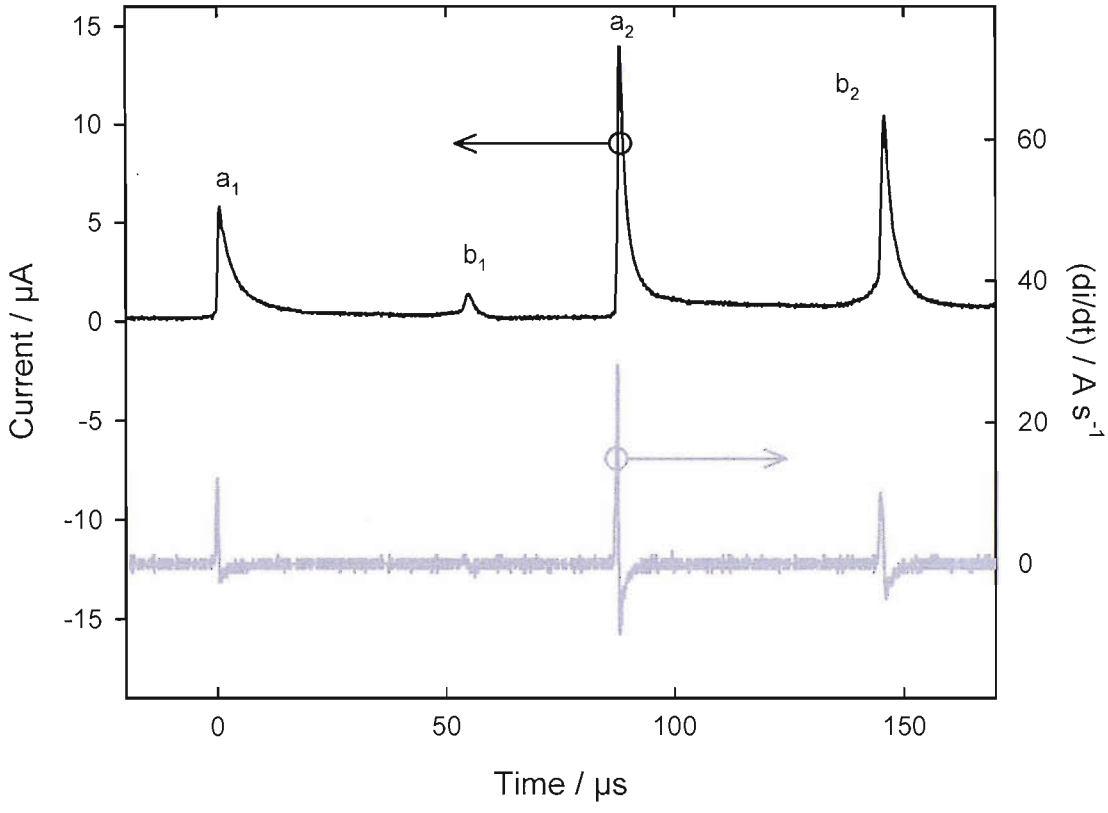

Figure 4.5: Current time plot (—) to show an example of the presence of slow rising 'secondary' transients ($b_{1,2}$) as well as fast rising normal transients ($a_{1,2}$) on an 250 μm diameter aluminium electrode held at 0 V *vs.* a Ag counter/reference electrode after the surface has become damaged by the inertial cavitation events. The ultrasonic drive frequency was 23.16 kHz, voltage amplitude to the horn was 100 V (zero to peak). Included on the plot is the differential (—) with respect to time.

After an aluminium electrode had been held within a cavitating environment for long periods of time (upward of 1000 s exposure) the surface erosion/corrosion events recorded tended to be more secondary(b) in nature than primary(a). Figure 4.6 shows two events with fast rise times that can be considered normal or primary events (designated a_1 and a_2 respectively) each of which is followed by a series of peaks (six and two respectively) which exhibit slow rise times and thus are considered to be secondary events (designated $b_{1a\text{-}f}$ and $b_{2a\text{-}b}$). The repeated nature of the secondary events precipitated the examination of the electrode under a microscope to compare the surface before (figure 4.6 image A) and after exposure to cavitation (figure 4.6 image B). The complete restructuring of the surface of the electrode seen in figure 4.6 image B would suggest that the cause of the secondary events was associated with a change in the morphology of the surface. This, in turn, may act as a nucleation centre for further inertial events. This mechanism suggests, correctly, that nucleation

sites as well as pressure amplitude are important for erosion/corrosion event detection.

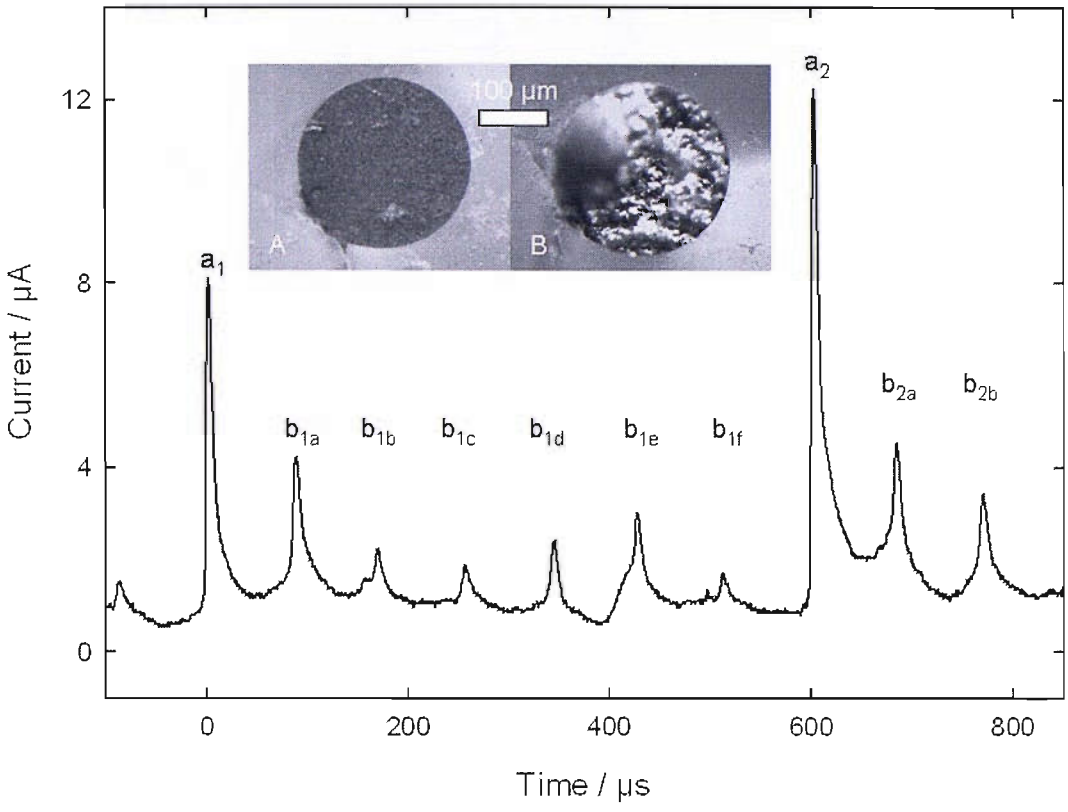

Figure 4.6: Current time trace with two "primary" peaks (a_1&a_2) followed by a number of secondary peaks (b_1&b_2) recorded on a 250 µm aluminium electrode the surface of which has degraded from a clean smooth surface (image A) to a totally reconstructed one (image B). The electrode was held at 0 V *vs.* an Ag counter/reference electrode and mounted 0.25 mm from the tip of an ultrasonic horn operating at 23.37 kHz and 100 V zero to peak in 0.1 M Na_2SO_4.

4.2.4. Damage of electrodes over time

The preceding section suggests that the surface of the electrodes were being damaged by prolonged exposure to cavitation. Further investigation into the extent of the damage was undertaken. Figure 4.7 shows images of two electrodes that have been severely damaged by cavitation and demonstrates that not only has the surface of the electrode become pitted from the repeated action of inertial cavitation events (figure 4.7 images A and B) but the aluminium wire which constitutes the working electrode has been both extruded from the support and eroded back within the epoxy support of the electrode (circled areas on images B and C).

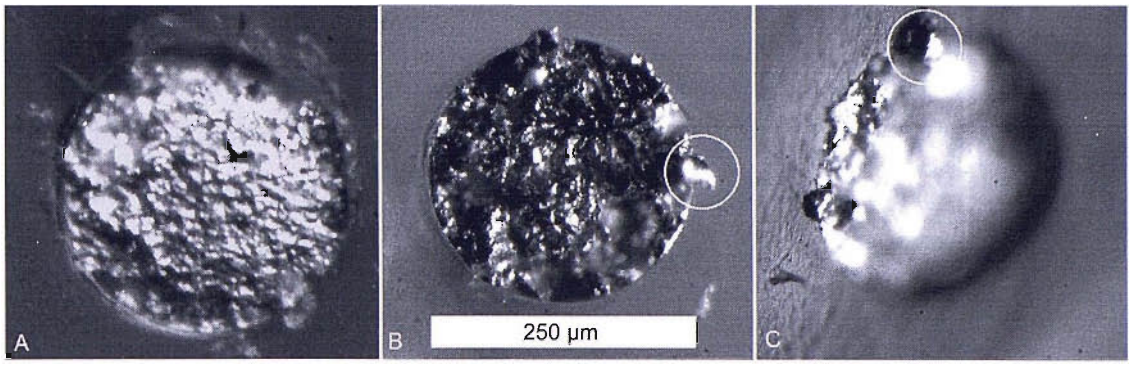

Figure 4.7: Images of two 250 µm aluminium electrodes damaged by the action of inertial cavitation at the tip of an ultrasonic horn. Image B and C are of the same electrode but from different angles.

The deformation of electrodes seen in figure 4.7 is obviously a less than ideal situation. In addition to the changes in the shape of the current time transients recorded on the electrode seen (figure 4.4) the working surface of the electrode is being receded away from the surface of the electrode support. This reduces the likelihood of inertial cavitation events taking place close enough to the electrode to register a surface erosion/corrosion event. To ascertain over what time frame the electrodes became damaged, an electrode was exposed to ultrasonic cavitation from the ultrasonic horn for 300 s and the electrode removed and imaged every 60 s (see figure 4.8).

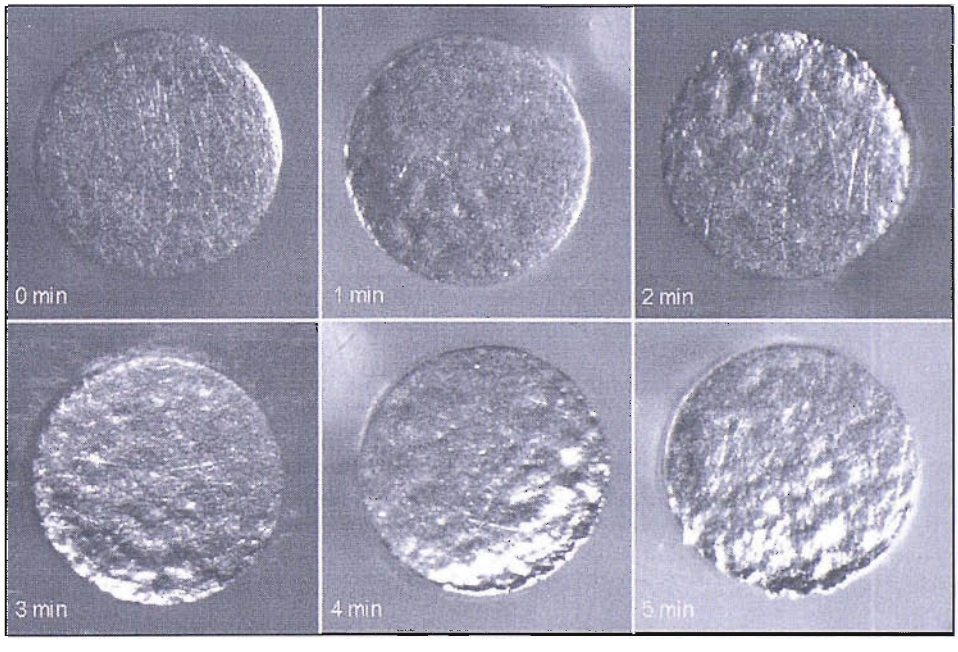

Figure 4.8: Showing the damage caused to the surface of the same aluminium electrode (diameter 250 µm) after 0, 1, 2, 3, 4 and 5 minutes held 0.5 mm from the tip of the ultrasonic horn. The ultrasonic horn was driven at 23.17 kHz and a voltage of 100 V (zero to peak).

Figure 4.8 shows that even after only 1 minute of exposure to the cavitation environment there is already evidence of pock-marking on the surface of the electrode. After each successive period of sonication the damage to the electrode becomes more distinct with a bias to one side of the electrode becoming apparent after 180 s of exposure. After 300 s it is possible to see that the aluminium of the electrode has started to be extruded over the edge of the epoxy support towards the bottom of the image.

The damage seen in figure 4.8 to the surface of an aluminium electrode over 300 s of sonication, though substantial, is not of the same order as that seen in either figure 4.6 image B or figure 4.7. It is inconvenient that secondary surface events are recorded in addition to those expected from the primary events. However, over the periods of sonication expected for measurements purposes, the extreme damage and highly recessed electrode surface (such as that seen in figure 4.7) can be avoided by the polishing of the electrode between measurements.

4.3. Titanium electrodes

As demonstrated above aluminium electrodes are susceptible to considerable damage when exposed to cavitation over prolonged periods. Consequently an alternative material for the working electrode was investigated. Principally the possibility of replacing of aluminium with titanium which is considerably harder was investigated (titanium is 4.0 on the Mohs scale compared to 2.9 for aluminium (*178*)). Titanium, like aluminium, forms a passive oxide film when held at 0 V *vs.* either silver or stainless steel and consequently also produces anodic current spikes when subjected to inertial cavitation surface erosive events.

4.3.1. Size and shape of transients

The current time transients recorded from the action of surface erosion/corrosion cavitation events on a titanium electrode are in general of a reduced amplitude and increased duration in comparison to those seen on aluminium. Figure 4.9 shows a typical titanium transient which is approximately one tenth the amplitude of those recorded on aluminium (such as in figure 4.2). Conversely the duration of the titanium transients are substantially greater with the current only returning to 10 % of

the peak value after ~ 200 μs has elapsed compared to ~10-40 μs for aluminium. Interestingly if the total charge passed during each event is compared there is little difference between the two materials; during the surface erosion/corrosion event on an aluminium electrode in figure 4.2 a total of 246 pC is passed and during the transient recorded with the titanium electrode in figure 4.9 a total of 192 pC of charge is passed.

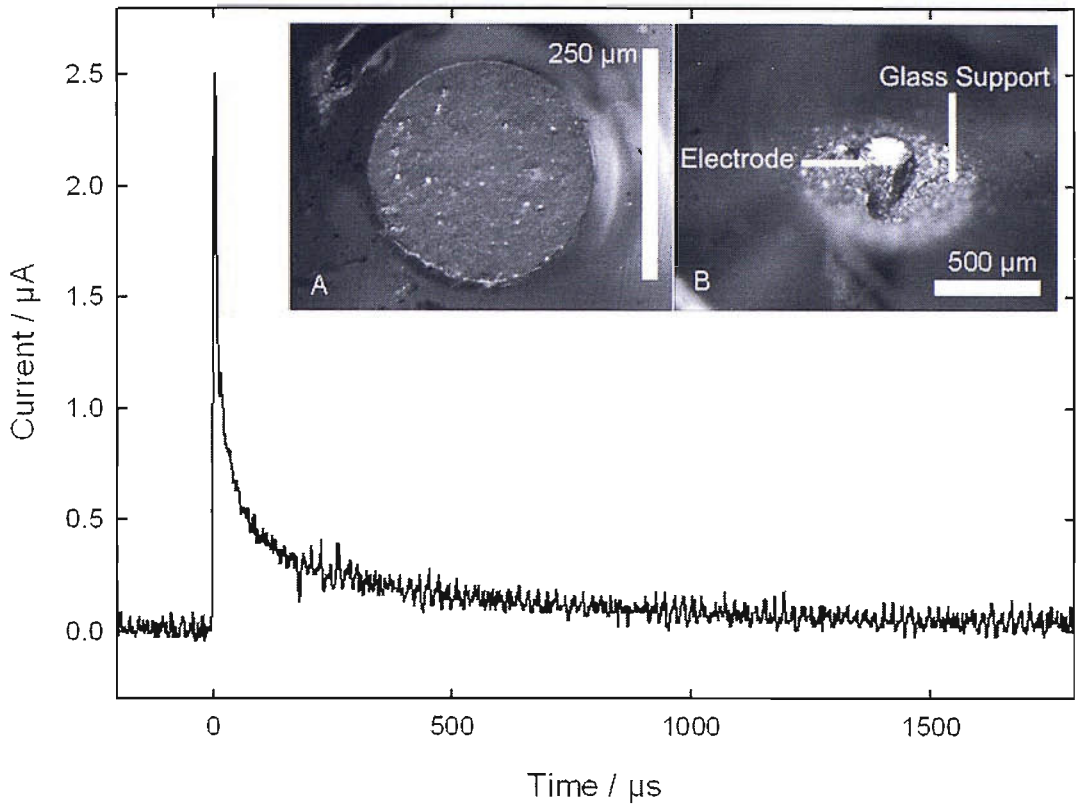

Figure 4.9: A typical transient from an inertial cavitation surface event on a titanium electrode (diameter 250 μm) positioned 0.5 mm from the tip of the ultrasonic horn. The ultrasonic drive frequency was 23.17 kHz, voltage amplitude to transducer was 100 V (zero to peak). Images A and B show the damage to two 250 μm diameter titanium electrodes both exposed to over 1000s of inertial cavitation in the NPL reference vessel and at the tip of an ultrasonic horn respectively.

Detection of surface erosion/corrosion events on titanium was more difficult than on aluminium due to the events being smaller and of longer period; the smaller magnitude of the events also made the measurements more susceptible to electrical interference and noise; the transient in figure 4.9 clearly shows the presence of high frequency noise. Despite the difficulties associated with conducting measurements using titanium electrodes, the increased hardness of titanium compared to aluminium allowed measurements to be made where an aluminium electrode would have suffered considerable damage. Image A and B in figure 4.9 show how even after an extended period in a cavitating environment a titanium electrode still retains a

comparatively smooth surface. In image B we can see that the glass support of the electrode is eroded away in preference to the electrode material.

4.3.2. Comparison of aluminium and titanium

If we compare directly the damage sustained by aluminium and titanium electrodes after a 10 minute exposure to inertial cavitation, the advantage of using titanium over aluminium becomes clear. In figure 4.10 the surface of the aluminium electrode can be seen to resemble a golf ball after the period of sonication where as the titanium electrode is not significantly affected.

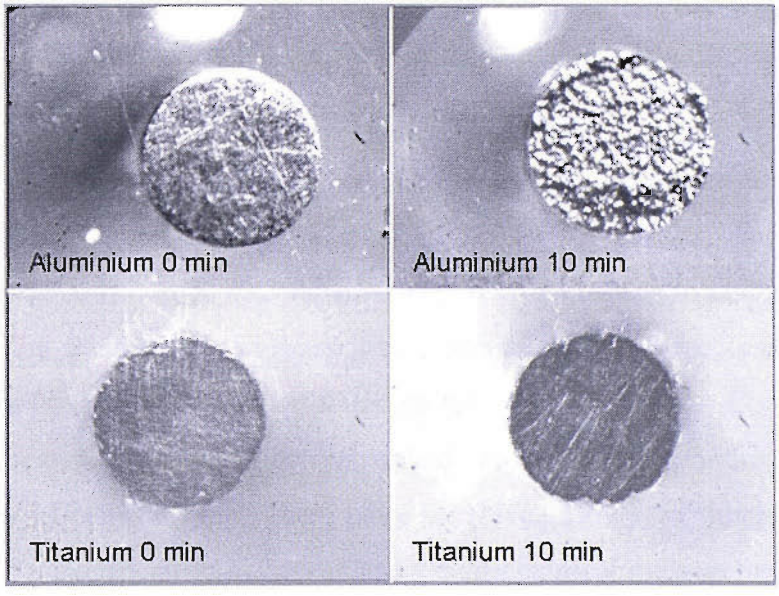

Figure 4.10: Images comparing the surface of 250 μm aluminium and titanium electrodes before and after ten minutes at the tip of an ultrasonic horn in the region of inertial cavitation. The ultrasonic horn was driven at 23.17 kHz and 100 V (zero to peak), the electrodes were held 0.5 mm from the tip of the ultrasonic horn in a central position.

The different characteristics of aluminium and titanium lend themselves to different measurement criteria. Surface erosion/corrosion events on aluminium produce large, fast current time transients that are easy to measure; the metal though is easily damaged limiting the period of time over which measurements can be made. Erosion/corrosion events on titanium produce smaller, harder to detect transients but the increased hardness of the metal allows measurements to be made over a prolonged period in highly active environments. Consequently aluminium electrodes are suited to making more accurate measurements over shorter periods of time or in less active environments, whereas titanium electrodes are good for making

measurements in conditions where aluminium electrodes would suffer prejudicial damage.

4.4. Sensitivity of the technique

4.4.1. Weight calculations

In order to compare the results made here to other measures of cavitation it is informative to contrast the loss of material from electrodes with other detection techniques which rely on material degradation. This, however, is not realistically possible because of the small amounts of material involved in erosion/corrosion events. If we consider a typical event like that in figure 4.2 it is possible to estimate the amount of material lost. During the transient 246 pC of charge is passed before the current returns to 10% of its peak value; using Faraday's law, the amount of oxide formed to replace that removed by the event is ~4.24 x 10^{-16} moles. This corresponds to a mass of 4.33 x 10^{-14} g or 43.3 fg of Al_2O_3. It is interesting to compare this mass with the erosion of materials in mass loss experiments. In these cases a detection limit of the order of ~1 mg can be found in the literature (*179*). Comparing these numbers indicates that the electrochemical erosion/corrosion measurement is approximately 11 orders of magnitude more sensitive. However, this is based on the comparison of a single cavitation event (the electrochemical measurement) with mass loss from many events (*179*). The activity measurements carried out in this work and in previous studies (*54, 74, 158*) have relied on between 10 and 10^7 electrochemical erosion/corrosion events to monitor the spatial characteristics of inertial cavitation. Hence, it is likely that the erosion event can be used with a 4 orders of magnitude[†] increase in sensitivity compared to direct mass loss with a 1 mg resolution.

An alternative method for comparing the detection of electrochemical erosion/corrosion cavitation events with other mass loss techniques would be the

[†] The size and hence charge associated with the erosion/corrosion event will change this estimation. However, the calculation was based on a large anodic event (current maximum ~50 μA) and can be considered as a worst case scenario. Hence this represents a conservative estimate of the sensitivity of the technique.

recording of the number and magnitude of events taking place over a prolonged period of time. This could then be compared to the mass of material lost from the electrode as it became damaged such as the one in figure 4.7. For a heavily eroded electrode such as that in figure 4.7 the aluminium wire that forms the electrode has been removed to a distance of approximately 100 μm from the surface of the epoxy support. With the wire of the electrode having a diameter of 250 μm this corresponds to a volume of aluminium metal removed of ~1.5 x 10^{-6} cm^3. Consequently, given that the density of aluminium is 2.7 g cm^{-3} (*180, 181*), the mass of aluminium eroded from the electrode is ~ 4 μg which is still three orders of magnitude below the detectable mass change levels (*179*).

4.4.2. Chronogravoampometric analysis (Time verses material plot)

The same calculation performed to ascertain the mass of aluminium oxide formed by an individual surface event can be applied to a current time trace, allowing the mass of material formed at the surface of electrode to be monitored as a function of time. Figure 4.11 shows such a plot and from this it is possible to see that for each peak in the standard time current trace (trace a) there is a corresponding step in the mass/charge change time trace (trace b). In particular it is possible to see that there is a significant change in the mass of material formed at the electrode corresponding to the first major peak at ~60 μs.

Though interesting on a purely inquisitive level the validity of the value of the mass change shown in figure 4.11 is debatable. In addition to the current that is passed thorough the circuit as a direct result of the cavitation event there is also a background current (as evidenced by the presence of a positive gradient preceding the first peak) as well as the effect of the double layer charging which, though lower in magnitude than the oxide reformation current, will reduce the accuracy of the mass calculation. It should also be considered that the effect of corrosion on the exposed material is not taken into account in the above calculations. The degradation of the metal and surface will be greater than that taken purely from the electrochemical current.

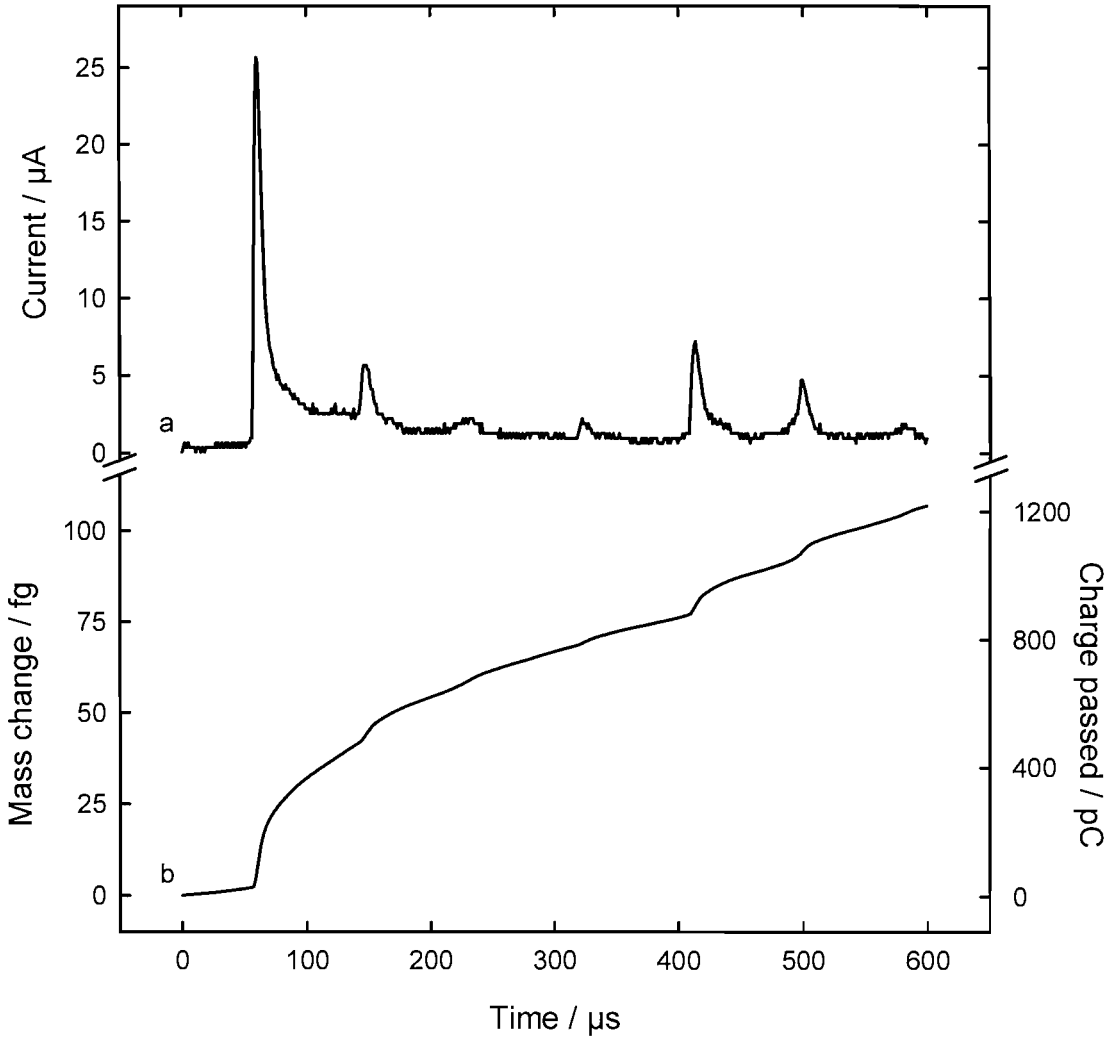

Figure 4.11: Plots showing a series of surface erosion/corrosion events (a) and the integrated charge and therefore mass change (b). Recorded on a 250 µm Al electrode held at 0 V vs. a Ag counter/reference electrode in 0.1 M Na_2SO_4. The electrode was held 0.5 mm away from an ultrasonic horn driven at 23.43 kHz and 100 V zero to peak.

4.5. Use of the electrodes for conducting measurements

Though measurement of individual surface erosion/corrosion events is instructive it is of little use in differentiating between areas of high and low cavitation activity. In order to achieve such measurements a method of recording activity over a prolonged period is needed. The suitability of a multi channel analyser (MCA) to fulfil this requirement is now investigated and its effectiveness in comparison to existing techniques considered. Having established the technique we shall look at the ability of the surface erosion/corrosion event measurements to map both the activity close to the tip of an ultrasonic horn and then within a single transducer ultrasonic reactor.

4.5.1. The MCA method

In order to translate the discrete events discussed so far in this chapter into a method for assessing the level of cavitation at a given point, a measurement has to be made over a prolonged period of time. In previous work conducted with lead electrodes this has been achieved by recording a current time trace using a PC based ADC card and then either recording the average current or the number of discrete peaks within that trace (*54*). By comparing either the average current or the total number of peaks between different points it was possible to discern the changes in the level of cavitation. In general a surface event on a lead electrode is longer in period than one recorded on an aluminium electrode; therefore in order to make comparable measurements a fast acquisition system is required. In addition to this, for this study one of the guiding principles was that any measurement technique developed would be applicable in a variety of different locations. The use of a computer based ADC card would therefore obviously severely limit the portability of the system. Given the requirement that the measurement device be both portable and be capable of making fast measurements; the use of a portable counting instrument was therefore pursued.

The portable device chosen was an Amptek Pocket MCA 8000A Multi Channel Analyser (MCA). The MCA is designed for use in XRF (X-Ray Fluorescence) spectroscopy and is capable of counting the number of peaks as a function of their magnitude over a set period of time at high resolution. Using computer control of the MCA (e.g. commercial control software or bespoke Visual Basic programs) it is possible to control the period over which the MCA collects data as well as the trigger voltage which the magnitude of a peak has to be greater than in order for it to be counted. Through the computer link the MCA transferred the data in two forms of interest; first, the total number of events over the threshold voltage and second, a histogram showing the distribution of these events as a function of their magnitude (see figure 4.12). Thus using the MCA it was possible to make a single measurement that gave information about both the number and magnitude of the surface erosion/corrosion cavitation events taking place on an electrode over a period of time.

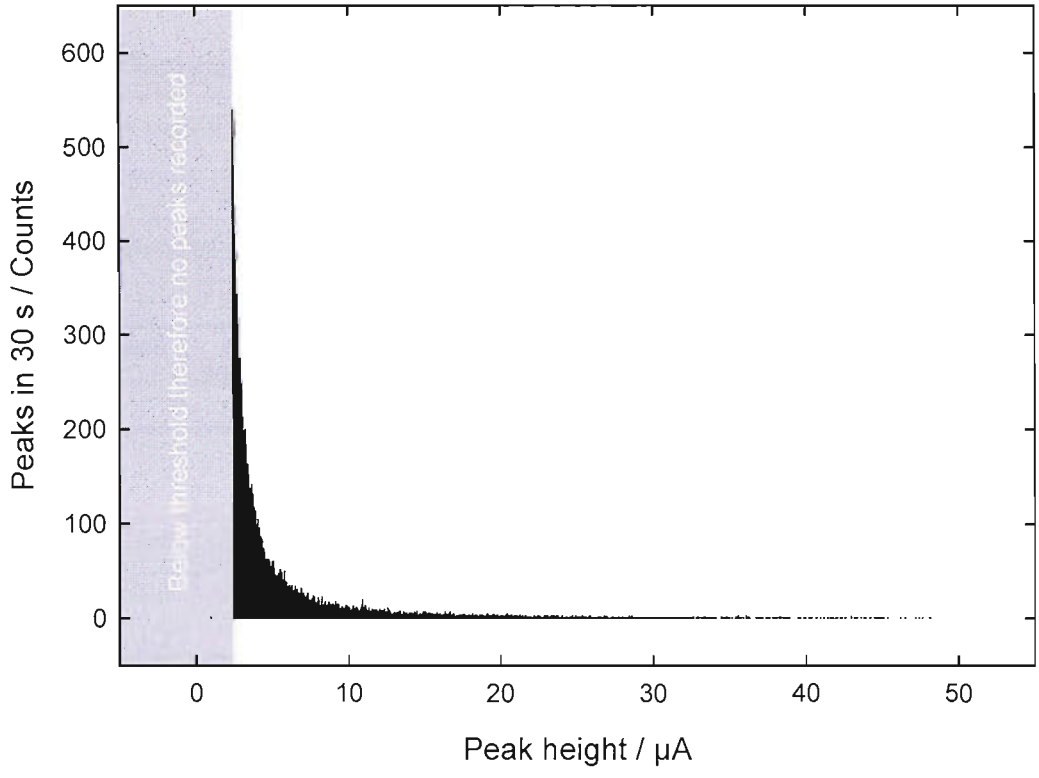

Figure 4.12: Example of a histogram of peak heights recorded using the MCA. The greyed out area indicates the counting threshold of 24.4 μA below which no events are recorded. The histogram contains 44,357 events recorded over 30 s on an aluminium electrode held at 0 V vs. an AG counter/reference electrode and 0.5 mm from the tip of an ultrasonic horn running at 22.65 kHz and 125 V zero to peak in a 0.1 M Na_2SO_4 solution.

The distribution of peak amplitudes in figure 4.12 is in broad agreement with similar measurements conducted for different electrode materials (*54*) with a high number of smaller events recorded dropping off as the peak amplitude increases. This is to be expected given that a smaller peak can be as a result of a large event taking place a distance from the electrode surface or due to a small event close to the surface of the electrode. Conversely a large peak requires both for there to be a powerful collapse and for it to take place in close proximity to the surface of the electrode and is therefore less likely.

The multi channel analyser was not designed for this specific purpose, therefore it is imperative to show conformity between results recorded using the MCA and results acquired using established techniques. In order to accomplish this, simultaneous measurements were conducted using the MCA and an ADC card (Measurement Computing PCI-DAS 4020/12) over a period of 30 seconds. The resultant current time trace from the ADC card was then analysed using a bespoke Visual Basic

program in order to ascertain the number and magnitude of peaks recorded. The program can be found in appendix C. The experiment was repeated 7 times with two different sets of conditions in order to investigate the validity of this approach. The number of events recorded using both the MCA and the ADC card are detailed in table 4.1.

Experiment	Horn distance / mm	Trigger threshold			MCA Count / Counts	ADC card Count / Counts	Average Current / nA
		/ bin	/ mV	/ μA			
1	1	75	91.6	9.2	57	49	15
2	1	75	91.6	9.2	65	44	18
3	1	75	91.6	9.2	4	1	18
4	1	75	91.6	9.2	7	6	19
5	0.5	75	91.6	9.2	17670	24112	186
6	0.5	75	91.6	9.2	91496	85071	459
7	0.5	200	244.1	24.4	44357	45447	875

Table 4.1: Comparing the number of peaks recorded using the MCA and an ADC card and software techniques.

The number of events recorded in table show that there is a good correlation between the numbers of events recorded using the different methods. The agreement between the number of events recorded using the two methods can be illustrated by plotting the number of events from the two methods together as in figure 4.13 (note the large variation in the number of events recorded under different conditions requires that the axes be logarithmic, however the 1:1 correlation is clearly apparent).

If we now look at the distribution of the amplitude of the peaks recorded using both the MCA and ADC approach then it is possible to see the correlation between the two methods. The two histograms presented in figure 4.14 correspond to the sixth experiment in table 4.1. As in figure 4.12 both the histograms in figure 4.14 show a steady reduction in the number of events recorded as the magnitude of the event increases. The slight increase in the number of events recorded at the highest peak current is as a result of all events with a magnitude greater than 50 μA being assigned as having this magnitude.

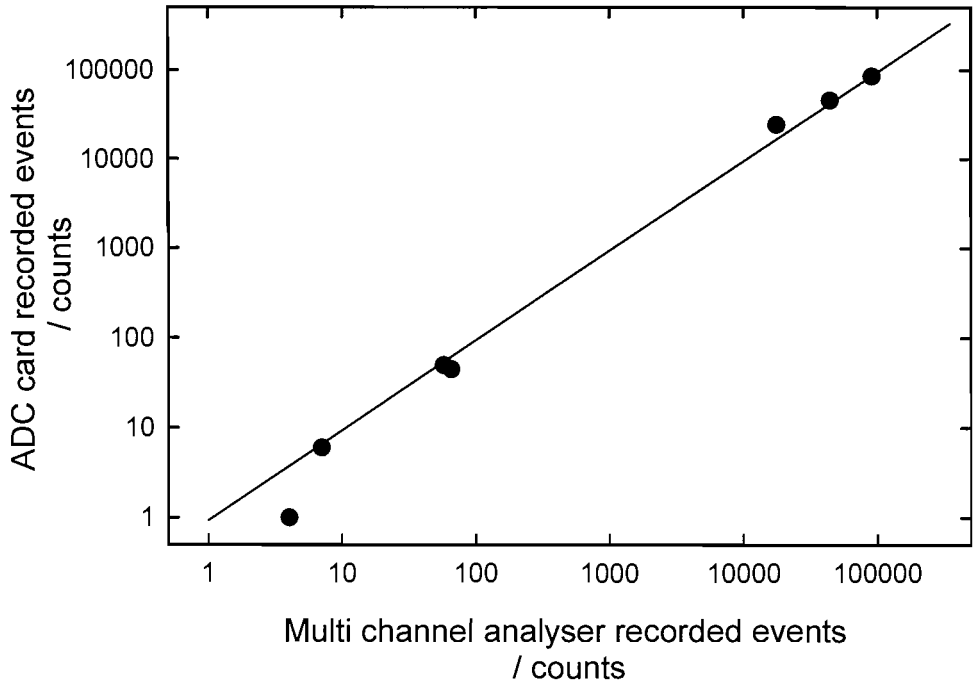

Figure 4.13: Plot comparing the number of events recorded using the MCA and ADC card and software techniques.

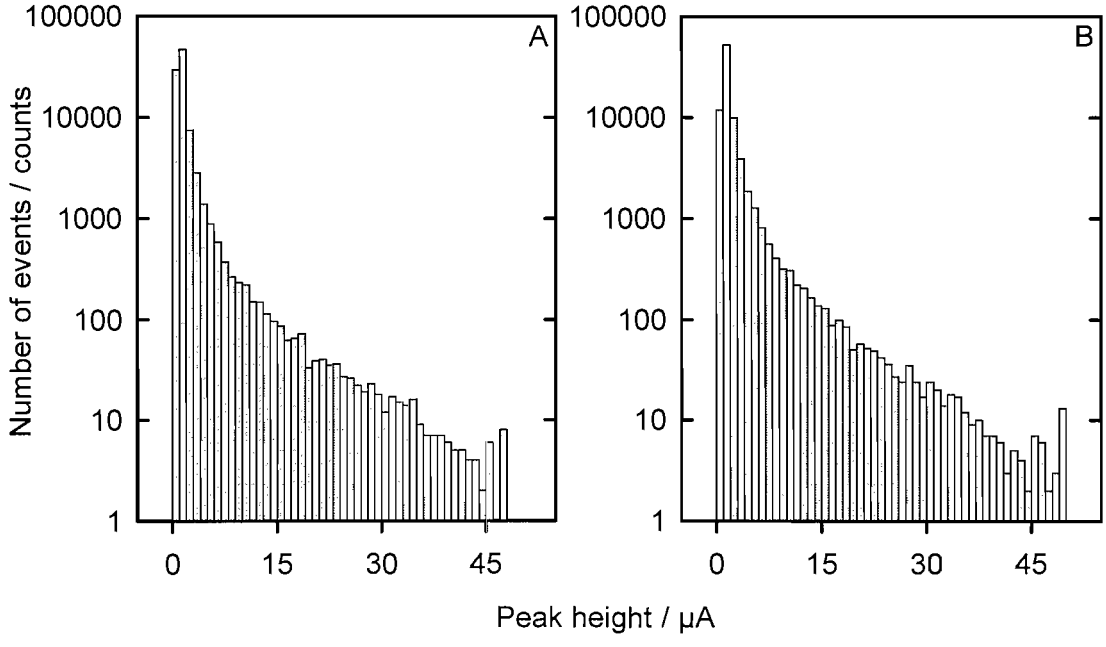

Figure 4.14: Comparison of the size distribution of events recorded using the MCA (A) and ADC card with software (B) counting techniques.

Any difference in the number of events recorded using the MCA and the ADC card counting methods are as a result of a number of factors. Some of the variation observed may be attributed to slight differences in the time at which the measurements were made; this is likely to be a small factor in comparison to the

differences in the time resolution and peak discrimination method of the two techniques. In addition for the purpose of this experiment the time resolution of the ADC card measurement is 500 kHz. Hence if the peak corresponding to an event were only slightly greater than the threshold or trigger voltage in the 2 μs between measurements then no peak would be recorded using the ADC card. This non-recording of some lower magnitude events can be seen regardless of the total number of events recorded. For experiments where there are a greater number of events, the ADC method resolves more peaks than the MCA. This increase is thought to be as a result of the peak counting method of the MCA which only counts discrete peaks where as the counting method used for the ADC card output may count multiple peaks more than once.

From the comparison experiments detailed in table 4.1 and figures 4.13 and 4.14 it can be seen that the MCA collects comparable results to the use of the ADC card and counting software but in a more portable and practical manner. It should be noted that in addition to making it possible to record the number of events taking place over an extended period time, the use of the MCA substantially reduced the volume of data recorded. The extended current time traces recorded for the comparison were each recorded at a resolution of 500,000 samples per second over 30 seconds. As a consequence each file consisted of 15,000,000 data points and had a size of approximately 250 MB. If a scan of a cavitating environment, such as those conducted in this chapter as well as later in this thesis, were to be conducted using this technique then even a relatively modest number of points would soon result in serious issues in handling the data. In contrast each individual file from the MCA is only 20 kb in size; a reduction in size of over 12,000 times.

4.5.2. Effect of trigger point

It is instructive to remember that the number of events recorded is highly dependent on the value chosen for the threshold or trigger value. In order to make reliable measurements the trigger voltage (and hence current) must be selected such that it is great enough that genuine peaks are identifiable from the background signal but low enough such that majority of events are recorded. Table 4.2 shows the effect of the

trigger voltage on the number of events recorded for a number of current time traces recorded using the fast ADC card.

Trigger		Experiment		
/ mV	/ μA	5	6	7
50	5	81403	321706	534239
92	9.2	24112	85071	262710
100	10	21416	73229	228666
200	20	8377	21122	66431
244	24.4	6528	15415	45447
500	50	2676	5424	13372
1000	100	1054	2037	4030

Table 4.2: Showing the affect that changing the trigger threshold has on the number of events recorded.

Consequently it is important that to compare two measurements conducted using the counting technique, be it using the MCA or ADC, the relevant counting thresholds are known.

4.5.3. Distribution of current passed

Modifying the to the data analysis program used to interpret the ADC data for table 4.1 it was possible to estimate the charge passed during the period of each event. The visual basic program on which the analysis is based can be found in appendix C. This analysis makes it possible to see in figure 4.15 the distribution of the current passed during individual events in the same way that the magnitude of the peaks was seen in figure 4.12.

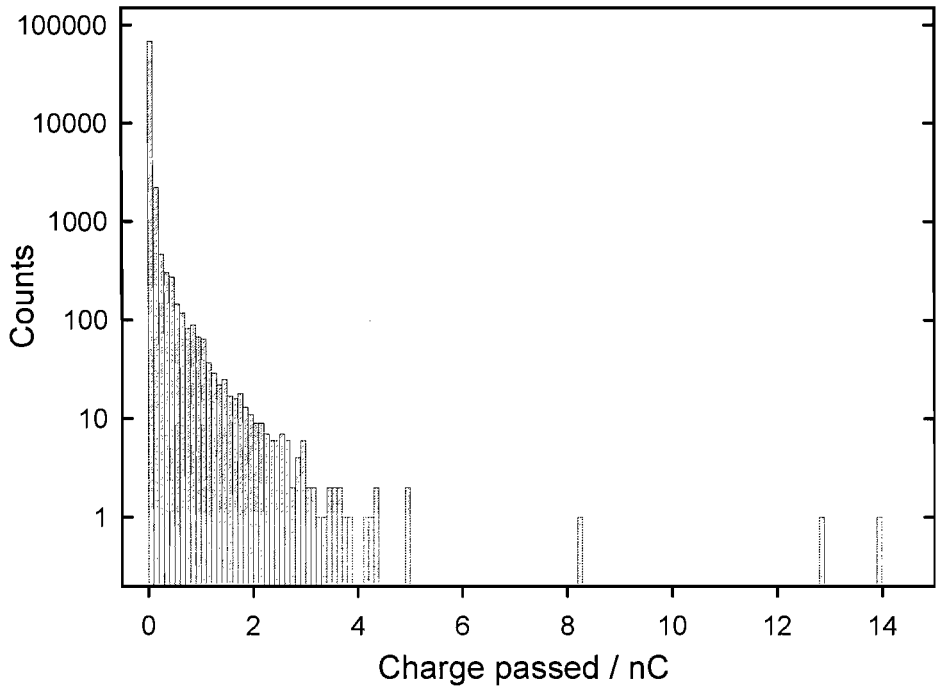

Figure 4.15: Histogram showing the distribution of the number of events as a function of charge passed.

The distribution in the level of charge passed during each event in figure 4.15 shows a similar form to that seen for the peak magnitudes in figures 4.12 and 4.14 with a large number peaks involving the passing of smaller quantities of charge and considerably fewer peaks for which greater charge is passed. Interestingly the quantity of charge passed for the events represented by the second column is similar to that used for the weight calculations in section 4.4.1, indicating that the values used are representative.

It should be noted that the method by which the current passed during each event was calculated was considerably cruder than the method used for the analysis of single events in section 4.5.1. Therefore the accuracy of individual measurements is low; this does not affect the validity of distribution as a whole. Similarly the manner in which the data was analysed lead to a difference in the number of discrete events identified; the current passed method recognised significantly fewer events than that for the peak finding (72175 compared to 85071). Two factors are thought to be responsible for this effect. First the current calculation analysis did not reset until the voltage had dropped below the trigger value resulting in some double peaks and some secondary peaks being counted with the initial peak. Second, smaller peaks that only just registered with the peak finding program would not have been identified by the

current passed analysis (the current had to be greater than the threshold for three measurements for a measurement to be recorded, see appendix C for details). Though individual measurements will be effected, the overall conclusions are still valid.

4.5.4. Repeatability

In section 4.2.5 we saw how over time the form and number of transients recorded on an electrode changed as the surface of the electrode was reconstructed by the effect of the cavitation. It would therefore not be unreasonable to expect that over a period of prolonged exposure there would be a substantial change in the number of events recorded on an electrode. Specifically the presence of high amplitude secondary events such as those seen in figure 4.5 will increase the number of peaks counted by the MCA. Any such increase in the number of events recorded will create an inherent error in any scanning measurements conducted where the same electrode is subjected to a prolonged period of sonication.

To test this hypothesis an electrode was positioned 0.5 mm from the tip of the ultrasonic horn and subjected to the effects of cavitation for a total of twenty minutes (1200 s) made up of 120 x 10 s bursts. In each burst the number of events taking place was recorded using the MCA. After this period of time the surface of the electrode had become seriously deformed (see figure 4.16 images B-D).

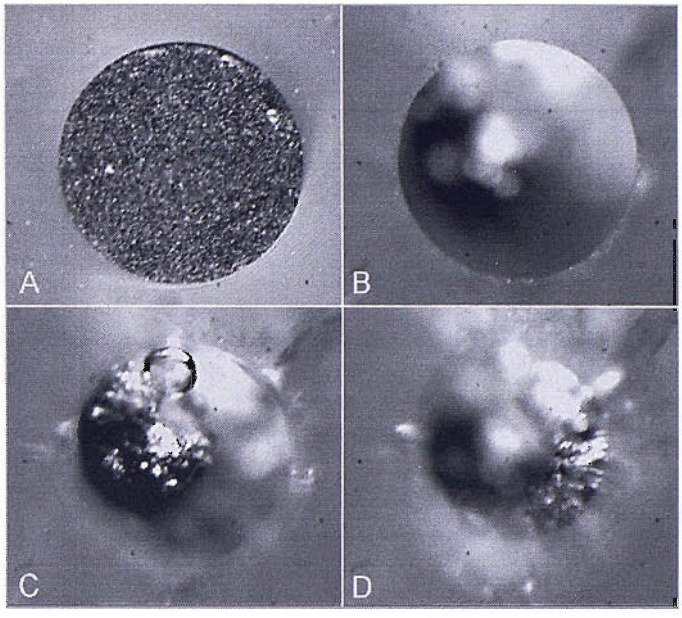

Figure 4.16: Images showing the effect on a polished 250 μm diameter aluminium electrode (A) that 20 minutes of exposure to cavitation has at the surface (B) mid way down the erosion (C) and at the deepest point of the erosion (D) approximately 100μm from the surface.

Images B-D in figure 4.16 correspond to the same electrode but are focused on different planes within the eroded electrode; B on the supporting epoxy resin at the tip, C at the top of the eroded aluminium and D on the furthest eroded portion of the electrode; approximately 100 μm from the surface. The pitted nature of the damage to the electrode made the removal of all the solution from the electrode before imaging impossible, as a result it is possible to see a bubble that has been trapped within the electrode in image C.

Figure 4.17 shows how the number of events recorded at the electrode varied during the sonication. When the electrode was new up until it had been exposed to approximately 170 s of ultrasound the number of events recorded fluctuated greatly. The number of surface erosion/corrosion events recorded then settled out at 80,000 in 10 seconds until around 1100 s of exposure when the number of events started to reduce. The initial instability in the number of events recorded may be as a result of the surface events starting to be damaged. Hence the electrode represents a nucleation site. This increases the likelihood of a surface erosion/corrosion cavitation event being reproducibly detected.

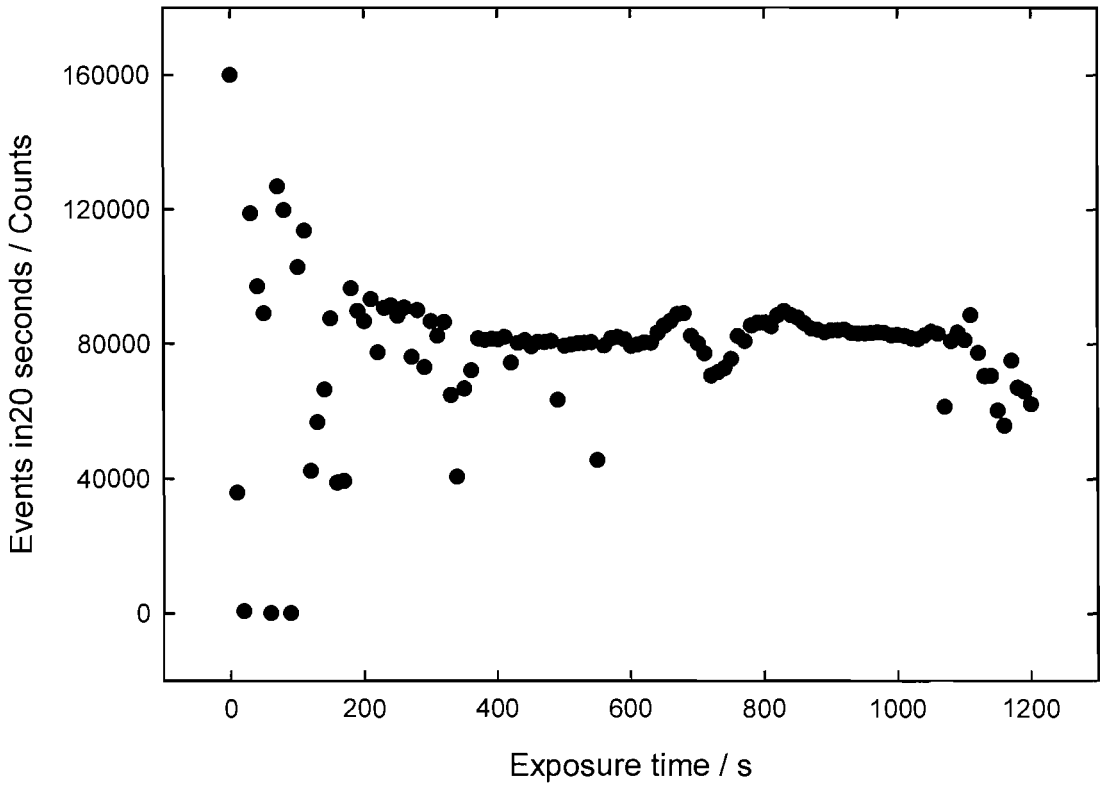

Figure 4.17: Plot showing the variation in the number of surface erosion/corrosion events recorded on an electrode as a function of exposure time. Recorded on a 250 μm diameter aluminium electrode held at 0 V vs. an Ag wire counter/reference electrode and positioned 0.5 mm from the tip of an ultrasonic horn operating at 23.38 kHz and 100 V zero to peak in a 0.1 M Na_2SO_4 solution. The MCA threshold set to 1.2 μA.

It was to be expected that there would be a certain level of variance in the number of events recorded at the electrode surface over time; not least because the conditions at the tip of the ultrasonic horn are unlikely to remain constant leading to a variation in the level of cavitation taking place. The spread in number of events recoded when the electrode is first exposed to the cavitation is all the same greater than would be hoped. After the electrode has been exposed for a short time (by which time the surface of the electrode will have become roughened) the number of events recorded stabilises to a value of around 80,000 counts in 10 s though still with several points at which the number of events recorded is below this value. Overall the short term repeatability when the electrode is newly polished is less than would be expected; conversely the repeatability in the counting measurements over a longer time period is greater than expected. Consequently though not perfect it has been shown that the number of events recorded on the electrode is stable over a prolonged period and thus can be used to measure variation in the level of cavitation between different points.

4.5.5. Map of an ultrasonic horn

Previous studies have made use of passivated lead electrodes to map the activity at the tip of an ultrasonic horn (*54, 74*). Consequently this provides an ideal way to demonstrate the ability of the aluminium electrodes coupled with the MCA to measure cavitation. The experimental setup of the scan can be found in chapter 2 figure 2.7. The electrode was scanned over an area 5 x 5 mm at a resolution of 0.5 mm and the sound switched off between measurements by a Visual Basic program.

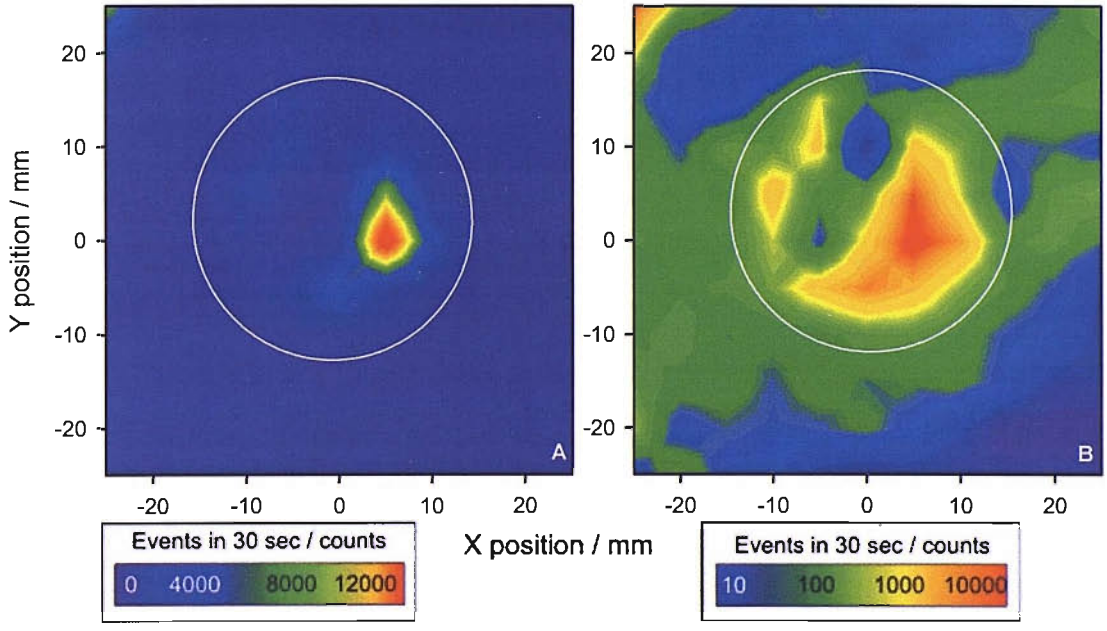

Figure 4.18: Linear (A) and logarithmic (B) contour maps of 2 dimensional surface event scan of a 3 mm diameter ultrasonic horn tip with a 250 μm diameter aluminium working electrode held at 0 V vs. a stainless steel counter/reference electrode and positioned 1 mm from the tip in the Z plane. Scan conducted at a resolution of 0.5 mm and events with a magnitude > 2.4 μA counted using a MCA. Horn driven at 22.58 kHz and 125 V in a solution of 0.1 M Na_2SO_4. The white circles represent the position of the horn relative to the scans.

The number of events recorded at each point varied from 0 to over 15,000 in 30 seconds depending on the location of the electrode with respect to the horn tip. As would be expected the greatest number of events were recorded close to the centre of the horn. There were though a significant number of events recorded beyond the edge of the horn where the cloud of cavitation from the horn was continuing to impinge on the electrode. In order to visualise the scan the results are presented in figure 4.18 in the form of two contour maps. Figure 4.18 map A is a map created using a linear scale for the number of counts; consequently the majority of the scan is hard to observe due to the prevalence of the highly active points at the centre of the

scan. Figure 4.18 map B uses a logarithmic scale for the number of counts instead and as a result more detail in the scans can be seen.

Figure 4.18 having shown that it is possible to map the cavitation activity surrounding the tip of an ultrasonic horn we shall now move on to look at the detection of surface events in a reactor.

4.5.6. Measurements in a reactor

The previous section has shown that the detection of erosion/corrosion events can be useful in the characterisation of inertial cavitation in the region surrounding the tip of an ultrasonic horn. However, this detection/characterisation system must be capable of monitoring the spatial characteristics of inertial events within other environments; specifically those found in a large ultrasonic reactor. In order to demonstrate this, the detection system was deployed in a single transducer cylindrical cell.

Whereas an ultrasonic horn generates a reproducible localised area of cavitation, an ultrasonic reactor has a cavitation field which is far more varied and frequency dependant (*155*). For example luminescent imaging of a cylindrical sonochemical reactor has shown that there are many regions of cavitation activity which are highly spatially dependant (*62, 155*). Using low light imaging techniques these areas can be observed from the multi bubble sonoluminescence (MBSL) produced by inertial cavitation. In the cylindrical reactor employed here, the regions of the liquid where inertial cavitation exists can be identified using the low light images. This enables accurate location of the electrode within an inertial cavitation zone. When this is done current time transient events similar to those seen when an electrode is located in close proximity to the tip of an ultrasonic horn are observed (see figure 4.19).

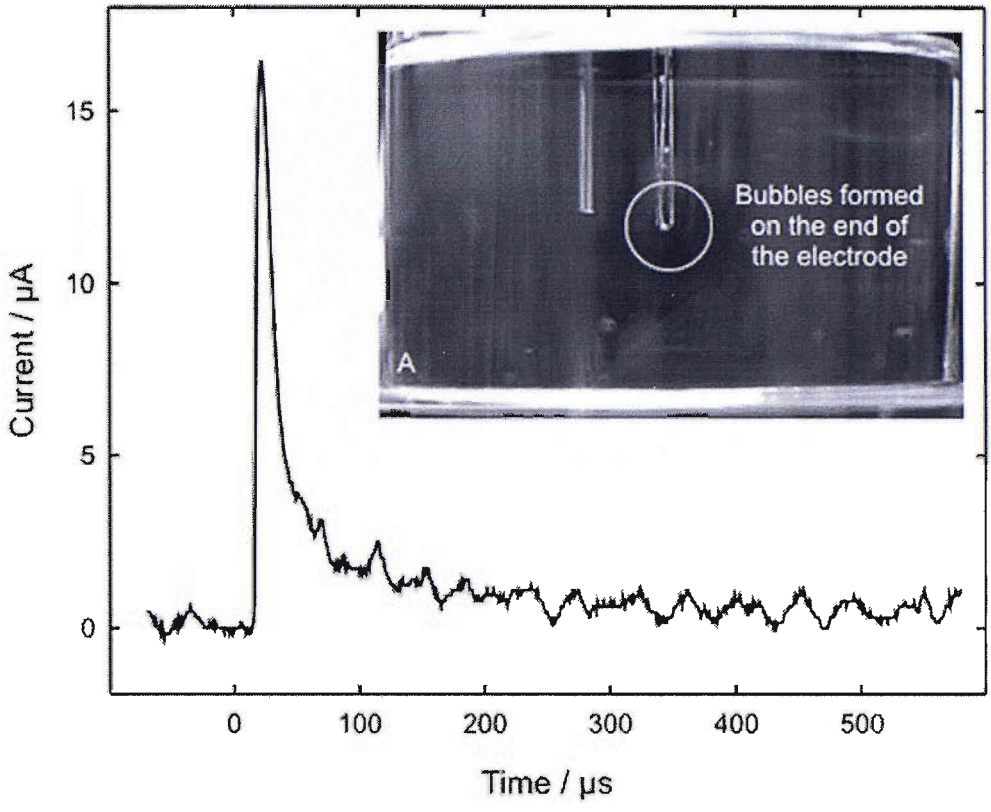

Figure 4.19: Example of a surface erosion/corrosion event transient recorded in a single transducer reactor. Event recorded on a 250 µm Al electrode held at 0 V vs. a SS counter/reference electrode and positioned centrally 80 mm above the base of reactor 4. The reactor contained 1 dm^3 0.1 M Na_2SO_4 and was driven at 22.81 kHz and 150 V zero to peak. Image A shows the presence of a bubble cloud at the tip of a similar electrode in reactor 2 operating at 38 kHz and 100 V zero to peak.

A characteristic of the ultrasonic horn was that when the conditions were such that inertial cavitation was taking place at the tip of the horn a cloud of bubbles could be seen in the vicinity of the tip. Similarly when an electrode was placed within an ultrasonic reactor at a point at which surface events were recorded it was often possible to identify a cloud of bubbles at the electrode tip such as that seen in image A in figure 4.19. Further to this if an intensified image of the reactor is taken (figure 4.20 a) it is possible to see that there is a corresponding region of light emission at the tip of the electrode (figure 4.20 c).

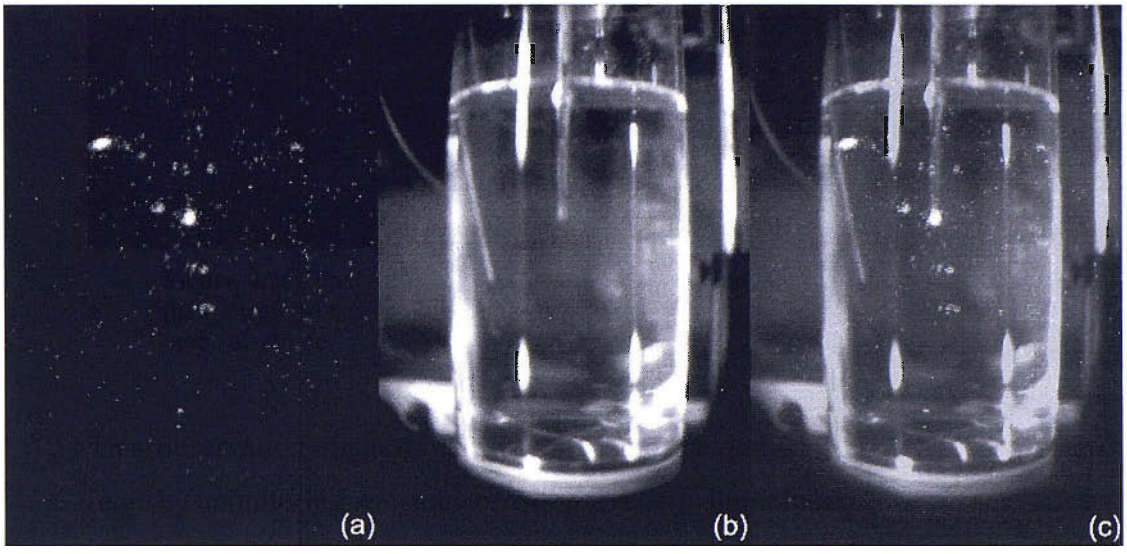

Figure 4.20: Images of an electrode in reactor 4 showing the MBSL (a) the ambient light image (b) and combined image (c). Images a & c show the luminescence at the tip of the electrode.

This observation suggests that when inertial cavitation is detected at the electrode (e.g. by monitoring erosion/corrosion events), luminescence is centred around the electrode tip. This occurrence is understandable as two criteria must be satisfied to generate inertial events. First, the acoustic pressure conditions must be sufficient to drive a bubble to inertial collapse. Second, an appropriate nucleation site must be available. Clearly placing an electrode within a pressure anti node will enable both criteria to be satisfied.

Another important consideration is affect that the electrode has on the pressure field within the reactor. Previous studies have shown that due to differences in the acoustic properties of an electrode compared to the solution in which it rests it is invasive; affecting the pressure and therefore cavitation field surrounding it. As a consequence in the same way that an electrode placed in the neighbourhood of an ultrasonic horn can result in an extension of the region of inertial cavitation field towards the electrode so it should be expected that the placement of an electrode within a cavitating vessel is going to have an effect on the regions of inertial cavitation within the vessel.

4.5.7. Correlation of surface and light effects in a reactor

A distinctive characteristic of cavitation within a single transducer cylindrical ultrasonic reactor is that given the correct conditions a stable and regular modal structure can be observed (*62, 155*). This modal structure can be seen as regular patterns in sonoluminescent images (see figure 4.21). When the reactor is viewed from the side this is manifested as a series of bands of light (see figure 4.21a); from above as concentric rings (see figure 4.21b). These perspectives are entirely expected and predictable given the three-dimensional structure of the sound field.

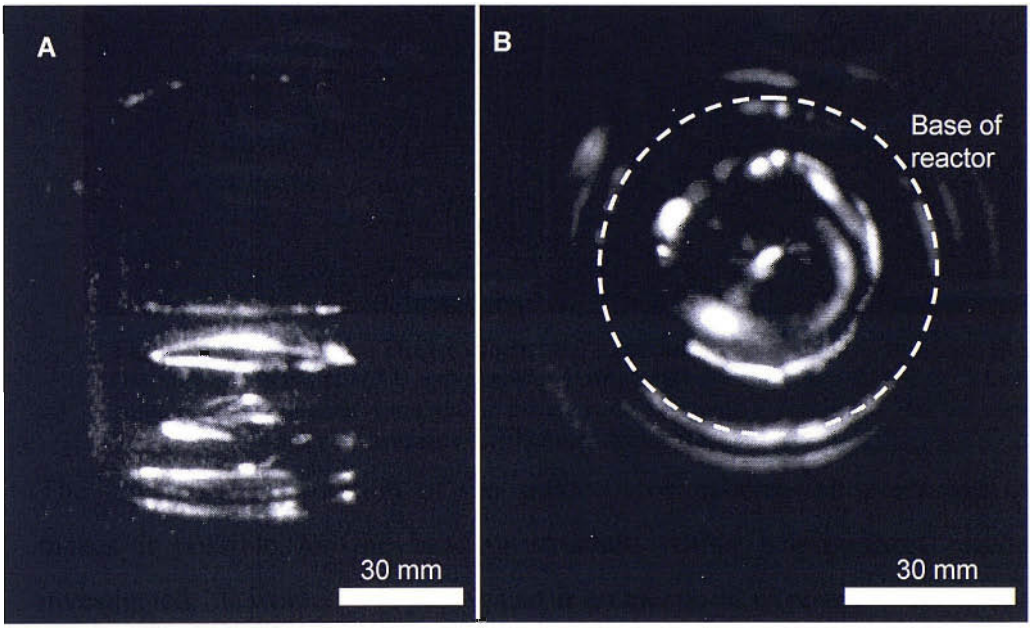

Figure 4.21: Intensified images of reactor 3 recorded from the side (A) and from above (B) showing banding (A) and concentric rings (B) formed from MBSL). Reactor contained 140 ml pure water and is driven at 40 kHz with a voltage of 100 V (zero to peak). Both images are averages of 100 individual images.

The high spatial resolution of the surface erosion/corrosion event measurements makes it possible for the banding structure within a cylindrical reactor to be investigated. It would be expected that if an electrode were to be drawn up through the reactor, stopping at regular intervals to make measurements, the band structure should be evident as regions of zero activity (where the acoustic pressure is below the critical threshold for inertial cavitation and being manifest by a lack of luminescence) interspersed with regions at which a number of surface cavitation events would be recorded (corresponding to locals where the pressure exceeds the critical threshold and the luminescent bands are seen). Thus by comparing the number of events recorded on an electrode the relative level of inertial cavitation activity can be found as a function of position within the vertical scan. In order to demonstrate this, a mode

was generated within a cylindrical reactor and an electrode placed in the centre of the cell and scanned vertically with a resolution of 2.5 mm. From the number of surface events recorded, using the MCA, the presence of bands of inertial cavitation activity can be seen (see figure 4.22).

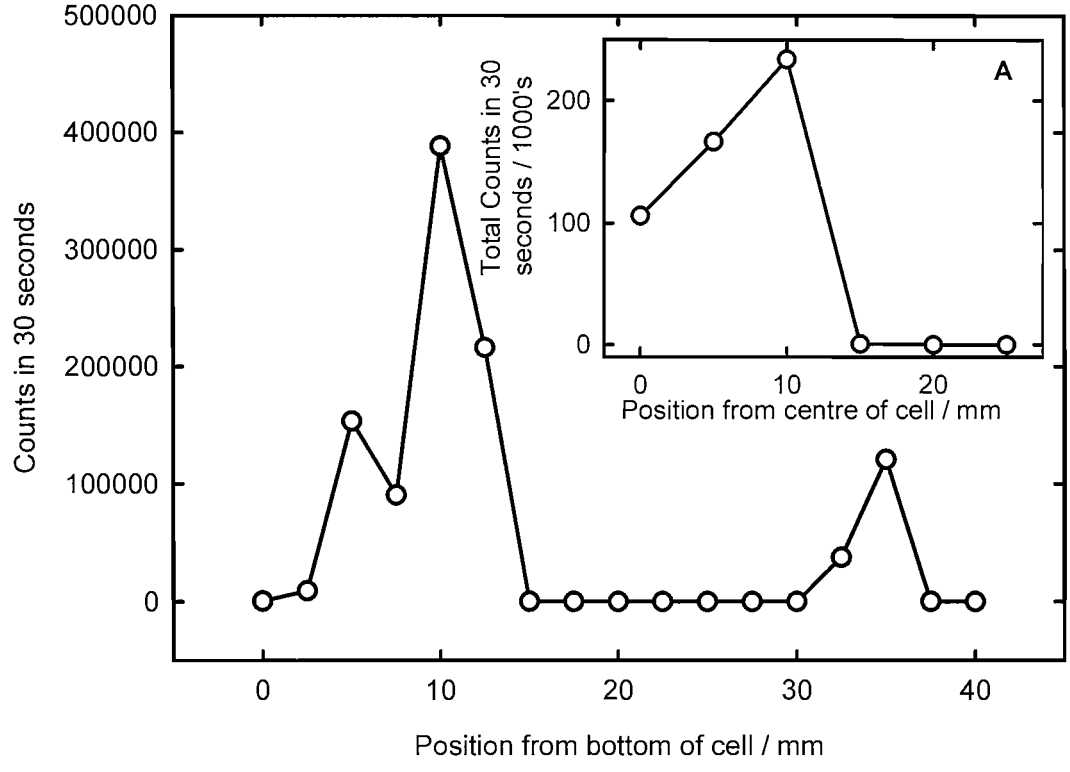

Figure 4.22: Variation in number of surface events recorded in 30 seconds as a function of vertical position within the reactor of a centrally placed electrode. Insert A shows the variation in the number of events as a function of horizontal position 7.5 mm above the base of the scan. MCA trigger set to channel 246 (0.3 V). 250 μm aluminium electrode held at 0 V *vs.* silver wire and current follower set to 10^5 V A^{-1} gain. Reactor 3 contained ~140 ml solution driven at 40 kHz and 100 V (zero to peak amplitude).

Figure 4.22 shows that the bands of inertial cavitation activity are separated by 15 ± 2 mm in the vertical direction. This compares to a spacing of 13 ± 2 mm measured from the luminescent image (see figure 4.21A). Similarly when an electrode was placed 7.5 mm from the bottom of a vertical scan (in a region where inertial events where detected in the centre of the cell) and then scanned horizontally across the reactor at 5 mm resolution, the horizontal activity was observed, figure 4.22 insert A. The horizontal scan across the reactor shows a ring like structure to the mode excited, similar to that observed in the low light images, figure 4.21B. Figure 4.22 insert suggests that the inertial activity not apparent at the edge of the cell (close to the liquid/solid interface at the water jacket). It should be noted that the mode generated

within the cylindrical vessel will have an influence on the interpretation of these scans. For example an asymmetrical mode will have pressure nodes on the axis of the cylinder and therefore no cavitation activity. Conversely a symmetrical mode would have pressure antinodes on the axis and hence cavitation activity. Care should therefore be taken in comparing the activities measured using single line scans within the cell.

4.6. Conclusions

This chapter has shown that it is possible to record surface erosion/corrosion events on both aluminium and titanium electrodes. We have seen that after prolonged exposure to the effects of cavitation the surface of aluminium electrodes become highly damaged and different, more "rounded", current time peaks are seen. In comparison titanium electrodes have been shown to be more resistant to damage and therefore suited to situations where aluminium would not survive. To enable the mapping of inertial cavitation activity a new, portable, counting technique has been developed. The technique was tested below an ultrasonic horn and within a single transducer reactor.

Although the electrochemical technique is simple, relatively accurate and portable, it would be wrong to say that it represents an 'ideal' inertial cavitation measurement technique. As with all localised measurement techniques (e.g. hydrophones), to map an entire vessel, a single electrode would have to scan all three dimensions of the cell, which is time-consuming (during which time the cavitation might change because of changes in the temperature, gas content etc.). Similarly a large array of electrodes capable of mapping large areas of the vessel would be invasive. However, the electrodes sensor represents a useful addition to the other measurement techniques available, in particular it has shown to be capable of resolving bands within a reactor.

5. High-speed imaging

The use of high-speed imagery to study the effects of cavitation, be it ultrasonic cavitation or laser induced cavitation, is extensive (*34, 37, 99-102*). Most pertinent to this study, the action of a collapsing bubble cloud impinging on a passivated electrode has been studied at great length by Offin *et al.* (*54*). In this section we will use high-speed imaging to look at the processes on aluminium electrodes. We shall look at 6 sets of data covering three separate situations.

1) Individual primary transients induced by the action of an ultrasonic horn
2) Primary and secondary transients generated by an ultrasonic horn; specifically examining any difference in their formation.
3) Events recorded on an electrode placed in a single transducer reactor.

For each situation simultaneous high-speed imaging and current time transients recorded at the electrode in question will be presented in order to interpret the events, and their erosive nature. A clearing of the observed bubble cloud is associated with the collapse of the bubbles due to cavitation (be it due to individual collapses or a cluster collapse). It is therefore expected that surface erosion/corrosion activity would be associated with such occurances.

5.1. Primary horn events

The current time transients and concurrently recorded high-speed images from two surface erosion/corrosion cavitation events on a 250 μm aluminium electrode generated by an ultrasonic horn are now presented. For each set of results the current time trace is annotated with a series of numbered circles representing the temporal position of the correspondingly numbered high-speed video frame.

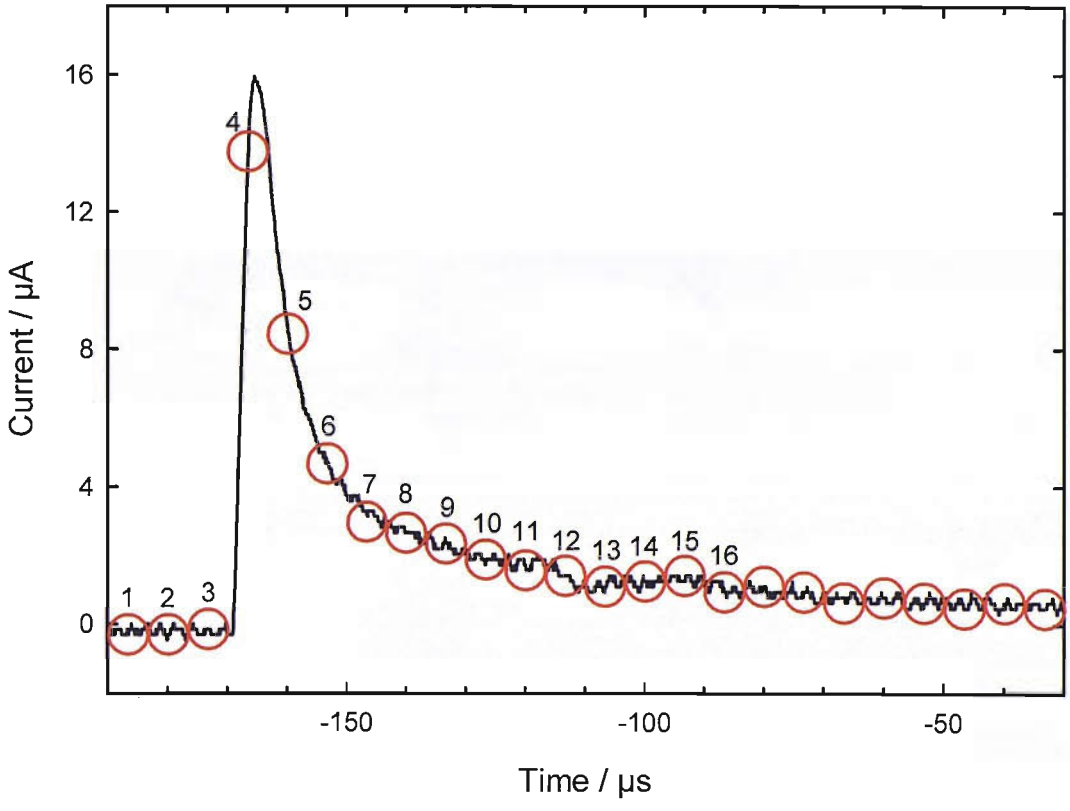

Figure 5.1: Plot of a current time transient formed as a result of erosion/corrosion of a 250 µm aluminium electrode recorded simultaneously with the images in figure 5.2. The numbered circles represent the duration and position of the high-speed video images in figure 5.2. Event recorded in 0.1 M Na_2SO_4 with the ultrasonic horn driven at 22.66 kHz and 110 V zero to peak. Electrode positioned 1 mm from the tip of the horn and held at 0 V vs. an Ag counter/reference electrode.

If we look at the current time trace in figure 5.1 and the corresponding high-speed images in figure 5.2, each image at a time we can see the action of the collapsing bubbles and how this results in the current time transient recorded. In images 1-3 it can be seen that there are a number of bubbles on or near the surface of the electrode. In particular a bubble can be seen just to the left of the centre of the electrode. In image 4 this bubble (along with the other bubbles present in the preceding images) is no longer visible and there is a sharp increase in the current passed corresponding to the reformation of the passivated oxide layer after its removal by the action of the collapsing bubble cloud. In images 5 through 8 the bubble cloud can be seen to be reforming the bubble cloud through the generation of a large number of smaller bubbles interspersed between the tip of the horn and the electrode. If we examine the same period of time in figure 5.1 it can be seen that the current passed is reducing as the oxide layer on the electrode is reformed; implying that there is no observable erosive mechanism here. For images 9 through 13 it can be seen that the bubbles

between the electrode and the ultrasonic horn reduce in volume in a similar manner as happened in images 1-3. On this occasion though there is not the same clearing of the bubbles as seen in image 4 and consequently there is not the same deflection in current.

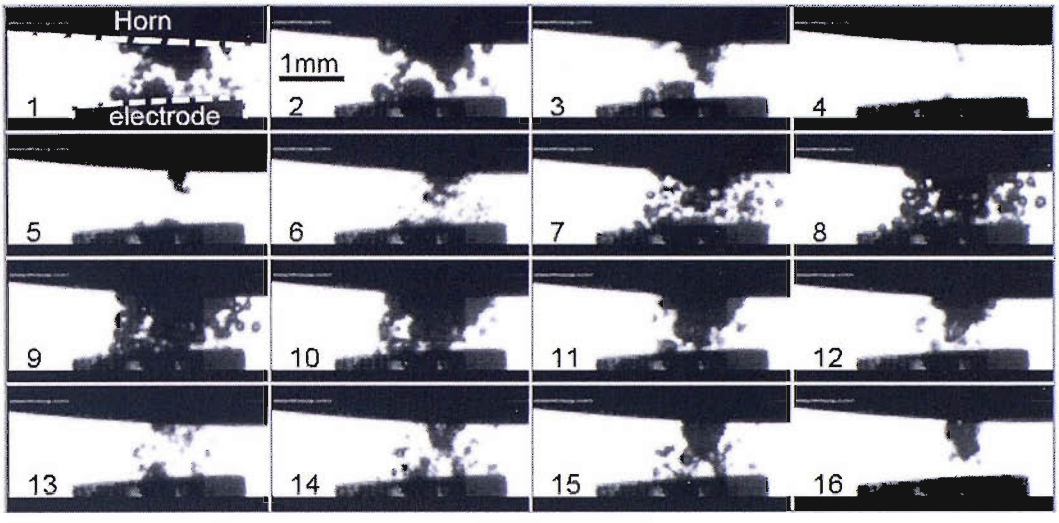

Figure 5.2: Simultaneous high-speed video images for figure 5.1. Recorded at 150,000 frames s^{-1} with a shutter speed of 1/150000 s.

Similarly if we look at the current time trace and images in figure 5.3 we can see that in images 1 to 3 there is a bubble cloud between the tip of the horn and the electrode. This can be seen to collapse away in image 4 such that there are no bubbles seen between the electrode and the horn. At the same point in time a substantial increase in the current passed is observed corresponding to the reformation of the damaged oxide layer. In image 5 it is possible to see the presence of some small bubbles indicating the reformation of the new bubble cloud. Images 6 to 8 show that a new bubble cloud has formed.

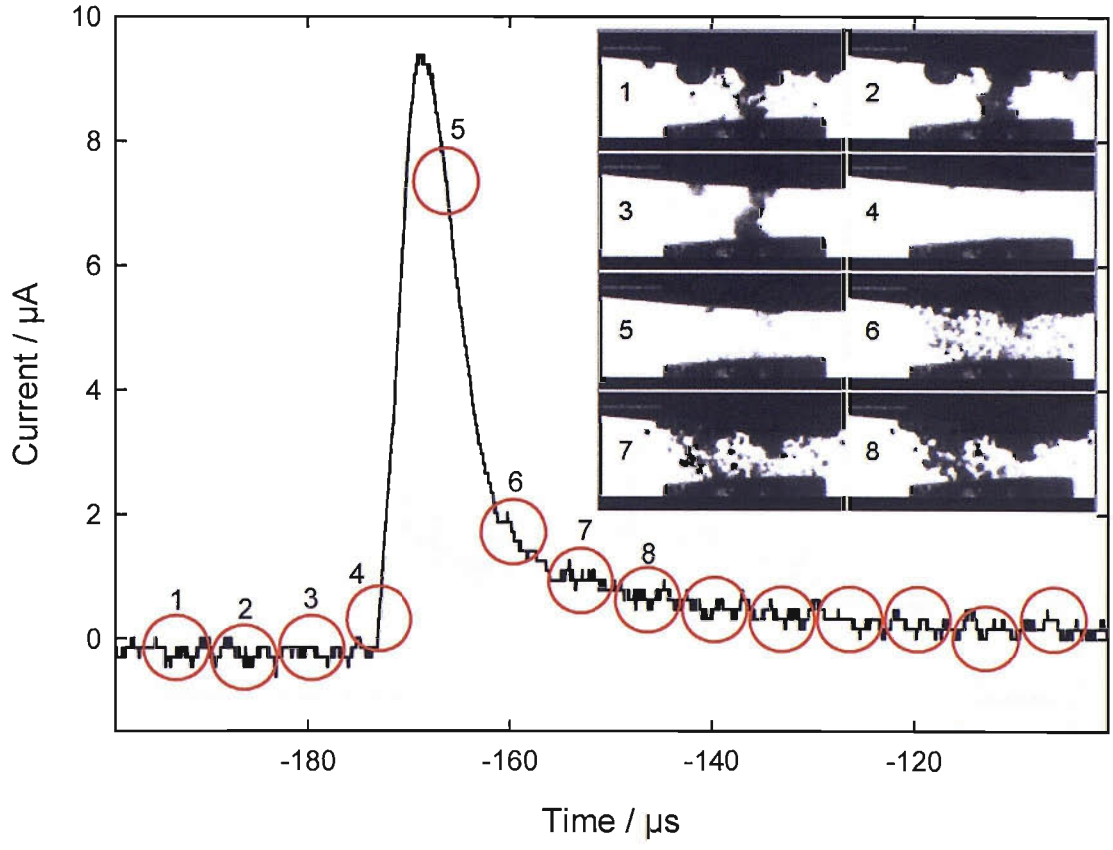

Figure 5.3: Current time trace of a surface erosion/corrosion event recorded on a 250 µm electrode and simultaneous high-speed video images. The numbered circles on the current time trace represent the duration and timing of the same numbered high-speed images. Event recorded in 0.1 M Na_2SO_4 with the ultrasonic horn driven at 22.66 kHz and 110 V zero to peak. Electrode positioned 1 mm from the tip of the horn and held at 0 V vs. an Ag counter/reference electrode. Images recorded at 150,000 frames s^{-1} with a shutter speed of 1/150000 s.

5.2. Secondary events

As discussed in chapter 4 after an aluminium working electrode had been exposed to surface cavitation for a prolonged period of time, in addition to the "saw tooth" like transients seen in figures 5.1 and 5.3, current time events with a slower rise time and more symmetrical peak shape are recorded. In chapter 4 these events were referred to as secondary events. Here we shall look at simultaneous electrochemical measurements and high-speed imaging to investigate the mechanism behind the creation of secondary events and whether it differs from that for primary events.

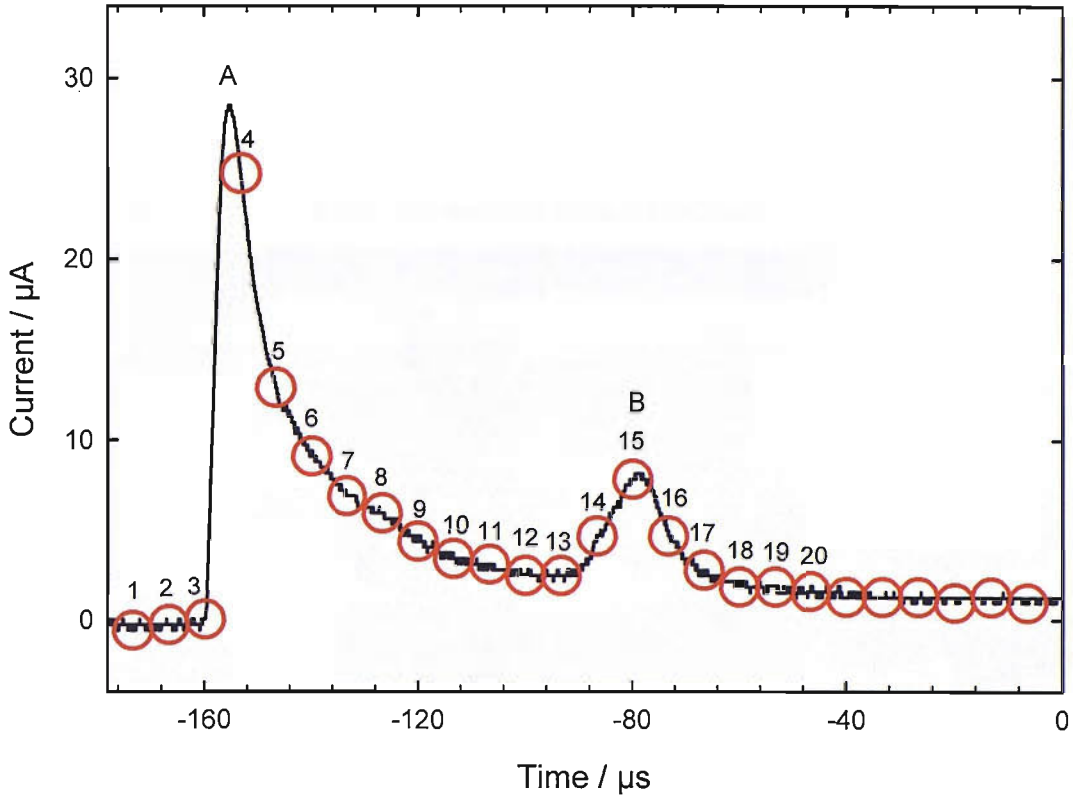

Figure 5.4: Current time trace of a primary (A) and a secondary (B) surface erosion/corrosion events recorded on a 250 µm aluminium electrode simultaneously with the high-speed video images in figure 5.5. The numbered circles represent the duration and position of the high-speed video images in figure 5.5. Event recorded in 0.1 M Na_2SO_4 with the ultrasonic horn driven at 22.66 kHz and 110 V zero to peak. Electrode positioned 1 mm from the tip of the horn and held at 0 V vs. an Ag counter/reference electrode.

The current time trace in figure 5.4 shows the presence of a saw tooth shaped primary peak at ~ -160 µs (marked A), followed 80 µs later by a more symmetrical secondary peak (marked B). Looking at the corresponding high-speed images (figure 5.5) it can be seen that prior to peak A the bubble cloud between the ultrasonic horn reduces in size (images 1-2) before clearing almost entirely (image 3), prior to frame 4 there is an increase in the current for peak A. This suggests that the same process responsible for the clearing is responsible for the erosion. The formation of a multitude of smaller bubbles (image 4) leading to the reformation of the bubble cloud between the horn and the electrode. After ~65 µs the current passed by the electrode begins to increase again for the start of peak B; reaching a maximum 80 µs after the apex of peak A before decreasing symmetrically. It was expected that the inherent difference in the shape between peaks A and B would be as a result of obviously different processes taking place at the surface of the electrode. If we look at the images corresponding to peak B (images 13-18) the behaviour of the bubble cloud between

the electrode and the horn is similar with that seen during the formation of peak A except that the current begins to rise prior to the clearing of the bubble cloud. As the current passed increases the bubble cloud collapses (images 13-14) resulting in a clearing of the cloud as a result of a shock at the point of maximum current (image 15). The current then reduces and the bubble cloud reforms (images 16–18).

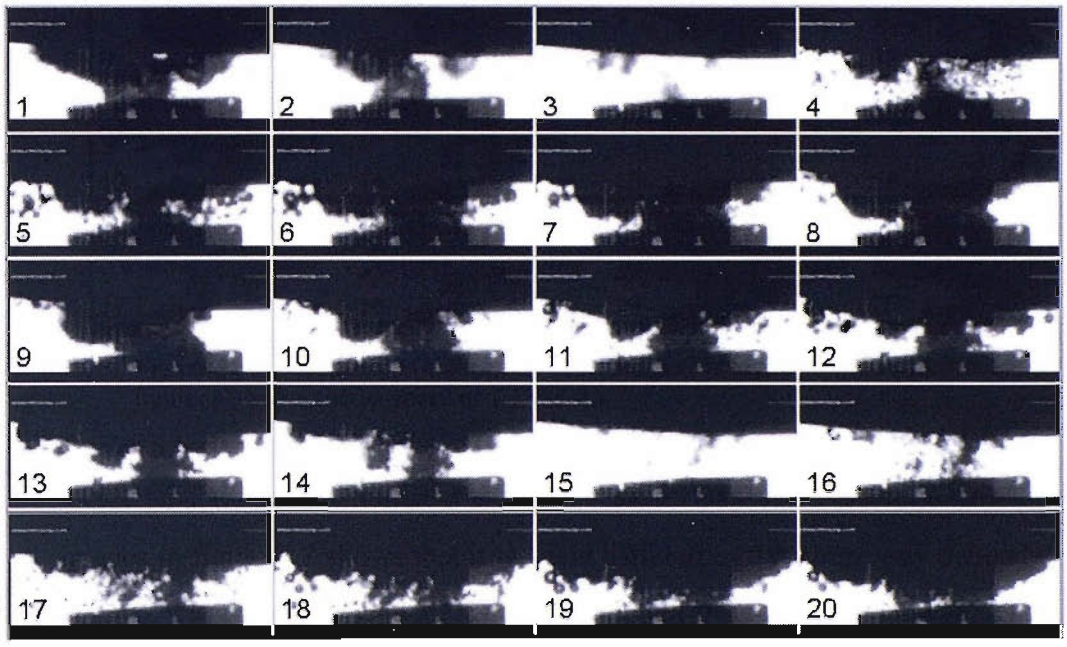

Figure 5.5: Simultaneous high-speed video images for figure 5.4. Recorded at 150,000 frames s^{-1} with a shutter speed of 1/150000 s.

Figure 5.6 shows another example of a saw toothed primary peak (C) being followed 83 μs later by a more rounded secondary peak (D). The corresponding high-speed images in figure 5.7 shows that it is again difficult to determine any difference in the process leading to the formation of the different peaks. Prior to peak C the bubble cloud rearranges (images 1-3) before clearing and showing possible material ejection from the surface of the electrode (image 4) as peak C is seen to form on current time trace (figure 5.6). After peak C has reached its maximum (image 5) the bubble cloud reforms (images 6-15) before clearing at the same point as peak D (image 16–18). If we compare the three images preceding the "primary" peak C (images 2-4) and the "secondary" peak D (images 15-17) it can be seen that despite the current time traces for the two peaks being markedly different the shape and action of the bubble cloud formed between the tip of the ultrasonic horn and the working electrode is the same in that there is a clearing of the cloud at the point of maximum current. It should be noted that when the current begins to rise for the formation of peak D, indicating the

beginning of the erosive corrosive action, there are bubbles in contact with the surface.

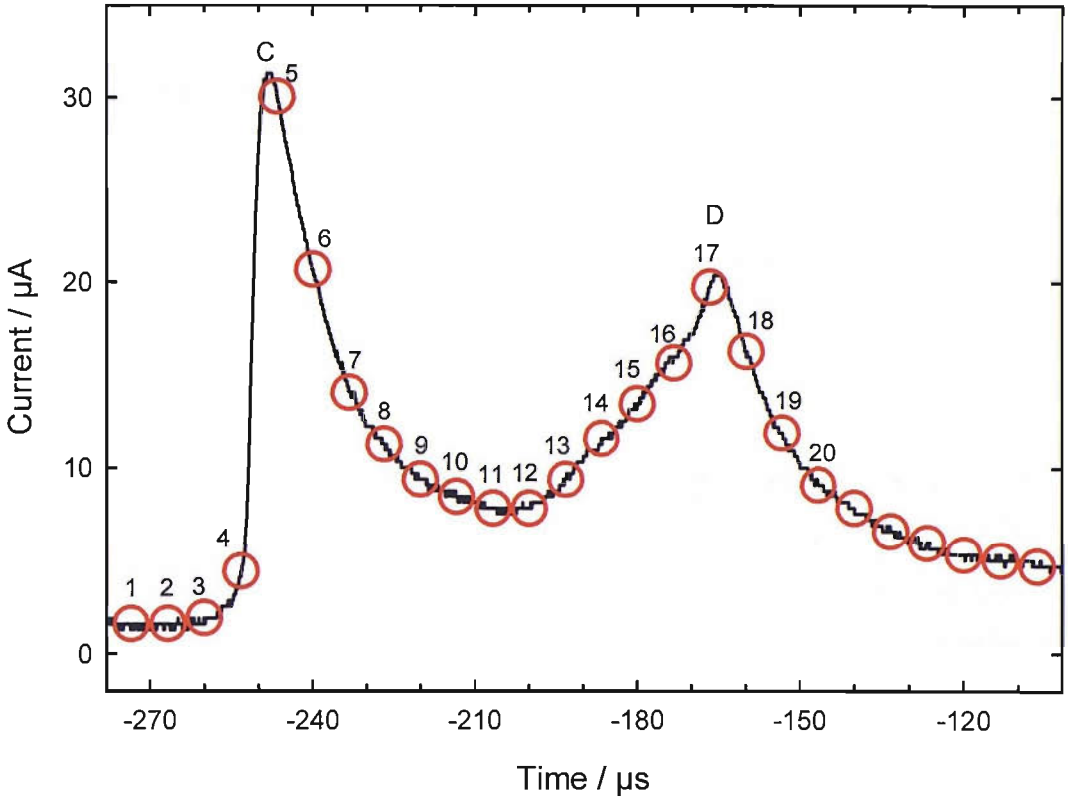

Figure 5.6: Current time trace of a primary (C) and a secondary (D) surface erosion/corrosion events recorded on a 250 µm aluminium electrode simultaneously with the high-speed video images in figure 5.7. The numbered circles represent the duration and position of the high-speed video images in figure 5.7. Event recorded in 0.1 M Na_2SO_4 with the ultrasonic horn driven at 22.66 kHz and 110 V zero to peak. Electrode positioned 1 mm from the tip of the horn and held at 0 V vs. an Ag counter/reference electrode.

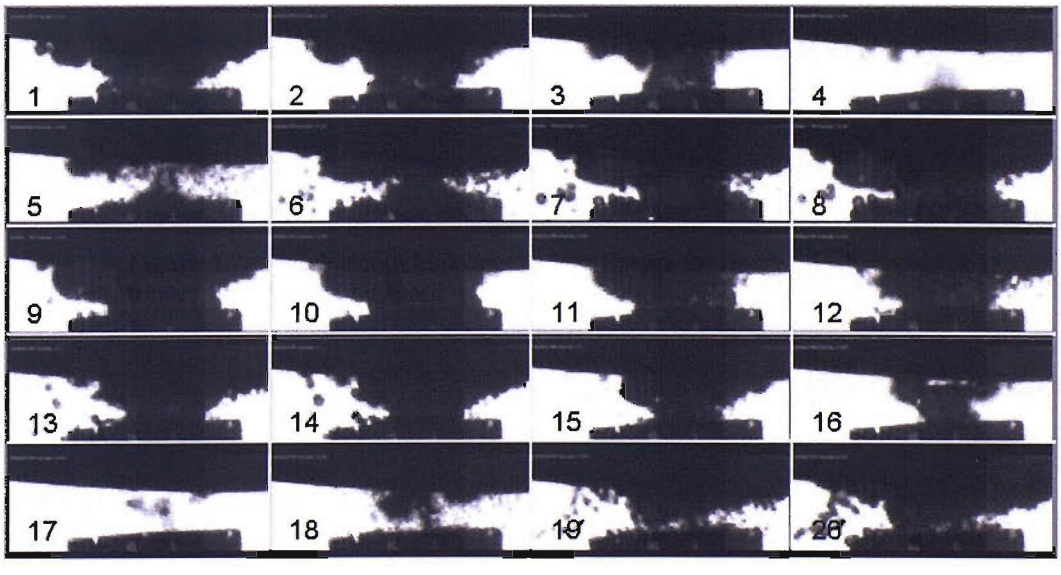

Figure 5.7: Simultaneous high-speed video images for figure 5.6. Recorded at 150,000 frames s^{-1} with a shutter speed of 1/150,000 s.

5.3. Reactor events

The use of an ultrasonic horn to study the processes that lead to the erosion/corrosion of the surface of an electrode is instructive. However, for most situations where an electrode is likely to be used for the measurement of such events the ultrasonic source is going to be remote from the electrode. Such an example is a single transducer reactor. Therefore we shall now look at simultaneous electrochemical measurements and high-speed imagery for an electrode in a single transducer reactor to determine if the mechanisms seen are the same as those at the surface of an electrode near the tip of an ultrasonic horn.

The acquisition of high-speed video sequences of the processes taking place in a reactor imposed a number of constraints. Primary amongst these, unlike for measurements at the tip of an ultrasonic horn, it was not possible to use glassware that had optical windows that assist imagery. Consequently the images recorded were less clear. Also the area that had to be covered by the images was greater as the bubble cloud formed at the tip of the electrode was not bounded by the tip of the horn. This necessitated the use of slower frame rates; decreasing the temporal resolution of the imagery.

The experiments carried out in chapter 4 have shown that it is possible to record individual surface erosion/corrosion events in a single transducer reactor (see figure 4.19); it was also shown that such events can only be recorded at certain points within the reactor due to the variation in the sound field and therefore the cavitation activity (see figure 4.22). As a consequence the position of the electrode within the reactor is of great importance. To conduct concurrent high-speed imaging and electrochemical measurements, the single walled reactor 4 was used to aid the imaging of the activity and the electrode placed in the central axis of the reactor 80 mm from the base; this being a position where it was known that there was high surface erosion/corrosion activity (see chapter 6 figure 6.9). We shall now examine two current time traces and accompanying high-speed images taken of reactor 4.

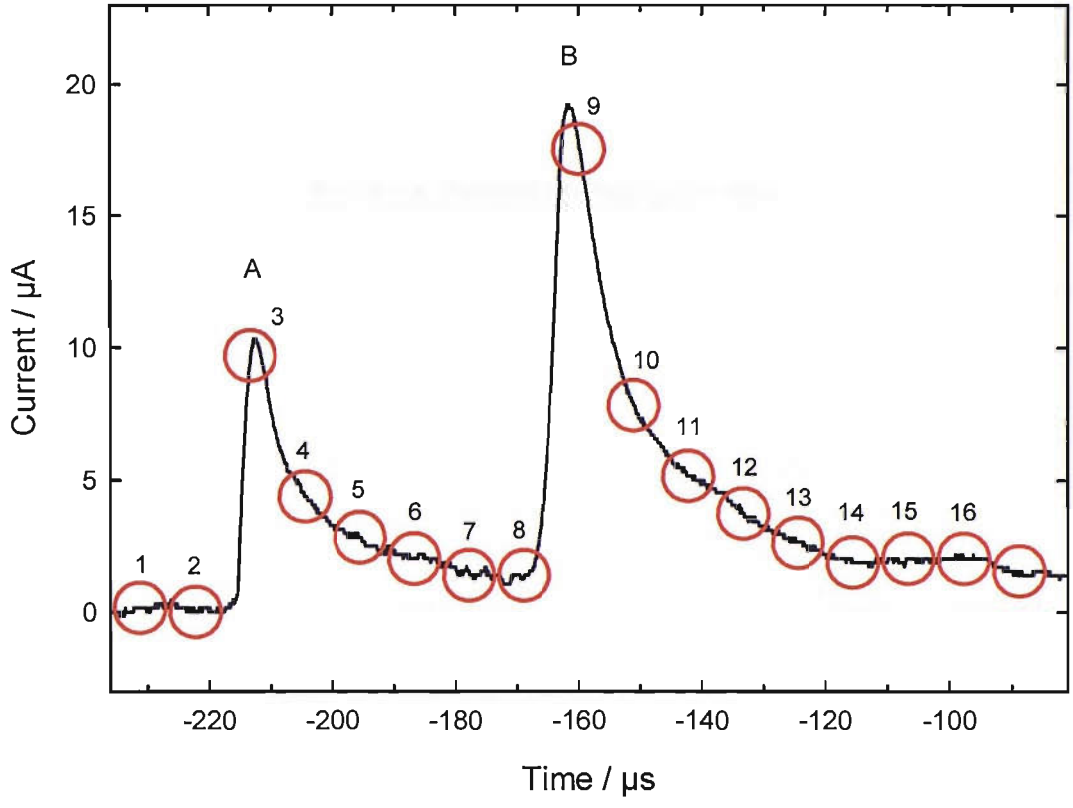

Figure 5.8: Two surface erosion/corrosion events (A & B) recorded on a 250 µm diameter aluminium electrode in reactor 4. The numbered circles represent the duration and position of the high-speed video images in figure 5.9. The electrode was positioned centrally 80 mm from the base of the reactor which contain 1 dm^3 Na_2SO_4 and held at 0 V *vs.* a stainless steel counter reference electrode. The reactor was driven at 22.81 kHz with a drive voltage of 150 V zero to peak.

Figure 5.8 shows a current time trace with two saw tooth like peaks (A & B) separated by ~ 43 µs or one pressure cycle (the reactor being driven at 23 kHz). These peaks being similar to those seen in figures 5.1 and 5.3 recorded at the tip of an ultrasonic horn. If we look at the accompanying images in figure 5.9 we can see that a bubble cloud similar to that seen at the tip of the ultrasonic can be seen. The bubble cloud is similar to that observed in figure 4.19 and is approximately 2 mm in diameter; located at the bottom of the downward pointing electrode. Concentrating on peak A we can see that the bubble cloud collapses prior to the peak (image 1&2) to a point where no bubbles are seen (image 3) before the bubble cloud reforms after the erosion/corrosion has taken place (image 4-6).

The same process can be seen to be taking place for peak B where the bubble cloud collapses and disappears prior to the increase in current (images 7&8) before the reforming of the bubble cloud (images 9-11). Interestingly the bubble cloud can be

seen to collapse once again (images 11-13) but this time there is no accompanying erosion/corrosion transient in figure 5.8. Throughout all of the images a nucleation point just off the electrode can be seen.

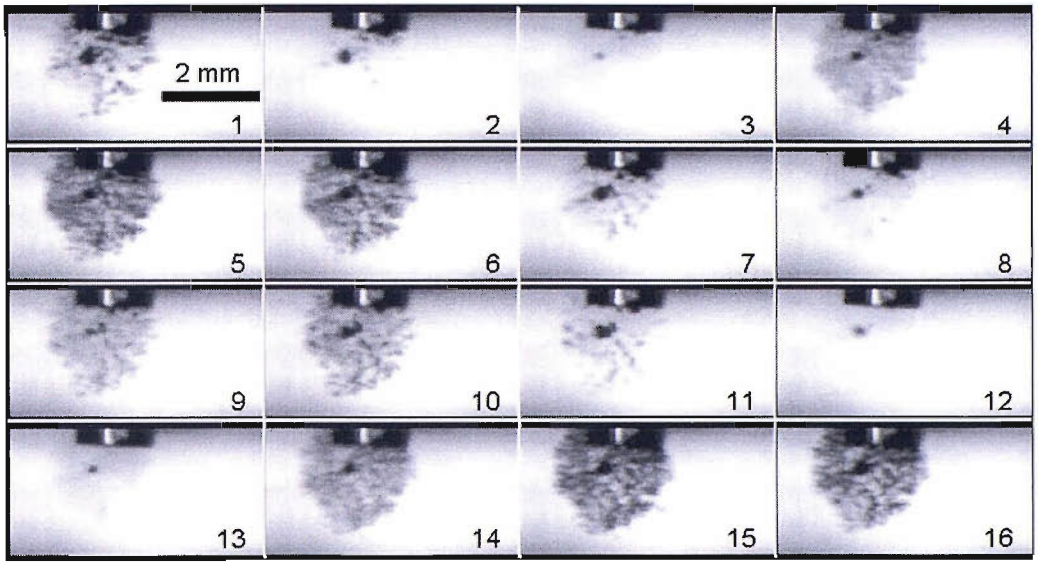

Figure 5.9: Simultaneous high-speed video images for figure 5.8. Recorded at 112,500 frames s^{-1} with a shutter speed of 1/112,500 s.

The presence of peaks with slower rise times and more rounded shape was not confined to when an ultrasonic horn was used. We shall now look at a set of data which contains two "saw tooth" peaks (A&B) and two "rounded" peaks (C&D).

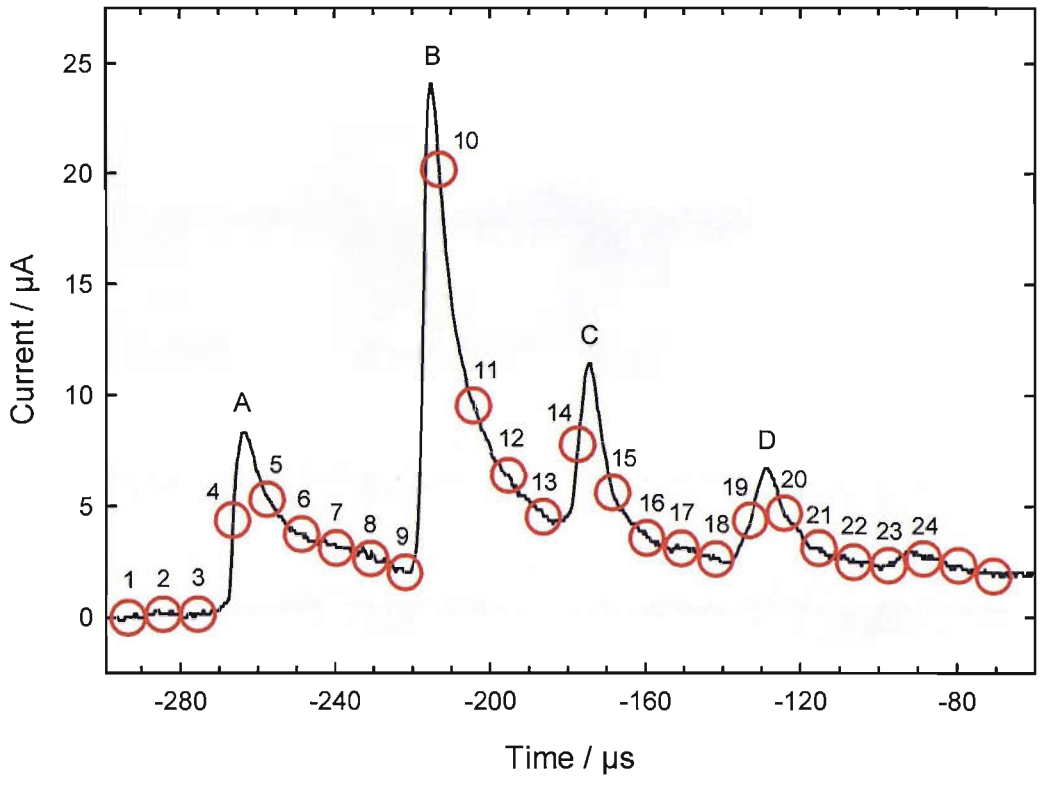

Figure 5.10: Two "primary" (A &B) and two "secondary" (C&D) surface erosion/corrosion events recorded on a 250 µm aluminium electrode in reactor 4. The numbered circles represent the duration and position of the high-speed video images in figure 5.11. The electrode was positioned centrally 80 mm from the base of the reactor which contain 1 dm^3 Na_2SO_4 and held at 0 V *vs.* a stainless steel counter reference electrode. The reactor was driven at 22.81 kHz with a drive voltage of 150 V zero to peak.

Comparing the high-speed images recorded in figure 5.11 preceding each of the four peaks in figure 5.10 it can be seen that there is very little difference between the saw tooth like "primary" peaks (A and B) and the more rounded "secondary" peaks (C and D). Preceding peak A the bubble cloud can be seen to collapse (images 1-3) before rebounding (image 4). The same process can then be seen to repeat for peaks B (images 7-9), C (images 12-14) and D (images 17-19). For the secondary peaks C and D the current can be seen to rise before the bubble cloud has dispersed and cleared.

Looking at the way in which the bubble clouds clear prior to each of the surface erosion/corrosion events; and in particular the surface of the electrode and its support; the presence of bubbles on the surface of the electrode can be seen in all cases. For the more rounded peaks C and D these bubbles appear to be larger in size suggesting

that bubbles that are in contact with the surface are in some way responsible for the broadening of the transients recorded.

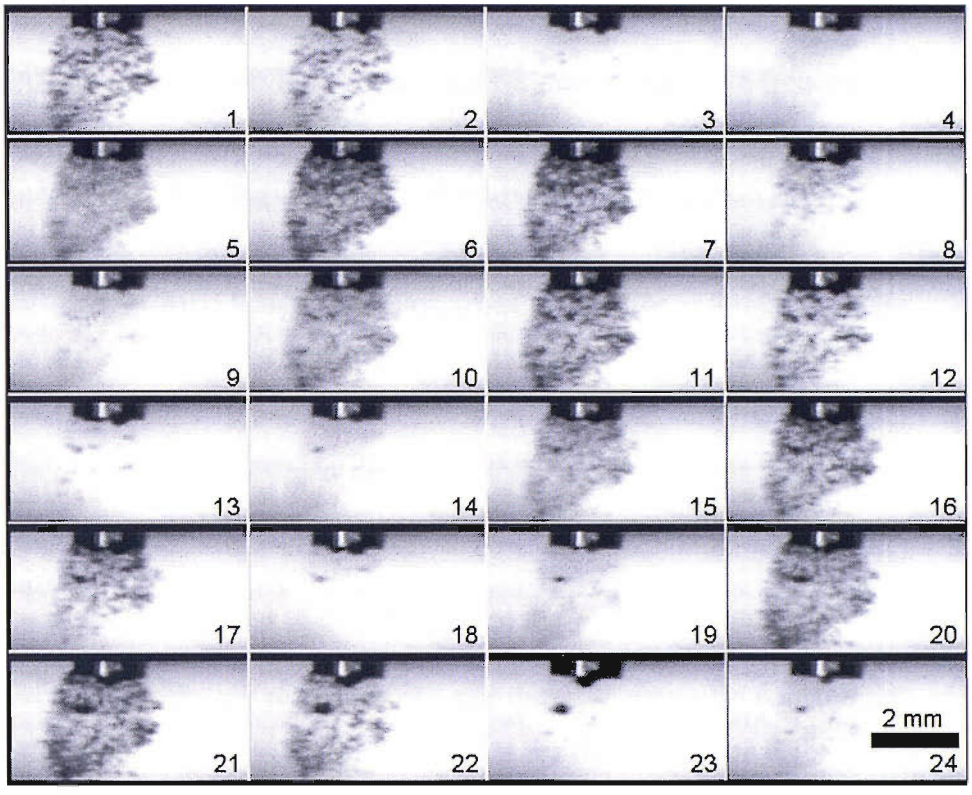

Figure 5.11: Simultaneous high-speed video images for figure 5.10. Recorded at 112,500 frames s^{-1} with a shutter speed of 1/112,500 s.

5.4. Conclusions

In this chapter we have examined the processes leading to erosion/corrosion events on aluminium electrodes caused by the action of cavitation through simultaneous high-speed imagery and electrochemistry. This has shown that a collapse and clearing of a bubble cloud surrounding the tip of the electrode causes damage to the electrodes surface; producing a current/time transient as the protective oxide reforms. This process was found to hold regardless of whether the electrode was positioned near the tip of an ultrasonic horn or in a single transducer reactor and whether the current time transient recorded was a fast rising primary event or a more rounded secondary event. No definitive difference between the generation of a sharp or rounded peak could be ascertained; the only possible cause for the more rounded peaks found was the interference of bubbles trapped on the electrode surface with the electrochemistry.

6. Characterisation of a reactor at different frequencies

It is well known from previous studies that changes in the drive frequency of a reactor can result in variation in the cavitation taking place (*62, 155, 177*). If all other parameters are maintained (temperature, drive voltage, reactor size, ac pressure and the liquid) then it is possible to "tune" a reactor to a given frequency that produces an elevated level of MBSL light emission from the reactor and therefore cavitation. In order to compare the measurements of the different sensing techniques already outlined in chapters 3 to 5 a reactor was driven at various frequencies and the response of the techniques recorded. Reactor 4 was chosen for these experiments due to its size; this allowed all techniques to be applied within the vessel at several different points in space.

Previous work with this reactor (*171*) and those of a similar construction (*62, 155, 177, 182*) has shown that conditions suitable for the generation of cavitation are only seen at certain frequencies. Therefore it was considered superfluous to conduct every available test at all available frequencies. Therefore certain frequencies were identified for study in greater detail.

6.1. Data collection

6.1.1. Light output

To identify the frequencies of interest, the MBSL light output of the Reactor 4 was measured at 1 kHz resolution between 20 and 160 kHz using a single photon counting module (SensL PCMplus SN 20). Light output was chosen for determining the frequencies of interest for 2 important reasons. First, light output is recognised as an important indication of the presence of inertial cavitation. Second, due to the *ex-situ* nature of the technique which allows a simple measurement pertaining to the global level of activity within the reactor, it is possible to conduct measurements at many frequencies in a relatively short period of time. Figure 6.1 shows the level of MBSL light emission from the reactor as a function of frequency.

Figure 6.1 shows that MBSL light generation as a result of cavitation occurs at a number of different frequencies, each of which can be identified by the level of light emission measured from the reactor being greater than the background level. However at a greater number of frequencies the level of light emission measured from the reactor was indistinguishable to the background level suggesting that no inertial cavitation was taking place. In order to investigate the reactor further, a number of frequencies were chosen for more detailed low light measurement as well as acoustic pressure, surface erosion/corrosion and chemical change measurements.

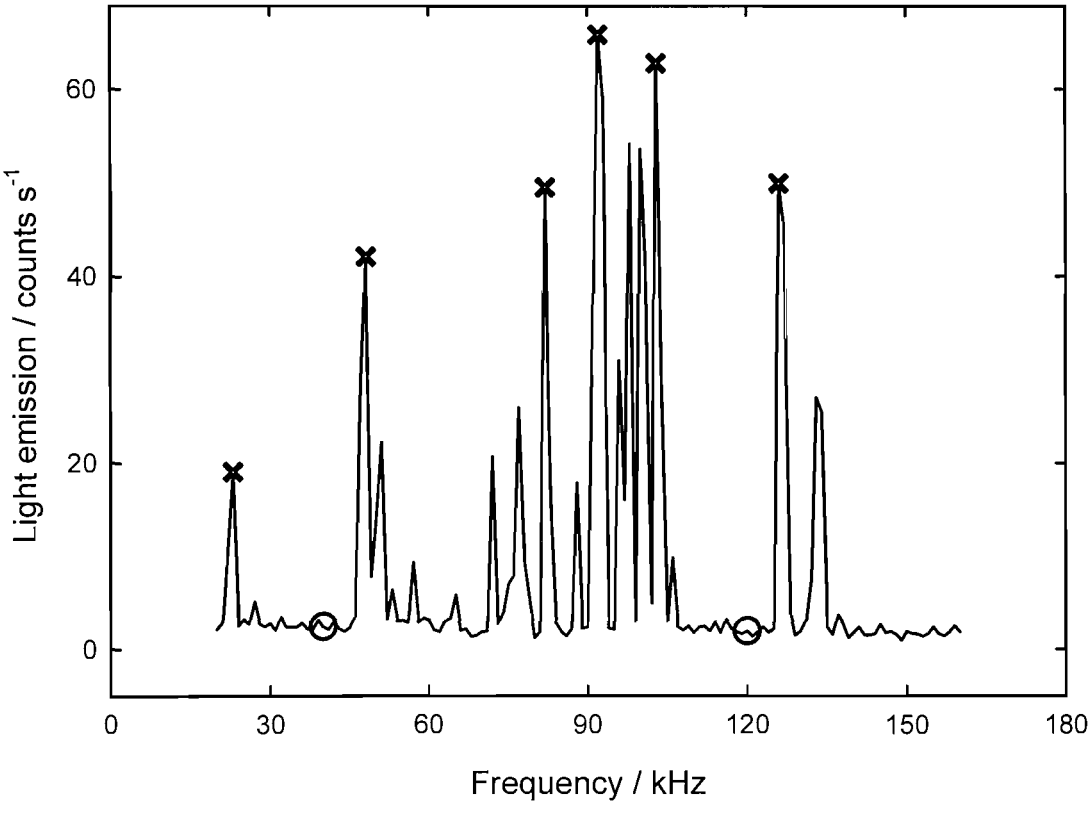

Figure 6.1: Plot of the drive frequency compared to the level of light output from the reactor. Recorded using a Sensl PCMPlus-20 intelligent photon counting module over a period of 20 s at each frequency. Reactor contained 1 dm^3 0.1 M Na_2SO_4 solution and was driven at 150 V. X marks the six high activity frequencies selected for further study; O marks the two low activity frequencies.

In total eight frequencies were selected for further investigation. At six of the frequencies selected the level of light emission from the reactor was measured to be greater then the background (23, 47.97, 82, 92, 103 and 126 kHz and represented by X in figure 6.1). For these frequencies it was assumed that inertial cavitation was taking place within the reactor. The other two frequencies selected (40 and 120 kHz,

represented by O in figure 6.1) corresponded to frequencies at which the measured light emission from the reactor was indistinguishable from the background light level, leading to the assumption that little or no inertial cavitation was taking place.

The photon counter measurements give an indication as to the presence of cavitation taking place within the reactor but generate little or no information as to the spatial location of this cavitation. In order to get a better idea as to the location of the light generating cavitation within the reactor; the reactor was imaged from the side and above using image intensified cameras at each of the selected frequencies. Figure 6.2 images a-i shows the reactor from the side at the selected frequencies.

From figure 6.2 (b and g) it is apparent that the frequencies at which no light was observed using the photon counting module, coincide with little or no luminescent area seen using the imaging techniques as expected. This leads to the conclusion that there is an absence of luminescence and therefore inertial cavitation (assuming that it is necessary to have inertial cavitation for luminescence). Of the frequencies at which a modal structure within the reactor can be seen there are great variations in the shape of the pattern induced. For 23 and 92 kHz (see figure 6.2 images a and e respectively) banding structure is seen occupying almost the entire volume of the cell; whereas for the frequencies 103 and 126 kHz (see figure 6.2 images f and h) the light (and therefore the cavitation) is seen to be localised along the central axis of the reactor. The images for 47.97 and 82 kHz reveal a more chaotic and less structured form (figure 6.2 images c and d) appearing to be an amalgamation of the central and dispersed forms seen at other frequencies.

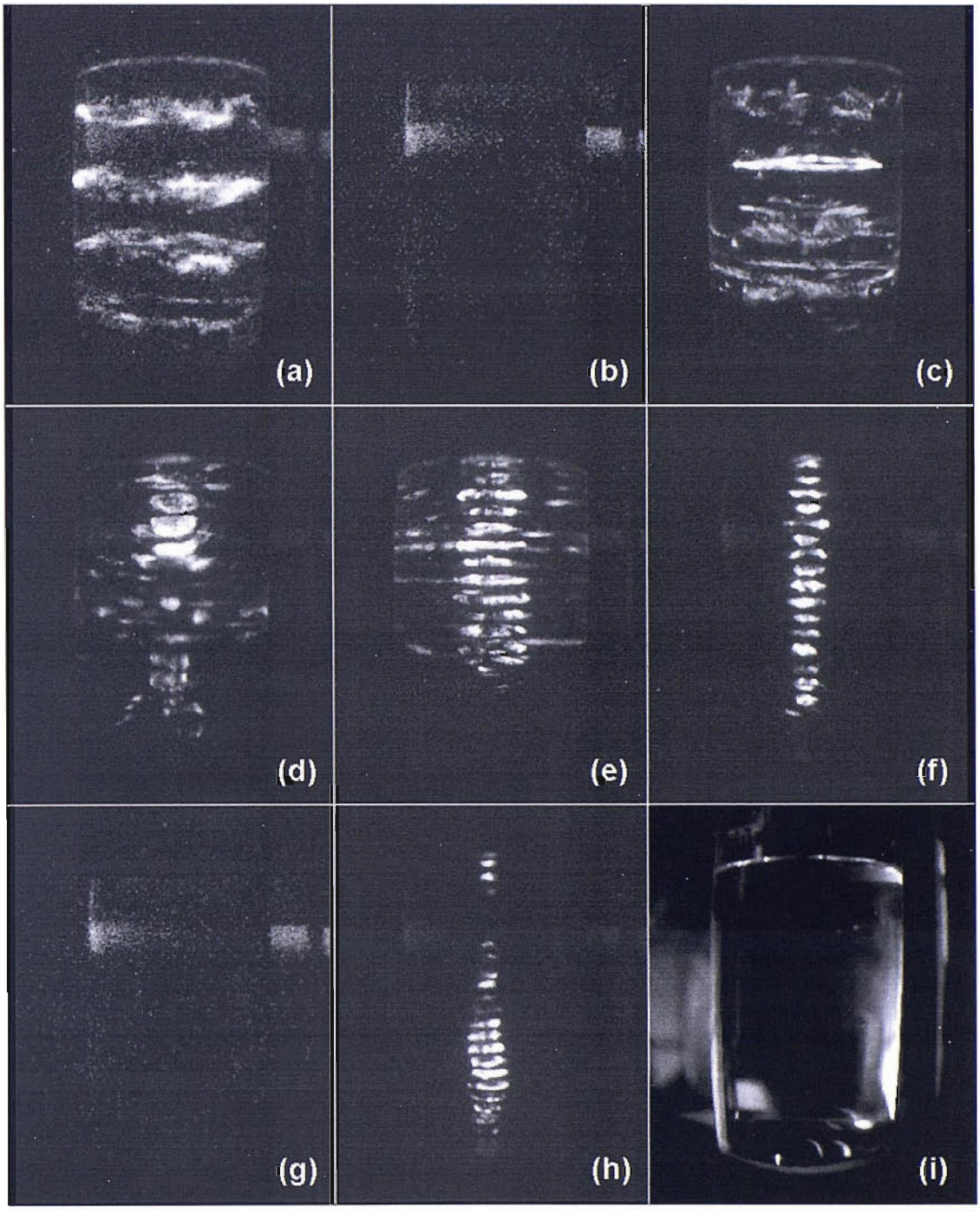

Figure 6.2: MBSL images of the reactor at different frequencies. Images correspond to; (a) 23 kHz, (b) 40 kHz, (c) 47.97 kHz, (d) 82 kHz, (e) 92 kHz, (f) 103 kHz, (g) 120 kHz, (h) 126 kHz and (i) image of reactor with light up. Reactor contained 1 dm^3 of 0.1 M Na_2SO_4 solution and was driven at 150 V zero to peak. Images are a stacked composite of over 100 images.

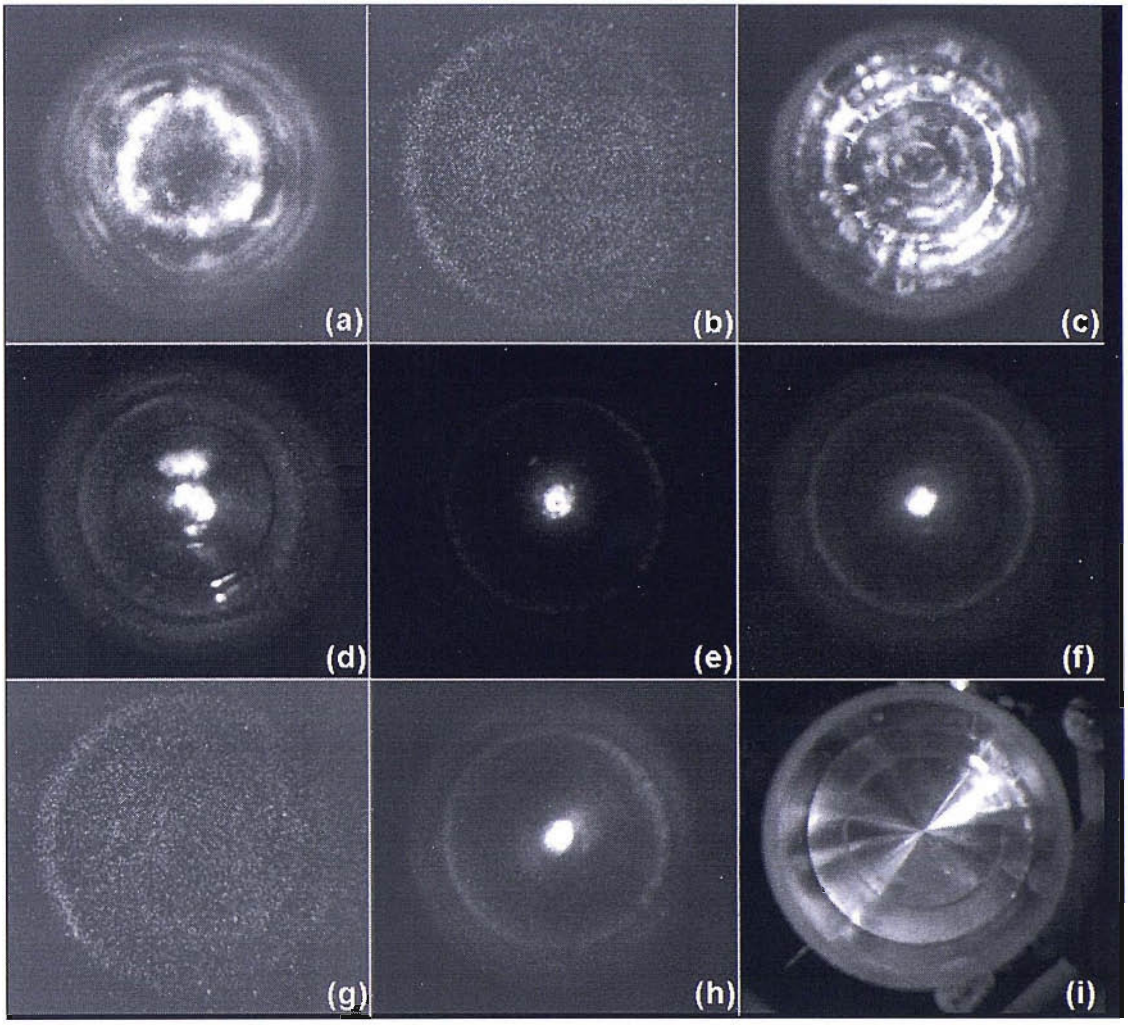

Figure 6.3: Stacked low light images looking down the central axis of the reactor at different frequencies. Images correspond to; (a) 23 kHz, (b) 40 kHz, (c) 47.97 kHz, (d) 82 kHz, (e) 92 kHz, (f) 103 kHz, (g) 120 kHz, (h) 126 kHz and (i) image of reactor with light up. Reactor contained 1 dm^3 of 0.1 M Na_2SO_4 solution and was driven at 150 V zero to peak. Images a stacked composite of over 100 images.

Figure 6.3 shows the reactor imaged from above at the selected frequencies. As with the imaging from the side of the reactor there is no discernable light output at either 40 kHz or 120 kHz (images b and g respectively). The frequencies that showed a central column of luminescence in figure 6.2 (103 and 126 kHz) are characterised by a central spot as would be expected. Correlation between the intensified images taken from the side and above the reactor is extended to all of the frequencies studied except 92 kHz where the extended luminescence seen in figure 6.2 is replaced by a single region of luminescence along the axis of the reactor in figure 6.3.

The light output of the reactor having been characterised both in magnitude (using the photon counter) and in position (using the image intensified imaging) we shall now

look to see as to whether of other key indicators of the level of cavitation (pressure measurements, chemical change and surface events) show the same frequency dependence and spatial distribution as the light output. First we shall examine the pressure as measured within the reactor at various points. Second we shall move onto investigating the presence of erosion/corrosion surface events. Third we shall look at the rate of chemical change within the reactor.

6.1.2. Pressure measurements

For inertial cavitation to take place it is well understood that the acoustic pressure with in the liquid must be greater than a threshold value and a nucleation site be present (*1*). Table 6.1 shows the calculated expansive pressure thresholds for the drive frequencies under investigation.

Frequency / kHz	Pressure threshold / kPa
23	119
40	126
47.97	128
82	138
92	140
103	143
120	147
126	149

Table 6.1: Calculated pressure expansive pressure thresholds for the frequencies of interest. Calculated using program developed by Power (*62*).

Consequently mapping the acoustic pressure within the reactor at the different frequencies gives an indication as to where inertial cavitation may be taking place. This can then be correlated with the measurements carried out for the light emission, erosion/corrosion events and chemical change.

The pressure measurements were carried out using a Gras Type 10 CT hydrophone connected to a Brüel & Kjaer 2635 charge amplifier. The hydrophone was taped to an 8 mm glass rod which was then mounted on a single axis positioner and the pressure scanned vertically through the cell. The hydrophone was scanned 100 mm in 2 mm increments; starting with the tip of the hydrophone 10 mm from the base of

the reactor, placing the centre of the hydrophone 20 mm from the base. The pressure at each point was recorded using a Measurement Computing PCI-DAS 4020/12 ADC card in a computer with the pressure amplitude extracted using a Visual basic program (see appendix C). The reactor was scanned in 4 locations; the central axis and at 10, 20 and 25 mm from the central axis. All four measurements were carried out in the same plane within the reactor as the reactor was considered to have rotational symmetry around the central axis (*155*).

Figure 6.4 shows the central pressure scans recorded at each frequency with the corresponding inertial pressure threshold. The frequencies at which light was recorded (23, 47.97, 82, 92, 103 and 126 kHz) the measured zero to peak pressure exceeds the calculated threshold. Conversely at the two frequencies where no light emission was recorded (40 and 120 kHz) the recorded pressures are considerably below the threshold.

Figures 6.5 and 6.7 show how the pressure amplitude varies as a function of position from the central axis towards the wall. This is done by plotting the four pressure scans conducted across the reactor at each frequency into a contour map.

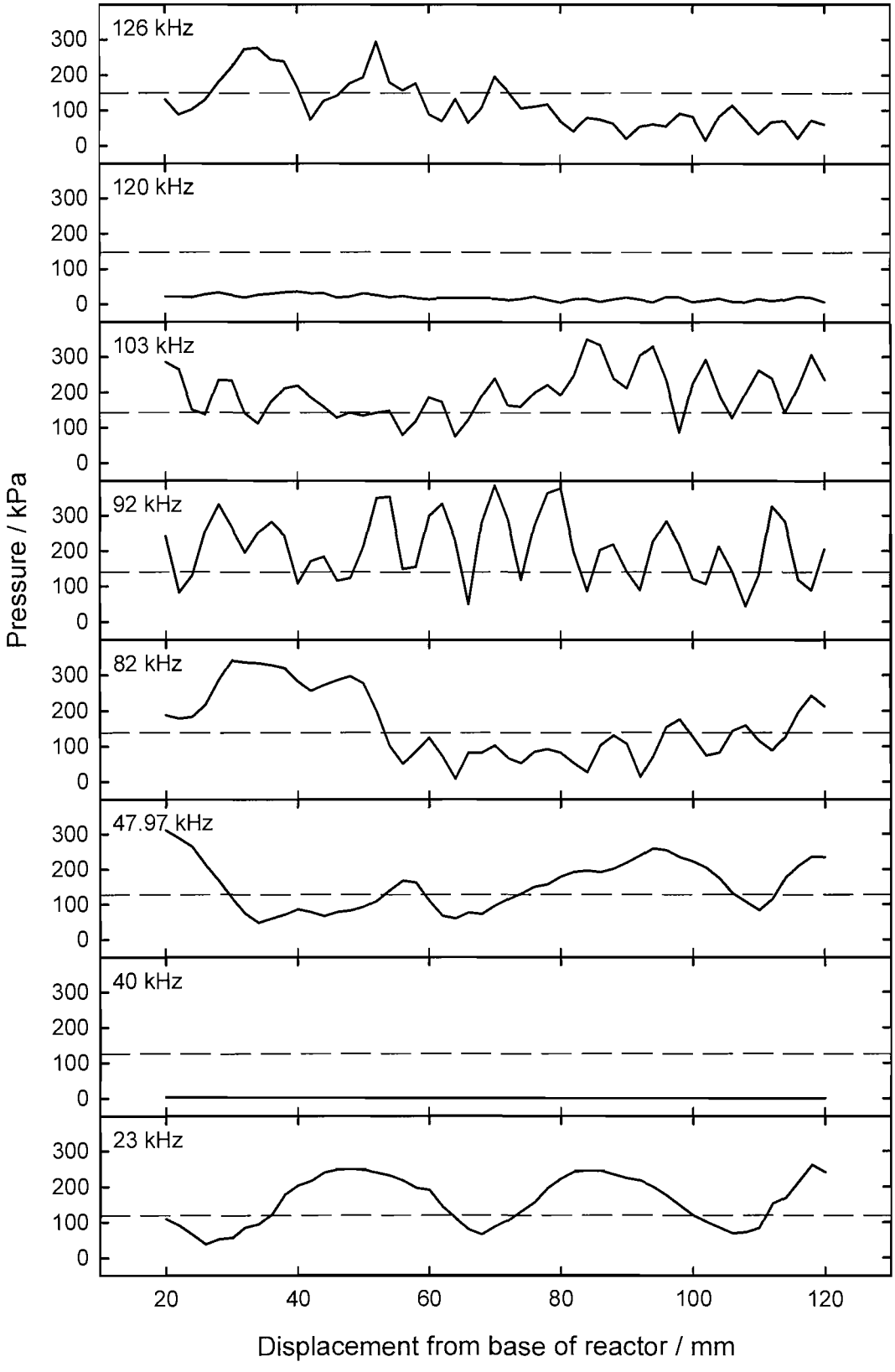

Figure 6.4: Centre axis zero to peak pressure as a function of position plots at 23, 40, 47.97, 82, 92 103, 120 and 126 kHz in reactor 4. Each plot consists of 50 point with a resolution of 2 mm. Reactor containing 1 dm^3 0.1 M Na_2SO_4 driven at 150 V. The relevant calculated inertial pressure thresholds are shown for each frequency (– —)

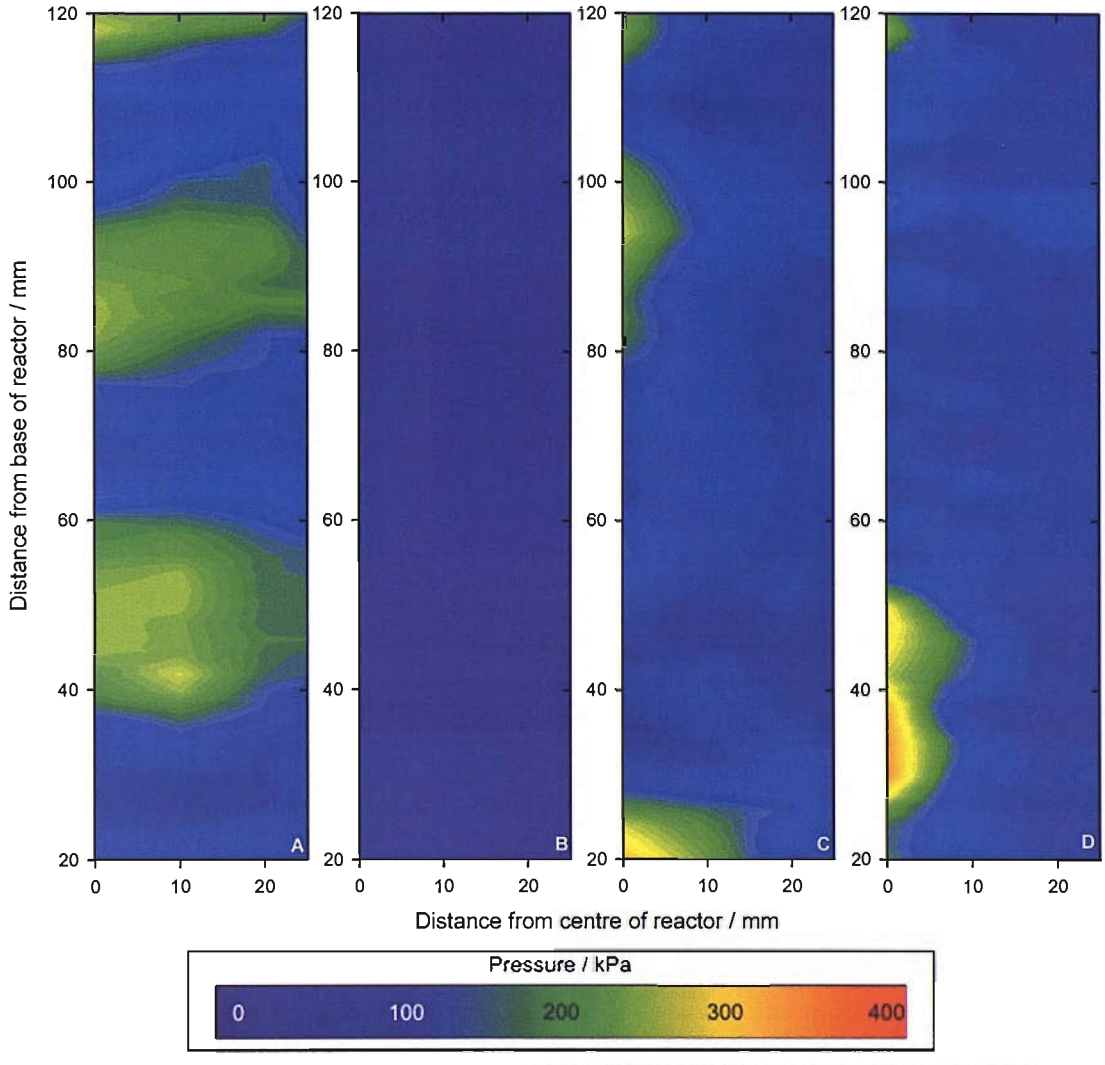

Figure 6.5: Contour maps of reactor 4 driven at 23, 40, 47.97 and 82 kHz corresponding to maps A, B, C and D respectively. Each map derived from four vertical scans with a resolution of 2mm at 0, 10, 20 and 25 mm from the central axis of the reactor. Reactor 4 containing 1000 ml 0.1 M Na_2SO_4 driven at 150 V.

Figure 6.5 map A shows that the banding at 23 kHz becomes more apparent with three bands (at approximately 50, 85 and starting at 120 mm from the base of the reactor) where the acoustic pressure exceeds the calculated presence threshold. The other frequencies in figure 6.5 show no definitive banding.

Figure 6.6 shows the constituent pressure scans used to construct figure 6.5 A. Though the absolute magnitude of the pressure was found to decrease towards the edge of the reactor, the position of the pressure nodes and antinodes within the reactor remained constant.

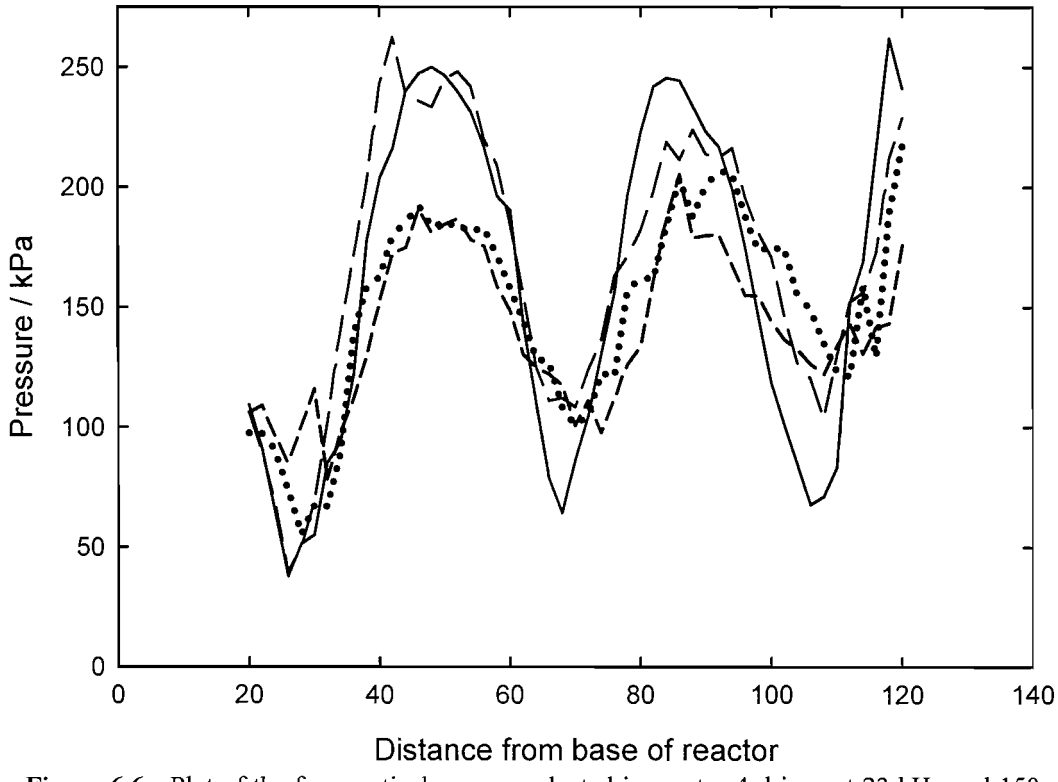

Figure 6.6: Plot of the four vertical scans conducted in reactor 4 driven at 23 kHz and 150 V. Vertical scans carried out at 0 mm (——), 10 mm (– – –), 20 mm (••••••) and 25 mm (– – – –) from the central axis of the reactor. Conducted in 1 dm^3 0.1 M Na_2SO_4 solution.

Figure 6.7 shows that at higher ultrasonic drive frequencies the banding in the z direction (vertically away from the transducer) is more evident. In particular the pressure map of the reactor at 92 kHz exhibits a regular banding with a period of ~8 mm throughout the entire height of the reactor.

The pressure maps in figures 6.5 and 6.7 show that as the ultrasonic drive frequency increases the spacing between pressure nodes decreases. This is in agreement with the theoretical model of a single transducer reactor presented by Birkin *et al* (*155*).

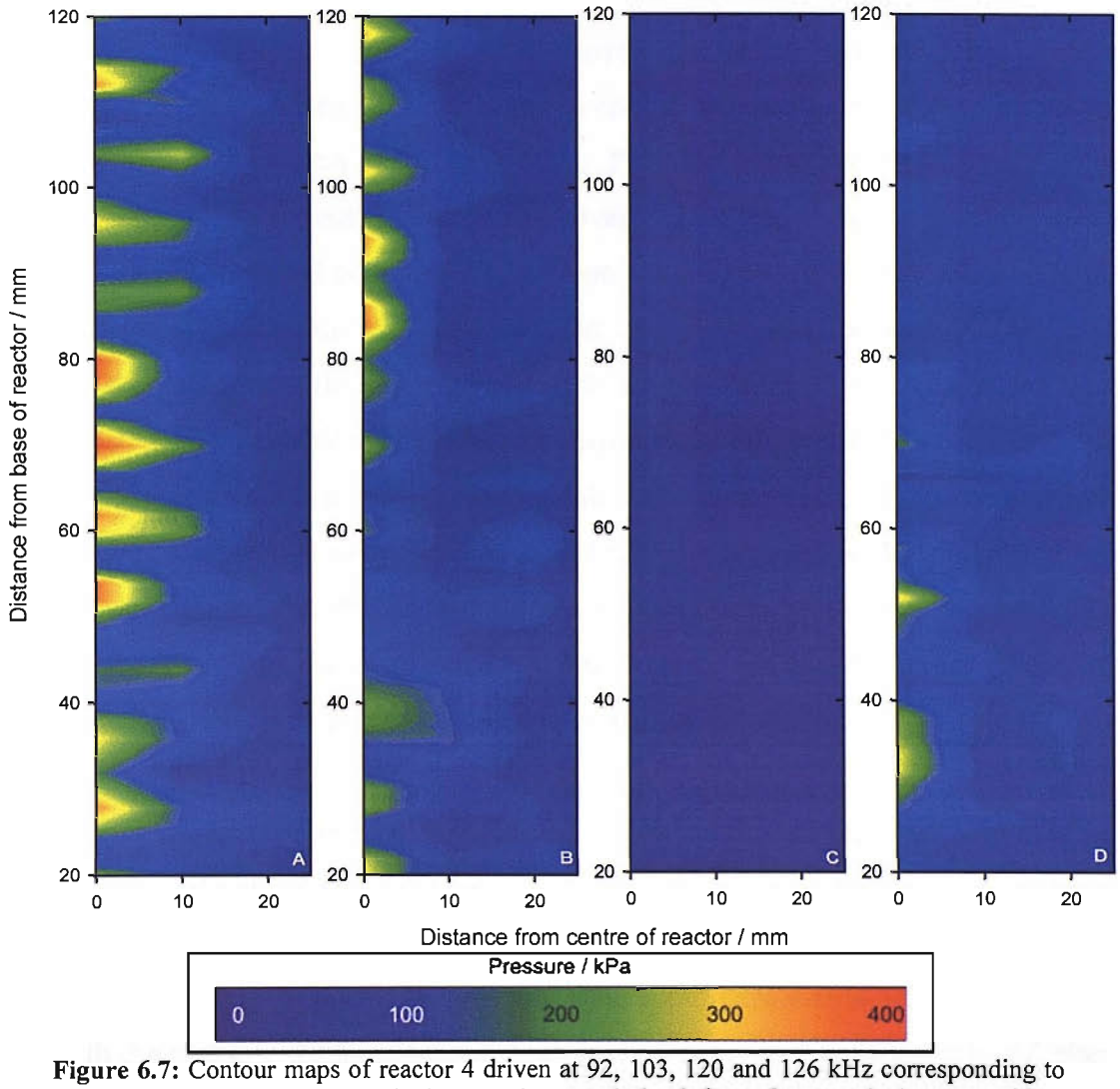

Figure 6.7: Contour maps of reactor 4 driven at 92, 103, 120 and 126 kHz corresponding to maps A, B, C and D respectively. Each map derived from four vertical scans with a resolution of 2 mm at 0, 10, 20 and 25 mm from the central axis of the reactor. Reactor 4 containing 1 dm^3 0.1 M Na_2SO_4 driven at 150 V zero to peak.

At all the frequencies at which it was considered that inertial cavitation was taking place (23, 47.97, 82, 92, 103 and 126 kHz) it is worth noting that towards the edge of the reactor the pressure drops considerably. The effect is seen least at 23 kHz (figure 6.5 a) where pressures in excess of 200 kPa are still recorded 25 mm from the centre of the reactor. Conversely at 103 k Hz and 126 kHz (figure 6.7 b and d respectively) no pressures over 200 kPa are recorded except for in the central region. This is similar to what was seen from the low light images in figure 6.2 where the area over which light was emitted was greater at 23 kHz than at either 103 or 126 kHz.

6.1.3. Surface erosion/corrosion event measurements

One of the significant physical effects of cavitation is the damage of a surface by the impingement of a collapsing bubble (micro jetting) or shockwave impact generated by a collapsing bubble on to the surface (*1*). Previous studies have shown that if the surface onto which the bubbles act is a passivated electrode, then it is possible, under the correct experimental conditions of solution and electrode potential, to monitor the destruction and reformation of the passivated layer using electrochemistry (*54, 158*). Hence by monitoring the output from such an electrode, it has been possible to characterise the cavitation environment surrounding an ultrasonic horn (*54*). In chapter 4 it was shown that it was possible to record such events with simple electrochemical circuits using aluminium and titanium electrodes. Specifically it was shown that it was possible to use an aluminium electrode to map the cavitation environment surrounding the tip of an ultrasonic horn and identify bands of activity within a different single transducer ultrasonic reactor.

In order to conduct the scans of reactor 4 a 250 μm aluminium electrode was attached to a plastic rod connected to the same positioner as that used for the pressure scans allowing an automated 100 mm travel in the Z direction as well as 25 mm manual positioning in the XY plane. A diagram of the setup used can be seen in figure 2.8. As with the pressure scans, instead of scanning the entire bath only a single YZ plane from the central axis to the edge of the reactor was scanned; the reactor assumed to have rotational symmetry. The electrode was 0 V *vs.* a stainless steel counter/reference electrode and the electrochemical signal amplified using an in house battery current follower. The number and magnitude of peaks generated by the surface cavitation events were recorded using a multi-channel analyser (Amptek Pocket MCA 8000A Multi Channel Analyser) connected to a PC. The MCA recorded over a period of 30 s (4096 levels over 5 V). The threshold for peak detection was set at channel 200 corresponding to a trigger voltage of 244 mV or peak height of 2.44 μA. To control the scanning process a visual basic program was written that controlled the MCA, automated positioner and provided a gating pulse to operate the drive signal for the reactor. The gating pulse for the drive signal was required due to the prolonged period of time required for the MCA to transfer data to the PC (>30 s, longer than the acquire time). Over such an extended duration of

sonication there is an increases in the likelihood of significant changes in the temperature and other conditions within the reactor. Figure 6.8 shows a schematic diagram of the order in which events took place during the scan process.

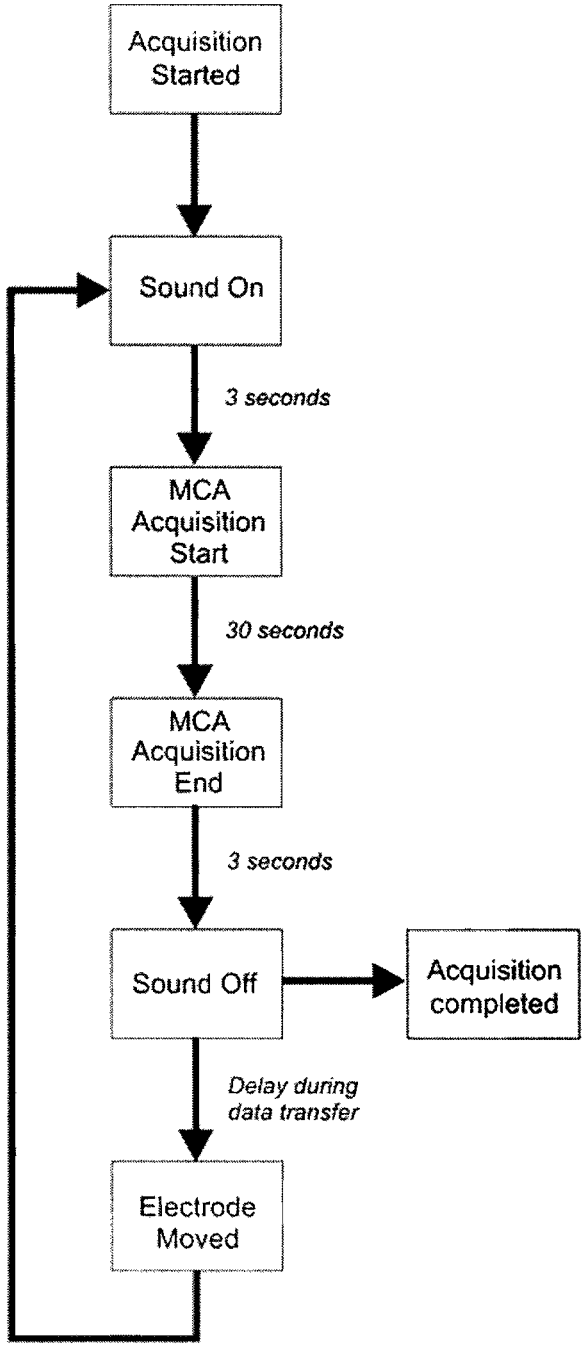

Figure 6.8: Schematic showing the procedure for surface scans of reactor 4

In addition, as discussed in chapter 4, after prolonged exposure to erosive cavitation events the aluminium electrodes cease to behave as expected. As a consequence the resolution of the scans used to investigate the surface events was less than that used in

the pressure measurements. Consequently the electrode used for the surface event scans was scanned vertically over 100 mm at a resolution of 5 mm in four positions at 0 10, 20 and 25 mm from the central axis of the reactor. However it should be noted that the sampling area of the electrodes is considerably less than that of the hydrophone. In order to attempt to investigate the same locations within the reactor for the surface scan as for the pressure scan the scan was started 20 mm from the base of the reactor.

The light emission and pressure experiments have shown little variation between the results seen for high and low frequencies; high pressure and increased light emission have been recorded for both. However the surface cavitation event measurements are more complicated with no events being recorded at the majority of the frequencies. As table 6.2 shows for only four frequencies were any events recorded. The number of events recorded at two of these frequencies (82 and 103 kHz) is three to four orders of magnitude less than the number seen at 23 and 47.97 kHz.

Frequency / kHz	Total surface events recorded / events
23	3238583
40	0
47.97	227921
82	18
92	0
103	266
120	0
126	0

Table 6.2: Details of the number of surface events recorded in each scan as a function of both frequency and position in reactor 4. All scans conducted with a 250 μm Al electrode held at open circuit potential vs. a stainless steel counter/reference electrode and the events collected using a multi channel analyser with counting threshold set to 2.44 μA. Reactor contained 1000 ml 0.1 M Na_2SO_4.

It should be noted that the absence of recorded events at certain frequencies could be as a result of the electrode sampling too small a volume and therefore missing the points within the reactor at which conditions are commensurate with events taking place. The number of points at which measurements were made within the reactor including numerous points recorded at the pressure maxima suggest that this was unlikely. The data presented in table 6.2 gives little indication as to the spatial variation of the surface cavitation events within the reactor. A better indication as to

the variation in the location of the surface events can be seen from the central scans of the reactor plotted in figure 6.9.

The presence of surface erosion/corrosion events is considered to be a threshold phenomena where by the conditions (specifically the acoustic pressure) has to be in excess of a certain value in order for any activity to be recorded. Consequently at the majority of points at which the threshold is not exceeded no events are recorded. Once the conditions at the electrode surface are such that surface erosion/corrosion events are recorded the number of events observed can vary from 10 to 100,000 leading to points at which few events are recorded being lost in the background in comparison to the points of high activity. Given that the presence of any number of events indicates the presence of inertial cavitation, it is prudent to plot the surface event scans using a logarithmic scale. It should also be considered that the central axis scans in figure 6.9 represent only a single scan through the reactor and repeated scans of the same axis would possibly have revealed more information.

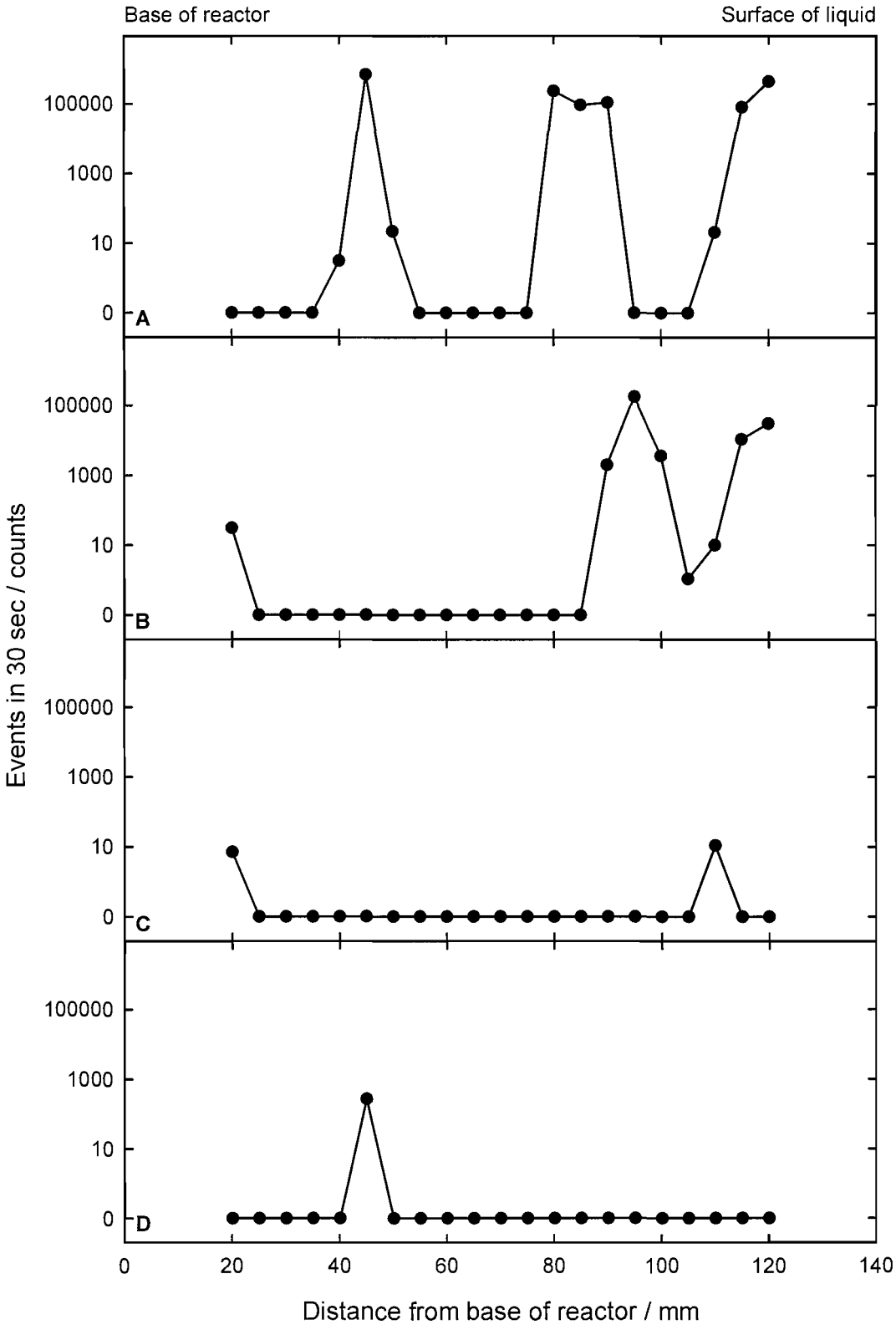

Figure 6.9: Plots of number of events as a function of position for the central axis surface scans in reactor 4 at 23, 47.97, 82 and 103 kHz in plots A, B, C and D respectively. All scans conducted with a 250 μm Al electrode held at open circuit potential *vs.* a stainless steel counter/reference electrode and the events collected using a multi channel analyser with counting threshold set to 2.44 μA. Reactor contained 1 dm^3 0.1 M Na_2SO_4 and was driven at 150 V Zero to peak.

By combining the four vertical scans conducted within the reactor it is possible to form a 2 dimensional representation of the surface event activity within the reactor. With no events having been recorded at four frequencies, only those at which events were recorded are plotted in figure 6.10.

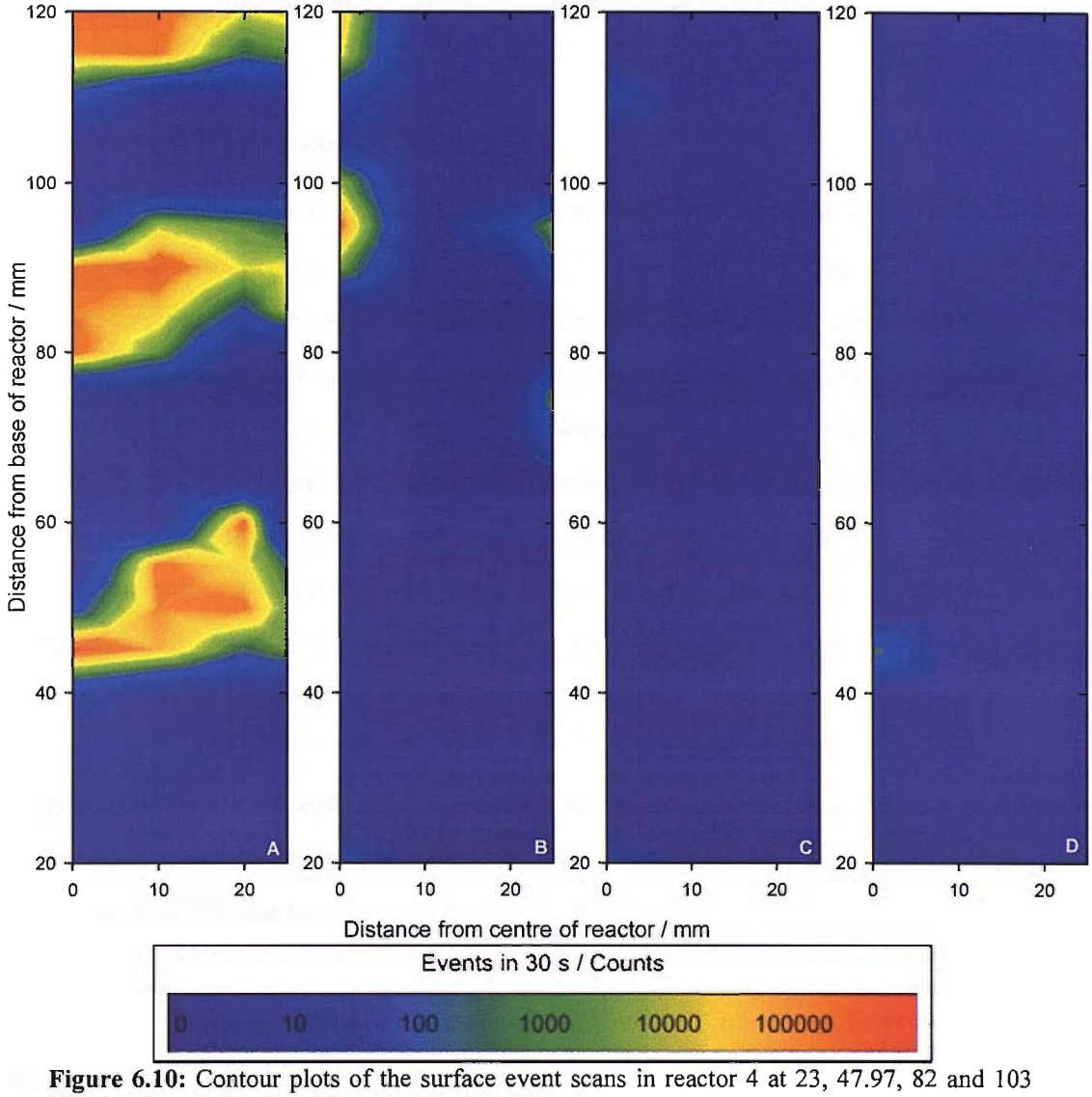

Figure 6.10: Contour plots of the surface event scans in reactor 4 at 23, 47.97, 82 and 103 kHz in plots A, B, C and D respectively. All scans conducted with a 250 μm Al electrode held at open circuit potential *vs.* a stainless steel counter/reference electrode and the events collected using a multi channel analyser with counting threshold set to 2.44 μA. Reactor contained 1 dm^3 0.1 M Na_2SO_4 and driven at 150 V.

The global view of the reactor afforded by figure 6.10 indicates the presence of similar banding at 23 kHz to that seen in both the pressure and light emission results. Three bands of recognisably higher activity can be seen at 50, 85 and 120 mm from the base of the reactor. With the reactor being driven at 47.97 kHz two areas of elevated activity can be seen at 95 and 115 mm from the base on the central axis of the reactor. There is also a corresponding region of activity seen towards the edge of

the reactor at 95 mm from the base. At higher frequencies (82 and 103 kHz) there is no evidence of the systematic banding seen in the pressure and light emission measurements, rather there are isolated points at which surface erosion/corrosion events were recorded. It should be noted that the number of events recorded at higher frequencies was four orders of magnitude less than the number recorded at 23 kHz.

6.1.4. Chemical Measurements

The high temperatures and pressures generated by bubbles collapsing during cavitation events cause the formation of $OH^{\bullet}$ and $H^{\bullet}$ radicals; making the measurement of the rate at which these are formed a good indication as to the level of cavitation. Though it is possible to detect the radicals directly, it is more practical to make use of a dosimeter. In chapter 3 the Weissler reaction was identified a suitable dosimeter and a system utilising an electrochemical flow to measure the rate of formation of I_3^- (the product of the Weissler reaction) developed. The system developed was employed within reactor 4 at the frequencies of interest to see if differences in the rate of formation of I_3^- (and therefore production of $OH^{\bullet}$ from cavitation) could be seen.

Two sets of measurements were made at each of the frequencies of interest; first a global measurement at the centre of the reactor and second a coarse scan along the central axis of the reactor.

The global measurements were made over 200 s with the sound field being applied for 120 s. Figure 6.11 shows the current time traces recorded at each of the frequencies, the period during which the sound field was applied to the reactor is shown by the shaded area. As the measurements were made successively the same solution was used at all frequencies and therefore the magnitude of the current increases for the start of each successive current time trace. The two frequencies that were associated with an absence of cavitation (40 and 120 kHz) showed no increase in current indicating that no I_3^- was generated as a result of $OH^{\bullet}$ radicals formed from cavitation. For all the frequencies at which MBSL light emission had been seen (see

figure 6.1) a noticeable change in current is seen during the period of sonication (figure 6.11 a, c, d, e, f and h).

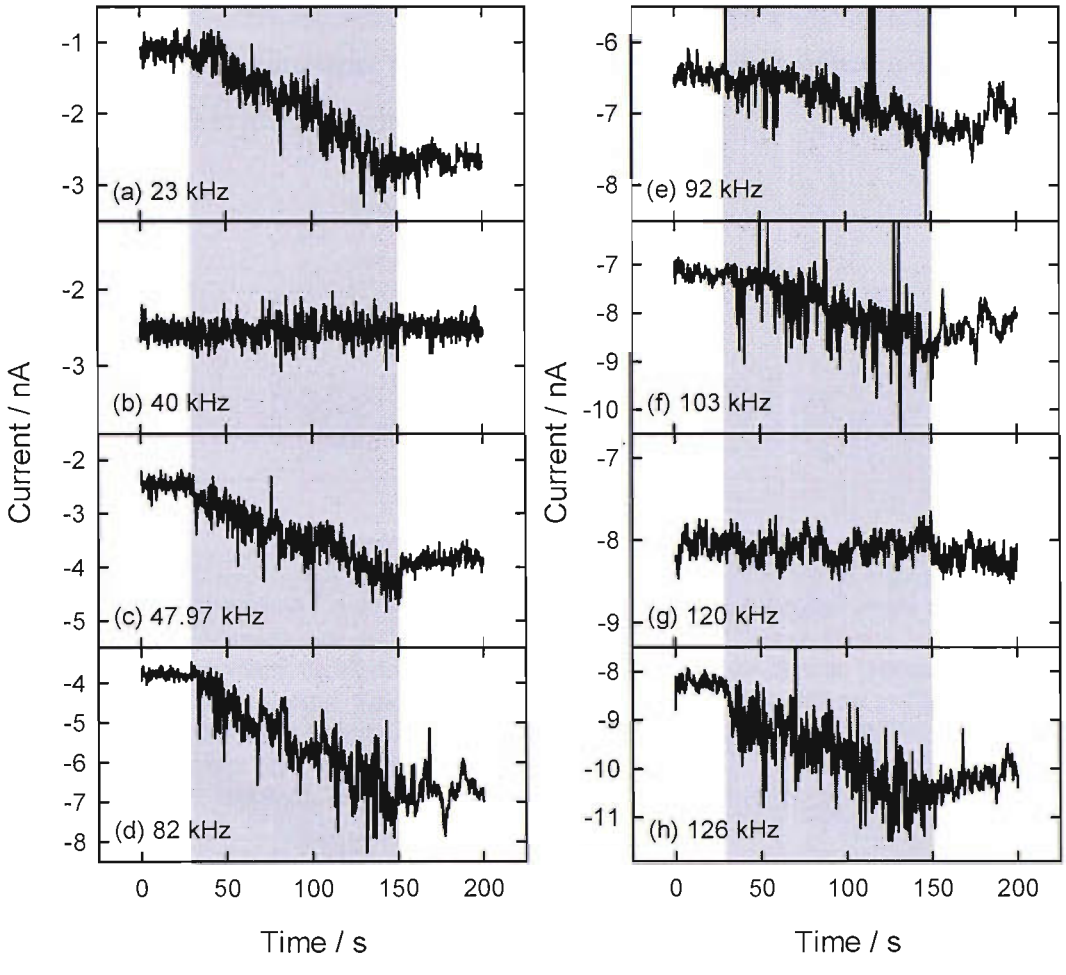

Figure 6.11: Current time traces showing the rate of chemical change at 23, 40, 47.97, 82, 92, 103, 120 and 126 kHz. All experiments carried out using the three electrode electrochemical flow cell with the needle inlet position in the centre of the reactor. Solution drawn through the flow cell at 388 ml hr^{-1} using the soft damped peristaltic pump. 0.5 mm Pt working electrode held at 0 V *vs.* a SCE counter/1reference electrode. Reactor 4 driven at 150 V at all frequencies with 1000 ml of 90 mM KCl and 10 mM KI solution.

To calculate the rate of formation of I_3^- (and therefore $OH^{\bullet}$) at each frequency the gradient of the current time trace in figure 6.11 between 40 and 160 s (the period of sonication) was calculated using Microsoft Excel. This gave the rate of change of current which is related to the change in concentration of I_3^- (see chapter 3 section 3.3). The discontinuities in the current seen at higher frequencies (figure 6.11 graph e, f and h) are thought to be as a result of bubbles being drawn up through the needle inlet to the flow cell, momentarily impeding mass transfer and therefore causing a temporary reduction in the magnitude of the recorded current.

It was found that the measurement technique employed was not capable of making accurate measurements as part of a scanning system. Therefore the measurements from the scans are not presented here in isolation but instead are averaged together with the global measurements performed in figure 6.11 to produce a single rate of formation of I_3^- for each frequency (table 6.3).

Frequency / kHz	Rate of I_3^- formation / nM s^{-1}
23	0.53
40	0
47.97	0.56
82	0.92
92	2.34
103	0.87
120	0.11
126	1.84

Table 6.3: Detailing the average rates of chemical change recorded in reactor 4 as a function of frequency. Average calculated from 6 positional measurements and one global measurement conducted in the centre of the reactor. All experiments carried out using the three electrode electrochemical flow cell with the needle inlet position in the central axis of the reactor. Solution drawn through the flow cell at 388 ml hr^{-1} using the soft damped peristaltic pump. A 0.5 mm diameter Pt working electrode was held at 0 V *vs.* a SCE counter reference electrode. Reactor 4 driven at 150 V at all frequencies with 1000 ml of 90 mM KCl, 10 mM KI solution.

6.2. *In comparison*

Having looked at the results from the various measurement techniques in isolation we shall now compare them to see the correlation between them. The first part of this section will deal with measurements taken for the reactor as a whole. The second part of this section will look at spatially resolved measurements and compare them to establish whether there is correlation.

6.2.1. Entire reactor measurements

Previous studies have found a relationship between the drive frequency of a reactor and the resulting MBSL light emission and sonochemical change within the reactor(*62, 128*). These studies have shown a general increase in the level of light emission and chemical change with higher drive frequencies(*62, 128*). To ascertain if a similar correlation could be seen for the results presented here the results taken from the light emission, acoustic pressure, surface cavitation events and chemical change

experiments were averaged over the entire reactor and plotted against the reactor drive frequency (see figure 6.12).

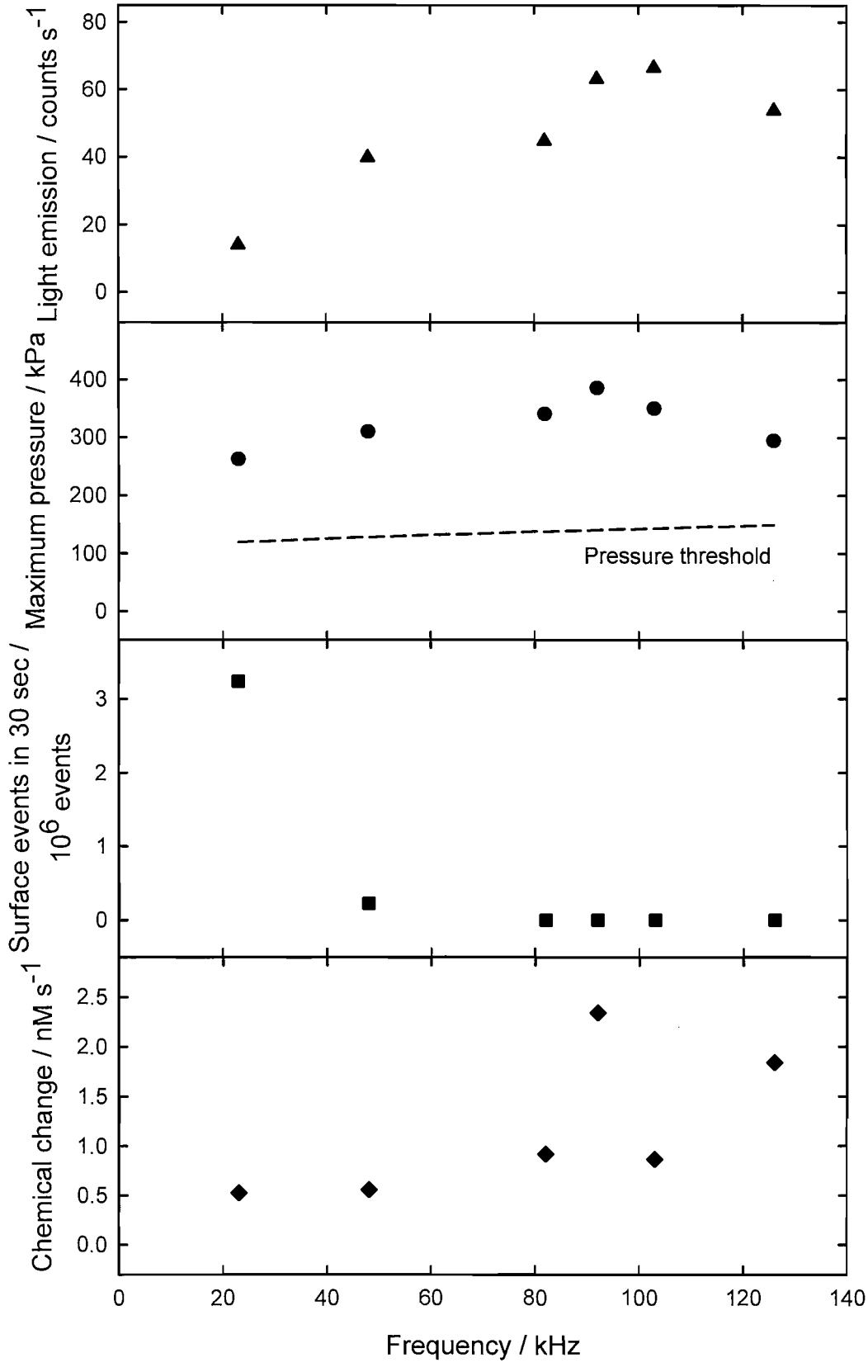

Figure 6.12: Plots comparing the light emission, pressure, surface events and chemical change as a function of drive frequency in reactor 4.

Figure 6.12 shows that, as reported elsewhere, there is a general increase in the light emission and sonochemical change at higher drive frequencies. There is also a noticeable increase in the maximum acoustic pressure recorded with frequency. Conversely if we look at the relationship between the drive frequency and the number of surface events recorded there is an inverse relationship; more events are seen at lower drive frequencies.

6.2.2. Spatial correlation between measurements

In addition to comparing the global measurements averaged over the entire reactor it is also instructive to compare the spatial measurements in order to investigate further the relationship between light emission, acoustic pressure and the presence of surface erosion/corrosion events. Looking at the results presented for the low light imaging and the pressures measurements (see figure 6.2 and figures 6.4 and 6.7 respectively) it is possible to infer a basic correlation between high AC acoustic pressure amplitude and the emission of light through MBSL. However, a direct comparison is hindered by the difference in position of the volume sampled and scale of the plots. We shall now concentrate on the results recorded at the two frequencies at which the spatial correlation between the MBSL light emission, acoustic pressure amplitude and surface event activity is most prevalent; 23 and 92 kHz. For both frequencies we shall investigate the relationship between light emission and maximum acoustic pressure amplitude as a function of position. In addition at 23 kHz we shall also include the results from the surface erosion/corrosion event experiments; this is not possible for the results recorded at 92 kHz due to no surface erosion/corrosion events being recorded.

6.2.2.1. Pressure and light measurements at 92 kHz

Figures 6.2 and 6.7 show that the experiments at 92 kHz exhibit the most pronounced and regular banding of all the frequencies investigated. It is possible to calculate the pitch of the pressure amplitude banding on axis to be 8 mm ± 1 mm. A direct correlating measurement from the intensified image shows the bands to be spaced by

8.5 mm ± 1.5 mm. It should be noted that the errors exhibited for the measurement taken from the lowlight images is due to the distortion in the image caused by the lens as well as normal random experimental error. A direct comparison between the light and pressure results can be shown by superimposing a contour map of the pressures recorded over the intensified image of the MBSL light emission. To enable the relative positions of the light emission and pressure maxima with respect to the reactor to be more easily visualised, in figure 6.13 both are superimposed over an image of the reactor taken utilising the same conditions as the low light image but with ambient light.

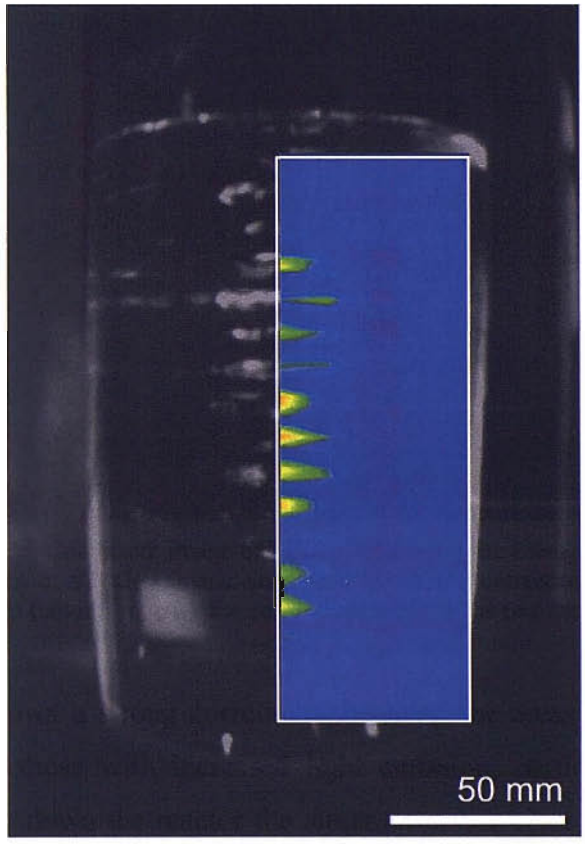

Figure 6.13: Composite image of reactor 4 showing the lowlight light emission image when driven at 92 kHz (black and white) with the corresponding acoustic pressure contour map (colour) to show the correlation between the two measurements.

Figure 6.13 shows a strong correlation between the areas exhibiting high pressure amplitude and those with increased light emission; particularly at the top of the reactor. Lower down the reactor the situation is less clear with a series of pressure maxima observed with no corresponding area of light emission. Note that the ambient light image of the reactor clearly shows that the image of the reactor is

distorted due to the lens. The base of the reactor is found to be 15 % narrower than the top in the image; this obviously has a detrimental effect on the comparison. Interestingly the underlying image also reveals that the uppermost band of light is in fact a reflection of one of the lower bands at the surface of the solution.

Figure 6.14 shows a plot of the light emission through the central region of the image on the same graph as the central scan of the pressure measurements giving a better indication as to the correlation between the results.

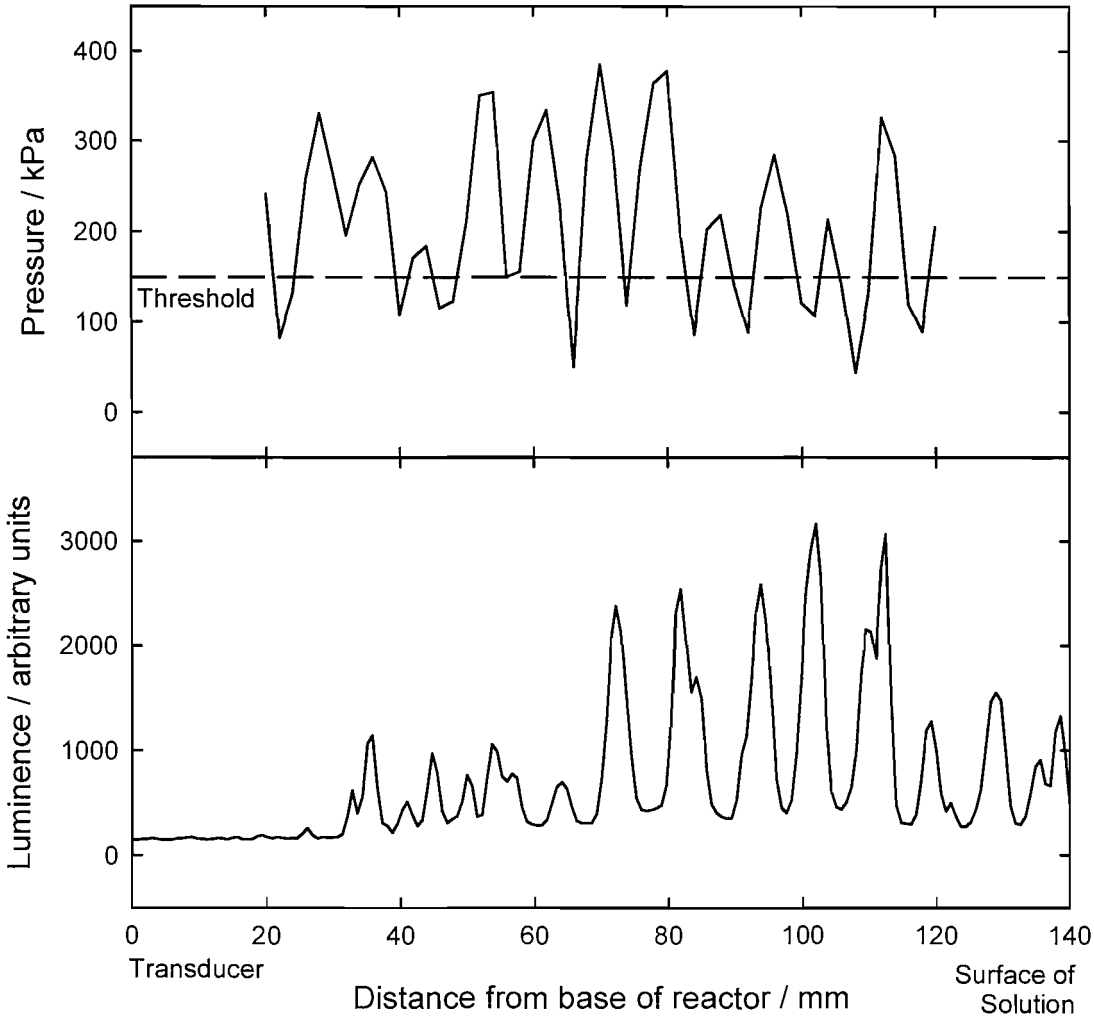

Figure 6.14: Plot comparing the central pressure scan and luminance trace from reactor 4 driven at 92 kHz as a function of distance. Pressure trace consisted of 50 point scan with a resolution of 2 mm. Luminance trace calculated from lowlight image using Matlab. For both measurements reactor 4 contained 1 l 0.1 M Na_2SO_4 driven at 150 V.

The confused nature of figure 6.14 makes a direct comparison between the light output and the acoustic pressure is problematic. Two factors hinder the comparison.

First the distortion of the original low light image makes the positioning of the luminence and pressure plots relative to each other difficult. Second the size of the active element of the hydrophone (6 x 6 mm) is greater than the scan resolution (2 mm) and congruous in size to the measured pitch of the banding (8 mm). Consequently there will be spatial averaging of the pressure signal; making it less well defined and harder to compare to other results.

6.2.2.2. Pressure, light and surface event measurements at 23 kHz

Like the images for 92 kHz the intensified images presented in figure 6.2 showing the reactor driven at 23 kHz are an excellent example of banding within the reactor. The pressure scans also exhibit the same banding which can superficially be assumed to be of the same pitch as that seen from the light measurements. In contrast to the experiments carried out at 92 kHz, at 23 kHz significant surface cavitation event results were recorded that can, as a result, be presented simultaneously with the light and pressure measurements. Direct measurement of the pitch of the banding from the different techniques gives the pitch as 38 ± 5 mm for the light emission measurements, 36 ± 2 mm for the pressure measurement and 35 ± 5 mm for the surface event measurements. The accuracy of the band separation measurements for the surface events is limited by the resolution of the scan being only 5 mm. The increased separation between the bands of cavitation at 23 kHz compared to 92 kHz reduces some of the problems seen at 92 kHz with correlating the measurements. The effect of the distortion of the intensified image is reduced and in particular the spatial averaging of the hydrophone has a significantly reduced effect. As a consequence the measuring of the bands is simpler; though assigning the points within the bands to measure between becomes more problematic. The plotting of contour maps showing the location of areas of increased acoustic pressure and surface event activity next to the corresponding low light images in figure 6.15 makes clear that there is a correlation between the different measurements.

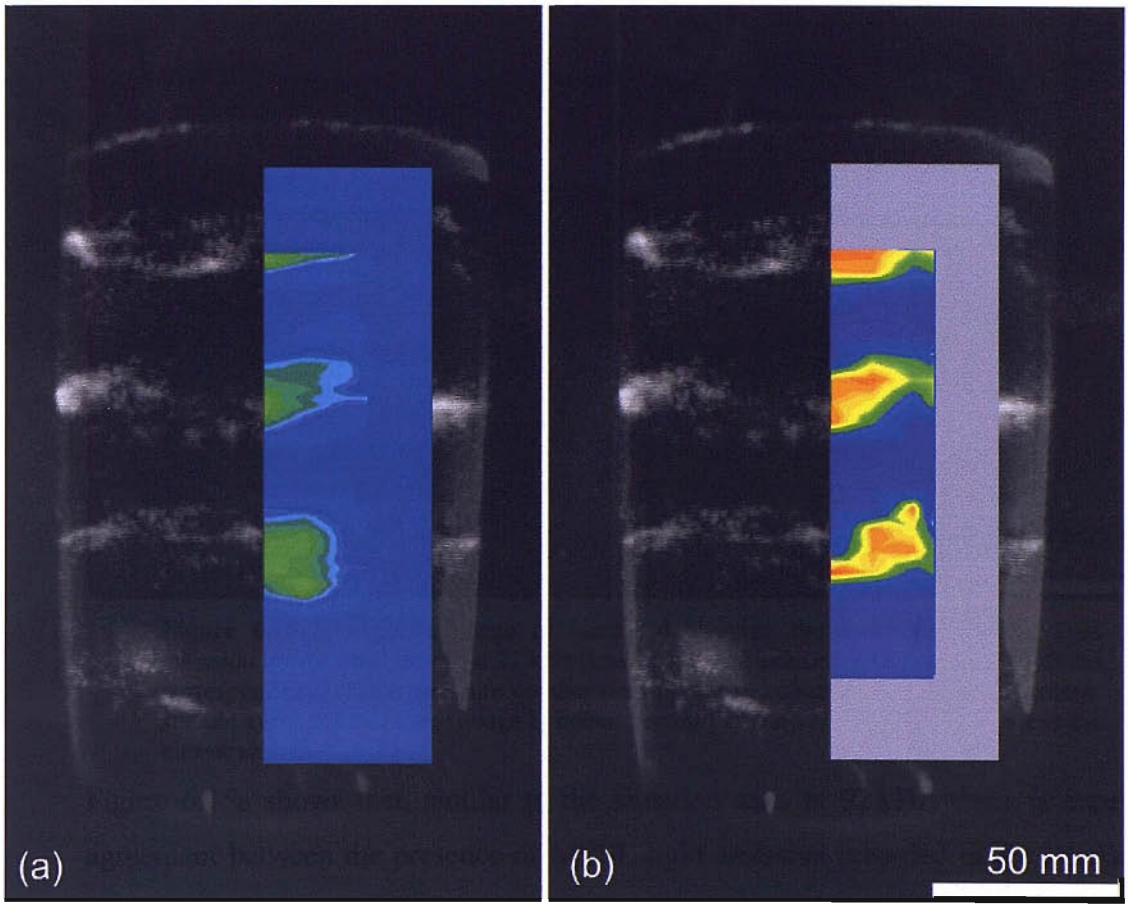

Figure 6.15: Composite image of reactor 4 showing the intensified MBSL light emission image when driven at 23 kHz (images a & b, black and white portions) with the corresponding acoustic pressure contour map (image a, colour portion) and logarithmic surface event contour map (image b, colour portion) to show the correlation between the measurements.

Figure 6.15a shows that, similar to the situation seen at 92 kHz, there is excellent agreement between the presence of MBSL light emission recorded in the intensified image and pressure maxima recorded by the acoustic pressure measurements. In addition figure 6.15b shows that locations at which an increased number of surface events were recorded correspond to the areas of light emission and increased acoustic pressure. The conformity between the measurements observed in figure 6.15 is a clear indication of the co-dependence of the phenomena, as would be expected.

The clarity seen for the results in figure 6.15 recorded at 23 kHz is greater than that seen in figure 6.13 with the reactor driven at 92 kHz. This increase in clarity is associated with the increase in the separation between the bands of activity, which resultantly makes the effects of spatial averaging of the hydrophone and distortion of the intensified images less pronounced.

Analysing the image intensified frame to find the light emission as a function of position with in the central scan (as done for the 92 kHz) further emphasises the agreement between the measurements. Figure 6.16 shows that when the light, pressure and surface event measurements are plotted together.

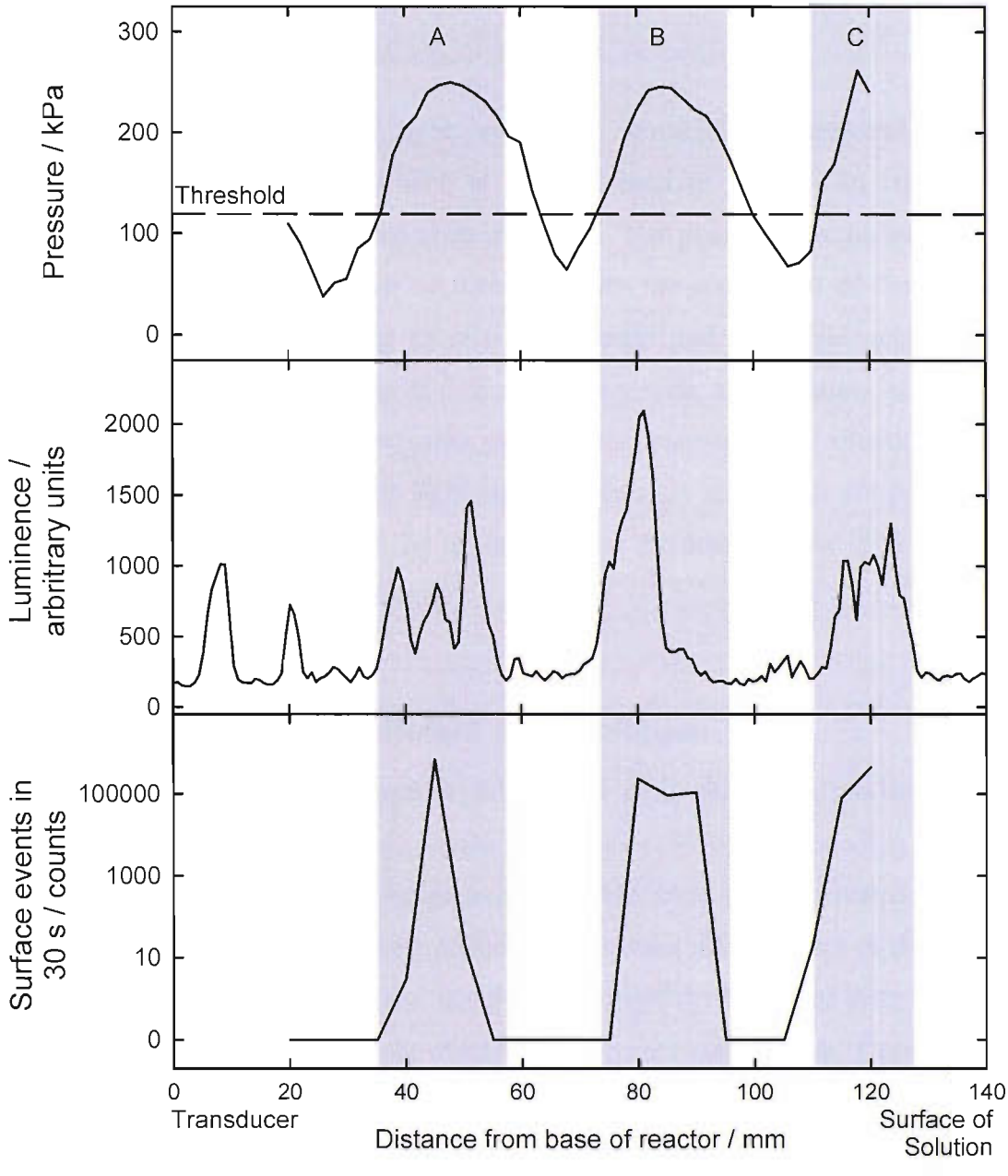

Figure 6.16: Plot comparing the central pressure scan and luminance trace from reactor 4 driven at 23 kHz as a function of distance with three bands of increased activity identified (a, b and c). Pressure trace consisted of 50 point scan with a resolution of 2 mm. Luminance trace calculated from lowlight image using Matlab. Surface scan consisting of 20 points with 5 mm resolution conducted with a 250 μm Al electrode 0 V vs. a stainless steel counter/reference electrode. Events collected using a multi channel analyser with counting threshold set to 2.44 μA For all measurements reactor 4 contained 1 dm^3 0.1 M Na_2SO_4 driven at 150 V.

Figure 6.16 clearly shows that all three measurements show maxima at between 40 and 60 mm from the base of the reactor and again between 80 and 100 mm. There is also an indication of a third maxima located between 110 and 130 mm from the base; this though extends beyond the bounds of the measurement area of the surface and pressure measurements.

The correlation between the light emission, acoustic pressure and surface erosion/corrosion measurements seen at 23 kHz seen in figure 6.16 confirms a relationship between the different measurements. The poor correlation seen at 92 kHz in figure 6.14 is as a result of problems with the acquisition of the data; in particular the spatial averaging of the hydrophone and distortion seen in the intensified images. This makes it difficult to say with any certainty if the two measurements are observing the same point in the reactor. The situation is not improved by the manner in which light measurements are made; it is not possible to sample a specific volume within the reactor, instead the measurement is in effect an average of a plane through the reactor.

6.2.3. Measurements at different drive voltages

With all the measurements presented in this chapter so far the reactor has been driven at the maximum voltage allowable for the equipment (150 V corresponding to a P_{max} of 350 kPa; 3.45 Atm). Using the greatest available drive voltage created the most intense cavitation within the reactor making the resultant effects easier to detect. By making measurements this way and using only a single drive voltage does constrain the number of different pressures at which measurements can be made. Consequently in addition to the detailed measurements of the reactor presented above a selection of measurements were made at lower drive voltages and hence pressure amplitude values.

6.2.3.1. Pressure measurements

With the variation within the reactor being of less interest at the lower voltages, pressure and surface scans were only conducted on the central axis of the reactor and only a single, global, chemical change measurement carried out. Similarly

measurements were only carried out at two frequencies: 23 and 126 kHz. The pressure measurements presented in figure 6.17 show that varying the drive voltage did result in a variation in the pressures recorded as expected.

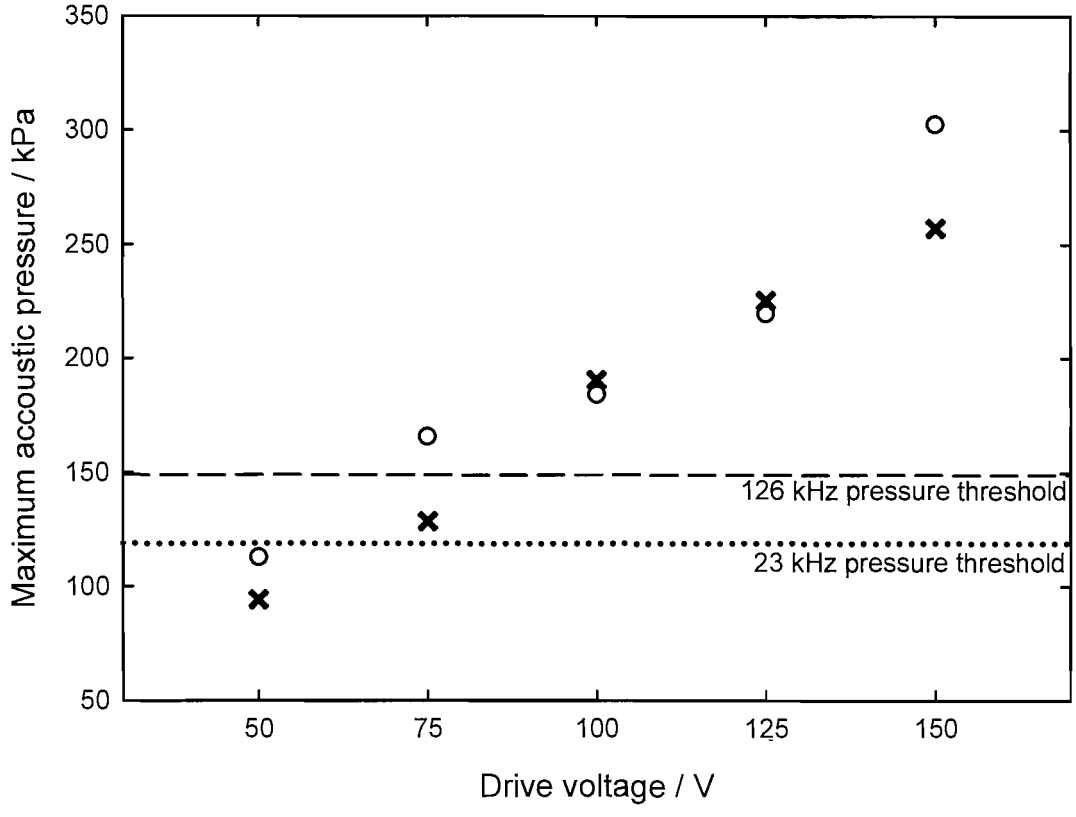

Figure 6.17: Plot of maximum acoustic pressure *vs.* drive voltage at 23 kHz (**x**) and 126 kHz (**O**). Measurements taken along the central axis of reactor 4 containing 1000 ml Na_2SO_4.

Figure 6.18 shows that at 23 kHz there a maximum in the pressure towards the top of the reactor. As a consequence the maximum pressure calculated for the purposes of figure 6.17 is derived only from points up to 100 mm from the base of the reactor as a similar maximum had not been seen in other measurements. Figure 6.17 shows that there is a relationship between the drive voltage and the zero to peak acoustic pressure. In agreement with the measurements carried out at maximum drive voltage the pressures recorded at the higher drive frequency, 126 kHz (represented by **O** in figure 6.17) are generally greater than the pressures recorded at the lower frequency, 23 kHz (represented by **x** in figure 6.17). The variation in the pressure within the reactor as a function of position on the central axis of the reactor can be seen for 23 kHz in figure 6.18.

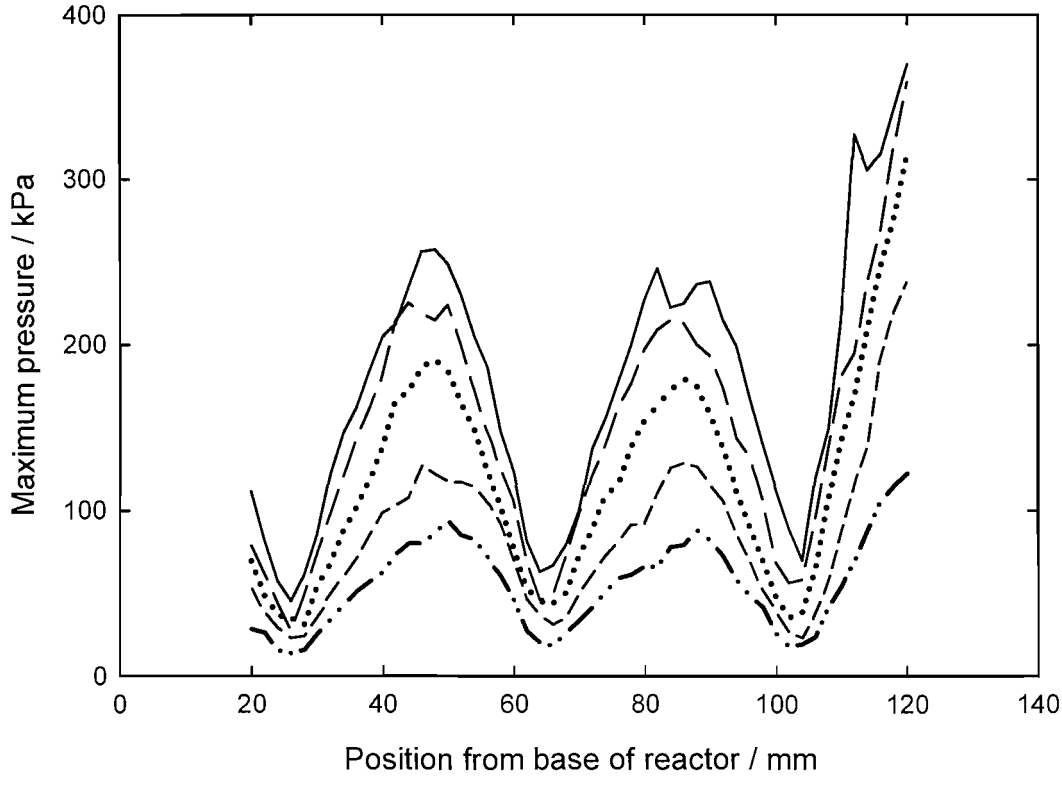

Figure 6.18: Central axis pressure as a function of position in reactor 4 driven at 23 kHz and at drive voltages of 50 (-·-·-·), 75 (- - -), 100 (•••••), 125 (— —) and 150 V (——). Measurements conducted in 1000 ml 0.1 M Na_2SO_4 solution.

Figure 6.18 shows the repeated pressure scans along the central axis of the reactor at different drive voltages. Note that at all drive voltages the banding seen in figure 6.4 is maintained.

6.2.3.2. Light measurements

Figure 6.19 shows the relationship between the peak to peak acoustic pressure and the light emission at 23 and 126 kHz. The level of light emission recorded is substantial less than that recorded in the measurements purely at the maximum drive voltage in figure 6.1. Light emission is only recorded when the zero to peak pressure is in excess of the calculated inertial cavitation pressure threshold.

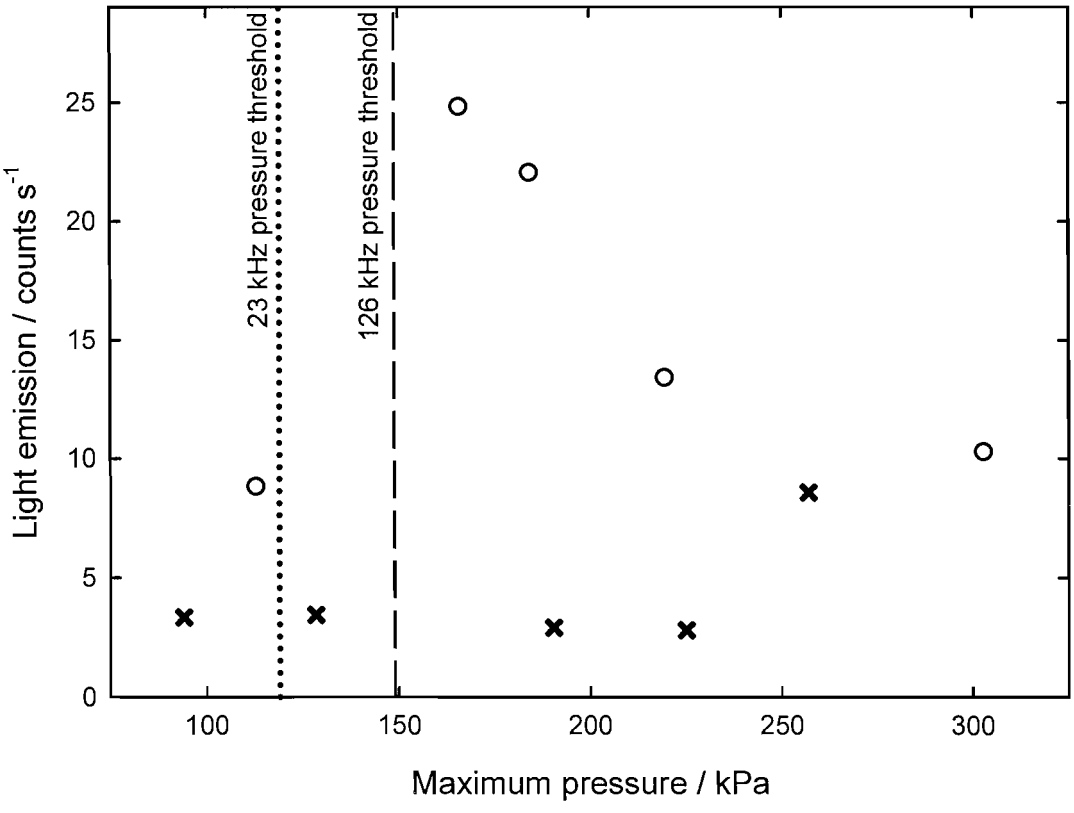

Figure 6.19: Plot of light emission *vs.* maximum acoustic pressure at 23 kHz (x) and 92 kHz (o). Measurements taken over 30 s with photon counter module held 6 cm above the centre of reactor 4 containing 1000 ml Na_2SO_4.

The low light images at both 23 and 126 kHz go some way to explaining the cause of the odd light measurements in figure 6.19. For the images of the reactor at 23 kHz in figure 6.20 it can be seen that the characteristic banding seen in figure 6.2 is only present at 150 V (figure 6.20, image a). At all other drive voltages the image shows a reduced localised emission that significantly is not present along the central axis of the reactor, down which the photon counter measurements are made. This explains why at voltages below 150 V levels of light only just above background are recorded.

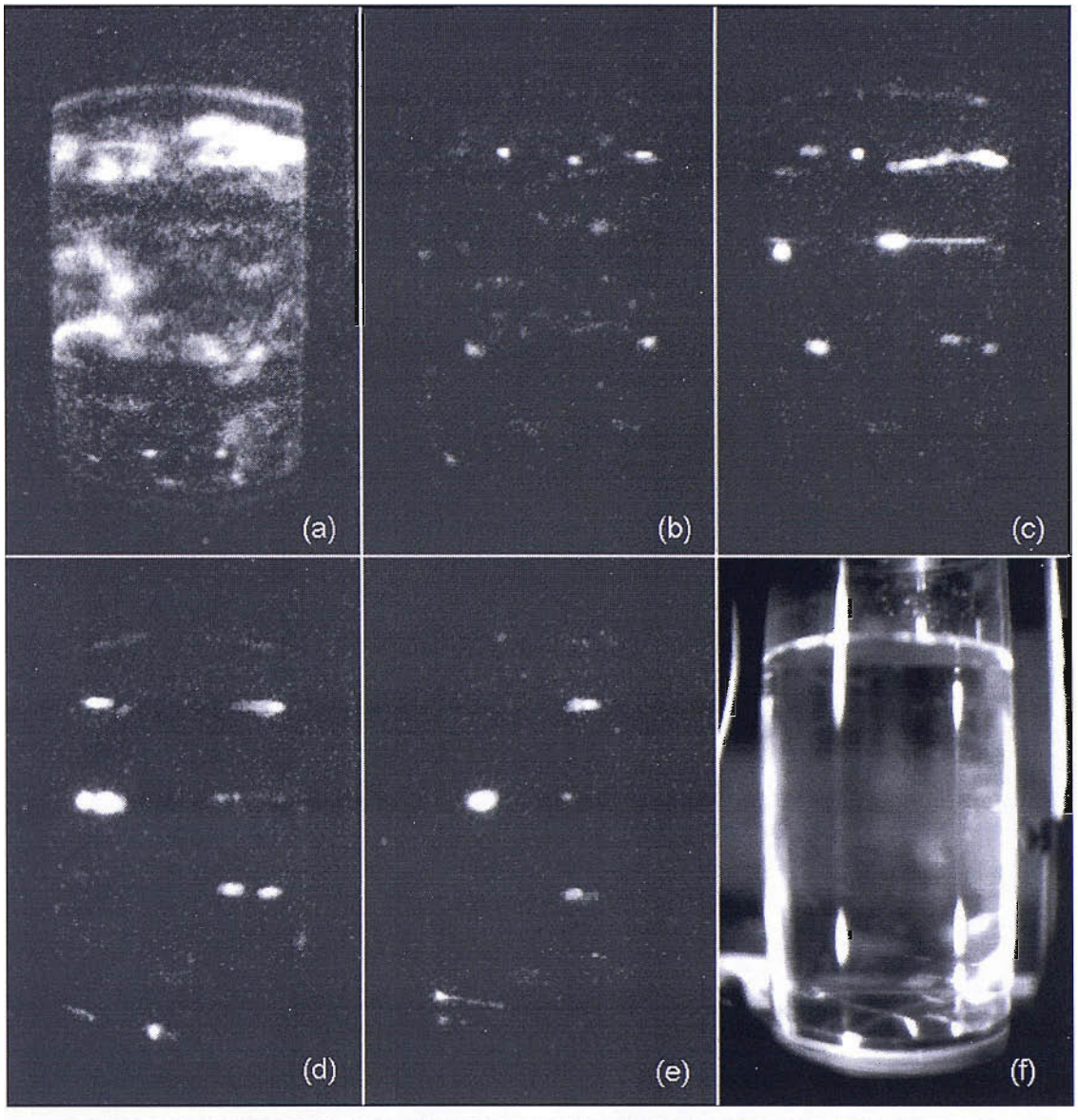

Figure 6.20: Lowlight images of reactor 4 driven at 23 kHz with a drive voltage of 150 (image a), 125 (b), 100 (c), 75 (d) and 50 V (e) and reference image of the reactor with ambient light (image f). Images a to e composites of 100 images stacked together. Reactor 4 filled with 1 dm^3 of 0.1 M Na_2SO_4 solution.

Similarly, though to a lesser extent, the intensified images in figure 6.21 relating to the reactor driven at 126 kHz show that the light emission within the reactor changes as the drive voltage is reduced. At 150 V (figure 6.21 image a) the low light image shows extensive banding that extends through out the width of the reactor with the area of the greatest light intensity being situated towards the base of the reactor along the central axis. As the voltage (and therefore pressure) is decreased the light emission becomes concentrated towards the centre of the reactor and moves upwards. In figure 6.19 it can be clearly seen that the photon counter measurement at the lowest acoustic pressure (corresponding to a drive voltage of 50 V) is significantly

lower than those recorded at the other pressures. On first inspection it would appear that the low light images are in disagreement with this but it should be noted that for the low light image of the reactor at 50 V (figure 6.21 image e) the image intensifier gain is a factor of ten greater than for the other measurements in order for the image to be seen. Interestingly MBSL light emission is seen despite the pressure measurements in figure 6.17 suggesting that the conditions are not suitable for inertial cavitation to take place.

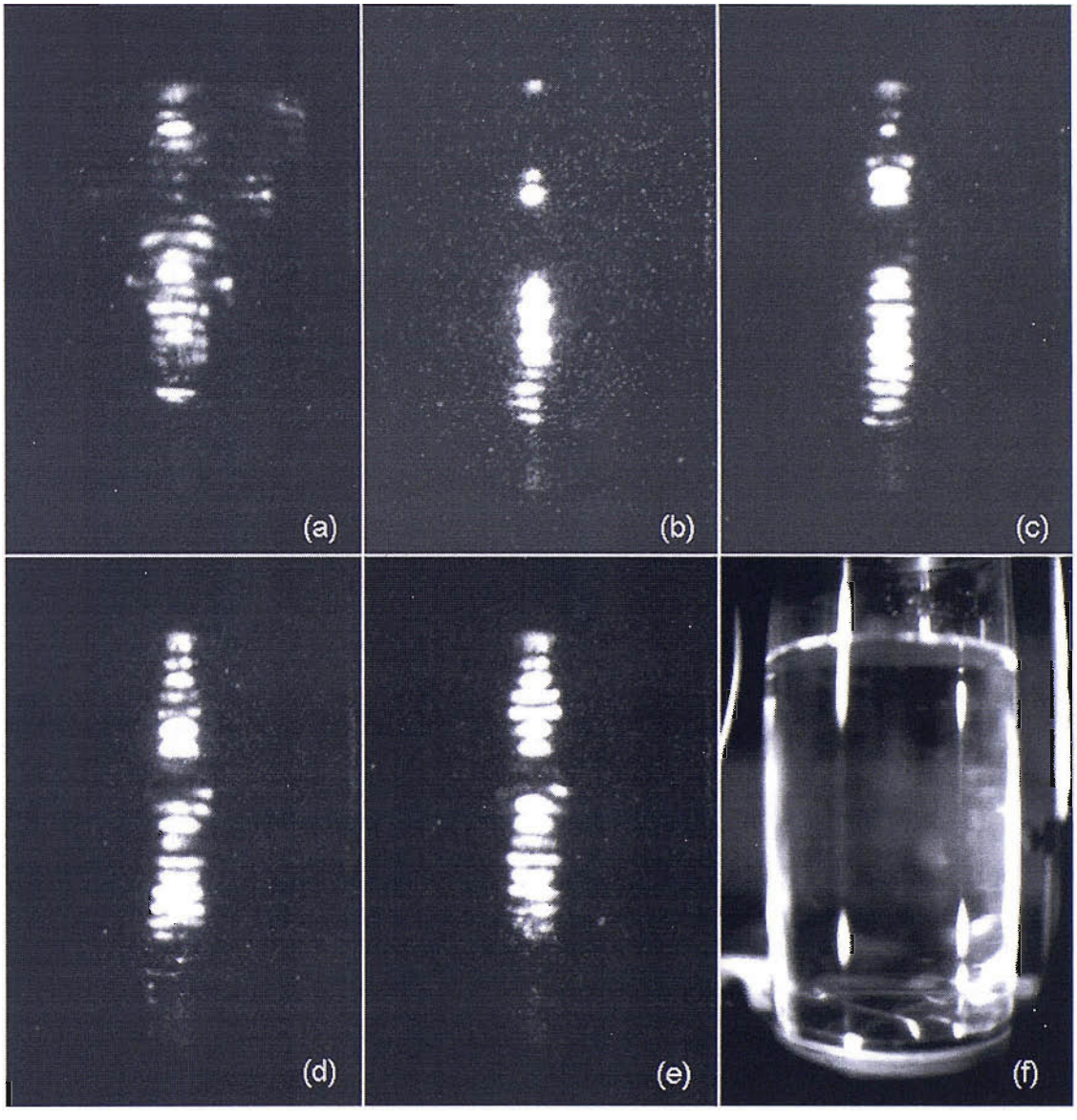

Figure 6.21: Lowlight images of reactor 4 driven at 126 kHz with a drive voltage of 150 (image a), 125 (b), 100 (c), 75 (d) and 50 V (e) and reference image of the reactor with ambient light (image f). Images a to e composites of 100 images stacked together. Images a to d acquired at an intensifier gain of 8 and image e acquired with a gain of 10. Reactor 4 filled with 1000 ml of 0.1 M Na_2SO_4 solution.

6.2.3.3. Surface measurements

The relationship observed between the pressure amplitude and the number of surface events is not as straight forward as would be expected. The plot of pressure amplitude verses total number of surface events in figure 6.22 shows that the number of events reaches a maximum at a pressure of ~190 kPa and reduces either side of this pressure. Interestingly there are a number of surface events recorded at 90 kPa, substantially below the calculated inertial cavitation threshold.

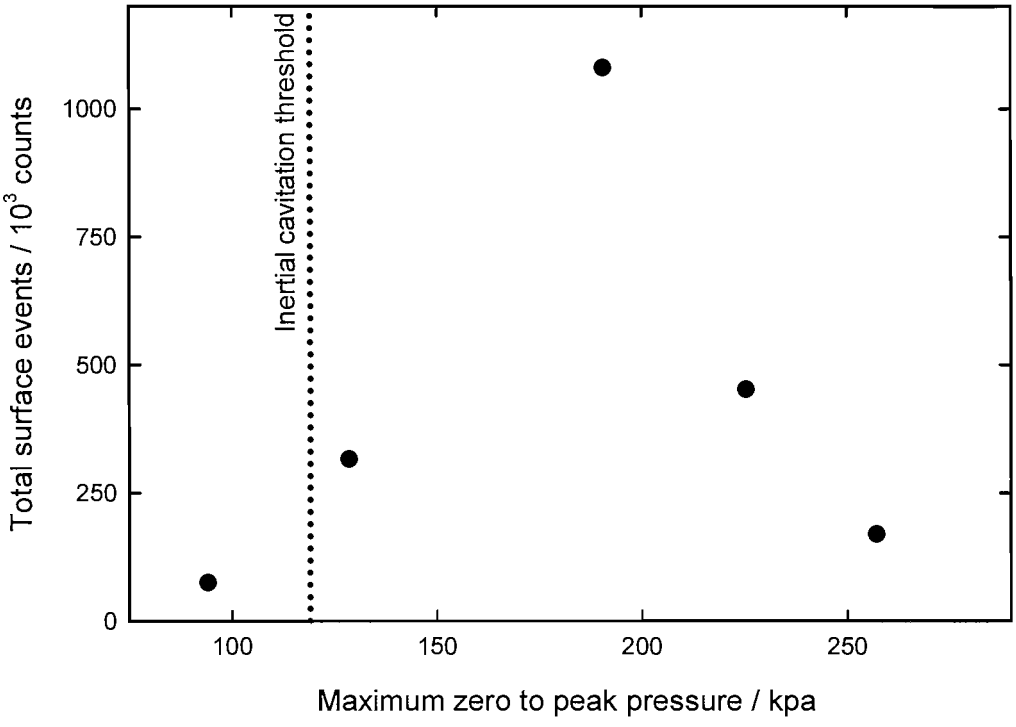

Figure 6.22: Plot of surface events *vs.* pressure at 23 kHz in reactor 4. Number of events at each point a summation of events recorded in a 20 point scan along the central axis of the reactor conducted with a 250 μm Al electrode held at open circuit potential *vs.* a stainless steel counter/reference electrode. Events collected using a multi channel analyser with counting threshold set to 2.44 μA For all measurements reactor 4 contained 1000 ml 0.1 M Na_2SO_4 solution

Figure 6.23 the set of individual scans through the central axis of the reactor. Clearly the presence of banding can be identified at all pressures. At 190, 225 and 257 kPa it is possible to see strong bands at 60 and 100 mm from the base of the reactor with the presence of a third band becoming apparent at 120 mm from the base at maximum pressures of 190 and 225 kPa.

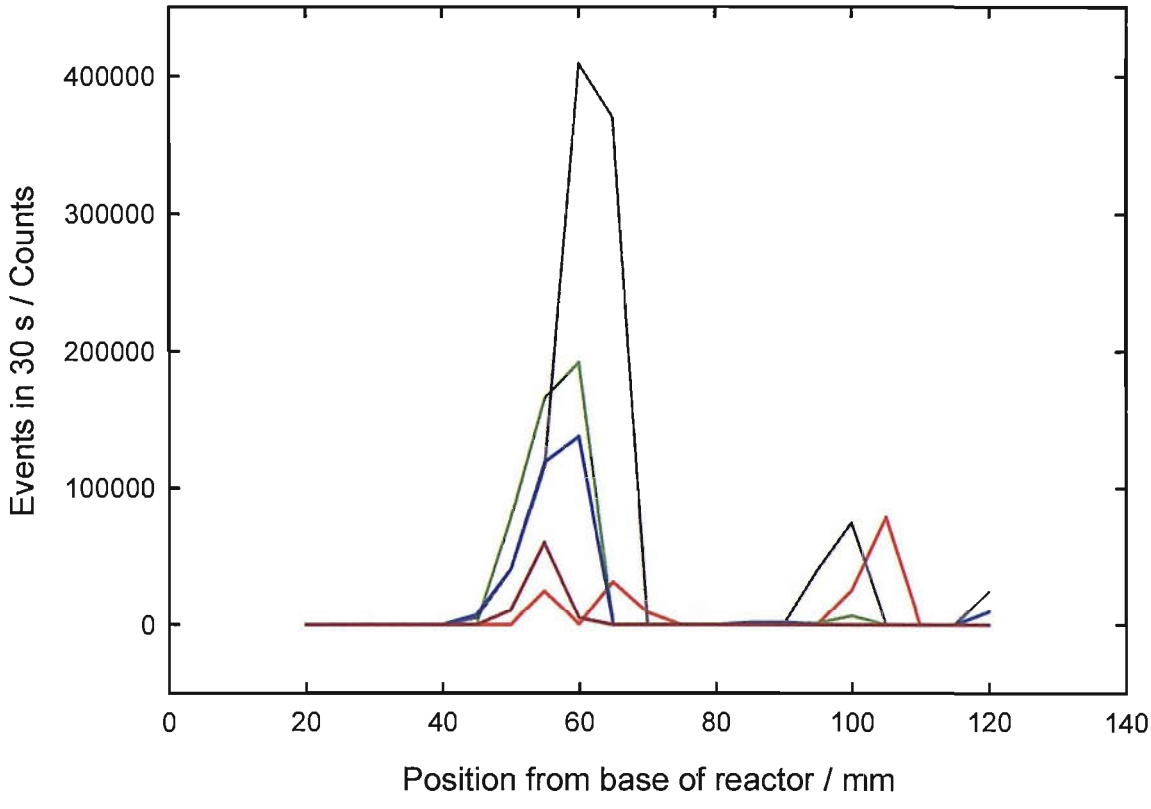

Figure 6.23: Central axis surface event scans conducted at 23 kHz with maximum zero to peak acoustic pressures of 257 kPa (—), 225 kPa (—), 190 kPa (—), 128 kPa (—) and 94 kPa V (—) in reactor 4. Scans conducted with a 250 μm diameter Al electrode held at open circuit potential *vs.* a stainless steel counter/reference electrode. Events collected using a multi channel analyser with counting threshold set to 2.44 μA For all measurements reactor 4 contained 1 dm^3 0.1 M Na_2SO_4 solution

6.2.3.4. Chemical measurements

With the limited ability of the electrochemical measurement apparatus to spatially resolve variation in the rate of chemical change only a single measurement from the centre of the reactor was carried out at each drive voltage. As with the measurements made at different frequencies the rate of chemical change was calculated from the gradient of the current time trace as the current proceeded cathodically. Figure 6.24 shows the variation in the rate of sonochemical change as a function of maximum pressure.

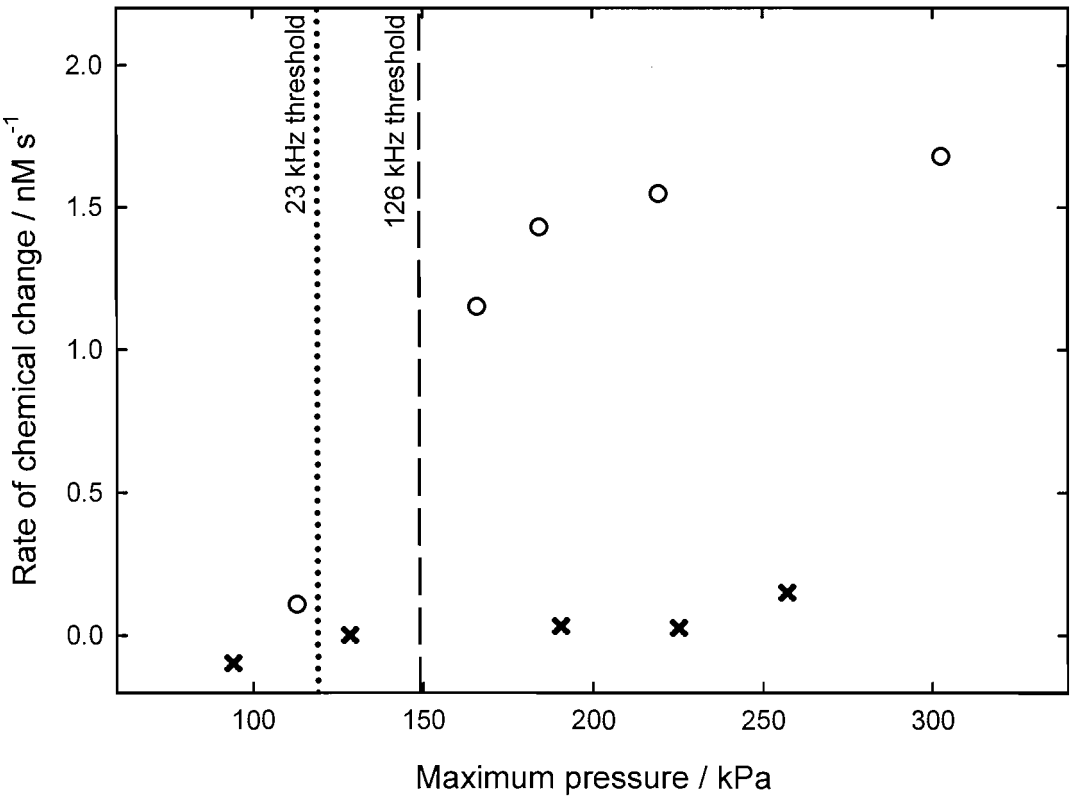

Figure 6.24: Plot of rate of chemical change *vs.* acoustic pressure at 23 (x) and 126 (o) kHz.

Figure 6.24 shows that below the calculated inertial threshold the rate of chemical change at 126 kHz reduces to approximately one tenth of the value seen above. At 23 kHz significantly lower rates of sonochemical change are recorded. Of the five points corresponding to reactor being driven at 23 kHz, only that with the maximum pressure above 250 kPa shows sonochemical change.

The measurements conducted at different drive voltages, and hence acoustic pressure, have shown that the below a certain threshold the level of activity with the reactor reduces significantly. The light, chemical and surface erosion/corrosion measurements have all been seen to reduce below the calculated threshold pressures. The pressure measurements made at 126 kHz are likely to be below the real pressures due to the active element of the hydrophone being large in comparison to the pitch of the banding within the reactor (active element 6 mm, banding ~6.5 mm from MBSL images). Consequently the measurements are spatially averaged, reducing the extremes of pressure recorded.

6.3. Conclusions

In this chapter we have looked at the cavitation field within a relatively large bench top cylindrical single transducer ultrasonic reactor. We have seen that whilst keeping all other factors the same it is possible to tune the reactor to have a high level of activity at a variety of different frequencies. From light emissive measurements 6 active and two inactive frequencies chosen for further study. A series of experiments were carried out to measure the light emission (both quantitatively and qualitatively), acoustic pressure, surface erosion/corrosion activity and level of sonochemical change as a function both of frequency and position. From these experiments and the supplemental investigation into the effect of variation in drive voltage at both lower and higher frequencies a number of trends could be observed.

As has been reported elsewhere (*62, 128*) a correlation between the light emission, acoustic pressure and the rate of sonochemical change can be seen at higher ultrasonic drive frequencies. At lower drive frequencies (specifically 23 and 47.97 kHz) the correlation is not applicable; even with acoustic pressures in excess of 250 kPa low levels of light emission and sonochemical change are recorded in comparison to the higher frequencies. Conversely at the lower frequencies a large number of surface erosion/corrosion events are recorded which are absent at higher frequencies.

The spatial correlation between the pressure field and the light emission could be seen at both high (92 kHz) and low (23 kHz) frequencies. Figures 6.15 and 6.16 have shown that at 23 kHz there is an excellent agreement between the light, pressure and surface event measurements.

Overall this chapter has shown that, with the techniques presented here, it is possible to accurately map the cavitation within a reactor for light emission, acoustic pressure and surface cavitation activity. From this it is possible to compare the effects and build up a more detailed picture of the activity within the reactor than would be provided by a single isolated measurement.

7. Applying electrochemistry to noisy industrial applications

7.1. Introduction

The work presented in section A has demonstrated the ability to locate and quantify inertial cavitation activity within an idealised reactor using electrochemical and other physical measurements. However, one of the major objectives of this work was to transfer measurements performed under these ideal conditions to the more robust and trying environments found in ultrasonic baths and large scale ultrasonic reactors. In particular measurements were to be carried out in a reference cavitation vessel that the National Physical Laboratory (NPL) has constructed as part of an on going project to assign a unit for cavitation(*161, 163, 164, 183*).

All the "real world" devices studied in this work were built around a metal vessel connected to electrical earth. Initially it was intended that the metal of the vessel could be used as the counter/reference electrode for electrochemical measurements; reducing the number of electrodes and simplifying the system. When the baths were powered up, even before the sound field was initiated, the effective earthing of the entire solution generated high levels of electrical noise in the instrumentation. Consequently any electrochemical signal generated by the effects of cavitation, be it as a result of a surface erosion/corrosion event or change in the chemical composition of the solution, was obscured in the electrical interference.

The use of a separate counter/reference electrode did not reduce the level of interference in the electrochemical signal. In figure 7.1 the high amplitude noise in the electrical signal obscures any electrochemical component in the current time trace. In essence the earthed metallic walls of the vessel acted as an additional interferent electrode within the cell. For measurements to be carried out in the "real world" applications a means of isolating the sensitive electrochemical apparatus from this additional interferent electrode had to be developed.

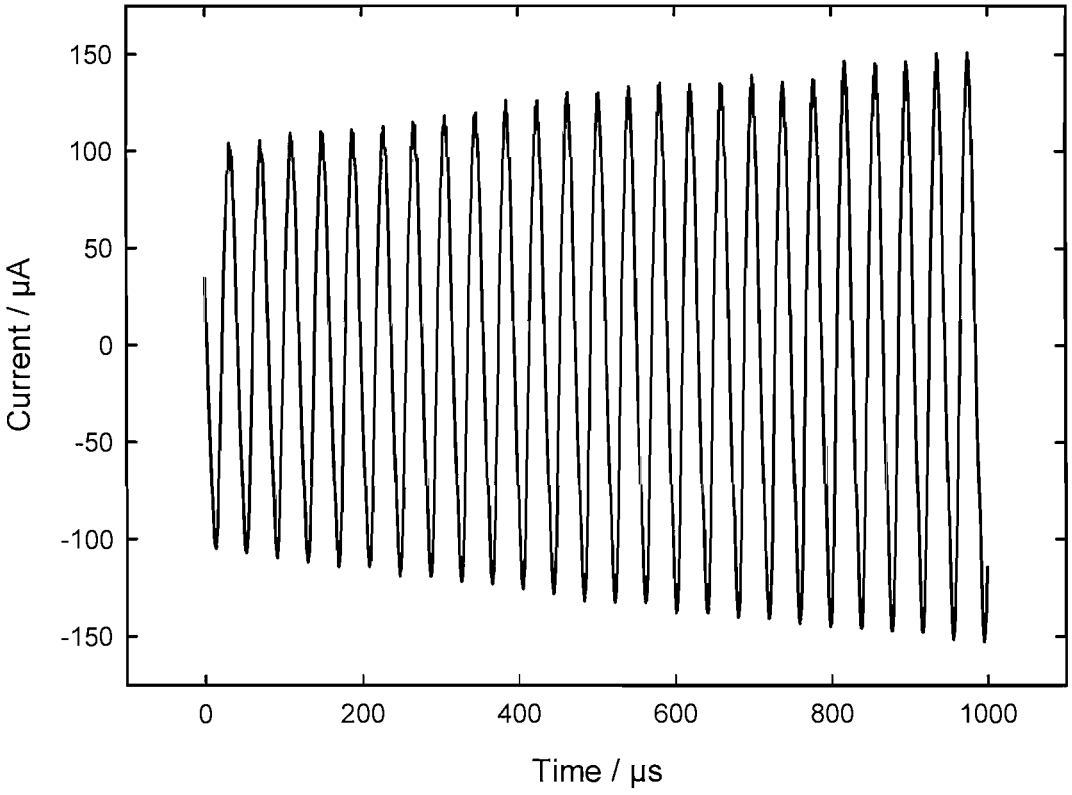

Figure 7.1: Current time trace displaying the dominating noise recorded in the NPL reference vessel with the vessel running at 150 W. A 250 μm Ti electrode held at 0 V *vs.* an Ag counter reference electrode. Vessel contained an aqueous solution of 0.1 M $NaNO_3$.

Two methods of insulating the electrochemical cell from the earthed environment were investigated:

1) The use of a physical barrier between the electrodes and the earthed vessel
2) The use of electronics to electrically isolate the normal mains earth and a separate virtual earth for measurements thus allowing the electrochemistry to proceed unhindered.

We shall now examine these two methods and the effect that they had on the electrical noise; starting with the use of a physical barrier between the electrodes in the electrochemical cell and the remainder of the vessel. Note that barrier must be acoustically transparent so as not to perturb the sound field and associated cavitation processes.

7.2. Physical isolation of the cell

The simplest method available to attenuate the electrical noise from the earthed vessels was to create a physical barrier preventing ionic conduction between the electrochemical cell and the vessel; removing the path through which the noise was transmitted. In addition to the removal of the electrical noise, one of the perceived advantages of using a barrier method is that by isolating a reduced volume of the vessel it is not required to fill the entire reactor with the appropriate chemicals, be they a dosimeter or an electrolyte. Reducing the chemicals used and increasing the spatial resolution of any chemical measurements made.

Two different materials were used as barriers; small rubber balloons and latex glove fingers; both were chosen for being malleable, thin and of small volume. The effectiveness of the barriers was tested by placing both electrodes at the end of a long glass tube with the barrier (either a balloon or a latex finger) attached over the end with an elastic band. Electrolyte was then added to the top of the tube such that it filled the barrier and the then barrier manipulated to remove any trapped air bubbles. For experiments the entire assembly was lowered into the ultrasonic vessel such that the level of solution within the isolated system was the same as within the vessel.

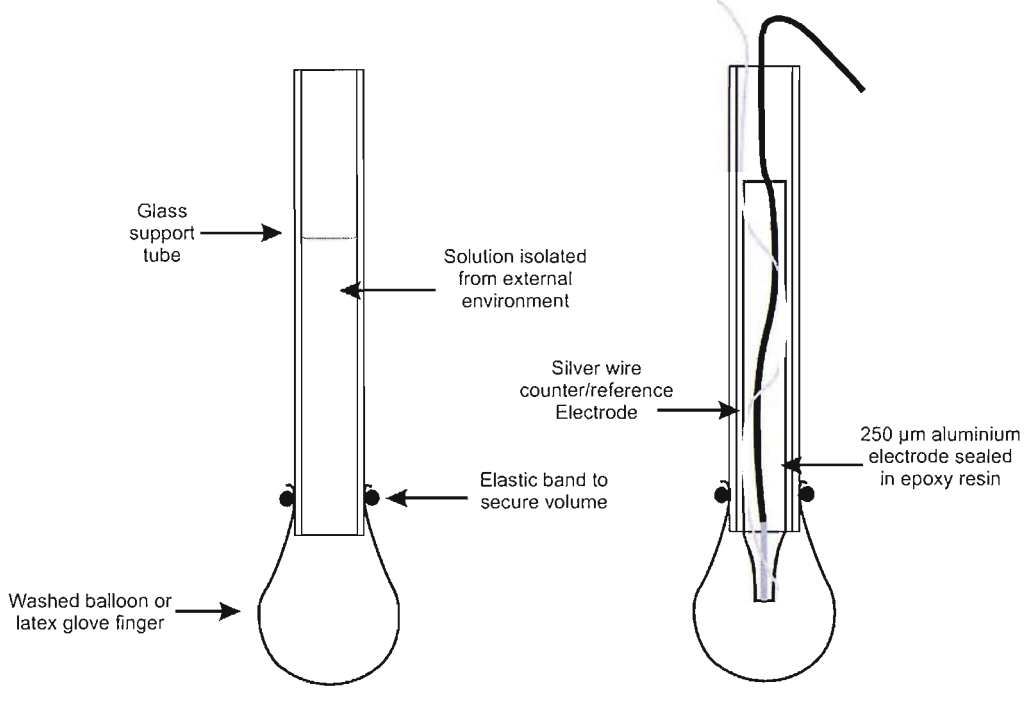

Figure 7.2: Diagram of setup used to test the effectiveness of the isolation barriers. A small balloon or latex finger was placed over the end of a glass tube in order to create a volume isolated from the rest of the reactor.

To ascertain the effectiveness of the barriers at removing the electrical interference, working and counter/reference electrodes were placed within a small balloon and lowered into the NPL reference vessel. When the vessel was switched on it became apparent that although there had been a substantial reduction in the level of noise recorded, it was still considerable as can be seen in figure 7.3.

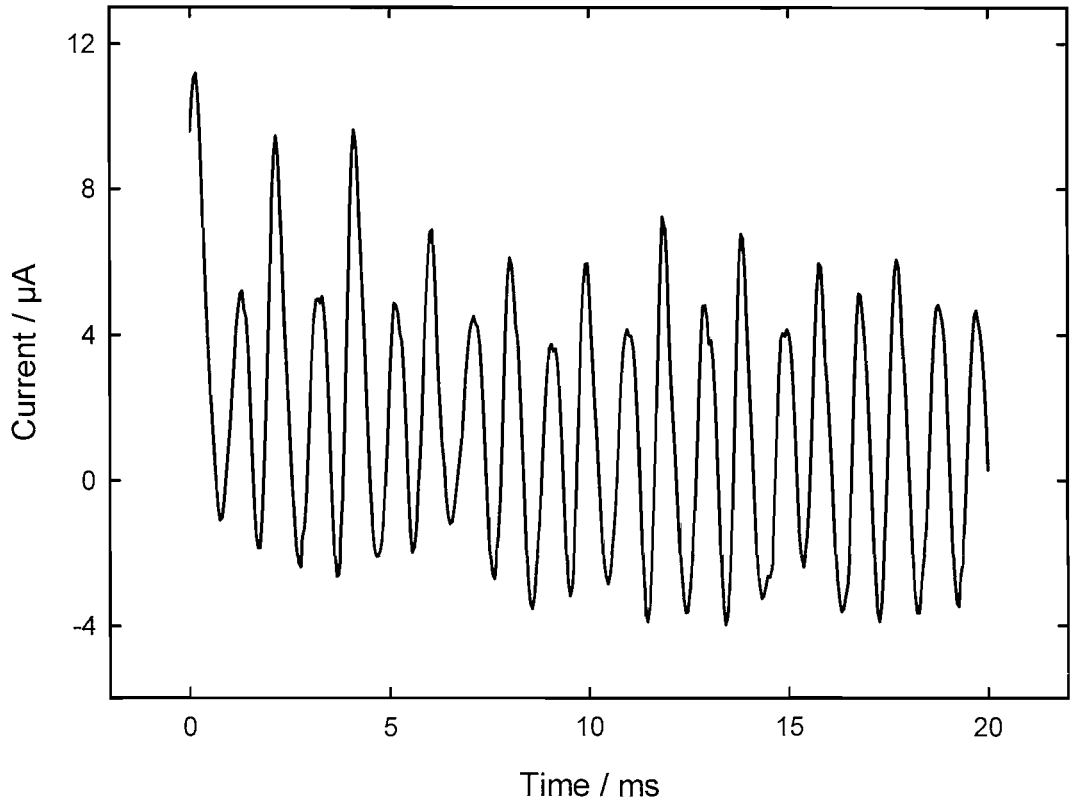

Figure 7.3: Plot of the electrical noise experienced inside of the balloon isolation setup when placed inside the NPL reference vessel at 100 W. 250 μm Al working electrode held at 0 V *vs.* an Ag counter/reference electrode in a solution of 0.1 M Na_2SO_4.

Figure 7.3 shows a reduction in the noise to about 10% of the level seen in figure 7.1. However this is still at too high a level for successful measurements to be made. Similar experiments with the latex fingers showed them to be even less effective. Further investigation into the insulating nature of the barriers found that though of high resistance neither was ionically insulating. Consequently neither barrier was capable of fully mitigating the effect of the earthed baths.

Though found to be of little use for electrically isolating electrodes from the reactors, a small volume of chemically isolated solution would still be of use for monitoring the production of the chemical bi-products of cavitation through UV/Visible absorbance spectroscopy. To investigate this possibility two 1.6 mm diameter Teflon tubes were fed down through the glass support tube into the isolated volume (with the

electrode removed). The tubes acted as the inlet and outlet for the optical flow cell (see figure 2.10). It was hoped that the small volume contained within the isolated volume would allow the variation in rate of chemical change within the reactors to be more easily studied as a function of position.

On exposure to ultrasound the solution within the glove became opaque as the material of the glove degraded. This prevented accurate absorbance measurements being made. Similarly it was found that the powder used to prevent the balloons from sticking together caused the solution held with in the balloon to become opaque. Through repeated washing and soakings it was possible to remove the powder such that absorption measurements could be made on the isolated solution. As in chapter 3 the chemical dosimeter used was potassium iodide reacting via the Weissler reaction(*60, 145*) to give I_3^- which easily detectable due to its strong absorbance at 350 nm.

The balloon was placed inside an ultrasonic bath at various points and the absorbance recorded. Global measurements on this bath had recorded an average rate of I_3^- production of 1.2 nM s^{-1}. Regardless of the duration of sonication no recordable level of I_3^- was found inside the balloon; a similar situation was found when an ultrasonic horn was placed inside the balloon and sonicated for 600s. When the same experiment was repeated in a glass vial for comparison low, but measurable, levels of I_3^- were recorded. Suggesting the material of the balloon was preventing the formation of I_3^-. Consequently barrier methods were rejected in favour of electronic methods of isolation.

7.3. Electronic isolation methods

It having been established that the use of physical barrier methods were insufficient to reduce the interference from the earthed vessels of commercial baths to a acceptable level; further work concentrated on isolating the electrochemical circuit electronically. Two different methodologies were used: the first using linear optocouplers and the second an isolating amplifier. The different time resolutions required for chemical change and surface erosion/corrosion event experiments necessitated that different optocoupled apparatus was developed for each system. As a consequence three sets of equipment were developed: a fast unipolar optocoupled current follower for surface measusurements, a slower bipolar optocoupled current follower for use in chemical change measurements and an isolation amplifier based current follower suitable for either measurement. The construction and performance of each is now discussed.

7.3.1. Optocoupled fast current follower for surface events

To overcome the noise problems seen in the earthed vessels, an optically isolating electrochemical device was developed. In this system the only connection between the earthed electronics (oscilloscope etc.) and the electrochemical sensor was via a linear optocoupler. In such a case the noise caused by the earthed vessel is removed by having the electrochemistry referred to a "virtual" earth that is not connected to mains earth. The linear optocouplers used consisted of an efficient AlGaAs LED emitter coupled to two independent PIN photodiodes (*184*) one of which transfers the signal from the virtual earth to the mains earthed side of the circuit and the other returns the signal to the virtual earth side of the circuit. Using a simple feedback circuit the linearity of the LED output can be controlled from the returned signal, making the chip accurate over a considerable drive current and independent of conditions such as temperature (*184, 185*). Due to the optocouplers being reliant on LED's this system in its simplest form is only unipolar; this does not pose a problem for measuring surface erosion/corrosion events which are also unipolar. The optocoupling integrated chips chosen for this application had a high band width of 200 kHz which is suitable for the measurement of surface events. The optocoupled bridge between the normal and virtual earthed environments was incorporated into a

circuit along with a fast current follower using an op amp (op amp 1 in figure 7.4) with a bandwidth of >200 kHz (OPA121KP) capable of gains between 10^3 V A^{-1} to 10^8 V A^{-1} by selecting different values for the feedback resistor. The counter/reference electrode was connected to virtual earth to leave the working electrode at a constant potential of 0 V *vs.* the reference electrode. Power for the circuit was supplied by 2 Tracor power DC/DC converters (model no. TEL 2-0521); separate components for the normal and virtual earthed circuits. The DC/DC converters supplied a stable +/- 5 V supply. The isolated power supply was powered by a 9 V PP3 alkaline battery and the mains earthed side by a 9 V mains DC adapter. The initial circuit diagram for the fast optocoupled current follower can be seen in figure 7.4.

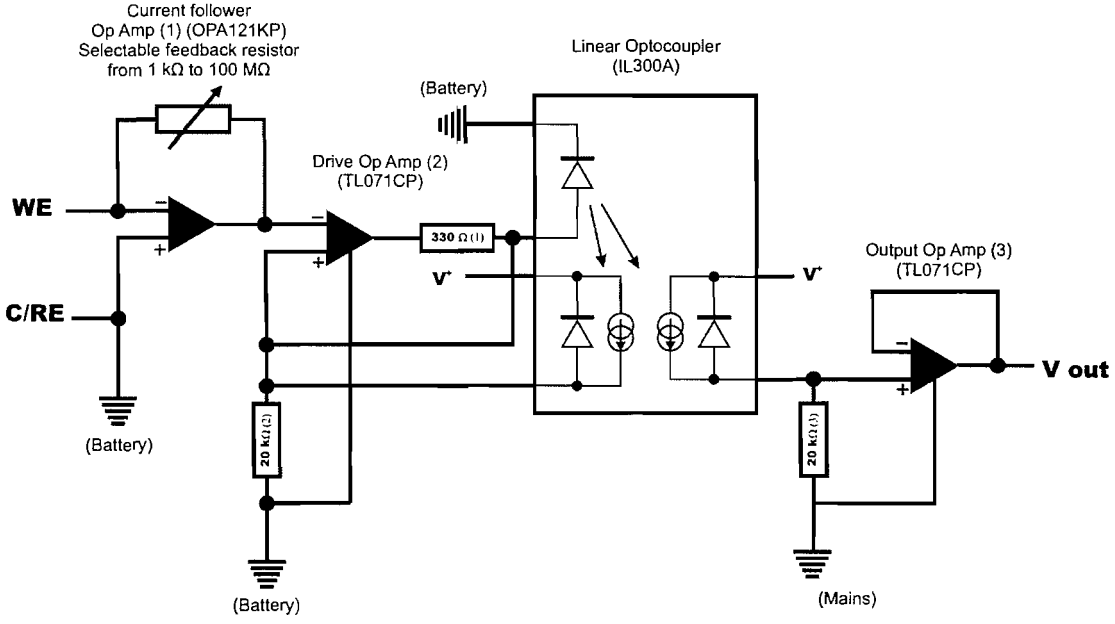

Figure 7.4: Initial circuit diagram of fast unipolar optocoupled current follower.

To ascertain whether the isolating current follower was functioning correctly the current follower was used in place of a standard current follower in the apparatus for measuring electrode surface events at the tip of an ultrasonic horn (chapter 4). When the ultrasound was switched on it was possible to see the detection of surface erosion/corrosion events on the oscilloscope. However, the short time span and high slew rate of the current spikes generated by the surface events appears to cause the optocoupled set-up to "ring" or oscillate after each event. An example of such an occurrence can be seen in figure 7.5. The ringing peaks have a period of 5.3 μs,

corresponding to a frequency of 190 kHz; similar to the frequency of the optocouplers suggesting they were responsible for the apparent oscillation of the circuit..

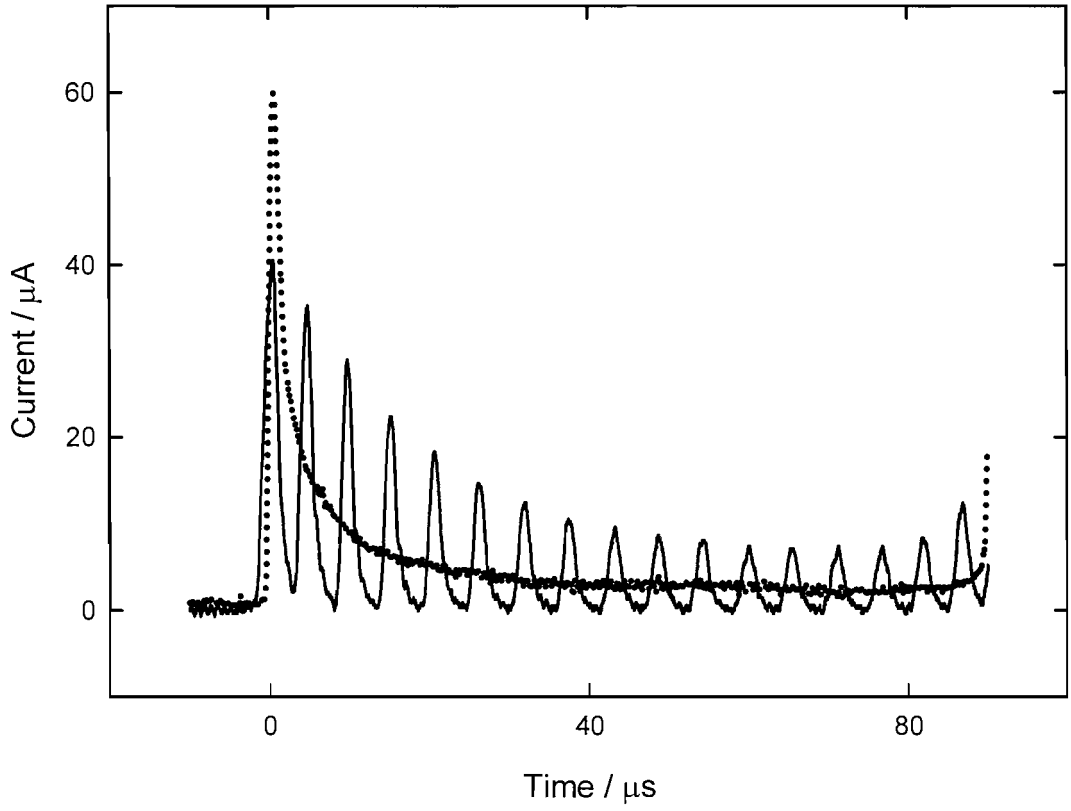

Figure 7.5: Trace of similar transients; one recorded directly (••••), and one via the optocoupler (——). Current follower gain in both cases set to 10^4 V A^{-1} on a 250 μm diameter Al electrode 0.5 mm from the tip of an ultrasonic horn operating at 23.24 kHz and 100 V (zero to peak amplitude). Recorded in aqueous 0.25 M Na_2SO_4 solution.

The repeating peaks in figure 7.5 prevent the accurate recording of the number and size of events as was done in Section A to ascertain the surface erosion/corrosion activity. Consequently for the optocoupled current follower to be usable the "ringing" or oscillation of the system had to be removed. To achieve this, a capacitor was added between the input of the optocoupler and the positive input of the drive op amp (op amp 2). By varying the value of this capacitor and that of the drive resistor (resistor 3) it was possible to remove the oscillation seen in figure 7.5. Figure 7.6 shows the modified circuit diagram.

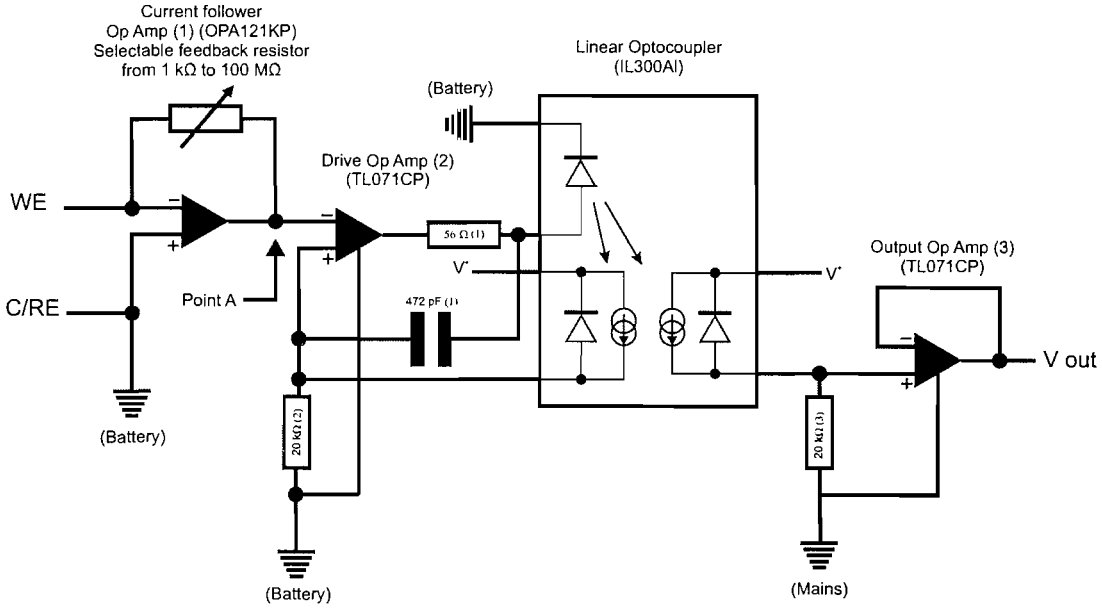

Figure 7.6: Modification of fast optocoupled current follower with added damping capacitor (capacitor 1) to remove the ringing.

After the modifications in figure 7.6 the current follower transmited bounce free transients (see figure 7.7). However, it was observed that there was an increased number of large amplitude events. To investigate this, an oscilloscope probe was connected to the output from the current follower op amp (point A in figure 7.6) and the signal before and after the optocoupling chip compared. The pre-optocoupler signal in figure 7.7 is represented by the dotted line (·····) and the signal post optocoupler by the solid line (——). Clearly the signals pre and post optocoupler are not the same; the signal post optocoupler being considerably greater. Furthermore the amplification does not appear to be linear. The non-linearity of the peaks makes it very difficult to correct the error whether it by electronics means or in post-experimental data-analysis.

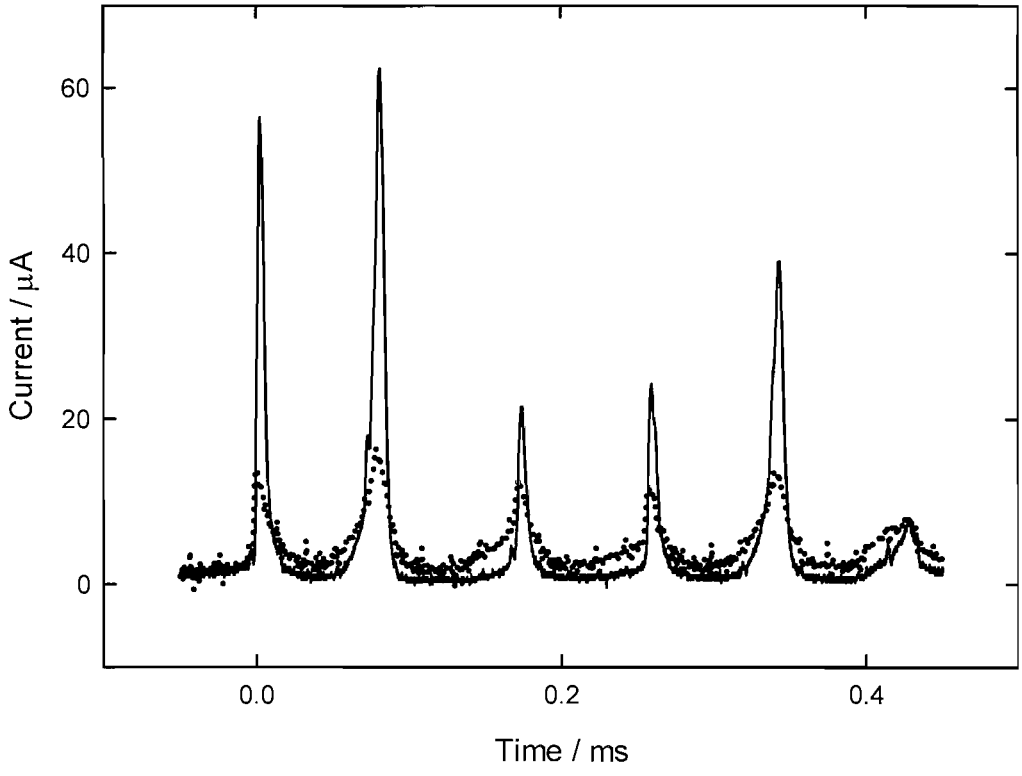

Figure 7.7: Traces of the signal before (••••) and after (—) going through the optocoupler showing the non-linear response of the optocoupling circuit. Current follower gain set to 10^4 V A^{-1} on a 250 μm Al diameter electrode 0.5 mm from the tip of an Ultrasonic horn operating at 23.24 kHz and 100 V (zero to peak amplitude). Recorded in 0.25 M Na_2SO_4 solution.

The non-linearity seen in figure 7.8 precluded the use of a damping capacitor to remove the ringing from the system. Consequently the other aspects of the electronics were re-examined in order to remove the ringing.

In figure 7.5 the "ringing" generated by the optocoupled original system had a frequency of approximately 200 kHz suggesting that the problem originated with the response time of the linear optocoupling chip. Further analysis of the circuit, specifically measurement of the current being passed by the drive resistor (resistor 3) to the optocoupler, revealed that the current draw on the drive operational amplifier greater than it was capable of. Consequently when a transient was passed to the optocoupling system both the drive op amp and the optocoupler would respond. At a given current, the strain on the drive op amp would become too great and causing it to cut out resulting in the output voltage from the optocoupler falling to zero. After the optocoupler had responded and the current had returned to a lower level, with the transient still preceding, the output current would again rise until the op amp cut out

as the current draw again became too great. This would be repeated until the voltage from the transient had reached zero resulting in the ringing seen in figure 7.5. Substituting the drive op amp (op amp 2) with an alternative model capable of passing high enough currents at a high bandwidth (a TS921IN) the ringing was removed. A further instability in the system was traced to the power supply; the drain on the 9 V PP3 battery was too great and as a consequence the battery was heating up and rapidly losing power. The battery was replaced by a higher power 6 V lead acid battery (Maplin Aino Micro AM 6-4.5, 6 V 4.5 A h). Figure 7.9 shows the final circuit diagram.

In certain circumstances, particularly when dealing with small signals, it became desirable to improve the signal to noise characteristics of the equipment further. Consequently an optional secondary amplification stage was added (op amp 4 in figure 7.9). Using a 1 kΩ resistor on the input stage and a 100 kΩ resistor for the feedback resistor this boosted the signal from the optocoupled system a further one hundred times. Given that it is only possible to make measurements using the MCA from a positive signal, an inverter was required after the amplification stage (op amp 5 in figure 7.9) for measurements to be made.

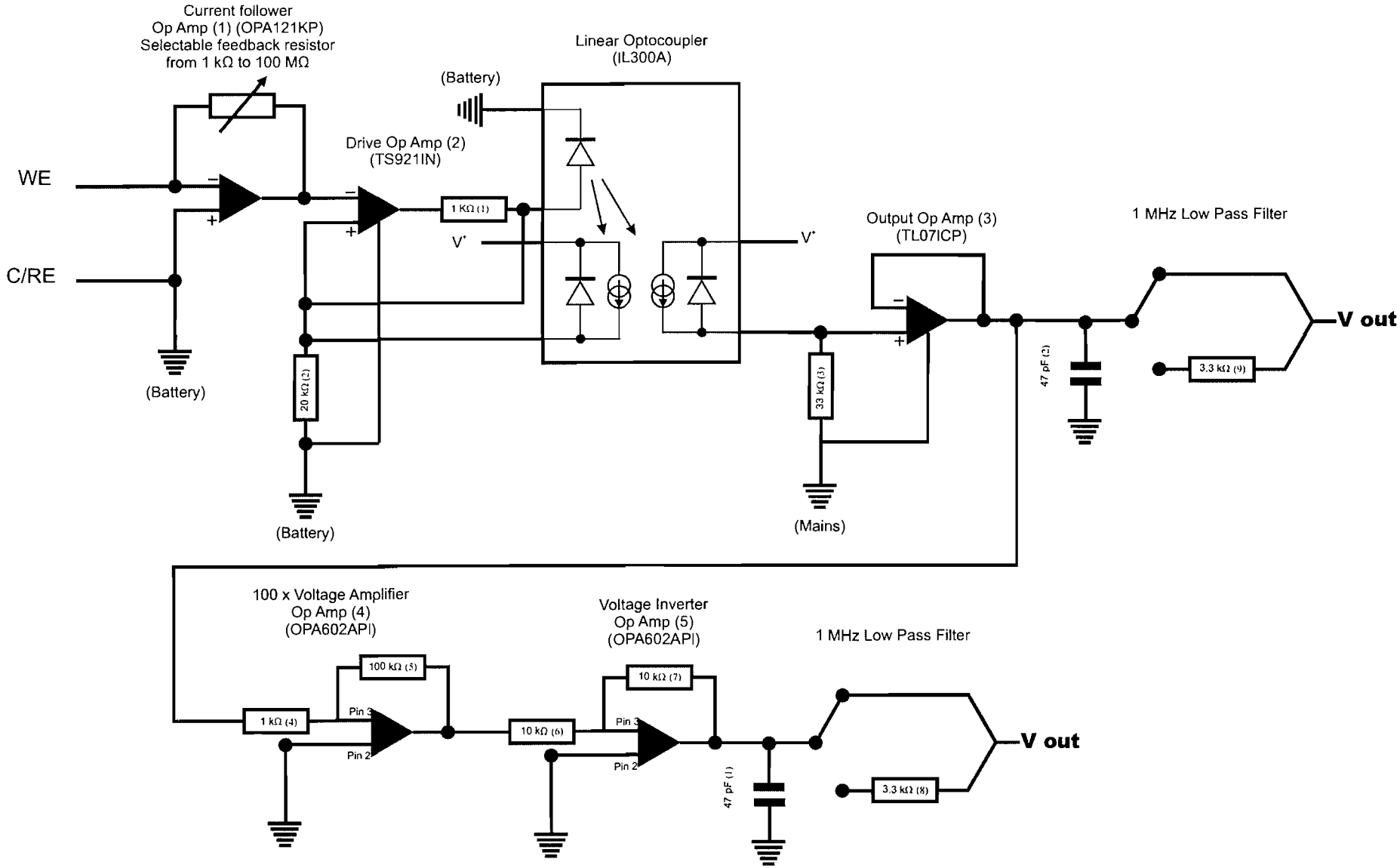

Figure 7.9: Final circuit diagram of fast optocoupled current follower with added magnification stage and 1 MHz low pass filter.

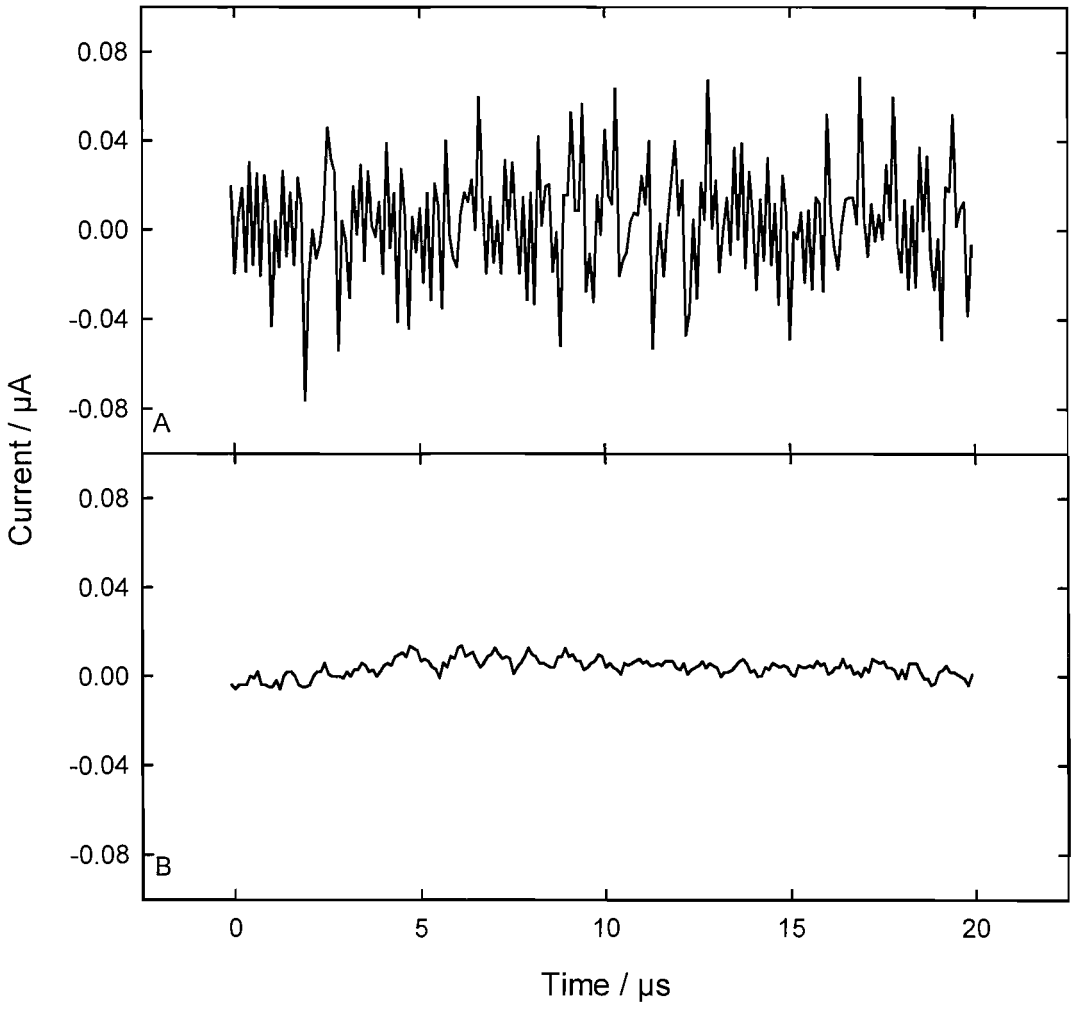

Figure 7.10: Plot showing the signal recorded in the dormant NPL tank through the fast optocoupled current follower with (B) and with out (A) the 1 MHz low pass filter. Signal collected from a 250 µm Ti working electrode held at 0 V vs. a Ag counter/reference electrode in a 0.1 M $NaNO_3$ solution.

Figure 7.9 also shows the addition of a 1 MHz filter that could be applied to either the 1x or 100x outputs. This was necessitated by the presence of some high frequency noise. Figure 7.10 shows the output from the current follower with (A) and without (B) the 1 MHz filter. Reducing the high frequency noise diminishes the chances of false events being recorded.

Ideally the fast optocoupled current follower should be capable of transmitting a linear signal in addition to isolating the electronics from the electrical noise associated with the earthed environment. To test the linearity of the current follower triangular waveforms from a signal generator were passed across a 120 kΩ resistor and onto the optocoupled current follower set to a gain of 10^5. Comparing the input and output waveforms at three different frequencies (1, 10 and 50 kHz) plotted in

figure 7.11 it was possible to see the extent of the linearity of the optocoupled current follower.

The use of a 120 kΩ resistor between the signal generator and current follower and the use of a 100 kΩ resistor as the feedback resistor leads to the setup acting as a 0.8x voltage multiplier. Consequently the transmitted waveforms in figure 7.11 at 1 and 10 kHz are of the order of 0.4 V in amplitude rather than the reference input signal amplitude of 0.5 V. The unipolar optocoupler results in only the negative portion of the input signal being transmitted through the current follower producing a rectified signal from the output.

In figure 7.11 it is possible to see that at the lower frequencies (1 and 10 kHz) there is an excellent level of linearity. At 50 kHz the linearity of the current follower is reduced as the signal is distorted by the limitations of the electronics. It is also interesting to note that there would appear to be a delay in the transmission of the signal being introduced of the order of between 5 and 7 μs. This results in a sharp lead in to the transmitted peak at the higher frequencies (10 and 50 kHz) as well as the shifting of the 50 kHz signals such that the transmitted peaks are no longer directly associated with the negative input peaks from which they were generated.

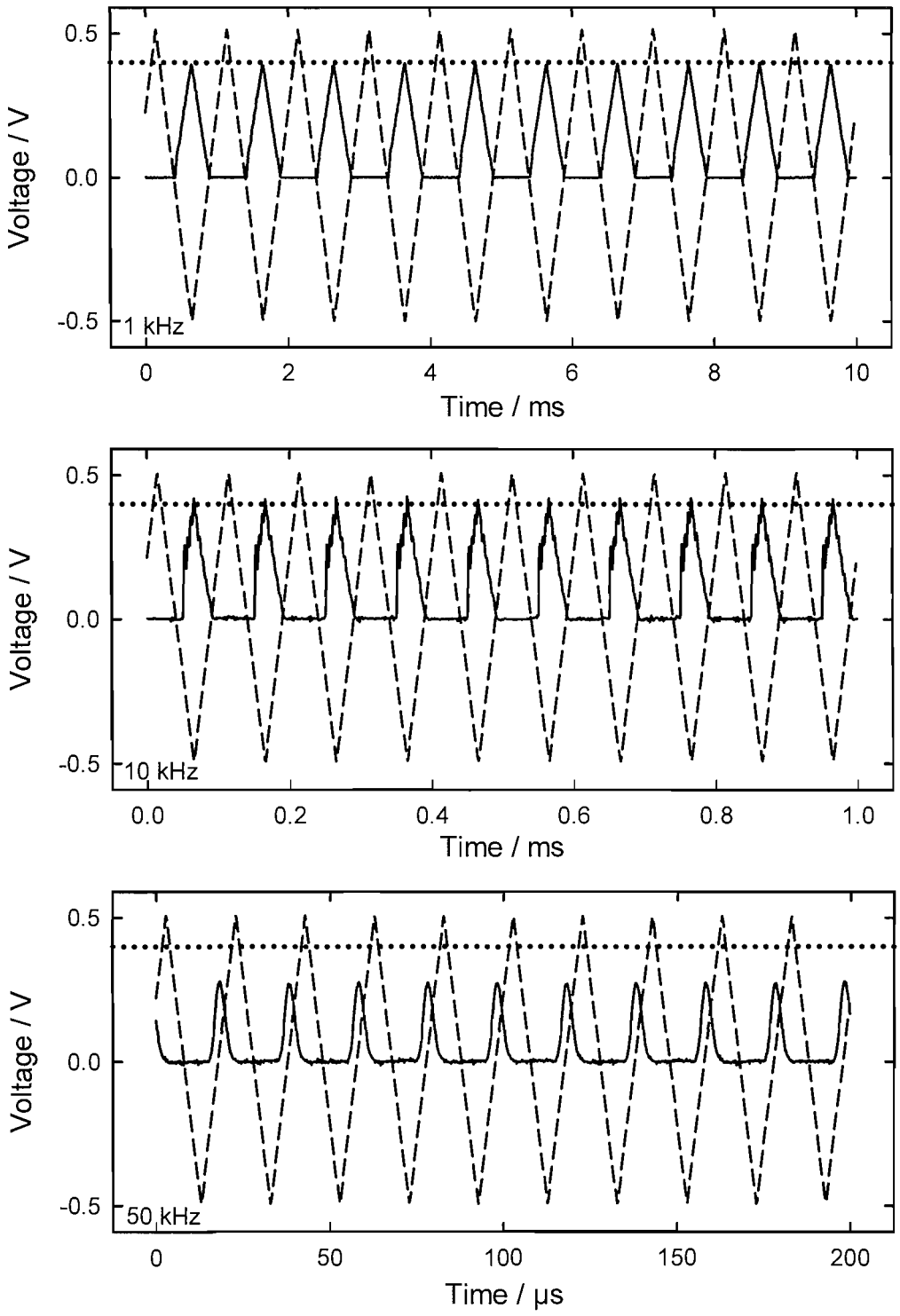

Figure 7.11: Comparison of the input (- - - -) and output (——) signals through the fast optocoupled current follower. 0.5 V triangular wave form passed cross 120 kΩ resistor and through the current follower with 10^5 gain. Note that the expected output voltage is 0.4 V (·····).

Figure 7.12 shows the linearity of the current follower with the 100x amplification stage in use. The extra amplification stage has reduced the linearity; even at 1 kHz there is a significant delay in the transmission of the signal and the deformation of the

triangular signal. At 10 kHz the signal now resembles saw tooth like peaks rather than the regular triangular shape of the input signal. There is also a more notable temporal offset with the peaks continuing beyond the expected cut off.

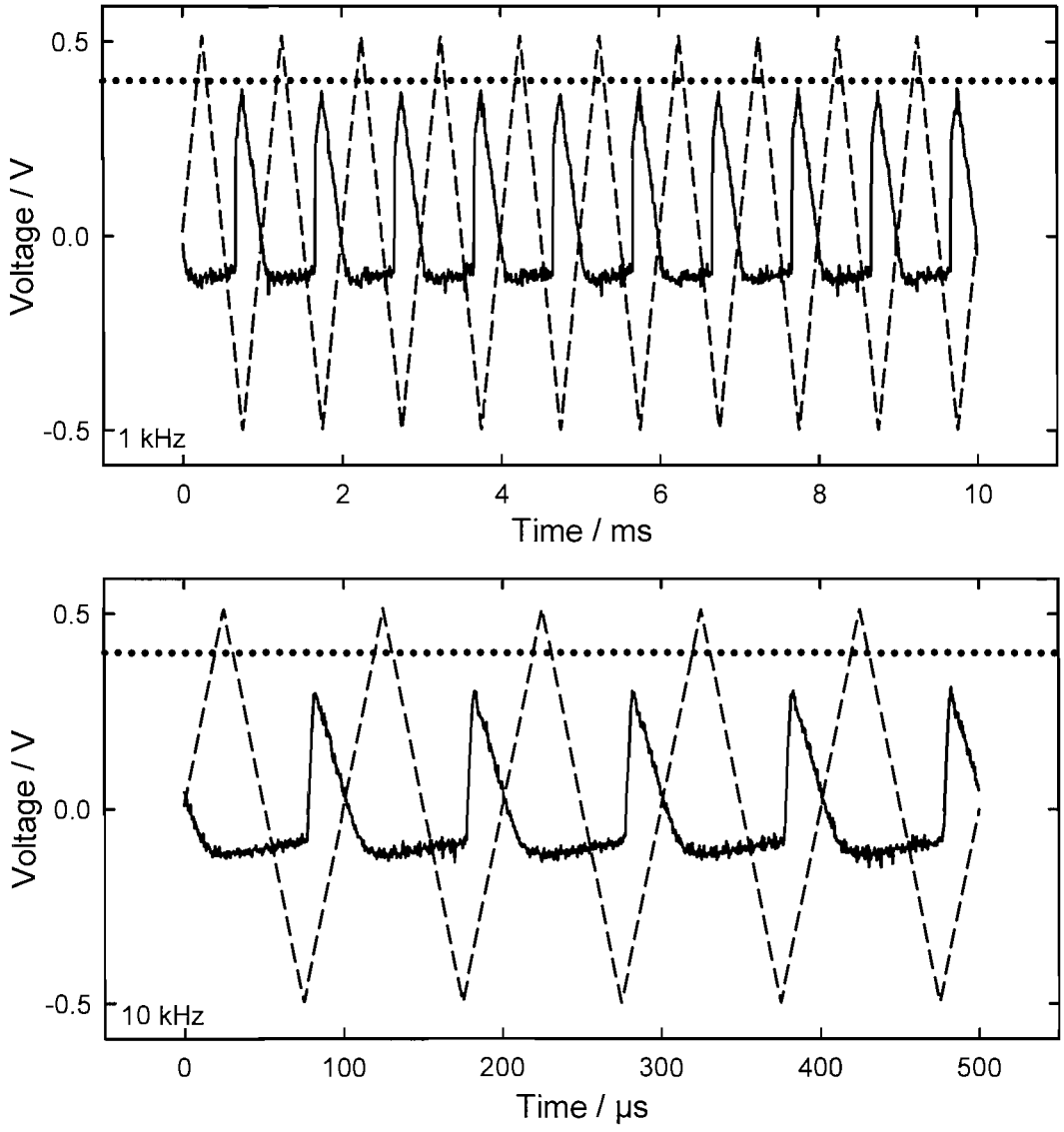

Figure 7.12: Comparison of the input (- - - -) and output (——) signals through the fast optocoupled current follower with 100x secondary amplification. Input signal 0.5 V triangular wave form passed cross 120 kΩ resistor and through the current follower with 10^3 + 100x gain. Note that the expected output voltage is 0.4 V (·····).

The linearity seen in figure 7.11 and in particular figure 7.12 is not ideal. Despite this the wave forms transmitted are repeatable and therefore meaningful measurements can be made with the optocoupled current follower. The elongated response and break down of the linearity at higher frequencies precludes the use of the output for time critical or detailed kinetic work. Given that for the majority of measurements of interest for this study the main importance of the current follower is to transmit a

signal from which it is possible to count the number of discrete events this, though regrettable, does not preclude the use of the current follower.

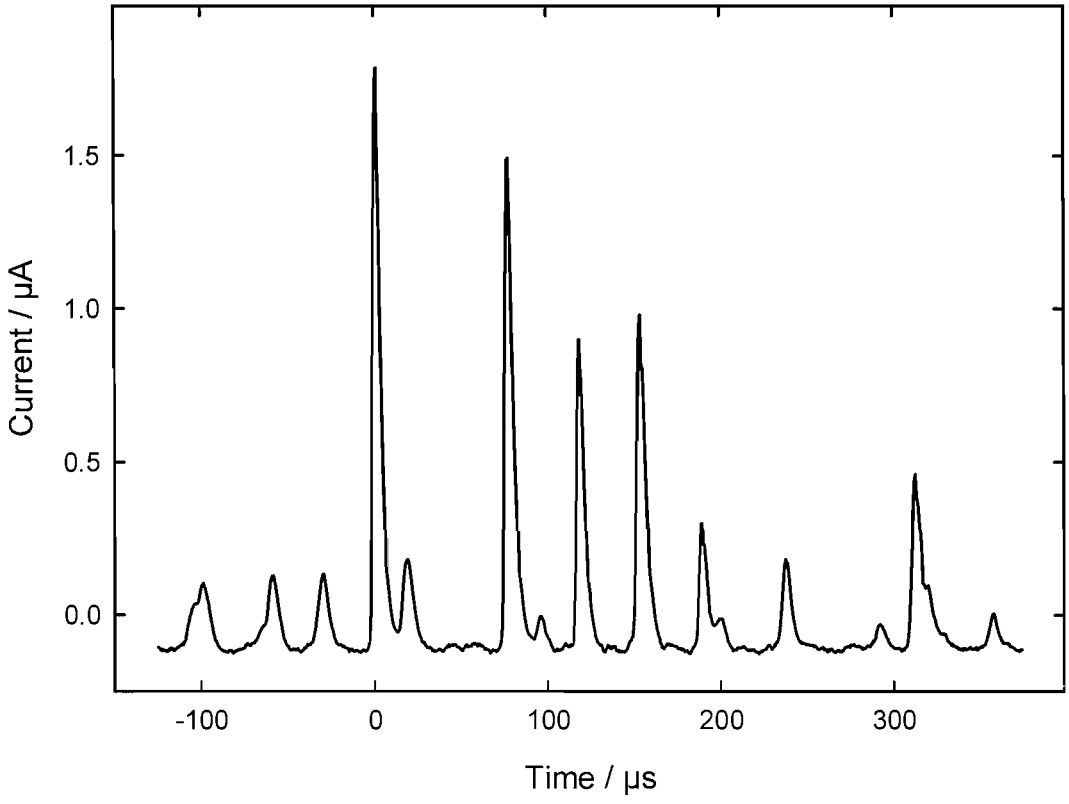

Figure 7.13: Time current trace showing a series of surface cavitation events recorded at the central point of the NPL reference vessel driven at 150 W. Event recorded on a 250 µm Ti electrode held at 0 V vs. an Ag counter/reference electrode in a 0.1 M $NaNO_3$ solution. Measurement made using the fast optocoupled current follower set to 10^4 gain with further 100 x signal amplification and 1 MHz low pass filter.

Having shown that the fast optocoupled current follower can transmit a wave form it is important to confirm that it is capable of making measurements within the earthed vessels for which it is intended. Figure 7.1 showed the high level of electrical interference seen with a standard current follower. When the same experiment is repeated using the optocoupled current follower in figure 7.13 a series of distinct events is easily identifiable and the level of electrical interference is substantially reduced. It should also be noted that the level of back ground noise in figure 7.13 is excellent and would be considered good inside of a faraday cage rather than in the inherently noisy environment experienced inside the NPL reference vessel.

7.3.2. Bipolar optocoupled slow current follower

Ampometric measurements do not require the short timescales that the surface repassivation measurements require. They do though require accurate currents to be recorded and for them to be bipolar. Therefore a second current follower was produced that was capable of passing both positive and negative currents accurately and repeatably. For the surface erosion/corrosion measurements there was no requirement for the potential between working and counter/reference electrodes to be varied. In contrast, though it is possible to make ampometric measurements at 0 V, it is often essential or at least advantageous to make chemical measurements at a variety of different potentials. Consequently the ability to alter the potential between the electrodes was integrated into the current follower.

The optocoupling circuit used for the bipolar optocoupled current follower was a modification of one discussed in an application note for Vishay linear optocouplers (*184*). The final circuit used for the current follower can be seen in figure 7.14. In addition to the circuit seen in figure 7.14 either a 330 Hz or 1 MHz low pass filter could be added to the output to reduce any higher frequency noise. Power was supplied to the non-isolated portion of the circuit by a multi-voltage supply set to 12 V; the isolated portion of the circuit was powered by a 12 V lead acid battery (Maplin Aino Micro AM 12-3.3, 12 V 3.3 A h) and both power supplies were passed through independent DC/DC (XP power IH1205S) to give stable bi-polar 5 V supplies. To enable the alteration of the potential between the working electrode and the counter/reference electrode a potentiometer was placed between the positive and negative battery power terminals. By varying the value of the resistance of the potentiometer it was possible to vary the potential between the electrodes (though it would theoretically be possible to construct an entirely optically isolated potentiostat this was considered as to have few advantages over the potentiometer based system used as well as being significantly more complicated to construct).

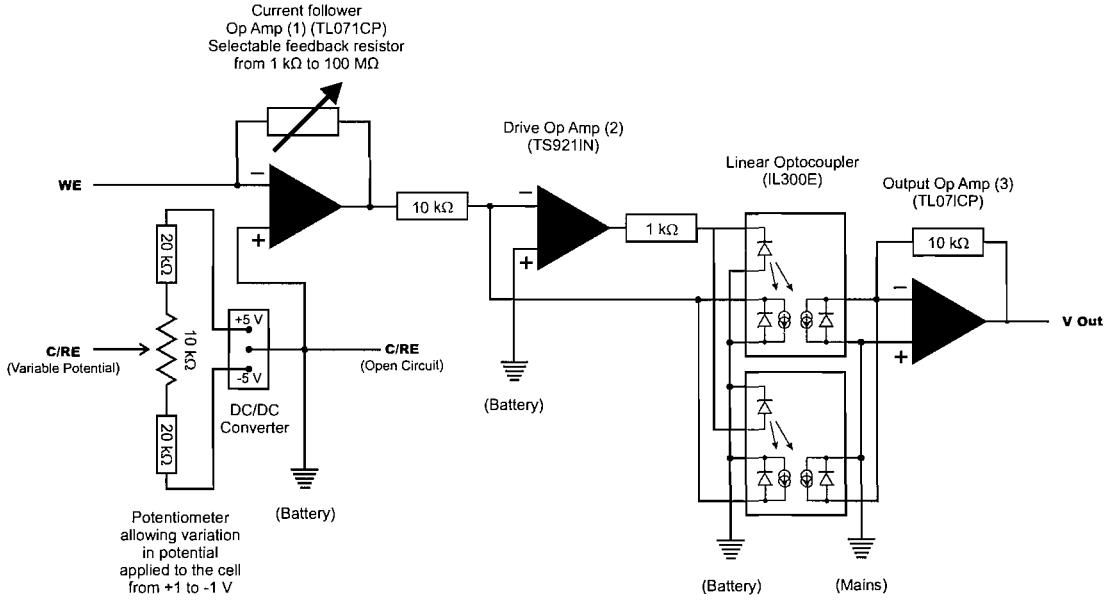

Figure 7.14: Circuit diagram of bipolar optocoupled current follower.

One of the principle requirements of the bipolar optically isolated current follower was that the current information passed was accurate such that they could be used to interpolate chemical concentrations within the analyte. To ascertain the linearity of the current follower a triangular wave form at different frequencies was connected to the input via a 120 kΩ resistor. As with the testing of the unipolar opticoupling current follower a range of frequencies were used but due to the different application of the bipolar system lower frequencies were focused upon. The use of the 120 kΩ resistor and a gain of 10^5 (as with the fast optocoupled current follower) coupled with a drive signal of 0.25 V amplitude resulted in an output signal of the order of 0.2 V in amplitude. In figure 7.15 triangular waveforms from two frequencies are presented; those at 1 kHz and 0.01 Hz. At both frequencies there is excellent linearity and agreement between the input and output signals. Due to the lower frequencies examined it is not possible to see if the temporal offset seen in figure 7.11 for the fast optocoupled system afflicts the bipolar system as well. Such an offset presents less of a problem for the intended purpose of the bipolar current follower as the time frame on which the events of interest take place is of the order of seconds rather than microseconds.

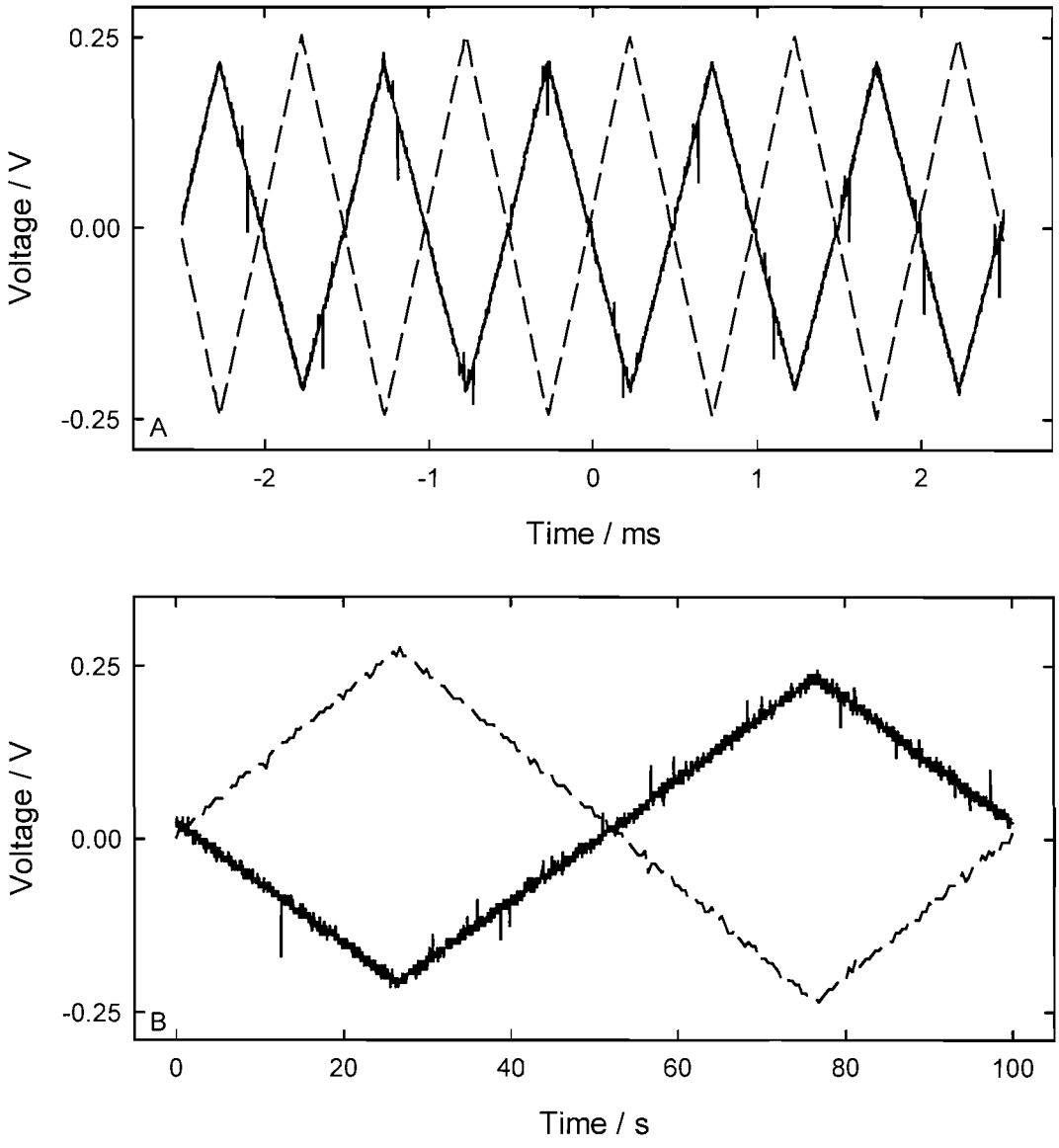

Figure 7.15: Comparison of the input (----) and output (——) signals through the bipolar optocoupled current follower. Plots A and B showing 1 kHz and 0.01 Hz 0.25 V amplitude triangular wave forms respectively passed across a 120 kΩ resistor and through the current follower set to 10^5 gain.

In the course of the testing it became apparent that the system was unable to handle output voltages greater than 300 mV; putting a constraint on the gain setting selected so that overloading of the optocoupling circuit did not take place. If the situation was encountered where it was necessary to increase the range of the current follower then this could be done by the reduction in the resistance between the drive op amp (op amp 2 in figure 7.14) and the optocoupler. Given the excellent stability of the overall system it was decided to leave the setup as it was.

In figure 7.15 it can be seen that the output signal from the bipolar optocoupled current follower has a number of high frequency noise spikes. Though not

overwhelming their presence is likely to affect any automated data processing. Therefore in order to remove these artefacts a 330 Hz low pass filter was added to the output. With the filter added the output from the current follower is cleared of the high frequency noise and still retains its linearity as can be seen in figure 7.16.

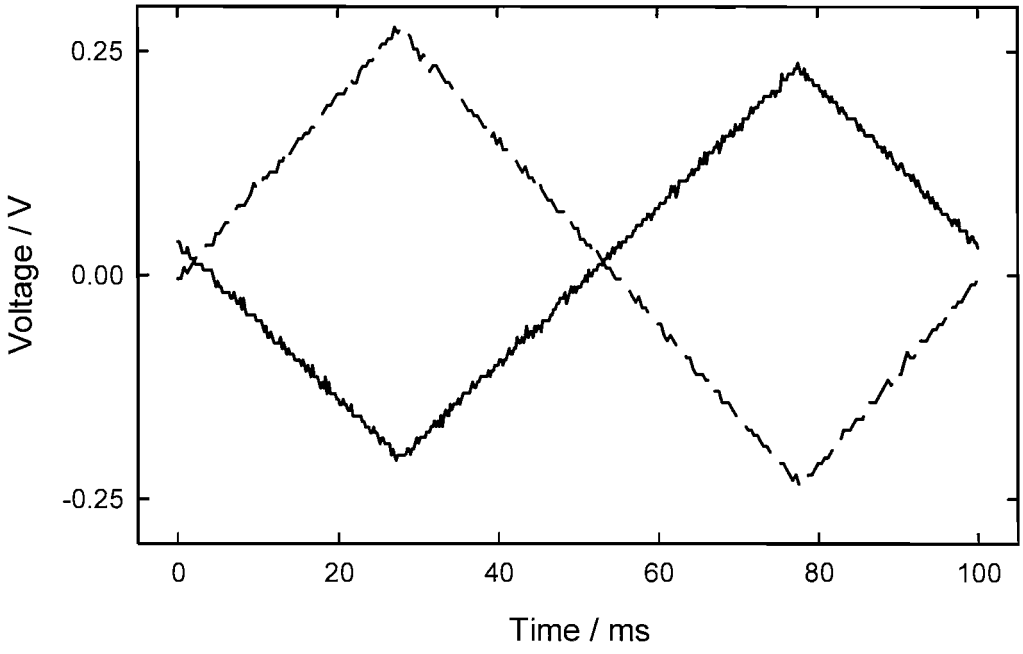

Figure 7.16: Comparison of the input (- - - -) and output (——) signals through the bipolar optocoupled current follower with 330 Hz low pass filter. A 0.01 Hz 0.25 V amplitude triangular wave form passed across a 120 kΩ resistor and through the current follower set to 10^5 gain.

The conformity of the bipolar optocoupled current follower with non optocoupled systems was established by running similar experiments with both a standard current follower and the bi-polar optocoupled current follower and comparing the results. Because the potential of the optocoupled system could not be altered as a function of time and therefore produce a cyclic voltamogram, in order to get a range of currents the pump rate for a flow cell was varied thereby giving different mass transfer coefficients and a corresponding change in the current passed. The two systems are compared in figure 7.17 and can be seen to be in broad agreement.

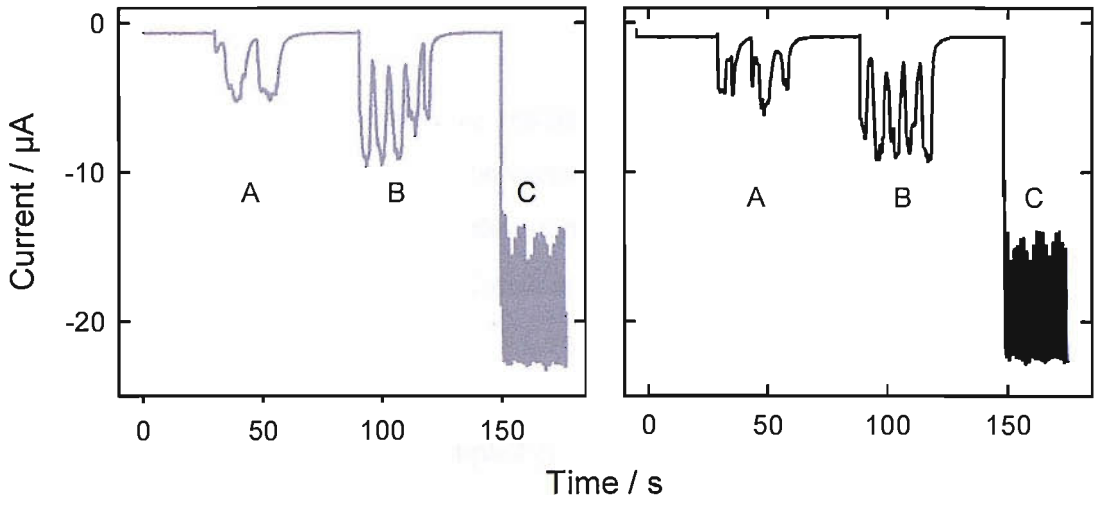

Figure 7.17: Plot showing the variation of currents observed at different flow rates for an undamped peristaltic pump (points A, B and C corresponding to flow rates of 40, 80 and 388 ml hr^{-1} respectively) and demonstrating the correlation between the normal (——) and the bipolar optocoupled (——) current followers. Measurements made using a needle inlet into the three electrode flow cell with a 0.5 mm Pt electrode held at 0 V *vs.* a SCE counter/reference electrode with a solution containing 5 mM $K_3Fe(CN)_6$ and 0.1 M $Sr(NO_3)_2$.

The same experiment conducted in figure 7.17 was repeated in a commercial earthed bath in figure 7.18 to demonstrate the isolating abilities of the optocoupled current follower.

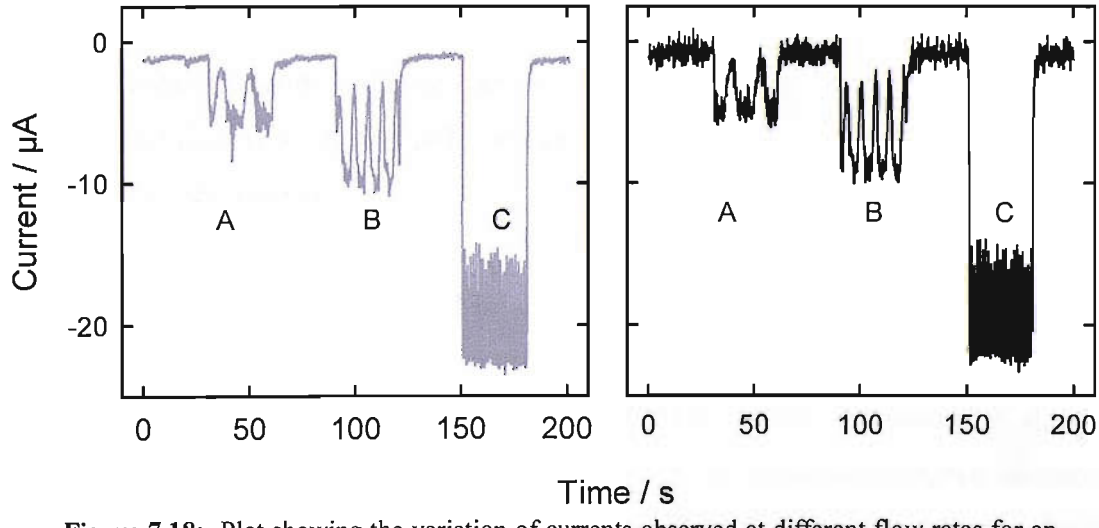

Figure 7.18: Plot showing the variation of currents observed at different flow rates for an undamped peristaltic pump (points A, B and C corresponding to flow rates of 40, 80 and 388 ml hr^{-1} respectively) and demonstrating the reduction in electrical noise seen with the bipolar optocoupled ( ) current follower in comparison to the normal current follower (——) when measurements are carried out in an operating commercial ultrasonic bath (Ultrawave U50, Bath A). Measurements made using a needle inlet into the three electrode flow cell with a 0.5 mm Pt electrode held at 0 V *vs.* a SCE counter/reference electrode with a solution containing 5 mM $K_3Fe(CN)_6$ and 0.1 M $Sr(NO_3)_2$.

Figure 7.18 shows that the optocoupled current follower reduces the electrical noise from the earthed system by two orders of magnitude compared to a standard current follower. The noise recorded for the standard current follower in figure 7.18 does not appear to be prejudicial to the conductance of measurements within the earthed vessel; it should be noted however that currents recorded from the redox couple used ($Fe(CN)_6^{3-}$ to $Fe(CN)_6^{4-}$) are several orders of magnitude greater than those expected from the chemical measurements. Consequently the levels of electrical noise recorded in figure 7.18 are too great for successful measurements to be made necessitating the use of the optocoupled current follower.

7.3.3. Isolation amplifier

The isolation circuits using linear optocouplers are complicated in nature and required a large amount of modification and prototypes before they were of practical use. As one of the aspirations of this project was to create a method of measuring cavitation that was simple and yet affective, an alternative to the use of linear optocouplers was investigated. Specifically a circuit employing a Burr-Brown ISO122 precision Isolation Amplifier was made. The isolation amplifier is a single chip device into which a signal can be fed directly without having to be passed through a series of chips and resistors. The chip then passes the signal digitally across a 2 pF differential capacitive barrier (*186*) isolating one side of the chip from the other. It was hoped that the isolation this offers would be capable of removing the electrical noise seen from the earthed systems.

The isolating amplifier was added to a simple current follower capable of a gain of 10^5 or 10^6 (the gains found to be most relevant to measuring surface events). The circuit (as with the fast optocoupled current follower) was designed such that the working electrode was held at 0 V with respect to the counter/reference electrode. The device was powered by Traco Power TEL2-0523 DC/DC converters; one for the isolated chips and the other for the mains side, each DC/DC converter was powered by its own 9 V pp3 battery. These produced a stable supply voltage of +/- 15 V required to power the isolating amplifier. The circuit diagram can be seen in figure 7.19.

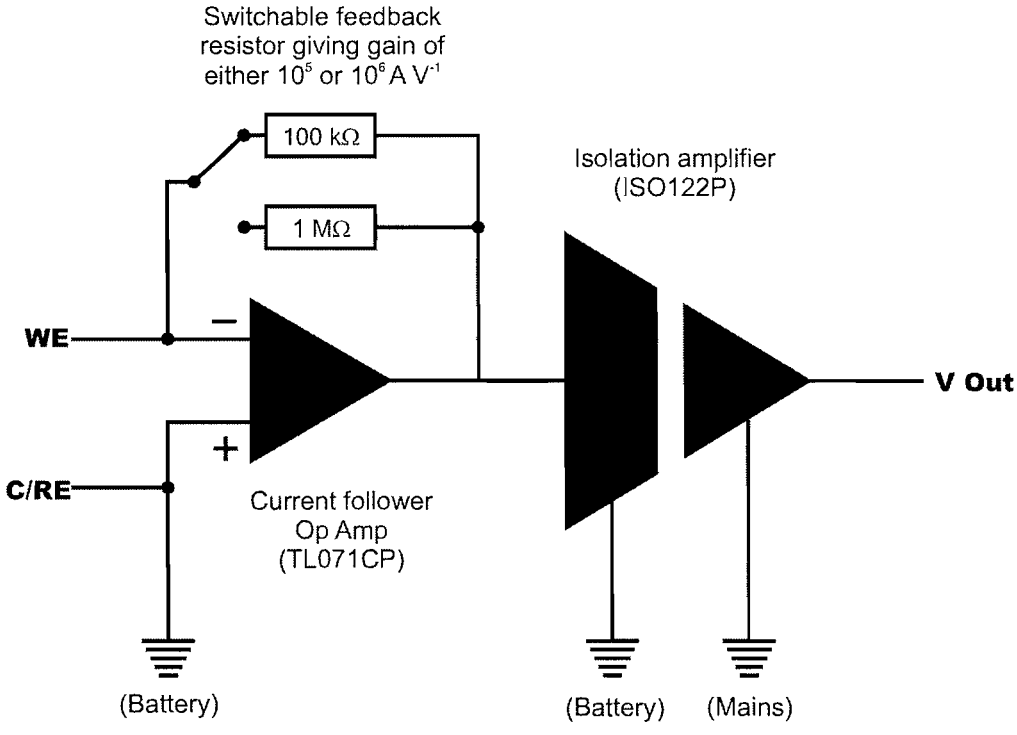

Figure 7.19: Circuit diagram of isolation amplifier based current follower.

The simplicity of the system is appealing with fewer parts in comparison to the optocoupler systems. When used in a commercial bath it was capable of removing the majority of noise as can be seen in figure 7.20. The reduction in noise allowed peaks corresponding to the reformation of the surface of the electrode after an inertial cavitation event to be recorded, such as that marked 1 in figure 7.20 plot (B).

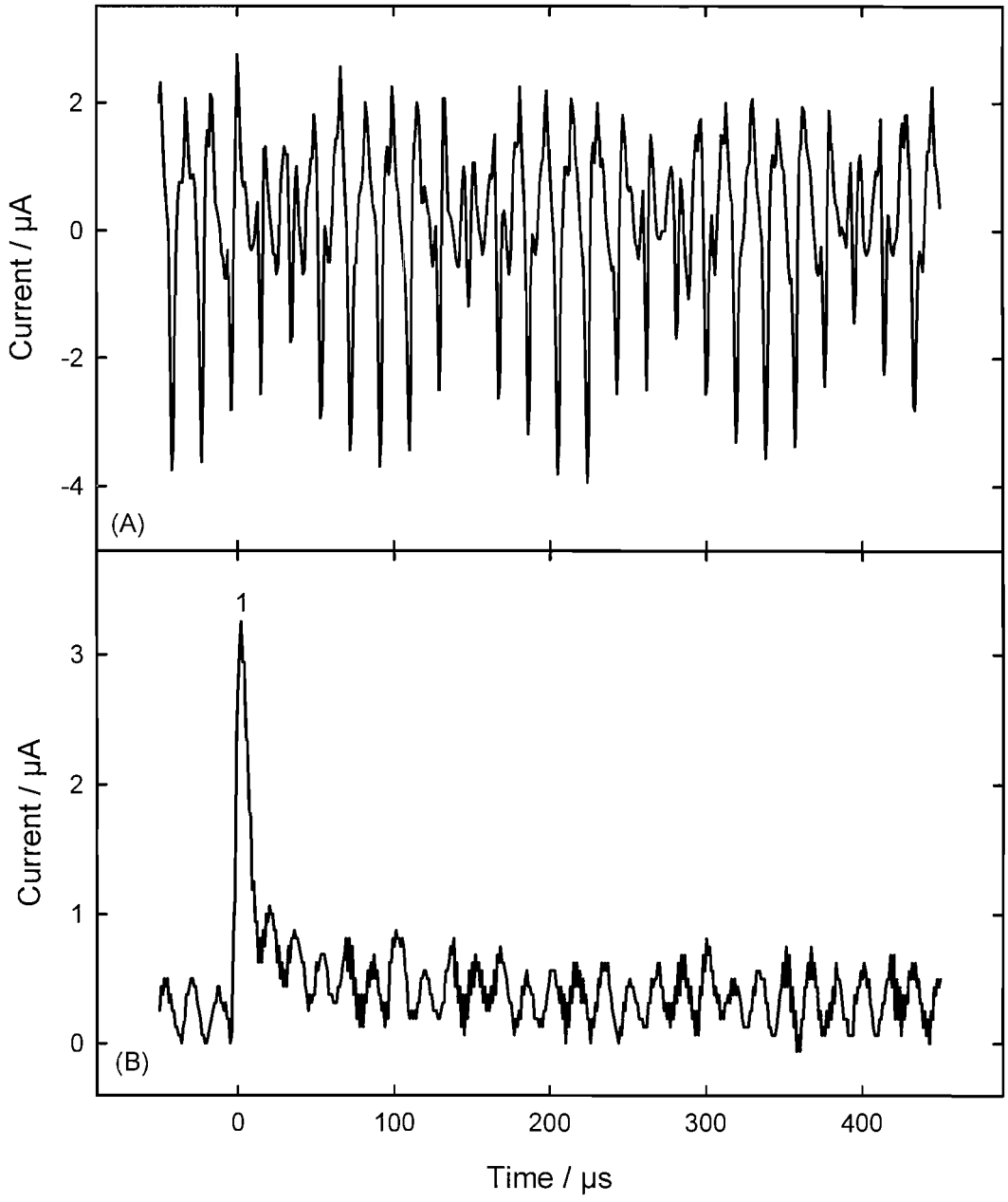

Figure 7.20: Plot comparing the signal recorded from a 250 µm Al electrode held at 0 V vs. Ag counter reference electrode in an operating Ultrawave U50 bath using a normal current follower (A) and the isolation amplifier current follower (B). Bath contained 500 ml of 0.1 M Na_2SO_4 solution.

When the isolation amplifier system was transferred to the NPL vessel the level of electrical noise seen was significantly less than that seen for a standard current follower. In figure 7.21 it can be seen that the standard current follower (trace A) is saturated out by the interference of greater than 5 µA, in contrast the isolation amplifier based current follower (trace B) exhibits a noise signal with an amplitude of only 0.2 µA

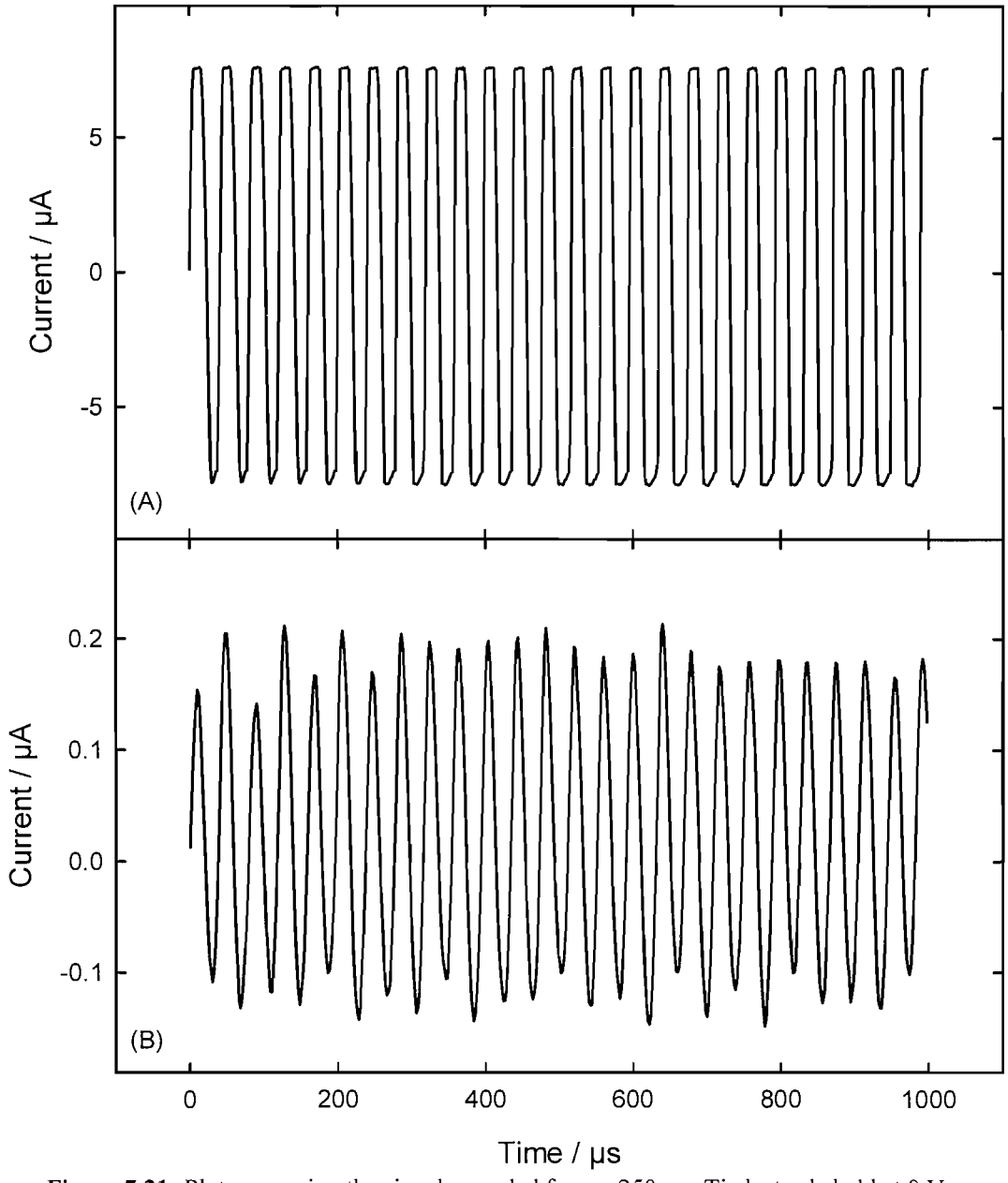

Figure 7.21: Plot comparing the signal recorded from a 250 μm Ti electrode held at 0 V vs. Ag counter reference electrode in the NPL reference vessel operating at 150 W using a normal current follower (A) and the isolation amplifier based current follower (B). Vessel filled with 0.1 M Na_2NO_3 solution. Note: scale (B) is significantly larger than (A)

The surface events recorded in figure 7.13 using the fast unipolar optocoupled current follower only have a magnitude of ~ 1 μA and therefore would be significantly influenced by the level of noise recorded in figure 7.21.

Figures 7.20 and 7.21 demonstrate that the isolation amplifier based current follower is capable of removing the majority of the electrical interference from the earthed vessels. However, the noise recorded is greater than that recorded for the

optocoupoled systems. As a result the current followers using the linear optocoupling systems were preferred.

7.4. Conclusions

When the methods developed for and in the idealised reactors of the laboratory were first transferred to the "real world" situations of a commercial bath and the NPL reference vessel it was thought that overcoming the noise problems seen would be trivial. In reality overcoming these issues resulted in the fabrication of two novel devices that allow both fast and slow measurements to be made in the hostile "real world" environments and the construction of a third less successful device. Though designed specifically for this project the optocoupled current followers have potential applications in many situations where low current measurements are required in electrically noisy environments. Pertinent to this project the development of the two optocoupled current followers (the fast unipolar variant for surface events and the slower bipolar variant for measuring the change in chemistry) allows the full range of electrochemical measurements devised in idealised isolated reactors to be carried out in commercial baths and the NPL reference vessel. The implementation of these experiments and their results will be discussed in the following chapters.

8. Analysis of commercial baths

8.1. Introduction

Ultrasonic cleaning baths are used in many applications. One could assume that objects placed within the bath will be cleaned to the same extent irrespective of at which point within the bath they are positioned. In this chapter we shall investigate this assumption of homogeneity of cavitation activity within commercial baths by systematically scanning and investigating three ultrasonic baths using low light, acoustic pressure measurements, surface erosion/corrosion from cavitation events and cavitation induced chemical change techniques. In addition to these measurements objects representative of items that might be placed within a bath in order to be cleaned are introduced to one of the baths and the effect this has on the cavitation field studied.

Initially we discuss the problems encountered in facilitating the scans before examining the results from the three baths. Finally the effect of the addition of objects to the cavitation field within the bath will be presented.

8.2. Testing of the baths

In total three baths were tested: an Ultrawave U50 bath, a Branson B1210E-MT bath and a Semat bath. These are designated Bath A, B and C respectively. Bath A (the Ultrawave U50 bath) was subjected to the most rigorous examination, having been used extensively in the adaptation and development of the sensing techniques explained in greater detail below. Chemical change measurements as a result of the sonochemical effects of cavitation were only conducted in bath A. The experiments conducted in each bath are detailed in table 8.1.

Measurement		Bath A *(Ultrawave U50)*	Bath B *(Branson B1210E-MT)*	Bath C *(Semat Bath)*
Low light imaging		✓	✓	✓
Photon measurements	counter	✓	✓	✓
Pressure scan		✓ (2)	✓ (1)	✓ (1)
Surface scan		✓ (2)	✓ (1)	✓ (1)
Chemical measurement	change	✓		

Table 8.1: Showing the experiments were conducted on each of the baths examined.

We shall now look at the techniques developed to conduct the measurements.

8.3. Problems presenting themselves with the scanning of the baths

The scanning of commercial baths presented a series of challenges not seen for the idealised cylindrical reactor studied in chapter 6. As previously discussed in chapter 7 the noisy, the earthed environment of the baths resulted in a bespoke electronic circuitry having to be developed in order for the electrochemical measurement of surface erosion/corrosion events and sonochemical activity to take place. In addition the size of the baths necessitated a change in equipment and procedure compared to those employed for the single transducer reactors investigated in chapter 6.

8.3.1. Three dimensional scanning

When scanning reactor 4 in chapter 6 it was possible to make a limited number of measurements in a single plane and assume that this was representative of the entire reactor due to the expected symmetry of both the reactor and the associated sound field(*62, 155*). The field within the commercial baths was found to be non-uniform.

The scanning system developed incorporated a GPIB controlled Parker DigiPlan XYZ stage (ICS Electronics USB-GPIB interface connected to a Parker Digiplan 1185-100 GPIB interface card controlling three Parker CD20 Stepping Motor Drives driving 3 Unislide steppers with a 450 mm travel in each axis) allowing either the entire bath (or specifically a plane within it) to be scanned as a single experiment. Two scanning programs were created; one to measure the acoustic pressure and another to record the number of cavitation erosion/corrosion events on the surface of an electrode. Both programs were developed in visual basic and allowed full XYZ

control of the scan and the measurements. A scanning program was not developed for chemical measurements as it was felt that the ambiguous nature of the spatial resolution of the technique did not warrant the conducting of full scans of the baths (Chapter 3). The orientation of the axes relative to the baths can be seen in figure 8.1.

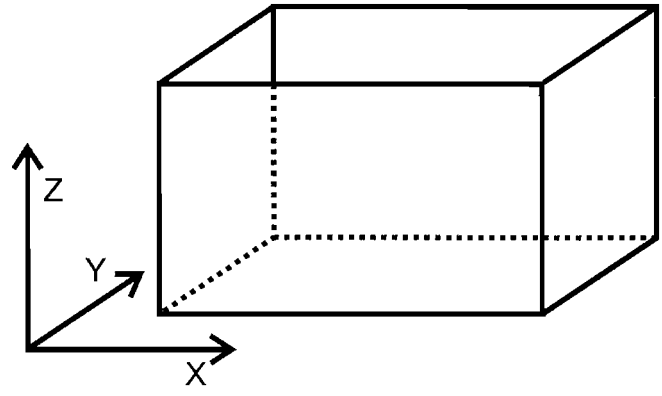

Figure 8.1: Schematic showing the direction of the X, Y and Z axis in relation to the baths

A simple raster system was used to scan each bath employed. This consisted of a series of X axis scans, at the end of each scan the electrode was moved the required increment in the Y direction before being returned to the original X position in a single movement and the next X axis scan initialised. The process was then repeated until the end of the scan was reached. Figure 8.2 shows a schematic of the scan for a 10 X by 4 Y scan.

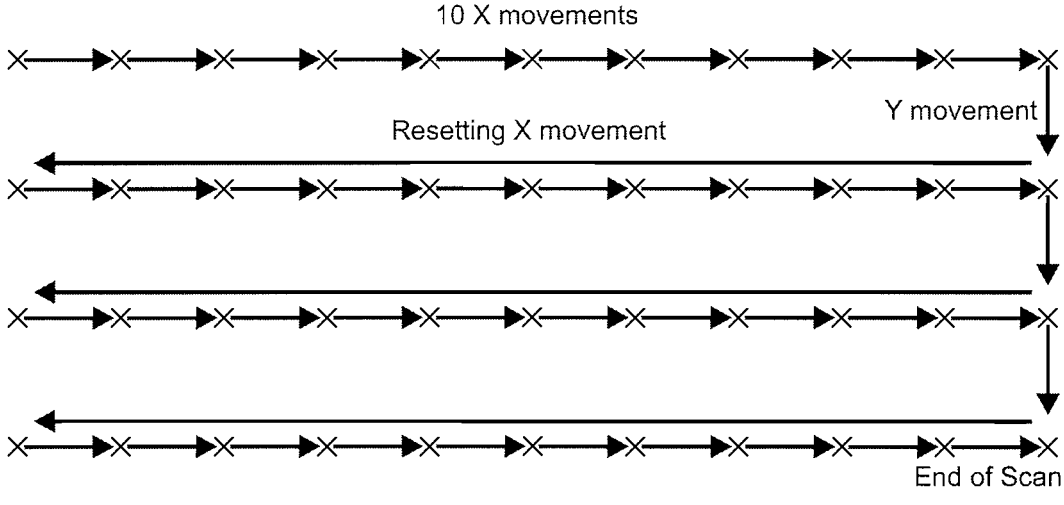

Figure 8.2: Schematic of the raster scans used to conduct XY plane scans of the baths with each measurement represented by X.

Though the system developed was capable of conducting measurements in three dimensions it was only utilised to make scans of single planes within the baths. In Bath A measurements were made in multiple planes as detailed in Table 8.1.

8.3.2. Temperature increase

It is well known that the temperature of a cavitating vessel is likely to increase over a period of extended irradiation(*1*). Associated with this increase in temperature is a change in the speed of sound of the liquid and therefore acoustic characteristics (*1*). To scan even a single plane within a bath takes an extended period of time; for a surface scan anything up to 4 hours. With the bath left in continuous operation for this period of time the temperature of the solution within the bath would increase by approximately 30 °C. Such an increase is unacceptable. Hence a number of alternative techniques (compared to continuous operation) were developed.

8.3.2.1. Direct cooling of the bath

To reduce the temperature increase within the ultrasonic baths a length of 6 mm copper tubing was placed into the bath and water from a water bath maintained at 25°C was pumped through it. The tubing was bent into a U shape and placed at one end of the bath to reduce its interference with the bath.

8.3.2.2. Reduction in the period of sonication

With no direct method of controlling the commercial baths from a computer an indirect method capable of dealing with mains voltages was required. Therefore a radio controlled mains socket system (Brennen Stuhl FE433) was modified by means of a relay chip such that it could be switched remotely using TTL pulses from an ADC card in a computer. Details and a circuit diagram of the device can be found in appendix B. The modified remote switching socket allowed the turning on and off of the commercial baths in the same way that it had been possible for the reactors. The remote switching and cooling system reduced the temperature rise during a four hour scan to less than 5 °C.

8.3.3. Light emission measurements

To acquire MBSL images of the baths the Photek image intensifier based camera was mounted vertically above the baths. The camera was positioned such that the entirety of the bath was within the image. The MBSL images provide a spatial indication as to the relative levels of light emission originating from the bath. Quantitative measurements were made using the SensL PCMPlus 20 single photon counting module mounted centrally 300 mm above the bath. It was necessary to increase the level of light emitted for some experiments, to achieve this a solution containing luminol was added to the bath which produced chemiluminescent (MBS(C)L) light emission in addition to the MBSL light emission; amplifying the emission (*62, 123, 127, 155*).

The level of MBSL light emission recorded from the commercial baths was significantly greater than would be expected given the low light images recorded at the same time. For completeness the MBSL photon counter measurements are included for bath A only but the MBS(C)L measurements are considered more accurate.

8.3.4. Pressure scans

A Gras Type 10CT Hydrophone was connected to a Brüel & Kjaer 2635 charge amplifier and attached to the XYZ positioning system by means of a 10 cm plastic tube held in a clamp. This allowed the hydrophone to be positioned anywhere within the bath. The signal from the charge amplifier was recorded using a computer based ADC card (Measurement Computing PCI-DAS 4020/12) and bespoke Microsoft Visual Basic based acquisition software which also controlled the positioning stage. Figure 8.3 shows a typical pressure time trace acquired within bath A. It should be noted that the pressure activity is chopped "on/off" at a frequency of 50 Hz.

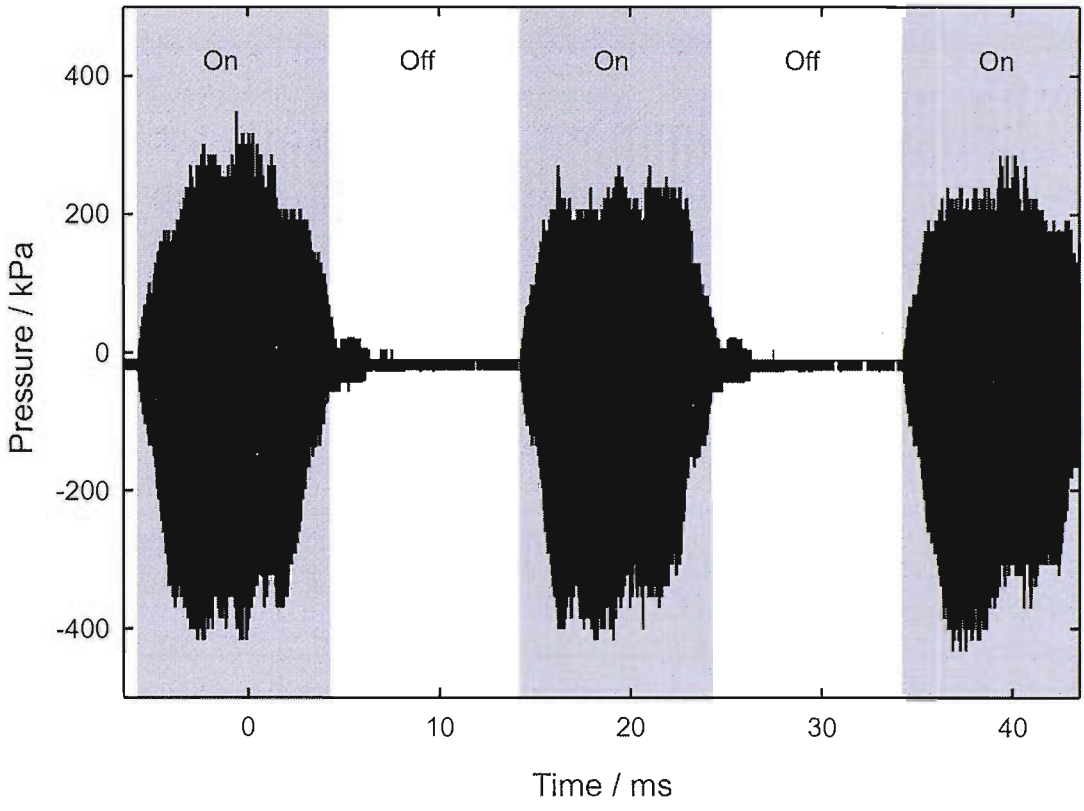

Figure 8.3: Plot showing the pressure as a function of time in bath A. The bursting on and off of the sound field within the bath can clearly be seen. Recorded centrally in bath A with 0.5 dm^3 0.1 M Na_2SO_4 solution at 25 °C.

The variation in the pressure output over time seen in figure 8.3 precluded the use of the measurement routine used for reactor 4 in chapter 6. In the continuously driven reactor it was possible to take a brief snap shot over a period of 2 ms and assume that the pressure was representative. When the same procedure was used in the baths some points fell within the time frame of the bath bursting "on" and others when it was "off" leading to a large variation in the pressure measurements for adjacent points. Figure 8.4 is a case in point showing the pressure traces from two successive points. For the first point it can be seen that the measurement was taken during a period of activity; conversely for the second point the bath was in a period of inactivity and consequently the pressure recorded is effectively zero. By increasing the period of time over which data was collected from 2 ms to 20 ms the complete sound cycle of the bath could be recorded ensuring that the pressure recorded was representative.

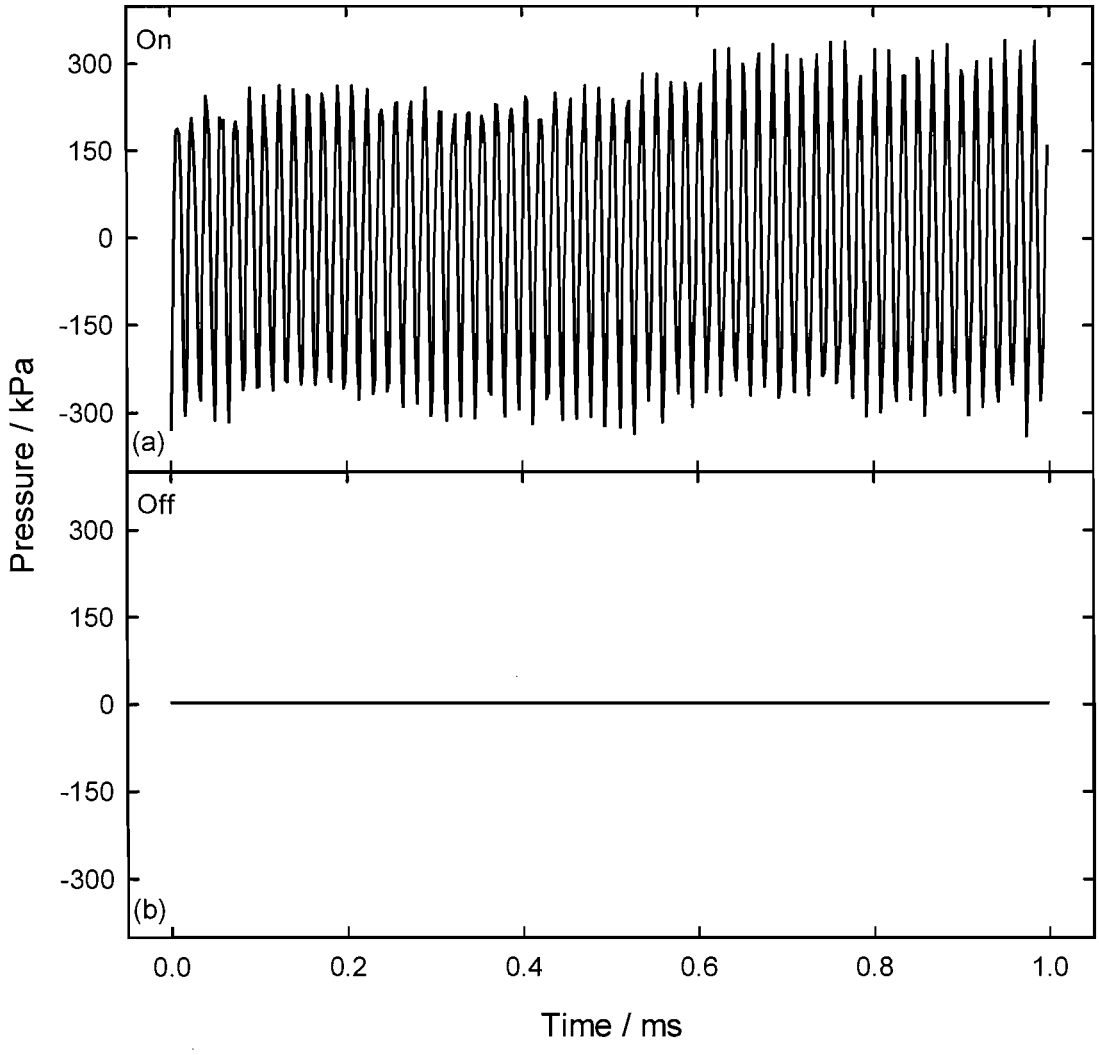

Figure 8.4: Plot of two successive pressure-time traces recorded in bath A as part of a scan of the bath. 5 mm separated the location of the two measurements, demonstrating the need for an extended period of data collection. Trace (a) corresponds to a time at which the sound field had burst on and trace (b) corresponds to a time when the sound field had burst off. Bath A contained 500 ml 0.1 M Na_2SO_4 solution at 25 °C.

8.3.5. Surface scans

The conditions within the ultrasonic baths studied were such that it was decided to use aluminium electrodes to measure erosion/corrosion events in this environment. A stainless steel electrode was used to act as the counter/reference electrode and was strapped to the glass support of the working electrode to maintain the same level of separation through out the experiment. The working electrode was maintained at 0 V *vs.* the counter/reference electrode. Both electrodes were held in a small spring loaded clamp that was attached to the positioning system by a boss connected to a rod held vertically in the positioning system clamp.

The signal from the working electrode was amplified and isolated using the fast optocoupled current follower described in chapter 7. An Amptek Pocket MCA 8000A Multi Channel Analyser (MCA) was used to record the number and magnitude of the events and a LeCroy 9310 AM digital oscilloscope used to monitor the signal. The MCA and positioning system were controlled using a visual basic program. By using the optocoupled current follower it was possible to record surface events on the working electrode, such as peak A in figure 8.5, which would not have been possible with a standard current follower due to the interference caused by the metal vessel.

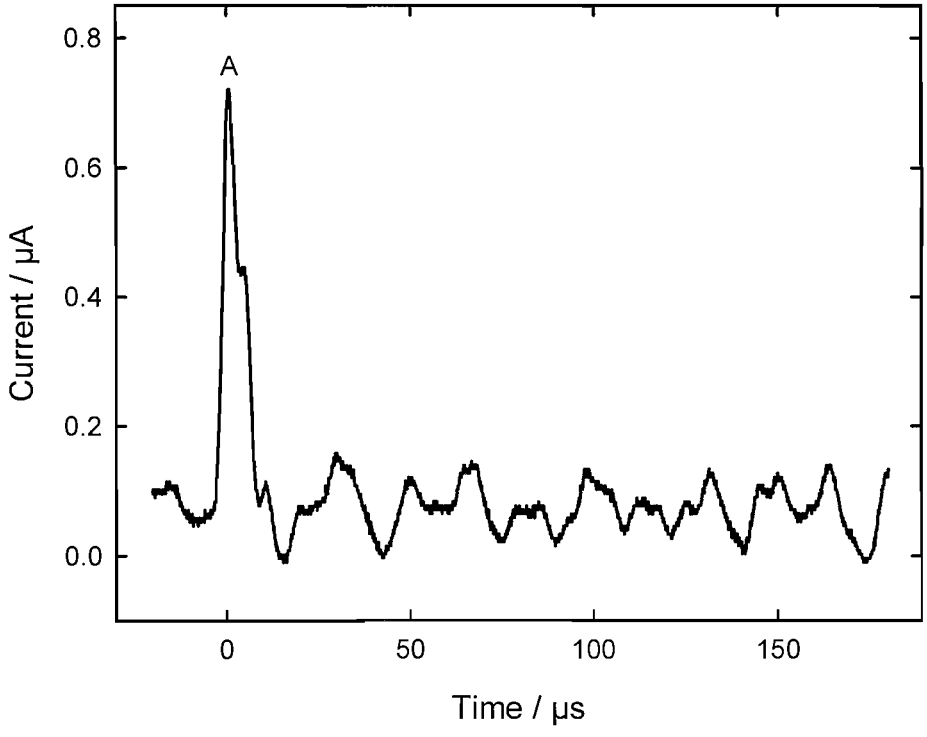

Figure 8.5: Plot showing an example surface erosion/corrosion event recorded on a 250 μm aluminium electrode in bath A. The working electrode was held at 0 V vs. a stainless steel counter/reference electrode in 500 ml 0.1 M Na_2SO_4 solution at 25 °C.

It should be noted that the events seen from the optocoupled current follower, like peak A in figure 8.5, are broader and less sharp than those seen from the standard current follower. This is caused by the reduced bandwidth of the optocoupling chip as described in chapter 7.

8.3.6. Sonochemical Measurements

Unlike the pressure and surface erosion/corrosion measurements the evaluation of the sonochemical activity of the solution as a result of the cavitation were shown to have a poor spatial variation in idealised reactors (Chapter 3). Consequently instead of scanning the entirety of the bath a series of spot measurements were carried out in Bath A (the only bath for which chemical measurements were conducted). As with the measurements carried out in chapters 3 and 6 the Weissler reaction was employed following the formation of I_3^- induced by the cavitation. Similarly the experiments were conducted using a three electrode flow cell with "soft damping" and a flow rate of 380 ml hr^{-1}, consequently from the recorded current it was possible to determine the concentration of the chosen dosimeter within the solution from the calibration carried out in section 3.3 of chapter 3 and the graph in figure 3.7. Given that the measurements were being conducted in the earthed environment of the industrial bath it was necessary to make use of the bipolar opotocoupled current follower developed and characterised in chapter 7. The results the techniques employed recorded in each bath are now presented, starting with bath A.

8.4. Bath A (Ultrawave U50)

Bath A was the smallest of the ultrasonic baths tested having a volume of ~0.5 dm^3 with internal dimensions of 150 x 85 x 65 mm. Figure 8.6 shows a schematic of the bath, as viewed from above, showing the coverage of the different techniques applied. All the results reported for this bath are orientated in the same manner as figure 8.6.

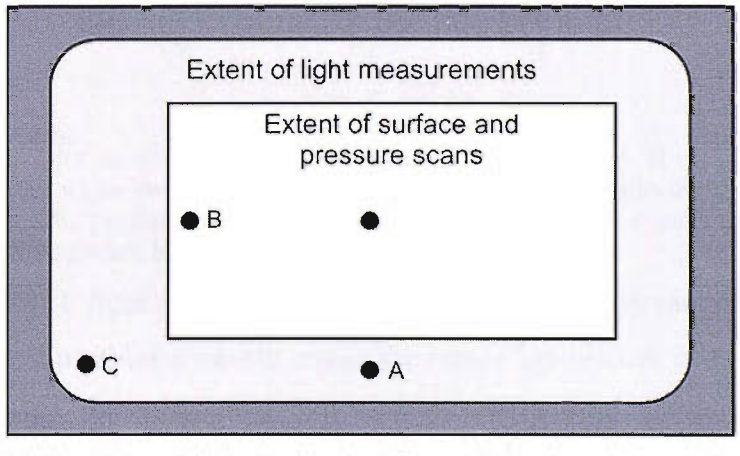

Figure 8.6: Plan view of bath A showing the extent and position of the low light measurements (light grey rectangle), the pressure and surface scans (white rectangle) and the positions at which chemical measurements were made (represented by •)

8.4.1. Light measurements

Intensified images and photon counting measurements of bath A were made using either a sodium sulphate solution or a luminol solution giving multi-bubble sonoluminescence and multi-bubble sonochemical luminescence respectively.

8.4.1.1. Sonoluminescent measurements

The MBSL light emission from Bath A was found to be approximately 300 counts s^{-1} with a background of ~ 6 counts s^{-1}. Figure 8.7 shows the output from the photon counter as it was repeatedly switched on (areas marked A) and off (areas marked B).

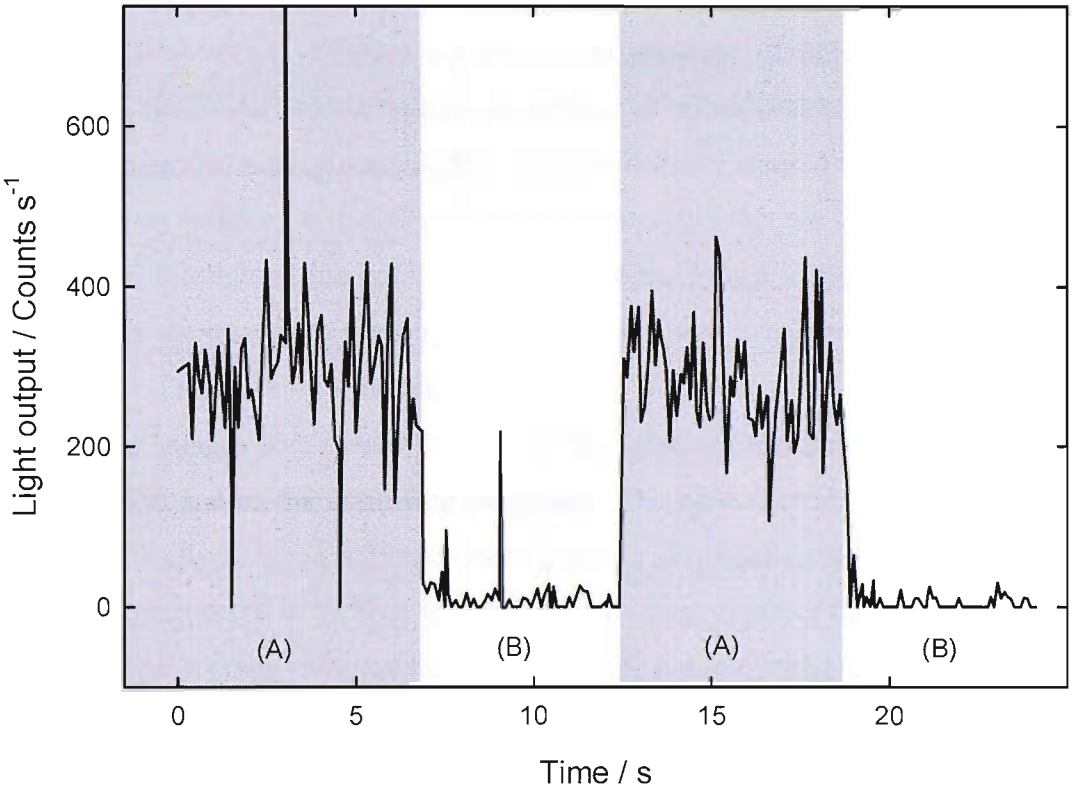

Figure 8.7: Plot showing the MBSL light emission from bath A as recorded by the photon counter whilst the bath was in operation (marked A) and whilst the bath was idle (marked B). The photon counter was mounted 30 cm above bath A containing 500 ml 0.1 M Na_2SO_4 solution; background 7 counts s^{-1}.

Although the MBSL light emission from the bath as detected by the photon counter is relatively high, to produce a usable image the image intensifiers were required to be at maximum gain. As consequence the images have a large amount of noise even after stacking and averaging (see figure 8.8).

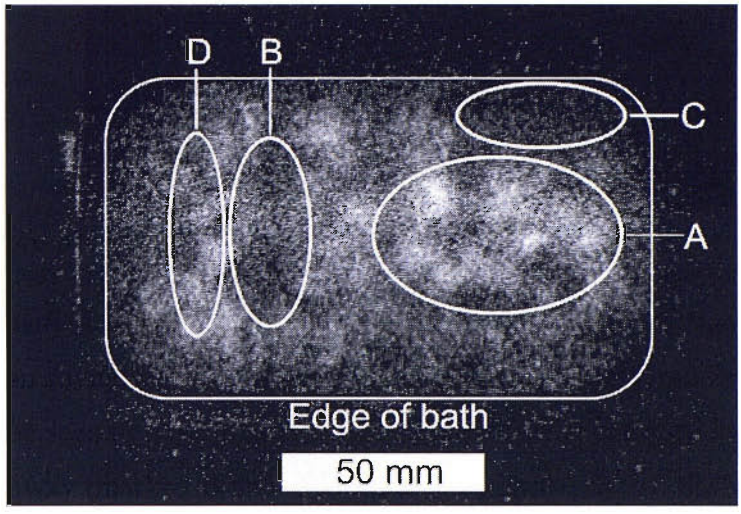

Figure 8.8: Image of MBSL produced from bath A made up of 101 stacked and averaged images. The bath contained 0.5 dm^3 of 0.1 M Na_2SO_4 solution.

The intensified image in figure 8.8 shows the presence of light emission (and by association cavitation) within bath A. A number of points (marked A and D in figure 8.8) can be seen to have greater MBSL light emission compared to those only a short distance away (marked B and C in figure 8.8) implying that the level of cavitation is not uniform throughout the bath. The clarity of the image in figure 8.8 is less than that seen for the images of the single transducer reactors in chapter 6 due to a number of factors. The lack of a stable mode within the reactor reduces the effect that stacking the images has; in addition the metal surface of the bath causes the emitted light to reflect and scatter confusing the image. The wide aperture used to acquire the images (typically f0.95 on a 25 mm lens) lead to a very shallow depth of field and, as cavitation is expected to be seen through out the entire depth of the bath, some of the light emission is going to be recorded out of focus; reducing the clarity of the image.

8.4.1.2. Sonochemiluminescent measurements

Though figure 8.8 gives an indication of the presence of areas of varying light output the low level of light emission and consequent high amplification employed make the images noisy and more difficult to interpret. Replacing the sodium sulphate solution used in figure 8.8 with a solution containing luminol the light emission from the bath was increased through the presence of sonochemical luminescence in addition to sonoluminescence. Consequently a lower gain on the amplifier was required to generate suitable images. The addition of the luminol solution increased the light emission from the bath, as measured using the photon counter, to 1260 counts s^{-1}.

Obviously the change in composition of the solution will result in some changes to the field within the bath; compared to the single transducer reactor examined in chapter 6 the field within the bath is less ordered and not forming standing wave modes and therefore the benefit gained from the increase in light emission is greater than any detrimental effect the change of solution might have.

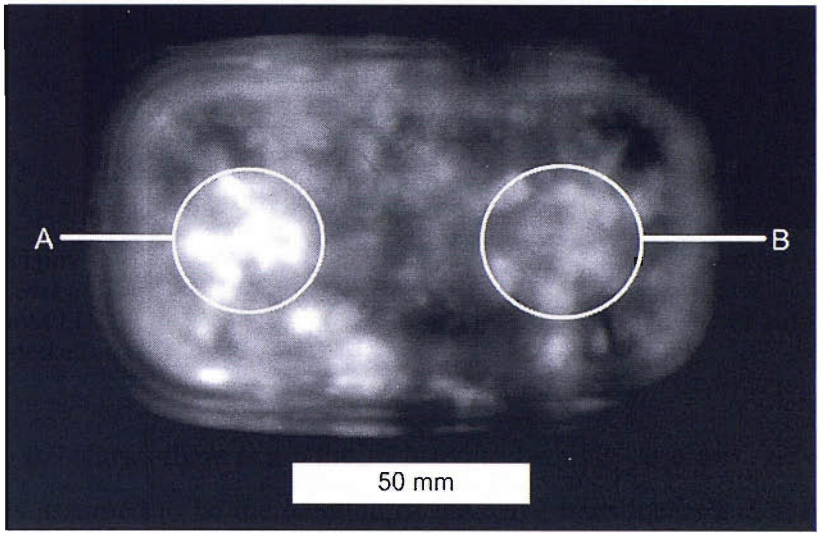

Figure 8.9: Intensified image of bath A containing a luminol solution to increase the level of light emission. The bath contained 0.5 dm^3 of a solution of 0.1 M Na_2CO_2, 0.1 mM EDTA and 5 μM luminol and the image is constructed from 100 individual images stacked and averaged together.

Figure 8.9 shows there is a point of increased activity at either end of the bath (over what is assumed to be the location of the drive transducers and marked A and B in figure 8.9). In addition to the factors causing the lack of clarity for the MBSL image in figure 8.8 (lack of stable mode, small depth of field and scattering from the baths internal surface) the precision of the image in figure 8.9 is reduced by the luminescence from the luminol solution persisting beyond the period under which it is subjected to cavitation; resulting in a level of "smearing" of the luminescence beyond the actual location of the cavitation.

If instead of looking at an amalgamated image (such as that in figure 8.9) we look at a series of images of the bath over a period of time and compare them to an average image it is possible to more clearly see how the position of the light emission within the bath varies over time. Figure 8.10 shows eight images recorded at 1 second intervals next to calculated images showing the difference of image from the average. Where the recorded image (1-8a) shows a greater level of light emission than the

average image (9) the calculated image (1-8b) is black; where the level of light emission is less the calculated image is white and where there is no change the image is grey.

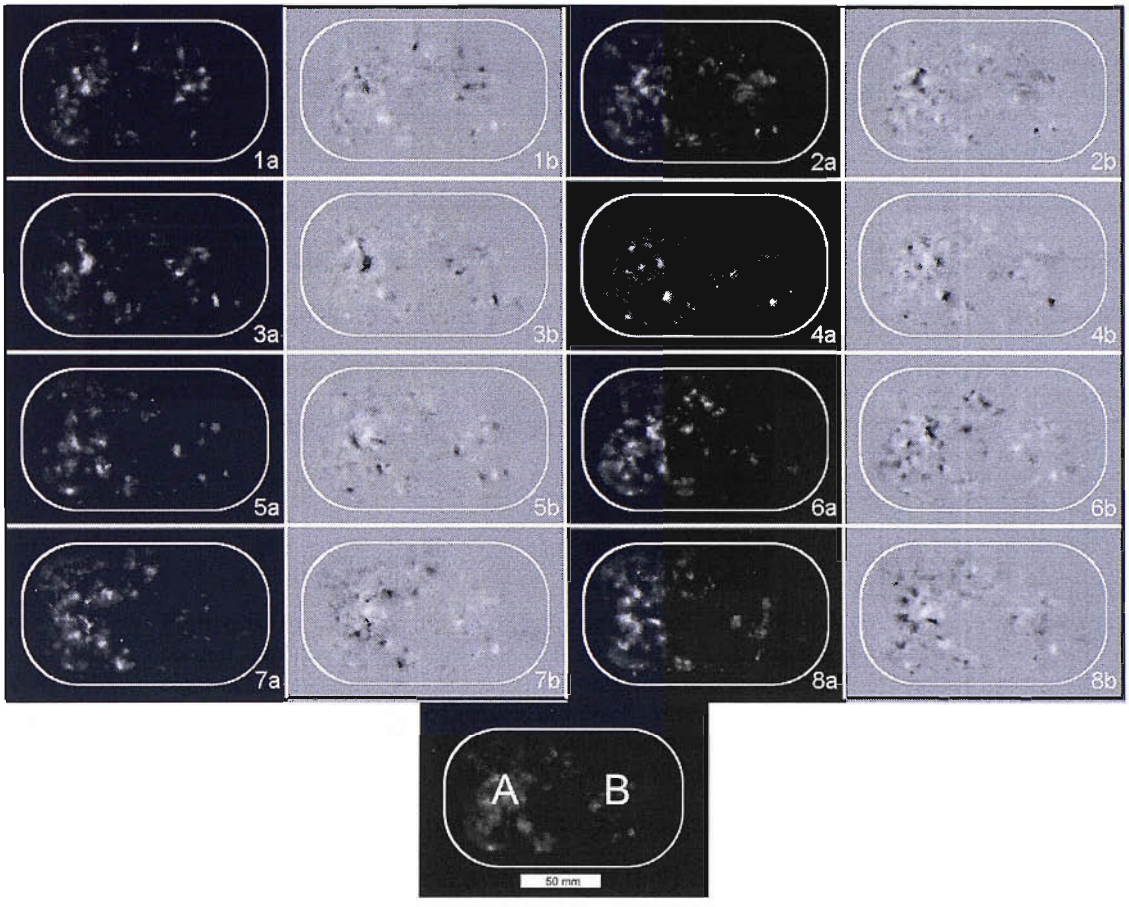

Figure 8.10: Shows a series of eight individual intensified images (1-8a) taken at 1 second intervals of the light emission from bath A containing a luminol solution and eight accompanying images (1-8b) showing their difference from the average image (9). Areas where the calculated images are black correspond to an increase in light emission compared to the average, white a decrease and grey no change. The bath was filled with 500 ml of a solution of 0.1 M Na2CO2, 0.1 mM EDTA and 5 μM luminol.

Figure 8.10 shows that though there are two significant areas of light emission within the bath (marked A and B on average image 9) that can be seen to be present in every one of the images the detail within these broad areas changes between each successive frame. Area A also appears to have a greater level of variation in activity compared to area B. This variation in the light emission from the bath as a function of time, and consequently the cavitation field, is likely to have an effect on the other measurements conducted on the bath in particular the pressure measurements which were conducted over a short period of time and as a consequence more susceptible to variations in activity.

8.4.2. Pressure Measurements

The size of the Gras Type 10CT hydrophone employed limited the vertical resolution in the bath. Consequently two planes within the bath were scanned; one at the base and one just below the surface of the bath. Figure 8.3 has shown that the sound field of bath A bursts in a 20 ms cycle, if we look at a Fast Fourier Transform of the pressure time trace in figure 8.11 it is possible to see a series of peaks corresponding to the fundamental frequency of the bath (60 kHz, X in figure 8.11) and a number of sub-harmonics. The short period pressure time trace in figure 8.11A elucidates a similar figure for the drive frequency of the bath. Between points 1 and 2 there are 17 μs corresponding to a frequency of 59 kHz.

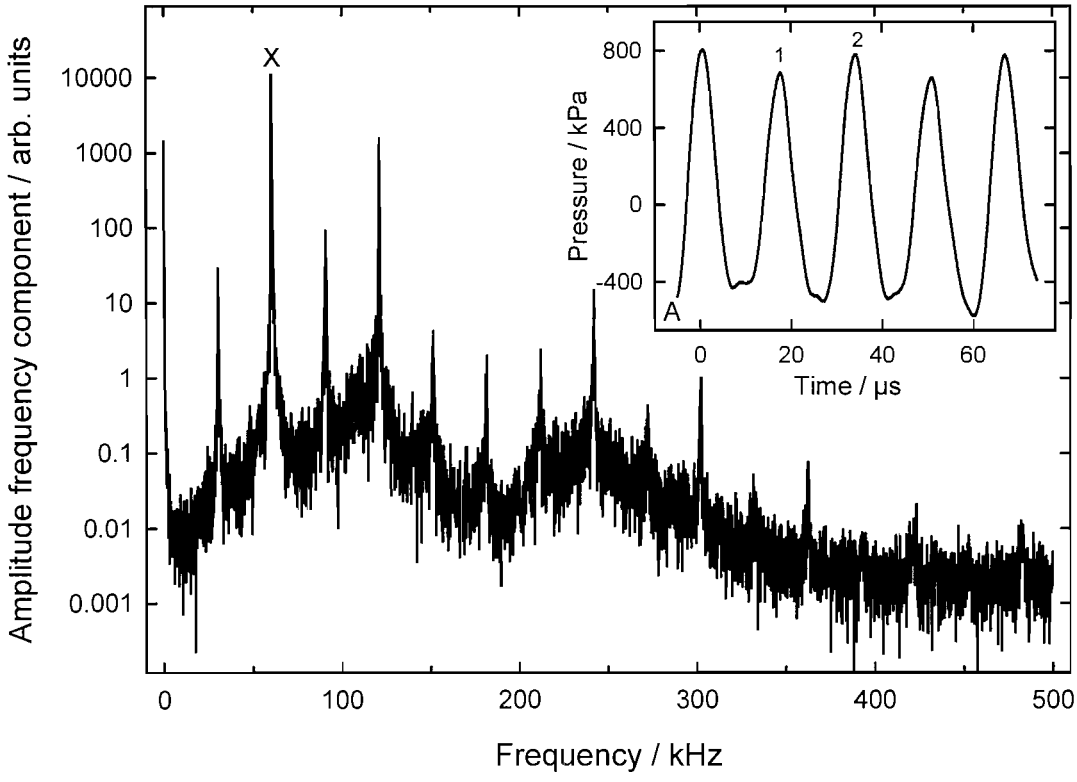

Figure 8.11: Plots showing the FFT pressure signal and direct pressure signal (insert A) from bath A. Recorded in 500 ml 0.1 M Na_2SO_4 solution.

In figure 8.11A (recorded on an oscilloscope) the positive pressure reaches a maximum of 800 kPa this corresponds to a voltage of 8 V from the charge amplifier‡. The ACD card used for the automated collection of data in the pressure scanning

‡ Without the use of the charge amplifier the direct signal from the hydrophone would be of the order of 80 V. The Charge amplifier was set to its lowest sensitivity setting to reduce the measured voltage to the greatest possible extent. It would have been theoretically possible to make use of a voltage divider to reduce the voltages recorded further but such equipment was not readily available.

program was only capable of measuring +/- 5 V. Any voltage that is greater than 5 V is recorded as being 5 V by the ADC card clipping the signal. The affect on the signal can be seen in the trace in figure 8.12 where signal from the hydrophone is clipped at both plus and minus 5 V (areas shaded dark grey).

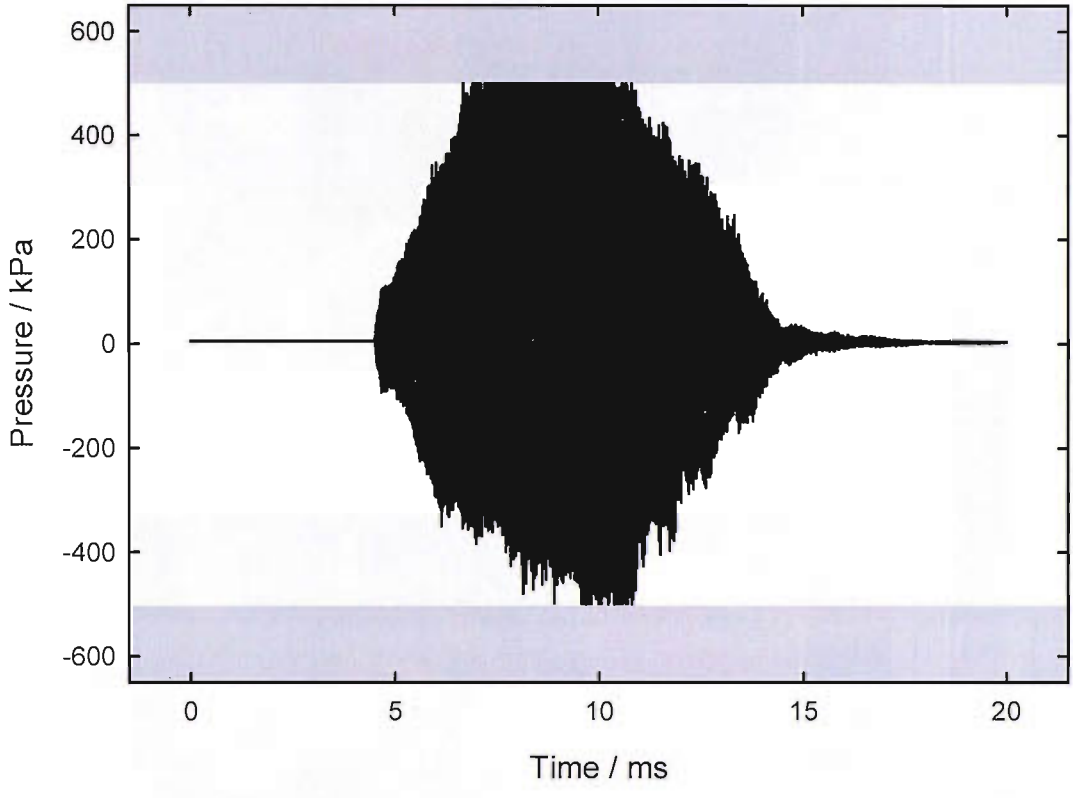

Figure 8.12: Plot showing the pressure time trace as recorded by the ADC card used for the pressure scans. The clipping of the signal at +/- 5 V can be clearly seen.

The methodology employed to calculate the pressure within reactor 4 in chapter 6 relied on identifying the maximum and minimum pressures and halving the difference between them; giving an effective zero to peak pressure amplitude. The clipping of the signal seen in figure 8.12 resulted in many points having recorded pressure amplitudes of 500 kPa.

The two planes within the bath that were scanned using the hydrophone produced decidedly different pressure contour maps. As can be seen in figure 8.13 in general the pressure recorded at the top of the bath (map B) is greater than that recorded lower in the bath (map A). There is also a marked variation in the location of the regions of high pressure between the two planes; at the top of the bath there is a large central region of saturated high pressure, where as lower in the bath the regions of higher pressure are concentrated towards the edges of the bath. The high number of

points in the scan near the surface of the bath for which the pressure measurement has saturated out (figure 8.13, map B) precludes any examination of the field in more detail.

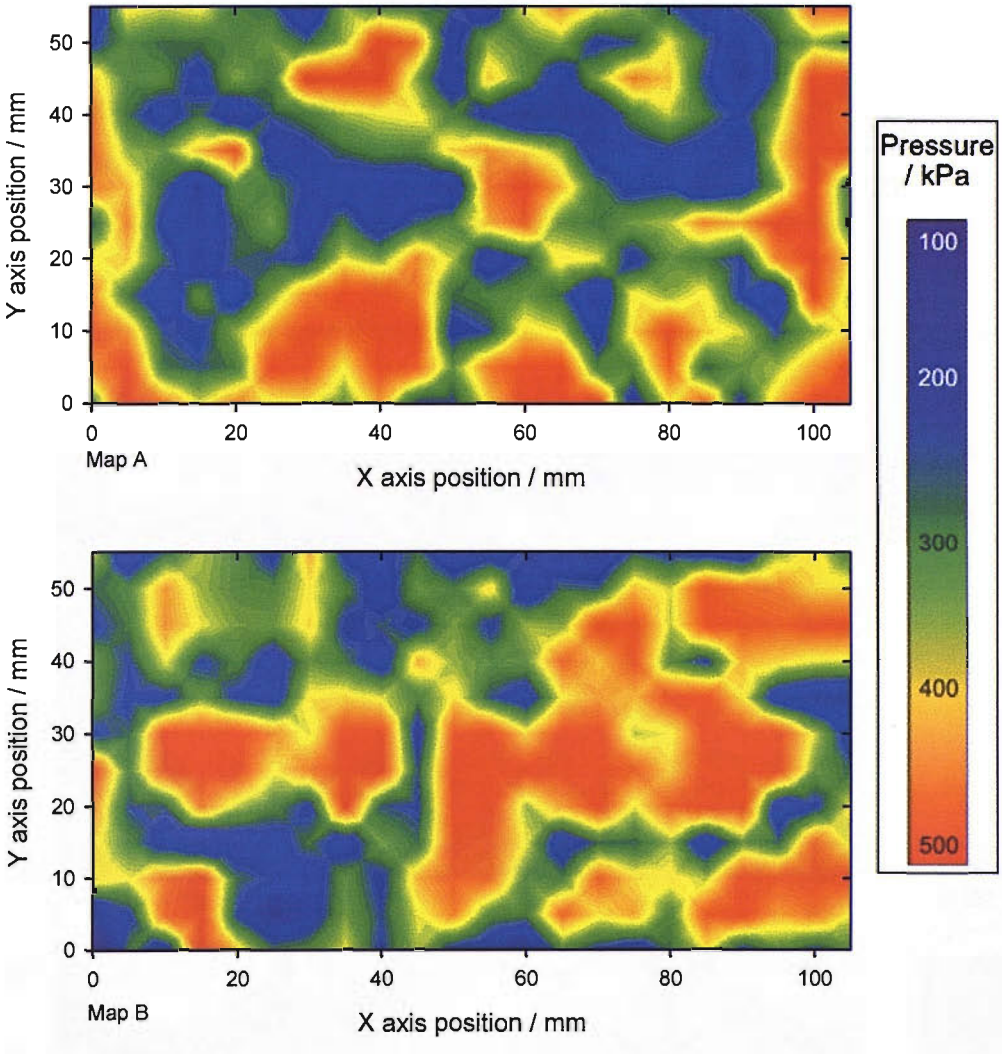

Figure 8.13: Contour maps of bath A showing the amplitudal pressure at the base and surface of bath A (Maps A and B respectively). The hydrophone was scanned over an area 105 by 55 mm at a resolution of 5 mm in 500 ml of 0.1 M Na_2SO_4.

8.4.3. Surface measurements

The electrode used for the surface erosion/corrosion event measurements was small in comparison to the size of the active element of the hydrophone. This would have allowed more planes to have been scanned within the bath but in order to be able to make valid comparisons the same two planes were examined. Similarly, though the electrode was smaller than the hydrophone, the dimensions of each scan were kept constant to allow a better comparison between the two sets of measurements and to reduce the length of time during which the electrode was exposed to the inertial

cavitation (degradation of the electrode having been seen in chapter 4 to lead to a change in its behaviour).

For the pressure scan at every point, even those at which no cavitation was present, a pressure could be recorded. In contrast the surface erosion/corrosion event scans (like those conducted in reactor 4) contained a large number of points at which no surface events were recorded as a result of the conditions not being conducive to inertial cavitation surface events. When the conditions surrounding the electrode were correct for surface events then transients similar to that seen in figure 8.5 were observed. These were counted as a function of position, using the MCA, and the results plotted as contour maps as in figure 8.14.

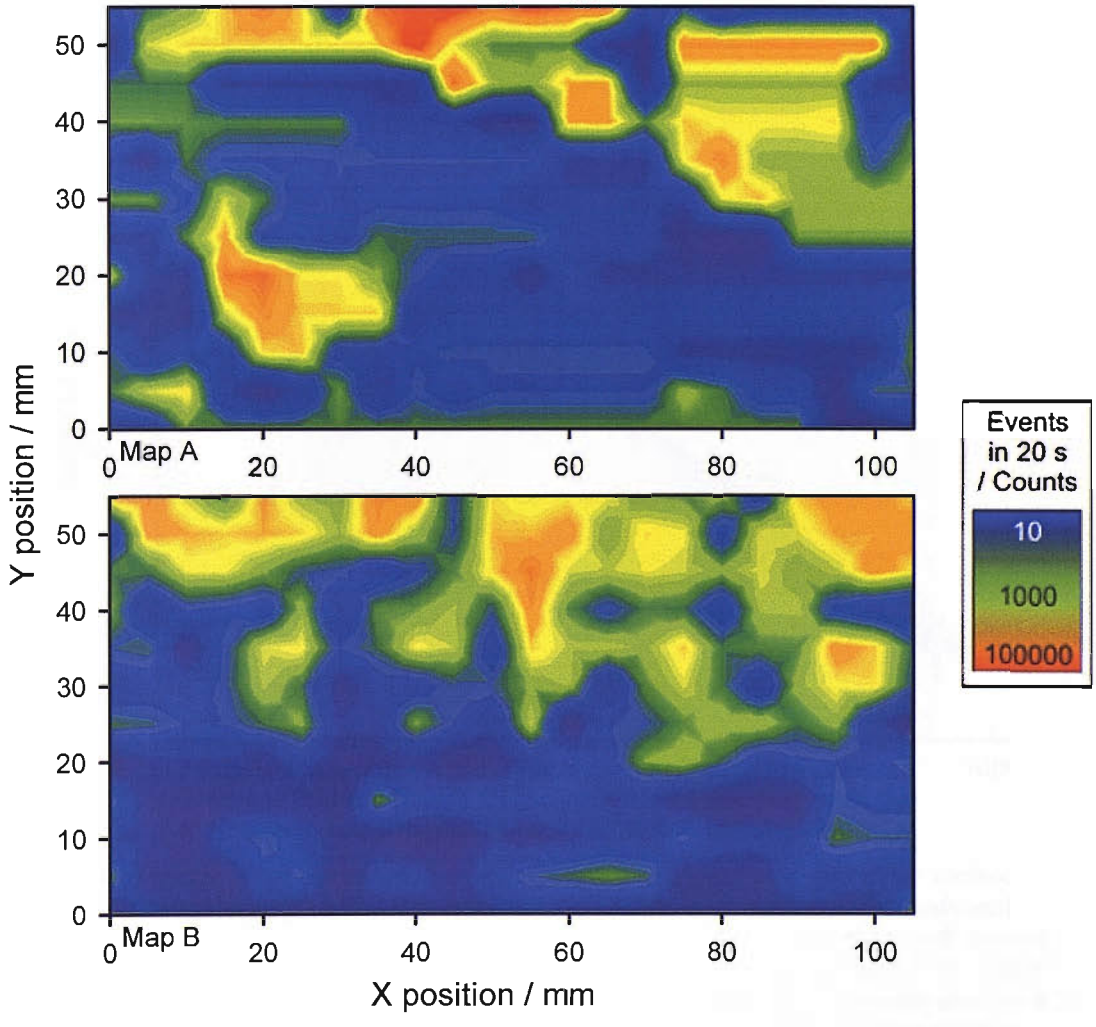

Figure 8.14: Contour maps showing the distribution of surface erosion/corrosion events at the top and base (maps A and B respectively) of bath A. Events recorded on a 250 μm Al electrode held at 0 V vs. a SS counter/reference electrode using the MCA collecting over 20 seconds with a threshold of 0.5 μA. Bath A contained 500 ml of 0.1 M Na_2SO_4.

The contour maps of the surface activity at the top and bottom of bath A in figure 8.14 show how the areas at which there is increased levels of cavitation activity vary as a function of position in three dimensions. In both the map relating to the scan conducted near to the surface of the bath and that carried out near to the base of the bath there is a clear bias to the presence of surface event activity toward the top of the map, near to the edge of the bath.

8.4.4. Chemical measurements

As explained earlier in this chapter it was felt unnecessary to attempt to conduct a series scans of the bath using the chemical change apparatus. Instead a measurement in the centre of the bath as well as a series of spot measurements located around the bath were carried out to confirm that the rate of chemical change recorded was similar throughout the bath.

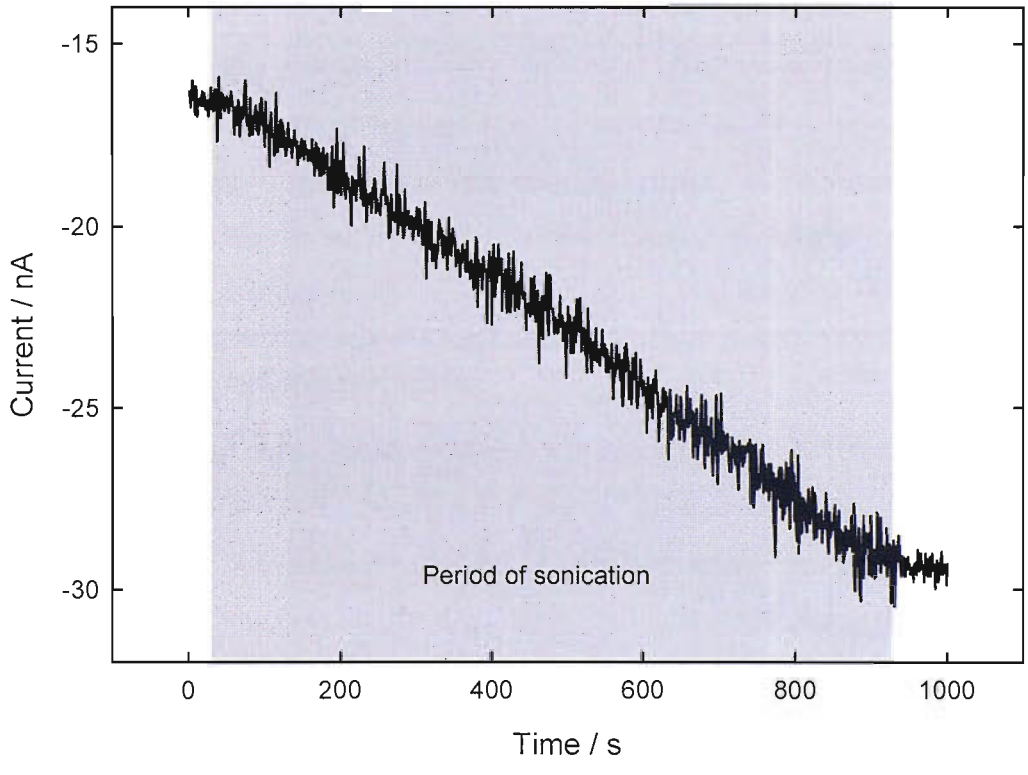

Figure 8.15: Plot of current as a function of time using a chemical tracer method to detect sonochemical effects of cavitation within bath A over a 900 s period (indicated by the grey shaded area). Recorded with the electrochemical flow cell with the soft damped peristaltic pump at 388 ml hr^{-1}. A 0.5 mm diameter Pt electrode held at 0 V *vs.* a SCE counter/reference electrode was used to monitor the change in I_3^- concentration as a function of time. The bath contained 0.5 dm^3 90 mM KCl 10 mM KI aqueous solution.

Figure 8.15 shows the current time trace from the central point within bath A. The area shaded grey corresponds to the period during which the bath was operational for (900 s) during which the current proceeds cathodically. This is due to the

sonochemical oxidation of I^- to produce I_3^-. By measuring the gradient of the current time trace the rate of chemical change taking place within the bath can be calculated to be 1.3 nM s^{-1} of I_3^-. Three further measurements were made at different points within the bath to see if any variation in the rate of cavitation induced chemical change could be found. Figure 8.6 shows the location of the three points A, B and C. Figure 8.16 shows the respective current time traces.

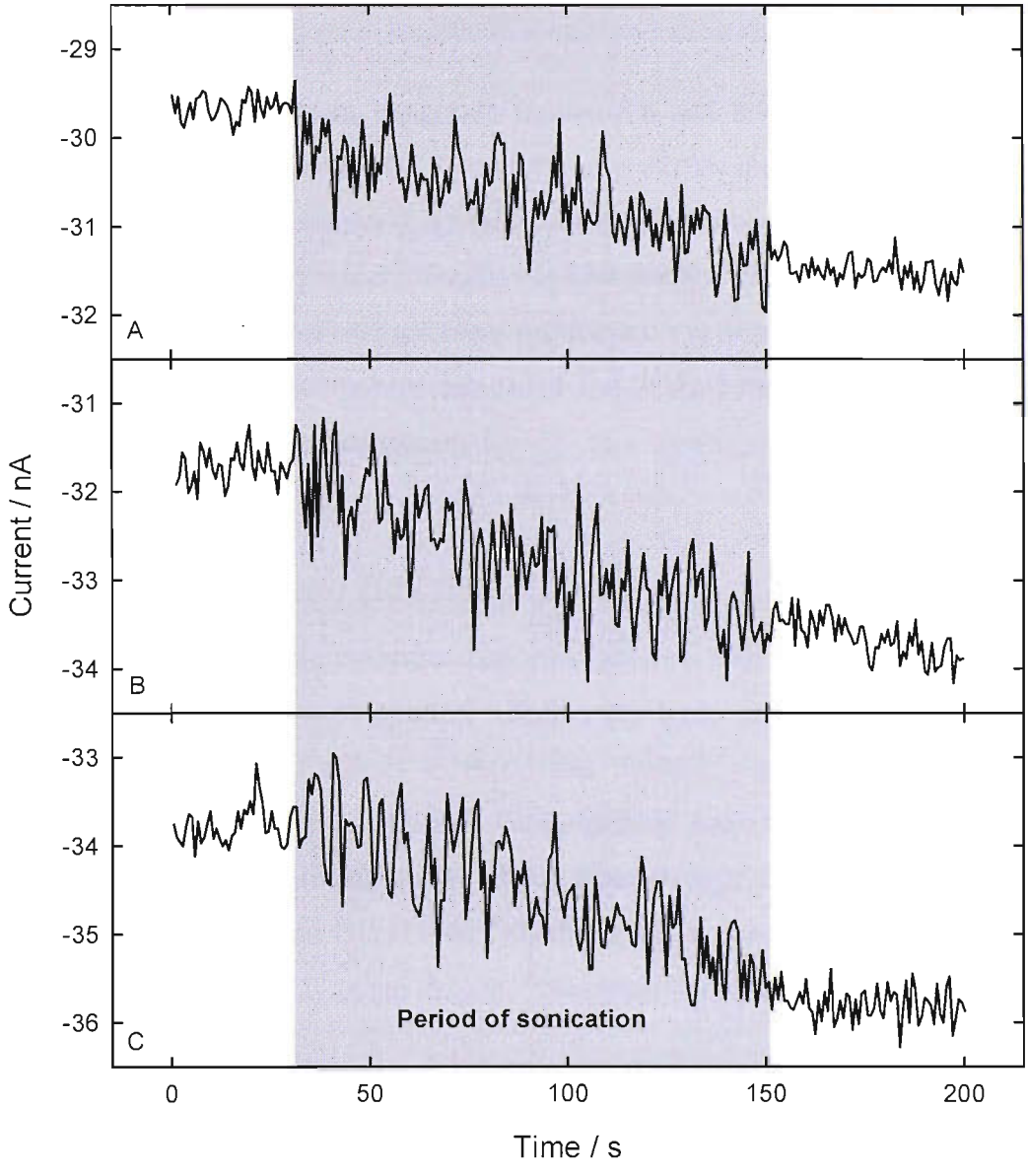

Figure 8.16: Plot showing the variation of currents as cavitation leads to a change in the chemical composition of the solution at three points within bath A (traces A, B and C corresponding to the same named points in figure 8.6) during a period of sonication (indicated by the grey shaded area). Recorded with the needle fed three electrode flow cell with the soft damped peristaltic pump running at 388 ml hr^{-1}. A 0.5 mm Pt electrode held at 0 V *vs.* a SCE counter/reference electrode was used to monitor the change in I_3^- concentration as a function of time. The bath contained 500 ml 90 mM KCl 10 mM KI solution at ambient temperature.

The calculated rates for the three traces shown in figure 8.16 were 0.89 +/- 0.12, 1.27 +/- 0.14 and 1.31 +/- 0.13 nM s^{-1} for points A, B and C. A difference in the recorded rates of formation of I_3^- from the sonochemical effect of the cavitation can be seen between point A and points B and C but the differences recorded between the points is marginal. Acoustic streaming and general mixing of the solution within the bath will make the detection of any localised variation in the sonochemistry difficult.

8.4.5. In comparison

If we compare the low light images in figures 8.8 and 8.9 with the pressure and surface activity maps in figures 8.13 and 8.14 respectively it can be seen that, though not as explicit as that for reactor 4, there is a correlation between the presence of light emission, high acoustic pressure amplitudes and surface erosion/corrosion activity. In particular using all three measurement techniques it is possible to see the presence of increased activity at two points, one either end of the bath, thought to correspond to the location of the drive transducers.

8.5. Bath B (Branson B1210E-MT)

In addition to the extensive measurements conducted on bath A (Ultrawave bath) two other commercial baths were studied. Both were baths in general use within the laboratory and therefore access to them was limited; restricting the number of measurements that could be made. Consequently only surface event, acoustic pressure and light measurements were made; these thought to be the most pertinent. The two baths (a Branson B1210E-MT (bath B) and a Semat ultrasonic bath (bath (c)) were both considerably larger than the Ultrawave bath (bath A).

Bath B had internal dimensions of 135 x 150 x 100 mm deep. It had a quoted operating frequency of 47 kHz (found to be 49 kHz by experimental measurement) and nominal power consumption of 80 W. For the experiments the bath was filled with 1.5 dm^3 of 0.1 M Na_2SO_4 which corresponded to a level 1 cm above the minimum operating level.

8.5.1. Light Measurements

To acquire a usable image of the light emission it was necessary to use the highest available intensifier gain resulting in the somewhat noisy image seen in figure 8.17 B. The intensified image in figure 8.17 shows that the light emission from the bath is not uniform with a series of hot spots being present towards the edges of the bath and a more concentrated region of elevated light emission towards the centre of the bath. As image A in figure 8.17 demonstrates the top and bottom of the bath cover different areas in the final image and so attributing the luminescence to an exact point within the bath is difficult.

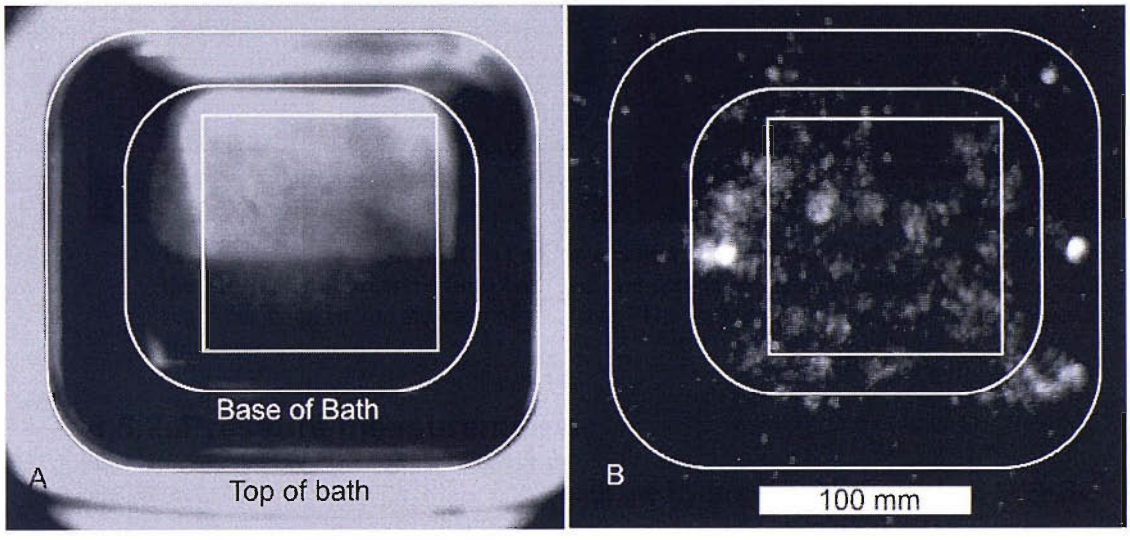

Figure 8.17: Ambient light (A) and intensified (B) images of bath B. Image B shows the MBSL light emission from bath and is a composite of 101 individual images. The scale bar is taken for the base of the bath. The bath contained 1.5 dm^3 0.1 M Na_2SO_4 solution.

8.5.2. Pressure measurements

To avoid contact with the side of the bath the hydrophone was scanned over the 100 x 100 mm area (shown by the superimposed squares in image A and B in figure 8.18) in 10 mm steps. The pressures seen in bath B were substantially lower than those recorded in bath A; consequently there were not the same problems associated with saturation of the ADC card used to record the pressure. Looking at the pressure signal over a relatively long period of time (see figure 8.19) it is possible to see that there is a variation in the signal similar to that seen for bath A (figure 8.3).

The variations in the pressure signal recorded in figure 8.19 have a period of 10 ms suggesting that the signal is associated with the 50 Hz variation in the mains signal (two "bursts" making up the 20 ms period of the mains supply).

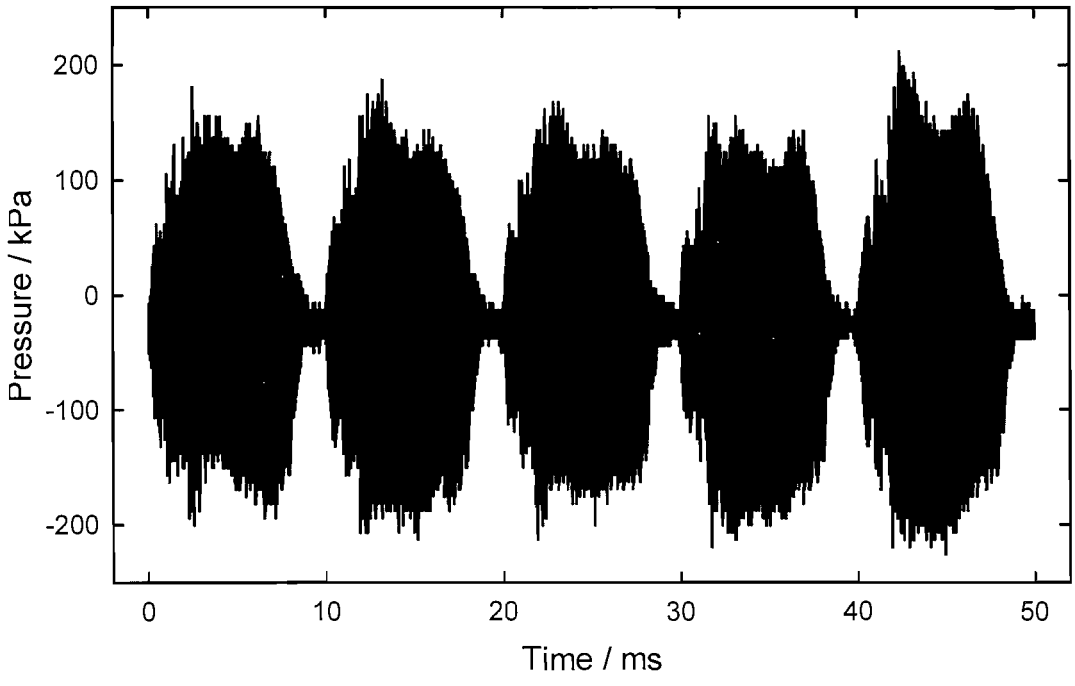

Figure 8.19: Plot of a long period pressure time trace recorded in bath B showing the bursting nature of the sound field within the bath. The bath contained 1.5 dm^3 0.1 M Na_2SO_4 solution.

If we look at the Fast Fourier Transform of the pressure signal from figure 8.19 in figure 8.20 it can be seen that addition to the fundamental frequency of the bath is 49 kHz (Peak X). In addition there are a number of other frequencies at which there is a significant pressure signal; unlike the measurements conducted for bath A these are not seen at the harmonics of the drive frequency. Figure 8.20 A shows the acoustic pressure signal over a short period of time. From this the period of the signal between points 1 and 2 can be calculated as 20.2 μs confirming the drive frequency of the bath to be ~49 kHz.

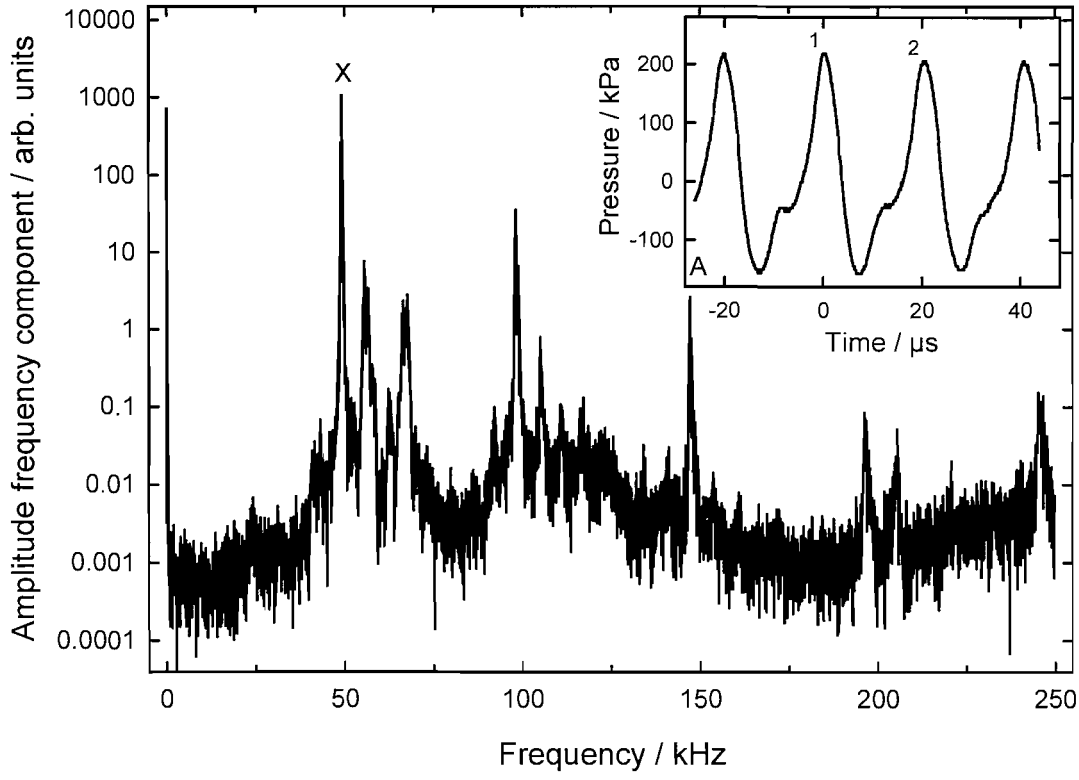

Figure 8.20: Plots showing the FFT pressure signal and direct pressure signal (insert A) from bath B. Bath contained 1.5 dm^3 0.1 M Na_2SO_4 solution.

Figure 8.21 shows the pressure amplitude within the bath plotted as a contour map. From this is possible to see that at relatively few points does the pressure within the bath exceed 200 kPa in contrast to what was seen for bath A. The pressure though is in excess of the calculated inertial pressure threshold (129 kPa) at almost every point within the scan. Of significant interest is the distribution of the regions of increased pressure. It could be expected that the pressure field within the bath would be relatively uniform with the pressure at a maximum towards the centre of the bath where items to be cleaned are most likely to be placed. Instead of the expected semi-uniform distribution of the pressure maxima, the points at which the greatest pressure was recorded are concentrated towards the edges of the bath with a single hot spot towards the centre of the bath.

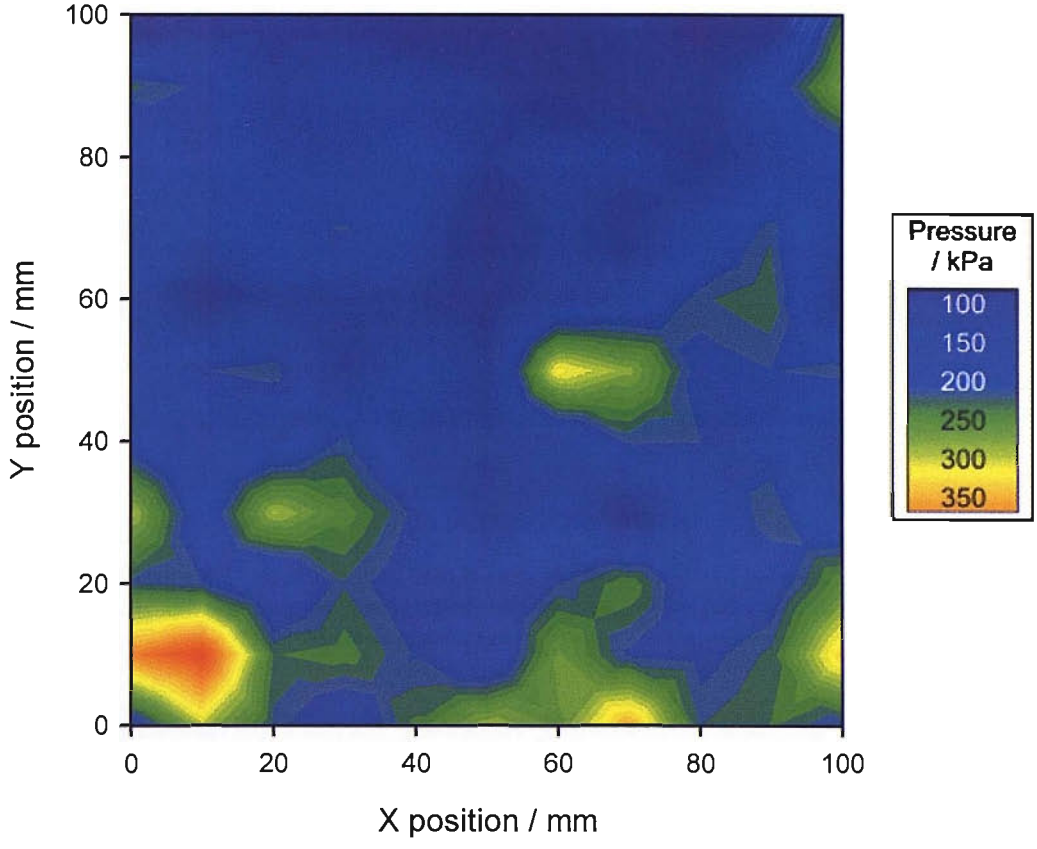

Figure 8.21: Contour map bath B showing the amplitudal pressure variation within bath B. The hydrophone was scanned over an area 100 by 100 mm at a resolution of 10 mm in 1.5 dm^3 of 0.1 M Na_2SO_4 solution.

8.5.3. Surface events

The surface erosion/corrosion measurements were conducted over the 100 x 100 mm grid as the pressure measurements, with the same 10 mm resolution. The procedure used to carry out the scan was the same as that used for bath A. The electrode was mounted such that the surface of the electrode was at the approximate midpoint vertically and then scanned through a single XY plane. Due to the threshold nature of the surface events there are no events recorded for the majority of points within the bath and those points for which events are detected vary massively. Consequently the contour map in figure 8.22 uses a logarithmic scale.

Figure 8.22 shows the presence of increased surface activity around the edges as well as a central hot spot. This is superficially similar to that seen for the pressure measurements but the location of the hot spots are not the same.

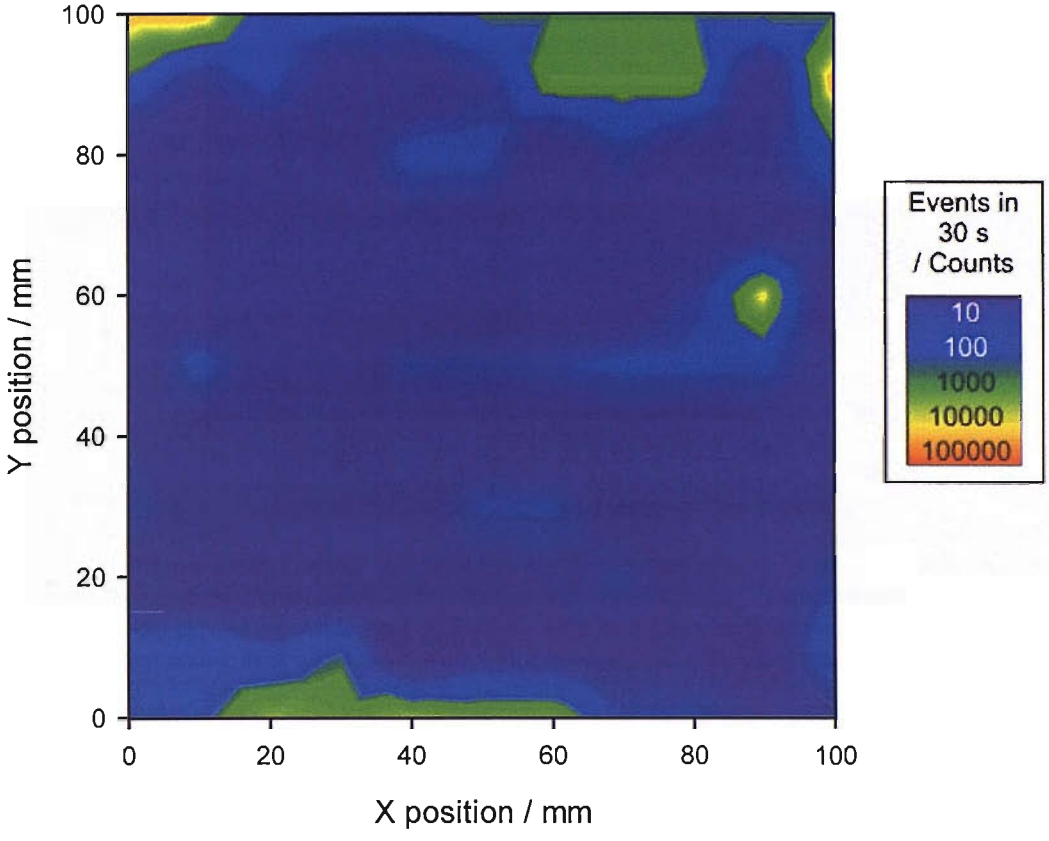

Figure 8.22: Contour map showing the distribution of surface erosion/corrosion events in bath B over an area 100 by 100 mm with a resolution of 10 mm. Events recorded on a 250 μm Al electrode held at 0 V vs. a SS counter/reference electrode using the MCA collecting over 30 seconds with a threshold of 0.85 μA. The bath contained 1.5 dm^3 of 0.1 M Na_2SO_4.

8.5.4. In Comparison

When the low light images (figure 8.17), pressure (figure 8.21) and surface event scans (figure 8.22) are compared it can be seen that there is little in the way of correlation between the image and the scans. Whereas the low light image indicates the presence of cavitation throughout the area of the bath the scans exhibit large areas for which there is a relatively low pressure and an absence of surface erosion/corrosion activity.

8.6. Bath C (Semat)

Bath C was the largest bath tested having internal dimensions of 240 x 140 x 100 mm deep. The drive frequency of the bath was found to be 46 kHz by experimental measurement. For these experiments the bath was filled with 2 dm^3 of 0.1 M Na_2SO_4 which corresponded to a level 6 cm; this being above the minimum operating level.

8.6.1. Imaging

The intensified imaging of the bath required a high degree of amplification to record an image. Consequently there is a high level of noise even in the stacked image.

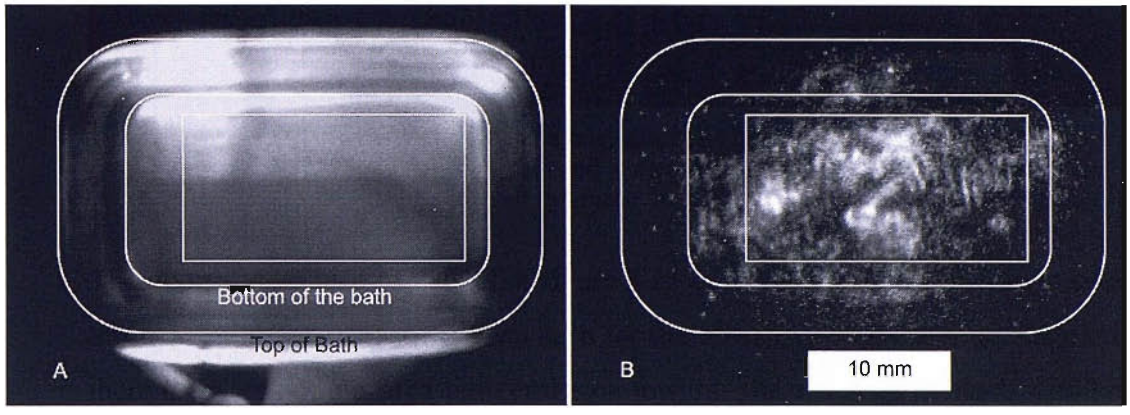

Figure 8.23: Ambient light (A) and intensified (B) images of bath C. Image B shows the MBSL light emission from bath and is a composite of 101 individual images. The scale bar is taken for the base of the bath. The bath contained 2 dm^3 0.1 M Na_2SO_4 solution.

The intensified image of bath C in figure 8.23 exhibits the variation in light emission through out the vessel as has been seen for the other two baths studied. In particular there is an area of elevated light emission towards the centre of the bath with little in the way of light emission towards the edge of the bath.

8.6.2. Pressure measurement

The pressure scan was carried out over an area 190 x 100 mm the position of which relative to the base of the bath is depicted by the rectangle in figure 8.23. The scan had a resolution of 10 mm with the hydrophone positioned at the midpoint of the solution vertically. As with bath B the pressures recorded were substantially less than those recorded for bath A and as a consequence there were no problems with the clipping of the ADC card used to acquire the data. In contrast to the pressure bursting recorded in the other two baths the pressure recorded in bath C did not have distinct times of the pressure being either on or off. As can be seen in figure 8.24 instead there was a more complex situation where a period of intense pressure was followed by a period of reduced pressure before the onset of the next period of high pressure. Though the variation was less pronounced than that seen for baths A and B it was still necessary to conduct measurements over a time period greater than 10 ms in order to achieve a consistent pressure measurement.

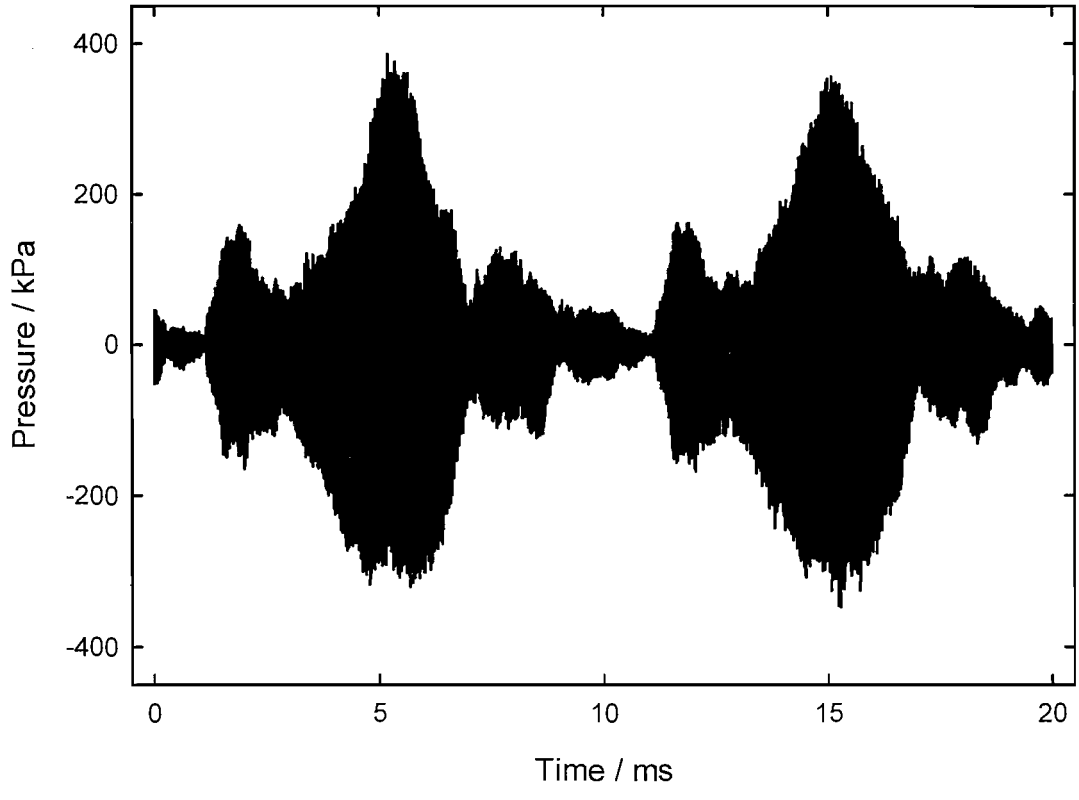

Figure 8.24: Plot of a long period pressure time trace recorded in bath C showing the varying nature of the sound field within the bath. The bath contained 2 dm^3 0.1 M Na_2SO_4 solution.

Figure 8.25 shows a contour map of the pressure scan within bath C. The pressures were significantly less than that recorded in bath A, but greater than those recorded in bath B. Of particular note is the presence of pressure in excess of 400 kPa being recorded towards the centre of the bath, similar in location to the areas of elevated light emission seen in the low light image in figure 8.23.

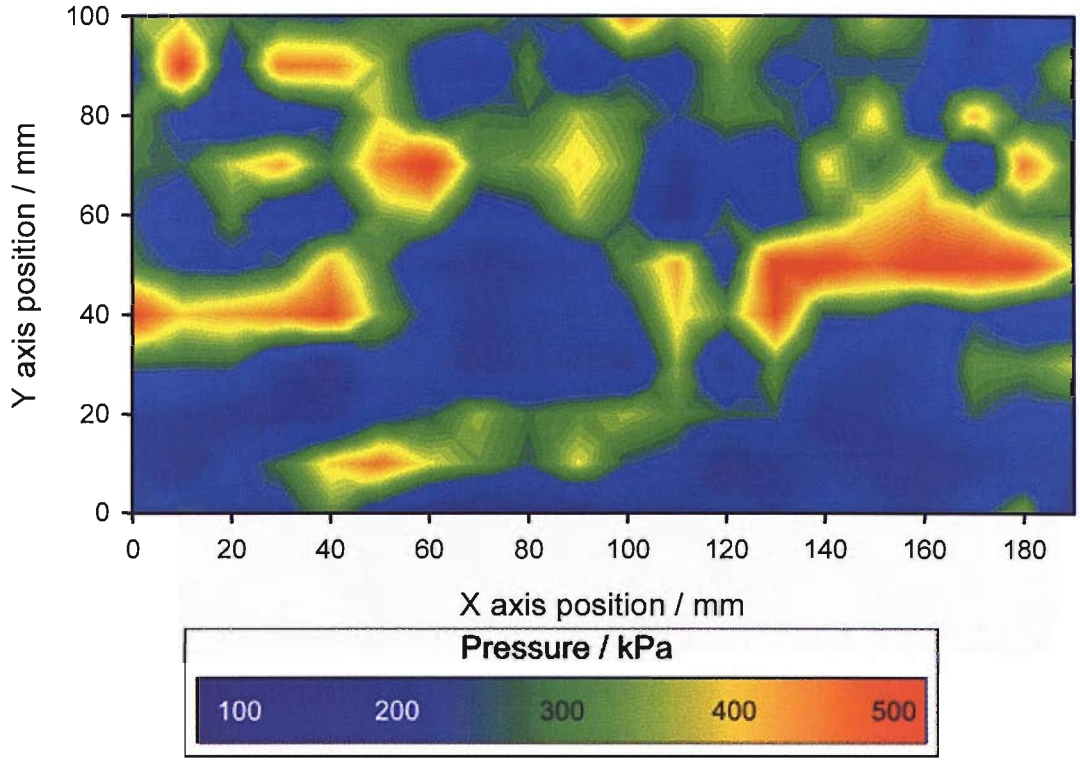

Figure 8.25: Contour map showing the amplitudal pressure variation within bath C. The hydrophone was scanned over an area 190 by 100 mm at a resolution of 10 mm in 2 dm^3 of 0.1 M Na_2SO_4 solution.

8.6.3. Surface measurement

The surface erosion/corrosion scan was conducted over the same area and with the same resolution as the pressure scans covering an area 190 x 100 mm area with a resolution of 10 mm. The scan was conducted 30 mm from the base of the reactor placing the electrode at the mid point of the solution within the bath. The procedure for the scan was the same as that for baths A and B.

Figure 8.26 shows a contour map of the surface erosion/corrosion event scan. Again due to the threshold dependence of the technique no events are recorded at a large number of points. The areas at which a significant number of events were recorded are concentrated towards the centre of the bath in the same way as the light emission and pressure measurements were in figures 8.23 and 8.25. The limited number of events recorded towards the bottom of figure 8.26 as we look at it is unexpected, as are the two apparent lines of high activity of angling from the centre of the bath towards the edge. This may be as a result of the scan only being conducted through a

single XY plane within the bath and further investigation of the bath may have shown a more ordered distribution.

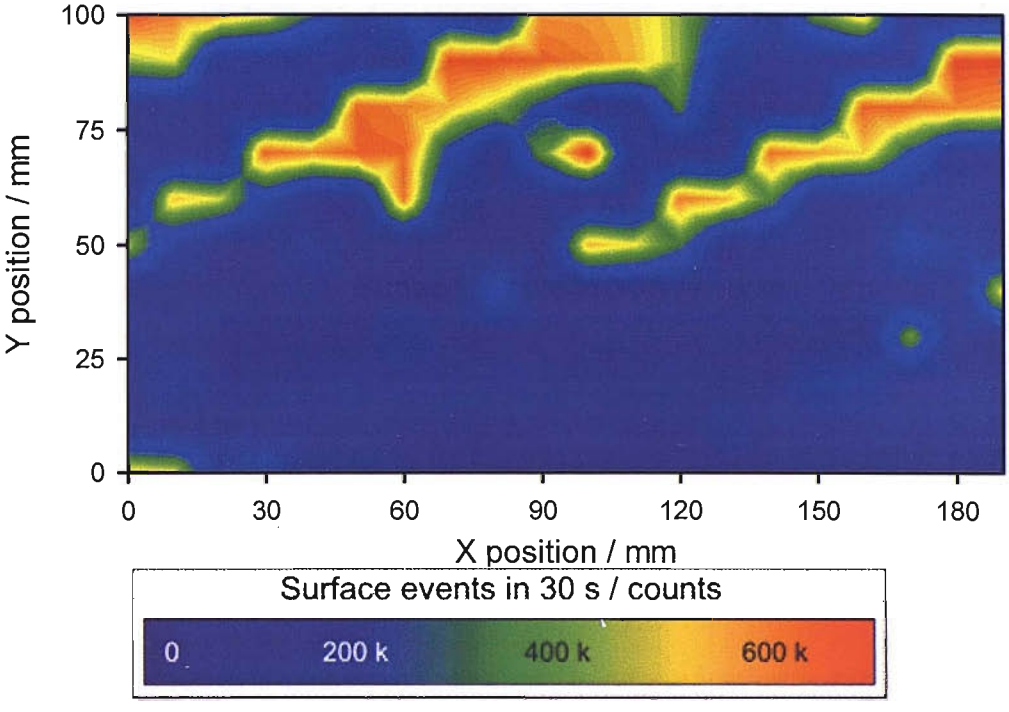

Figure 8.26: Contour map showing the distribution of surface erosion/corrosion events in bath C over an area 190 by 100 mm with a resolution of 10 mm. Events recorded on a 250 μm Al electrode held at 0 V vs. a SS counter/reference electrode using the MCA collecting over 30 seconds with a threshold of 0.85 μA. The bath contained 2 dm^3 of 0.1 M Na_2SO_4.

8.6.4. In comparison

Through all the measurements conducted on bath C it is possible to see an increase in the likelihood of the presence of cavitation towards the centre of the bath. In particular the low light images and pressure measurements (figures 8.23 and 8.25 respectively) show a similar indication as to where cavitation is taking place. The surface measurement in figure 8.26 is less clear showing the same increase in activity towards the centre of the bath seen for the other two measurements but with this only tending to one side of the bath rather than the more even distribution observed with the other techniques.

8.7. Effect of addition of cleaning items

All of the measurements presented so far in this chapter have been conducted in ultrasonic baths with the minimal disturbance to the field possible. The addition of the measuring equipment for the pressure, surface activity and chemical change experiments (a hydrophone, electrode and needle respectively) as well as the copper piping utilised to cool the baths will have had an effect on the field but it was hoped to have been minimised. This is an artificial situation when compared to how small cleaning baths, such as those examined here, would be used in practice. Commonly when baths are used multiple objects are normally placed within them in addition to methods of supporting the items such as a basket all of which is likely to alter the sound field and hence the type of cavitation taking place. This may have an influence on the cleaning power of the bath. In the final section of this chapter we shall examine the effect on the measured cavitation within bath A of the addition of several items to be cleaned.

First, we shall look at a series of experiments conducted using purely light emissive methods to ascertain the effect of a number of sample objects. Second, a set of experiments investigates the effect of a single item on a small portion of the bath using pressure and surface erosion/corrosion event measurements in addition to luminesence measurements.

8.7.1. Effect on light emission

Photon counting measurements and intensified imaging were used to monitor the effect of sample cleaning items on the luminescence from bath A. The emission from the bath was recorded first with the bath alone as a reference, the basket provided by the manufacturers to support items in the bath was added and the effect on emission recorded before two sample cleaning condition (a 10 ml glass vial and three coins) were examined. It would be possible to use MBSL light emission to monitor the effect that placing objects within the cleaning bath (this is done in the section that follows this). However, as can be seen when comparing the images in figure 8.8 and figure 8.9 the use of a solution capable of MBS(C)L increasing the light output and therefore makes changes easier to detect. Consequently this series of experiments

was conducted with a solution containing luminol. For all the experiments the camera and photon counter were placed vertically above the bath in order to give a view over the entire vessel.

Figure 8.27 shows the light emission from the bath as a function of the items added. Clearly the addition of only the basket used to support items to be cleaned reduces the light emission from the bath by a factor of 2. An even greater reduction was seen when the sample items were added; the addition of the coins to the bath having the greatest detrimental effect on the light emission.

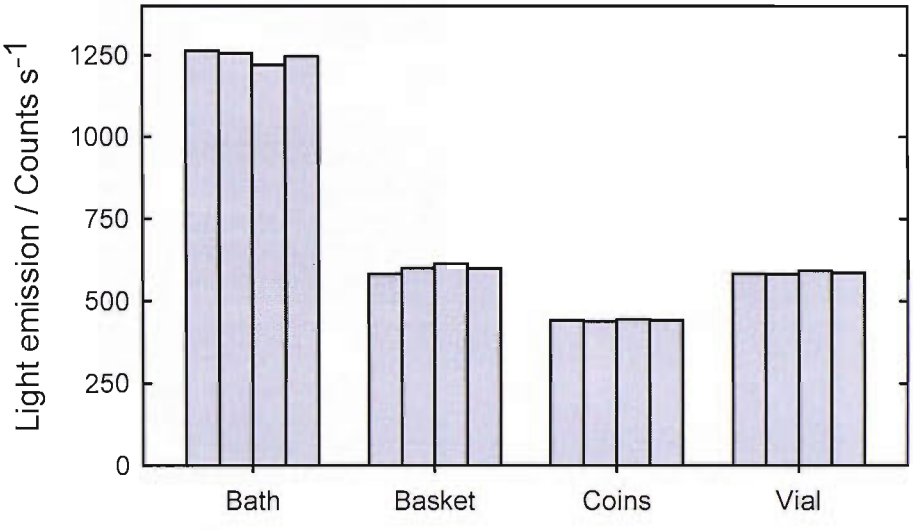

Figure 8.27: Plot showing the difference in light emission from bath A with the bath alone (Bath); the bath plus wire support basket (Basket); the bath, basket and three coins (Coins) and the bath with the basket and a vial of solution added (Vial). The photon counter was mounted 30 cm above the bath and each measurement repeated four times (represented by each bar). The bath contained 500 ml of a solution of 0.1 M Na_2CO_2, 0.1 mM EDTA and 5 μM luminol.

The change in light emission caused by the added items can also be seen in the relevant low light images. The images shown in figure 8.28 show the bath with and without the added items. Note the intensifier gain used to acquire the images d, f and h in figure 8.28 being nearly eight times greater than that used to acquire image b (image b acquired at a luminous gain of ~9,000; images d, f and h acquired at a luminous gain of ~70,000 (*106*)).

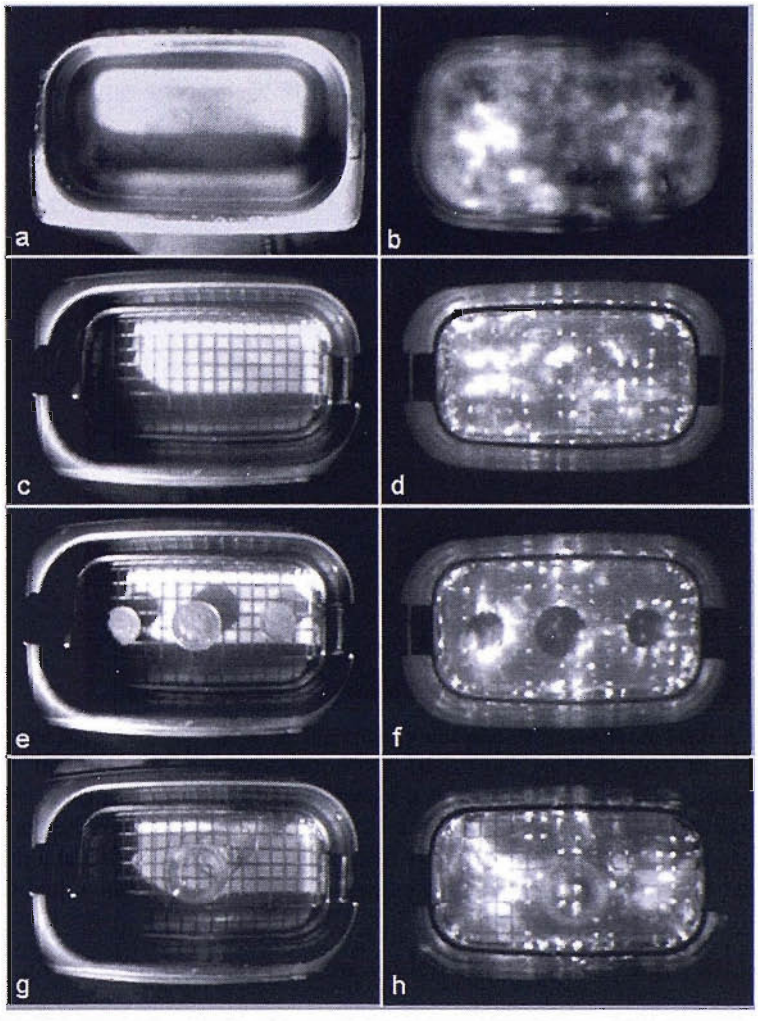

Figure 8.28: Images showing the change in light emission from bath A unperturbed (b), with the addition of a wire supporting basket (d), with the addition of the basket and three coins (f) and with the addition of a wire basket and a vial of solution (h) and the respective ambient light images (a, c, e and g) to indicate the location of the added items. Each intensified image is a stacked and averaged combination of 101 individual images. The bath contained 500 ml of a solution of 0.1 M Na_2CO_2, 0.1 mM EDTA and 5 µM luminol

Figure 8.28 shows the effect of the added items on the light emission from bath A. The addition of only the basket used to support items within the bath has a large effect on the light emission seen (image d). The same regions of activity are seen, but in addition there are localised bright spots at the intersections of the wires of the basket. The effect of addition of the coins to the basket (image f) is mainly to obscure possible luminescence from below; possibly explaining the reduction in light recorded by the photon counter module. The glass vial being transparent appears to have less effect than the coins on the image (image h). It would appear that the addition of the basket confines the light emission to the volume between the base of the bath and the basket. Consequently the addition of further objects to the bath has less of an effect on the light emission.

8.7.2. Localised effects

Having investigated the effects of adding items to a bath on a bath wide scale we shall now look at the local effects. Specifically we shall look at the effect on the pressure, surface erosion/corrosion and MBSL light emission in a small section of a bath when a sample cleaning item is added. The experiment involved a sample object (1 p coin, 20 mm diameter) being placed into bath A on the wire basket and measurements conducted in the bath without any additions, with the basket present and with the basket and the coin added. The pressure and surface measurements were conducted over a 30 x 30 mm portion of the bath at a resolution of 5 mm centred on the coin.

8.7.2.1. Light emission

Figure 8.29 shows the intensified images of the bath with the no addition (a&b), the wire basket (c&d) and the basket and coin (e&f).

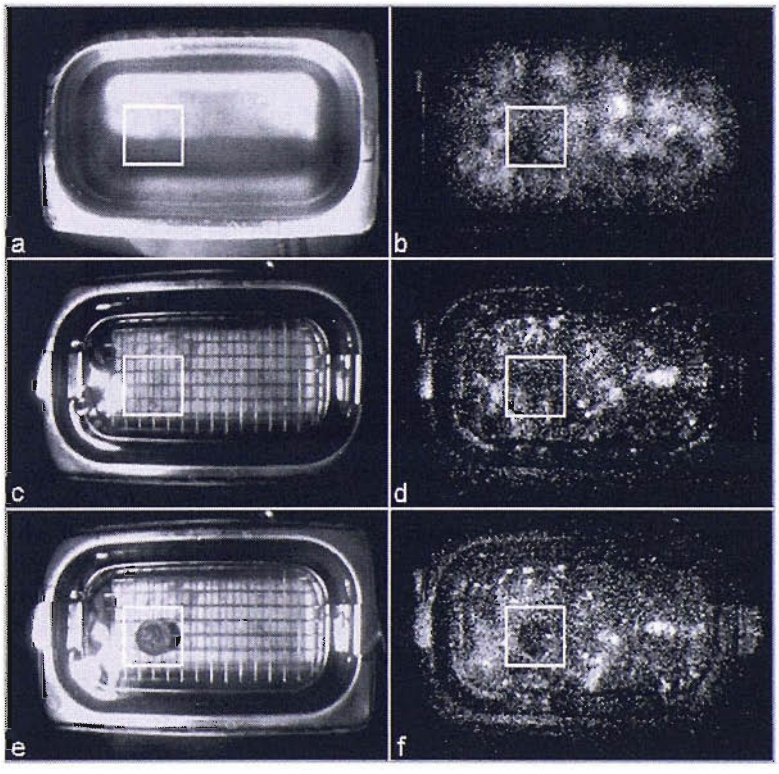

Figure 8.29: Images showing the change in MBSL light emission from bath A unperturbed (b), with the addition of a wire supporting basket (d) and with the addition of the basket and a coins (f) and the respective ambient light images (a, c and e) to indicate the location of the added items. The white square superimposed onto the image corresponds to the region scanned by the pressure and surface measurements. Each low light image is a stacked and averaged combination of 101 individual images. The bath contained 500 ml of a solution of 0.1 M Na_2SO_4 solution.

The images in figure 8.29 show that as with the measurements made using MBS(C)L the addition of the basket has a large effect on the light emission. The further addition of the coin makes little further difference except to prevent any light emission from below. The overall level of light emission can not be directly measured from the images due to the processing that takes place to generate the final images, an indication as to the relative light emission can be inferred from the stack divisor required to produce a usable image[§]. In this case image b required a divisor 4 times greater than that for images d and f suggesting a significantly greater level of light emission. As with the images obtained with the assistance of chemiluminescence in figure 8.28 it is possible to see in images d and f the presence of localised regions of elevated light emission at the intersections of the wires from the supporting basket.

8.7.2.2. Pressure measurements

The reduced area of the bath over which the pressure and surface scans were conducted is indicated by the white boxes in figure 8.29 images a-f. The hydrophone was positioned within the bath such that the tip of the hydrophone was 2 mm above the surface of the basket. The procedure for carrying out the pressure scan was the same as that used for the pressure scans of bath A. As the measurements were conducted in bath A there were again issues with the clipping of the ADC card due to the large pressures involved. The pressure maps corresponding to the bath alone (a) with the basket added (b) and with the bath and coin added (c) are presented in figure 8.30.

The pressure maps in figure 8.30 show very clearly how the addition of items to the bath alters the pressure field. The pressure map of the unperturbed bath (figure 8.30 map a) it can be seen that the majority of the area under investigation is subjected to pressures in excess of 400 kPa peak to peak amplitude. The addition of the wire

---

[§] The image stacking software used for the lowlight images (Tambaware Image Stacker V1.03) generates the final image by adding the luminance data from all the images and then dividing this by the divisor to give the luminance data for final image. Therefore the smaller the divisor required to produced a useable image the lower the level of initial light emission.

basket to the bath (figure 8.30 map b) dramatically reduces the pressures recorded with few points now being recorded with pressures in excess of 300 kPa and numerous points where the pressure is below 200 kPa. The further addition of the coin to the bath (figure 8.30 map c) causes a further reduction in the areas at which higher pressures are recorded.

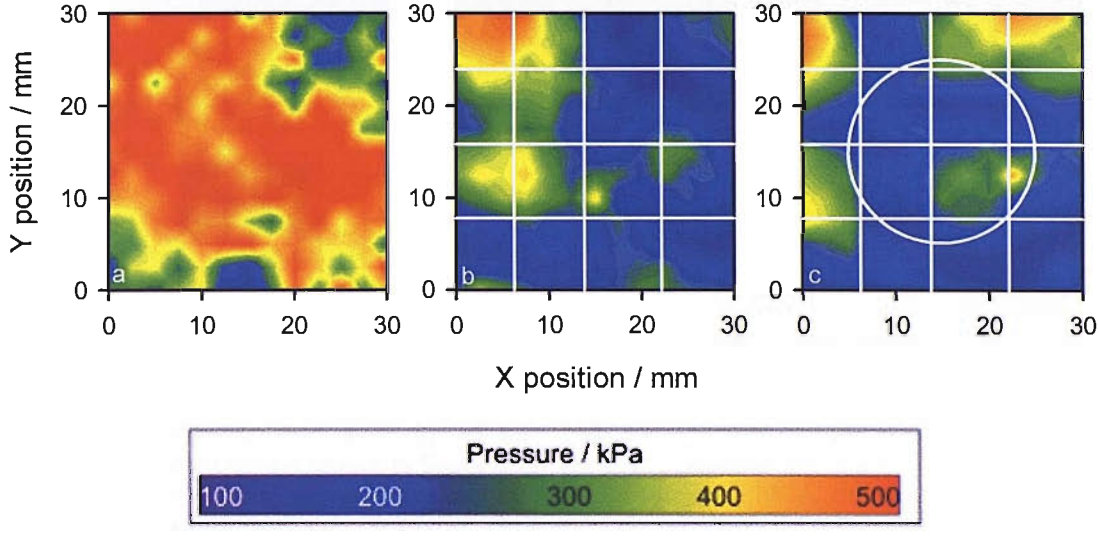

Figure 8.30: Contour maps showing the variation in the amplitudal pressure over the same area in the unperturbed bath (a), in the bath with the addition of the wire support basket (b) and with the addition of the basket and a 1 p coin (c). The hydrophone was scanned over a 30 by 30 mm area corresponding to the white squares superimposed onto figure 8.29 with a resolution of 5 mm. The bath contained 500 ml 0.1 M Na_2SO_4 solution.

The expansive pressure threshold for a system running at 59 kHz, such as bath A, is 133 kPa. Looking at the amplitudal (zero to peak) pressure after the addition of the items to the bath the acoustic pressure is still well in excesses of this. This suggests that the presence of inertial cavitation should still be detected.

8.7.2.3. Surface events

The surface event scans were conducted over the same area as the pressure scans shown by the white boxes on images a-f in figure 8.29 with a resolution of 5 mm and with the electrode held 2 mm above the bottom of the basket. The same measurement procedure was used for the reduced area as for the scans of the entire bath. The resultant maps of the surface event activity corresponding to the bath alone (a) with the basket added (b) and with the bath and coin added (c) are presented in figure 8.31.

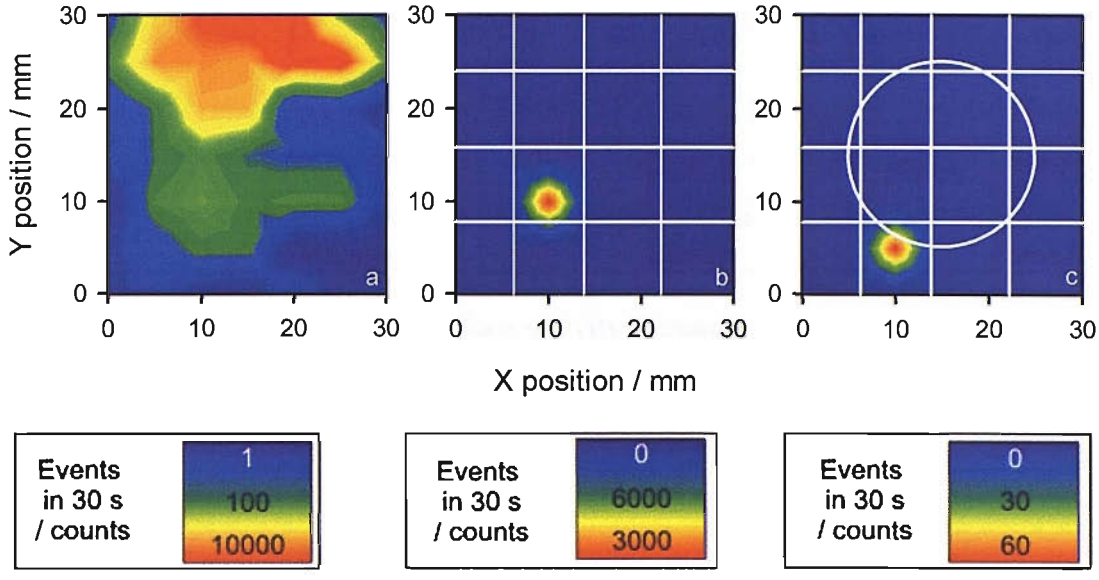

Figure 8.31: Contour traces showing the distribution of the surface erosion/corrosion activity over a portion of bath A in the unperturbed bath (a), in the bath with the addition of the wire support basket (b) and with the addition of the basket and a 1 p coin (c). Scans conducted over a 30 by 30 mm area corresponding to the white squares superimposed on the images in figure 8.29. Events recorded on a 250 μm Al electrode held at 0 V vs. a SS counter/reference electrode using the MCA collecting over 30 seconds with a threshold of 0.85 μA. The bath contained 2 dm^3 of 0.1 M Na_2SO_4.

The contour maps of the surface activity in figure 8.31 show the dramatic reduction in the relative activity caused by first the addition of the wire basket (map b) and then the addition of the coin (map c). To illustrate the reduction further if the total number of events recorded for each situation (140268, 7483 and 73 events for maps a, b and c respectively) are considered it can be seen that the level of cavitation surface events taking place within the bath is significantly affected by the addition of items to the bath. This agrees with the MBSL, MBS(C)L and pressure measurements.

8.7.3. Conclusions

The examination of the affect of the addition of items to cleaning bath A has shown that, as would be expected, there is a large affect on the level of light emission, acoustic pressure and surface event activity even from the addition of a wire basket used to support items to be cleaned

8.8. Conclusions

In this chapter we have seen how it is possible to systematically scan commercial baths using the same techniques previously employed in idealised reactors. Through this it has been possible to see that the cavitation within the bath rather than being uniform is present in distinct patches that can be detected separately using light emission, acoustic pressure and surface activity measurements. It has also been seen that it is possible to measure the rate of chemical change within an ultrasonic bath through electrochemical means.

Having established that the spread of cavitation within the cleaning baths was not even sample objects were added to bath A and their effect on the level and distribution of the cavitation investigated using light emissive, pressure and surface erosion/corrosion techniques. From this it was possible to see that even the addition of a wire basket intended to support items to be cleaned within the bath lead to a significant alteration and reduction in the inertial cavitation taking place and the further introduction of sample items to be cleaned reduced the recorded levels to an even greater extent.

9. NPL tests

As part of an ongoing project to attribute a standard unit to cavitation, the National Physical Laboratory (NPL) has constructed a reference cavitation vessel in which different methods of quantifying cavitation can be compared and calibrated (*162*). This vessel enables techniques (such as those presented in the preceding chapters of this thesis) to be compared in an accurate manner. It was one of the principle aims of this project to transfer any methods developed in Southampton to the reference vessel so that they could be compared with other existing techniques. Due to the size of the reference vessel it was not possible for it to be transferred to Southampton for experiments to be conducted; all experiments having to be conducted at the NPL in Teddington. This seriously constrained the number of measurements that could be made.

In conjunction with the reference vessel, NPL has developed a broadband acoustic sensor that is hoped to be a quick and accurate sensor for cavitation. The sensor detects the high frequency broadband acoustic pressure signals generated by the cavitation bubble collapse. Extensive work has been carried out by NPL mapping the entire reference vessel with both their broadband sensor and a standard hydrophone at a variety of different drive powers and conditions (*162*). Supplementing these results with measurements of the light emission, surface erosion/corrosion cavitation events and chemical change, it was hoped to produce a rounded view of the reference vessel and the relationship between the measurements.

In this chapter will shall first discuss the procedures and results for the light emission, surface erosion/corrosion event and chemistry measurements and then compare these to the measurements carried out by NPL for the acoustic pressure and high frequency broadband emission. Finally the effect of NPL's broadband sensor (*163, 164*) on the conditions within a cavitating body will be investigated through the means of low light imaging.

9.1. Light emission measurements

In order to acquire both quantitative and spatial light emission measurements experiments were conducted using a photon counter (for quantitative measurements) and an image intensifying video camera (spatial measurements) in the same manner as for the measurements conducted on both the single transducer reactors and ultrasonic cleaning baths (see chapters 6&8). That the reference vessel was intrinsically tied to the laboratory at NPL prevented measurements being carried out in the same darkroom in which all other low light measurements had been made. Consequently for worthwhile measurements to be made it was necessary to create blackout conditions surrounding the vessel. The blackout conditions consisted of two levels of light reduction; first the room as a whole and second the enclosure surrounding the vessel. To reduce the light within the room as a whole all extraneous equipment was switched off and the all sources of light (such as windows) covered up. For all equipment that it was not possible to switch off, any status lights or other sources of illumination were covered up using black insulating tape. The level of light inside the enclosure was further reduced by completely covering the enclosure in fibre board. This was cut to shape and the secured by means of gaffer tape such that very little light could enter. The picture in figure 9.1 shows the enclosure with the added blacking out and the photon counter mounted in position for conducting a measurement.

The measures taken to reduce the extraneous light reaching the vessel reduced the light level within the enclosure to 4 counts s^{-1} a level comparable to that recorded in the dark room in Southampton (typical background 2 - 6 counts s^{-1}). The inability to use the darkroom to conduct the light emission measurements for the NPL reference vessel also precluded the use of the Photek intensifier based imaging system used in all other experiments. Instead measurements were conducted using a Photonics Science Darkstar image intensified camera attached to a Hauppage USB WIN-TV capture device and attendant software. This setup was not capable of the same level of light amplification as the Photek intensifier based system available in the dark room. As a consequence in addition to standard MBSL measurements the solution within the reactor was replaced with a solution containing luminol so that multi-

bubble sonochemiluminescent (MBS(C)L) measurements could be conducted with the accompanying increase in the level of light emission (*62, 123, 127*).

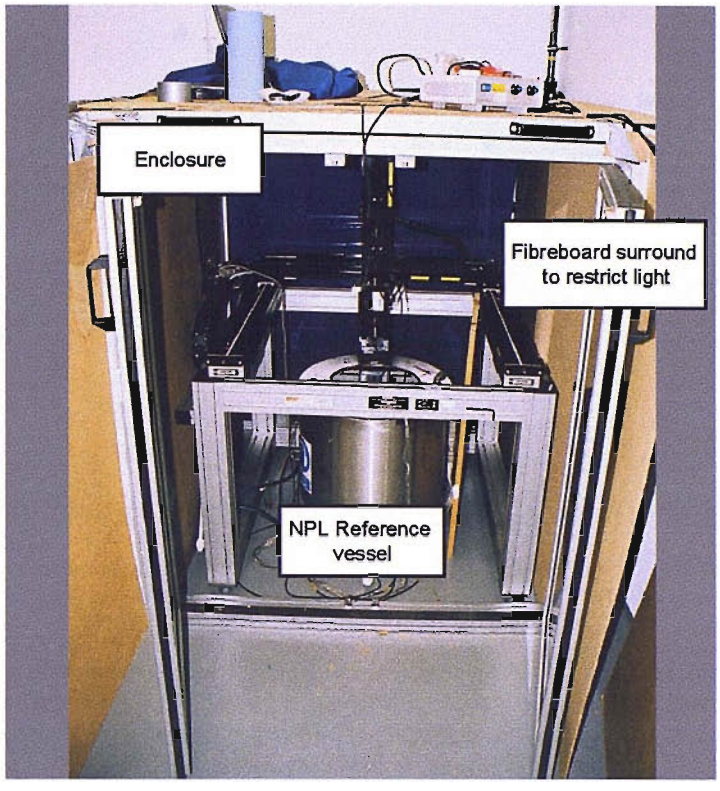

Figure 9.1: Image of the NPL reference vessel as setup for conducting intensified imaging and photon counting measurements. The enclosure surrounding the vessel was augmented with a fibreboard surround to prevent the ingress of light to the vessel. This reduced the level of light recorded within the enclosure to be reduced to 4 counts s^{-1}.

We shall now look first at the quantitative measurements conducted using the photon counter for both the MBSL and MBS(C)L cases before moving on to look at the intensified images.

9.1.1. Photon counting measurements

The photon counter was attached to the three dimensional positioning system of the reference vessel and positioned centrally above the vessel. For measurements covering the entire bath the photon counter was placed 250 mm above the centre of the bath but it was possible to reposition the counter as required. The light emission from the bath was measured for 20 s and the average light output over that period calculated. The level of light emission from the vessel was measured as a function of the drive power for MBSL emission and MBS(C)L emission from a solution containing luminol.

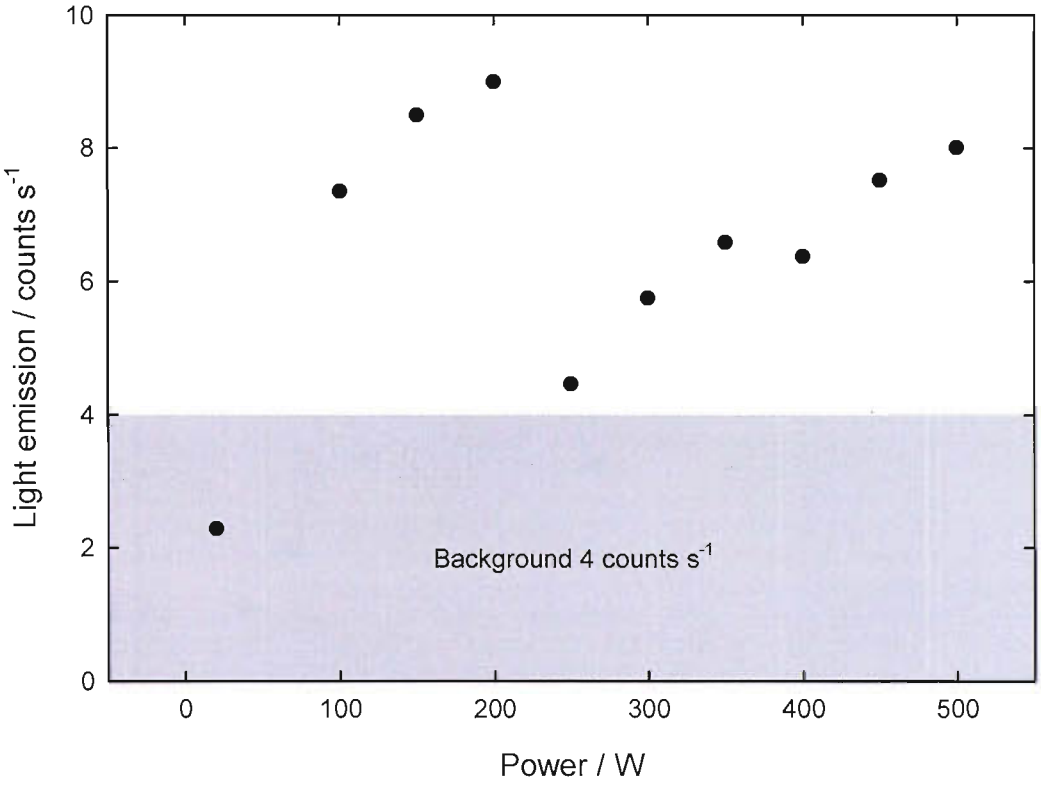

Figure 9.2: Plot showing the level of MBSL light emission from the NPL reference vessel as a function of the vessel drive power. Each point is the average of three separate measurements conducted with the photon counter mounted 25 cm above the centre of the vessel which contained an aerobic aqueous solution of 0.1 M $NaNO_3$.

Figure 9.2 shows the MBSL light emission from the NPL reference vessel as a function of drive power. From this it is possible to see that at all powers except from 20 W a measurable level of light was detected. The level of emission from the vessel is very low at all drive powers; being only slightly greater than the background level of 4 counts s^{-1} (in comparison reactor 4 driven at 92 kHz emits 64 counts s^{-1}). Consequently it is inadvisable to draw much in the way of conclusions from the data apart from to say that the presence of MBSL within the reference vessel can be inferred at all powers above 20 W.

To further the understanding of how the sonoluminescence from the reference vessel varies as a function the drive power, the solution within the vessel was replaced with an alkali solution containing luminol in order to increase the level of light emission (*62, 123, 127*). Figure 9.3 shows the resultant plot of the MBS(C)L as a function of the drive power of the reference vessel.

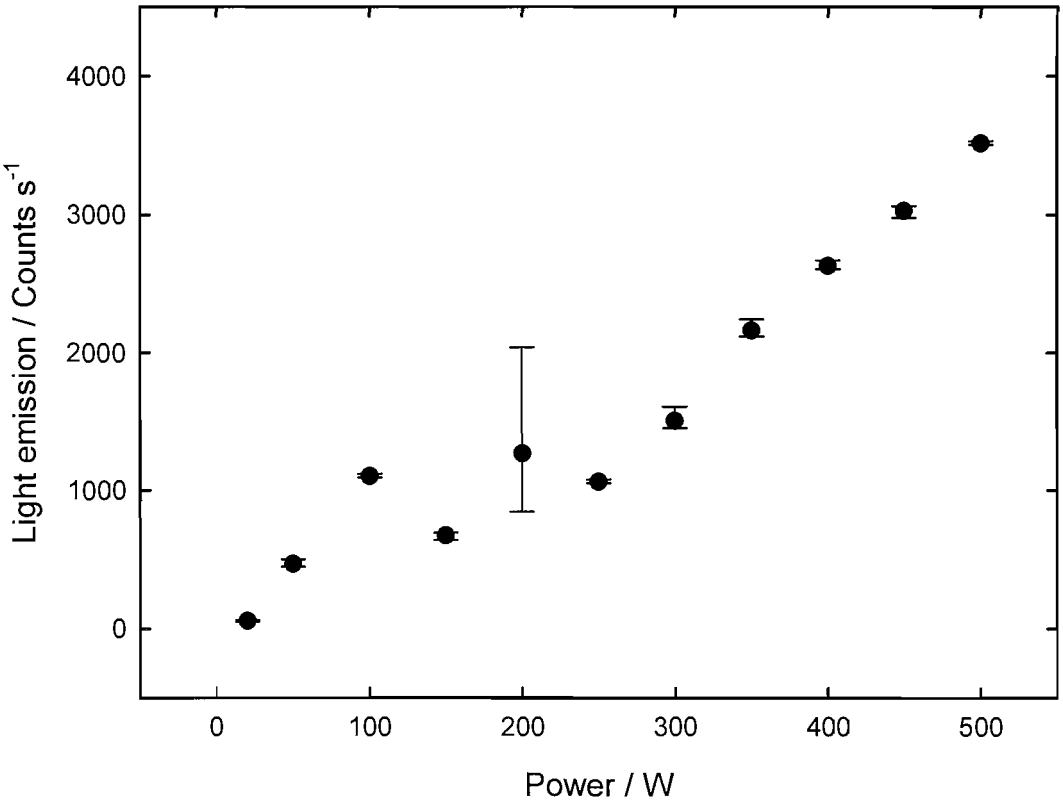

Figure 9.3: Plot showing the MBS(C)L light emission from the NPL reference vessel as a function of the vessel drive power. Each point on the plot is the average of three individual measurements conducted with the photon counter placed 25 cm above the centre of the bath. The sonochemiluminescent solution in the reference vessel contained 5 μM luminol and 0.1 M Na_2CO_3, was at room temperature (~25 °C) and was not degassed.

The addition of the solution containing luminol to the reference vessel resulting in the presence of both MBSL and MBS(C)L lead to a substantial increase in the light emission from the vessel. In figure 9.3 it can be seen the level of light emission has increased by over two orders of magnitude to levels that are detectable by the human eye (over approximately 1000 counts s^{-1}). As with the measurements conducted under purely sonoluminescent light emissive conditions in figure 9.2 the measurements conducted for sonochemiluminescence in figure 9.3 show an absence of light emission at a drive power of 20 W. There is an increase in the level of emission seen at powers of 50 and 100 W when the level of light emission plateaus at around 1000 counts s^{-1} at drive powers below 350 W before undergoing a steady increase to a maximum of just over 3,500 counts s^{-1} at a power of 500 W.

9.1.2. Intensified lowlight imaging

To conduct the imaging of the bath the Photonics Science camera was mounted onto the positioning system such that it was vertically above the centre of the bath. The

camera control box, video capture system and laptop computer used to store the images were located outside the vessel enclosure to reduce the level of light contaminating the image. Figure 9.4 depicts the setup used for the intensified image acquisition.

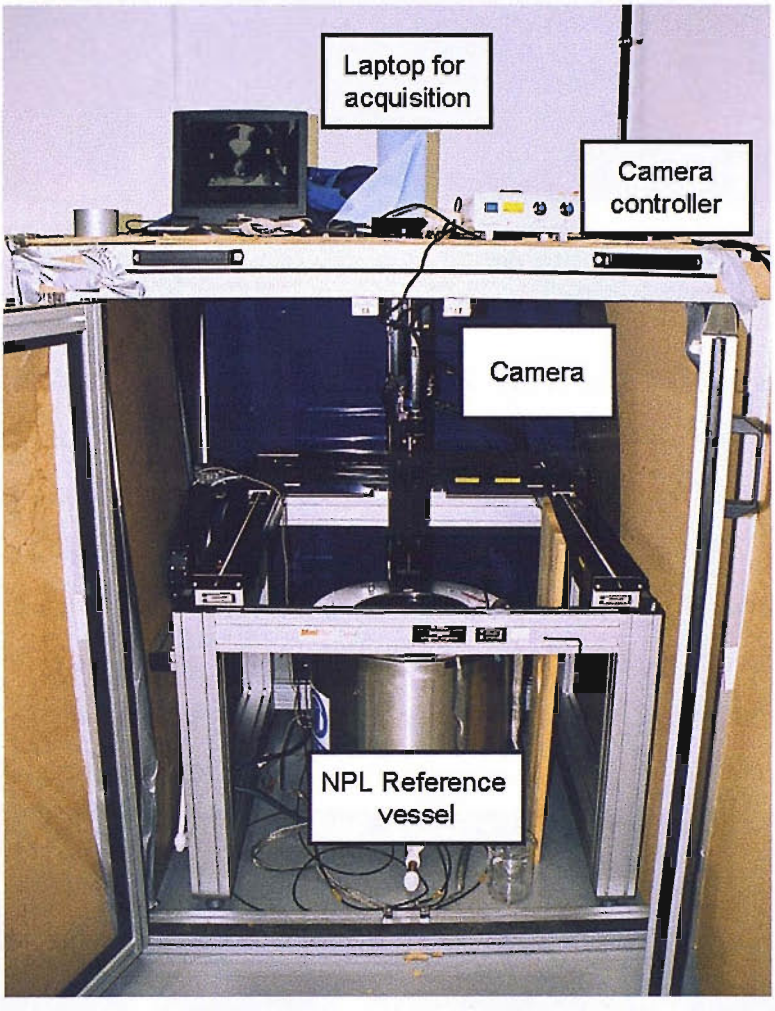

Figure 9.4: Image showing the setup used for the acquiring of intensified images of the light emission from the NPL reference vessel.

The low level of light emission from MBSL (see figure 9.2) and the limited gain of the Photonics Science intensified video camera seriously impaired the ability to image the non-chemically assisted luminesence emanating from the vessel. Even though there was a measurable level of MBSL light emission from the vessel in figure 9.2, as figure 9.5 shows no usable image could be recorded even at the 500 W, the greatest power available.

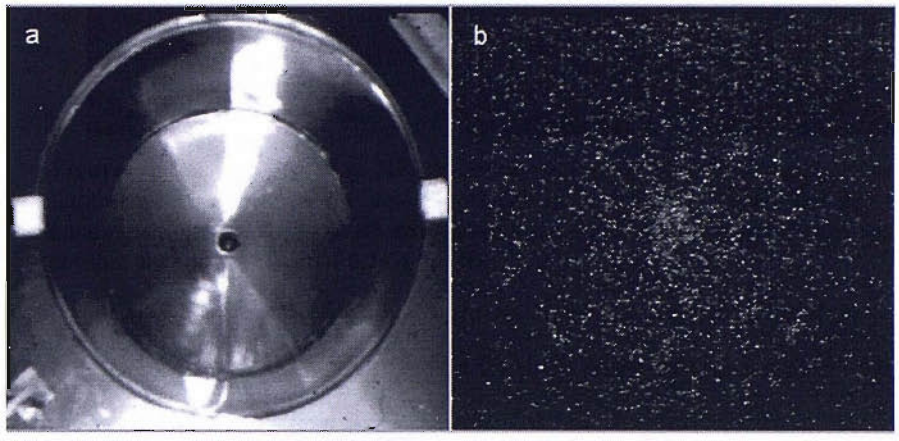

Figure 9.5: Images showing NPL reference vessel with ambient light (a) and MBSL light emission (b) when the vessel was driven at 500 W. Intensified image b is an amalgamation of 43 individual images recorded when the reference vessel contained an aerobic aqueous solution of 0.1 M $NaNO_3$.

Looking at the low light MBSL image in figure 9.5 (image b) it is just possible to discern the presence of light emission in the centre of the reactor. Due to the high level of noise associated with the image further deductions as to the location of the light emission relative to the vessel were not possible. Figure 9.6 shows that the addition of a luminol containing solution to the reference vessel increases the light emission to the point where an image can be easily recorded. It should be noted that figure 9.6 is recorded under the same conditions as figure 9.5 except for the addition of the sonochemiluminescent solution.

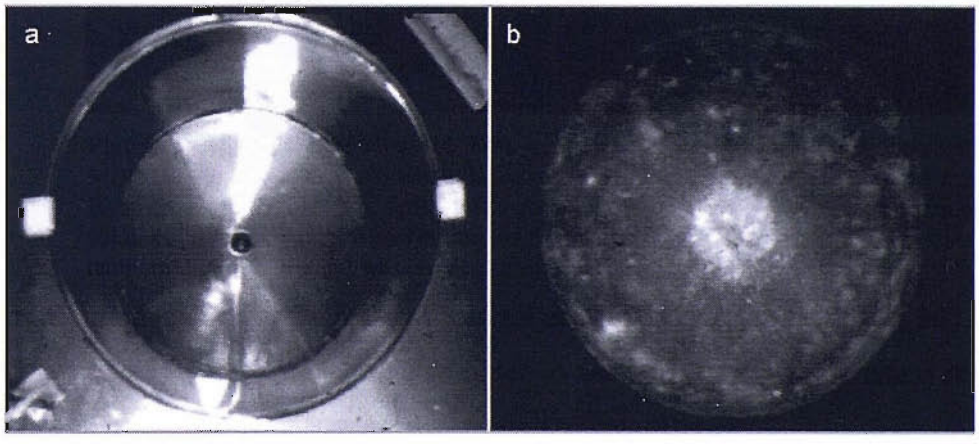

Figure 9.6: Images showing the NPL reference vessel with ambient light (a) and MBS(C)L light emission (b) when the vessel was driven at 500 W. Intensified image b is an amalgamation of a series of individual images. The sonochemiluminescent solution in the reference vessel contained 5 μM luminol and 0.1 M Na_2CO_3, was at room temperature (~25 °C) and was not degassed.

Intensified images of the reference vessel at 20, 50, 100, 150, 200,250, 300, 350, 400, 450 and 500 W were recorded in order to ascertain how the variation in the drive power affected the light emission from the reference vessel.

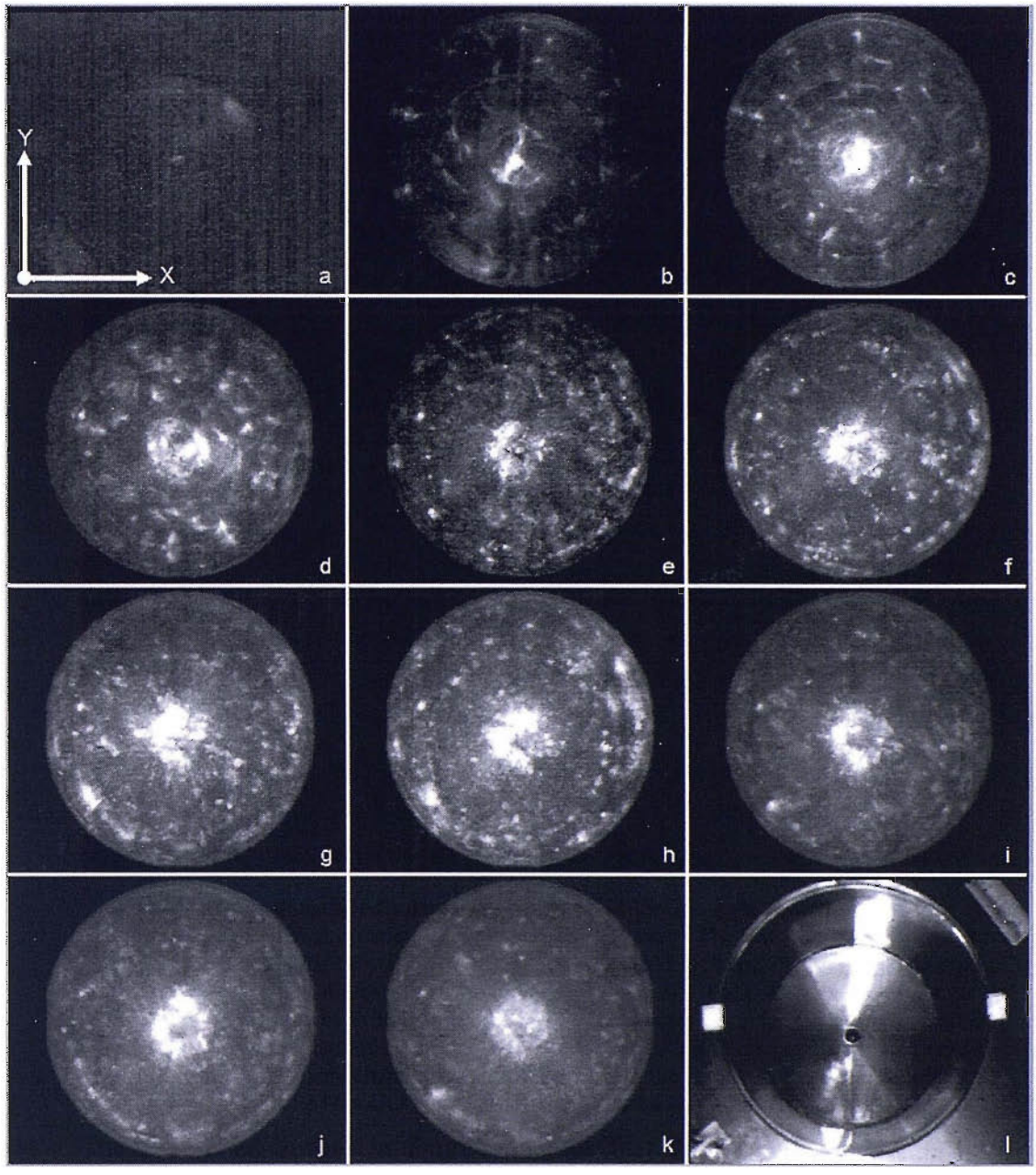

Figure 9.7: Intensified images showing the MBS(C)L light emission from the NPL reference vessel at a variety of different drive powers. The images a – k relate to drive powers of 20, 50, 100, 150, 200, 250, 300, 350, 400, 450 and 500 W respectively and image l is an ambient light image of the vessel. Each intensified image is an amalgamation of over 20 individual images; for images a – h the images were acquired at an intensifier gain of 10, image I was at a gain of 9.5 and images j and k an intensifier gain of 8. The sonochemiluminescent solution in the reference vessel contained 5 μM luminol and 0.1 M Na_2CO_3, was at room temperature (~25 °C) and was not degassed.

The intensified images in figure 9.7 show that the location of the light emission within the reference vessel changes significantly as the drive power is increased. At 20 W (the lowest power investigated and image a in figure 9.7) no significant light emission is recorded as would be expected from the photon counter measurements in figure 9.3. When the power of the vessel is increased to 50 W it becomes possible to see the presence of sonochemical luminescence towards the centre of the bath. The

intensity of the light emission at the centre of the bath increases at 100 W and in addition the presence of concentric rings away from the centre of the vessel becomes apparent; suggesting the presence of cavitation. At 150 – 250 W (images d –f respectively) the level of light emission surrounding the central spot increases and the central area of luminescence becomes less concentrated. The looser nature of the central spot is likely to have been partially responsible for the reduction in the photon counter measurements at these powers compared to those at 100 W; the photon counter being situated directly above the centre.

At drive powers above 300 W (figure 9.7 images g-k) the light emission steadily increases with the drive power and a hot spot at the bottom left of the vessel becomes apparent. To acquire images i, j and k recorded at powers of 400, 450 and 500 W respectively, the amplification of the camera had to be reduced due to the intense emission recorded at the centre of the vessel. As a result any activity away from this central point became harder to identify. Interestingly at the drive powers of 350, 400 and 450 W (images h, i and j respectively) it would appear that at the very centre of the central area of luminescence there is a reduction in the level of light emission.

9.2. Surface event measurement

The electrochemical monitoring of the presence of surface cavitation erosion/corrosion events within the NPL reference vessel required the use of specific equipment designed for this purpose. As was discussed in chapter 7 it was not possible to conduct electrochemical measurements in the tank without the use of specialised optocoulped current followers described previously. The novel current followers were required as a consequence of the interference caused by the earthed metal tank out of which the reference vessel was constructed. Using the fast unipolar optocoupled current follower it was possible to conduct measurements within the vessel with an acceptable level of electrical interference.

In order to allow the movement and exact positioning of the working electrode within the reference vessel the electrode was mounted at the end of a 45 cm long glass tube by means of an SQ13 screw joint and the glass tube which in turn was attached to the to the XYZ positioning stage. A silver wire counter/reference electrode was attached

to the outside of the glass tube and to keep electrical interference to a minimum shielded coaxial cable was used to connect both electrodes to the current follower. The setup used to conduct the measurements can be seen in figure 9.8.

The electrochemical surface erosion/corrosion measurements conducted within the reference vessel where all done so with a titanium working electrode held at 0 V *vs.* a silver wire counter/reference electrode. The current time transients induced by surface events on the electrode were recorded using a Tie Pie Engineering HS3 Handyscope USB oscilloscope and the number of events counted using an Amptek Pocket MCA 8000A Multi Channel Analyser (MCA). Unlike for other scanning measurements conducted as part of this thesis it was not possible to integrate the control programs for the MCA and the reference vessel and as a result the scanning of the vessel had to be conducted manually.

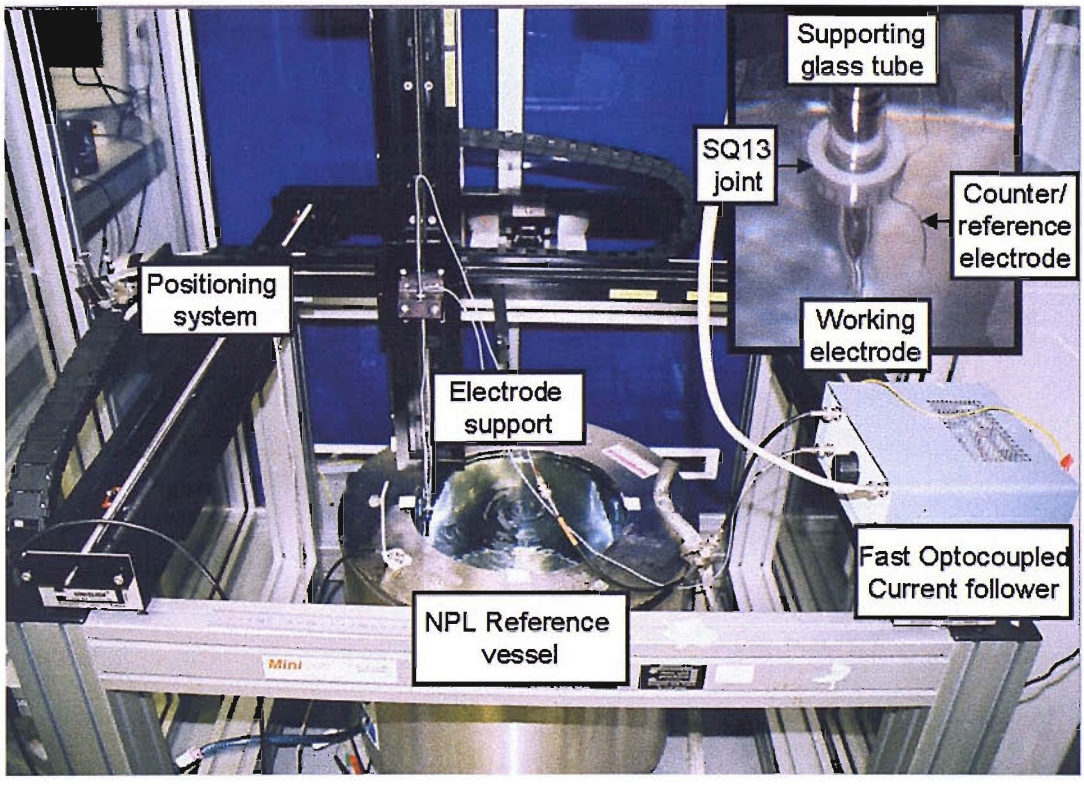

Figure 9.8: Image showing the experimental setup for the surface erosion/corrosion measurements in the NPL reference vessel.

The high powered conditions and long exposure time needed to conduct multiple or scanning measurements made it necessary that titanium electrodes rather than aluminium electrodes be used. In spite of titanium having been shown to be substantially better at withstanding the destruction caused by the action of cavitation on the surface of the electrode, the working electrodes had to be replaced after around

1 hour of exposure to the high power ultrasound due to the damage caused. An example of a damaged titanium electrode can be seen in figure 9.9 a. Damage due to the action of the cavitating liquid was not confined to the working electrode. In the same way the silver wire counter/reference electrodes became pitted and damaged after extended exposure to the conditions within the tank. To keep the electrode in working order it was cleaned with 1200 grade silicon carbide paper before each experiment. The damage caused to the reference electrode can be seen in figure $9.9b_{1\&2}$.

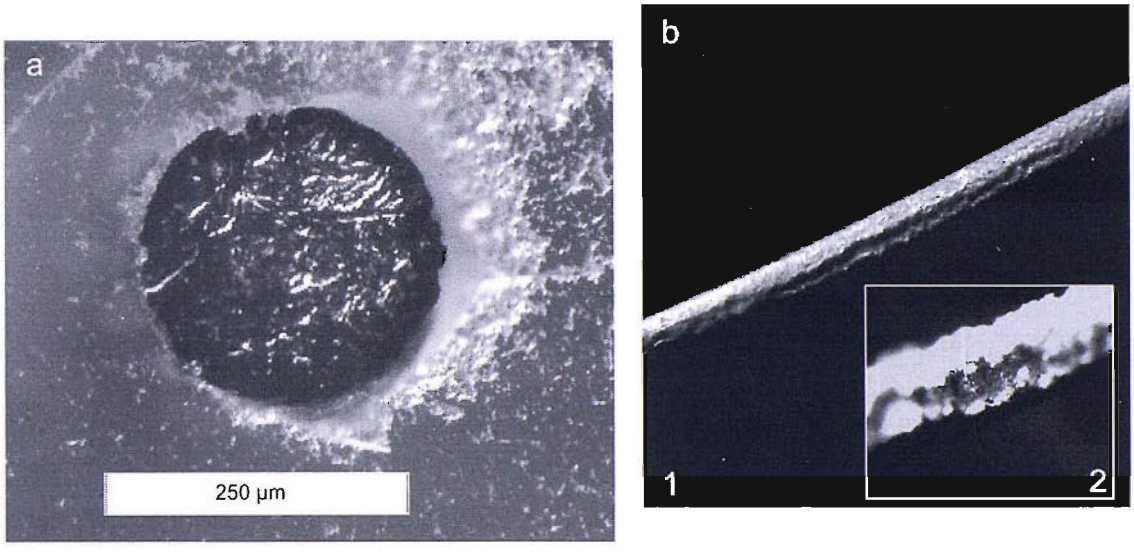

Figure 9.9: Images showing the damage done to the titanium working electrode (a) and the silver wire counter/reference electrode (b1 & 2) by the action of cavitation within the NPL reference vessel.

9.2.1. Individual measurements

Figure 9.10 shows a typical time current trace recorded from an electrode in the centre of the reference vessel. The use of the optocoupled current follower required to make measurements within the vessel results in the shape of the transients being less defined than those recorded in idealised conditions at either the tip of an ultrasonic horn or in an insulated reactor.

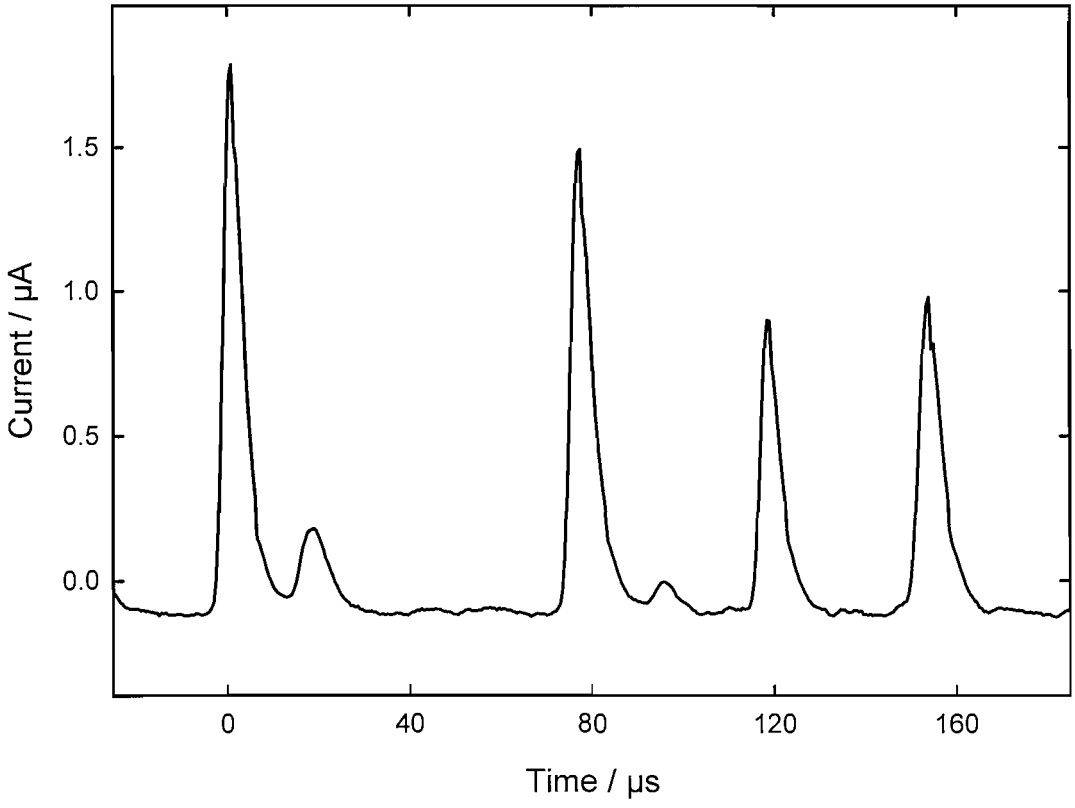

Figure 9.10: Time current trace showing a series of surface cavitation events recorded at the central point of the NPL reference vessel driven at 150 W. Events recorded on a 250 μm Ti electrode held at 0 V vs. an Ag counter/reference electrode in a 0.1 M $NaNO_3$ solution. Measurement made using the fast optocoupled current follower with the 1 MHz low pass filter.

In figure 9.11 the level of surface erosion/corrosion activity at the centre of the reference vessel is compared as a function of drive power. Trace A shows the number of events greater in magnitude than 0.18 μA. This shows a close correlation between the number of events recorded in 30 s and the drive power of the vessel. For trace B the threshold above which events were counted was increased to 1 μA. As a result the variation in the number of events recorded with the drive power of the vessel alters substantially. The number of events increases with drive power to a maximum at 100- 150 W before then decreasing as the power is increased further. This implies that at lower drive powers there are a small number of high magnitude surface events. When the drive power of the reference vessel is increased the number of events recorded increases but the magnitude of these events reduces significantly.

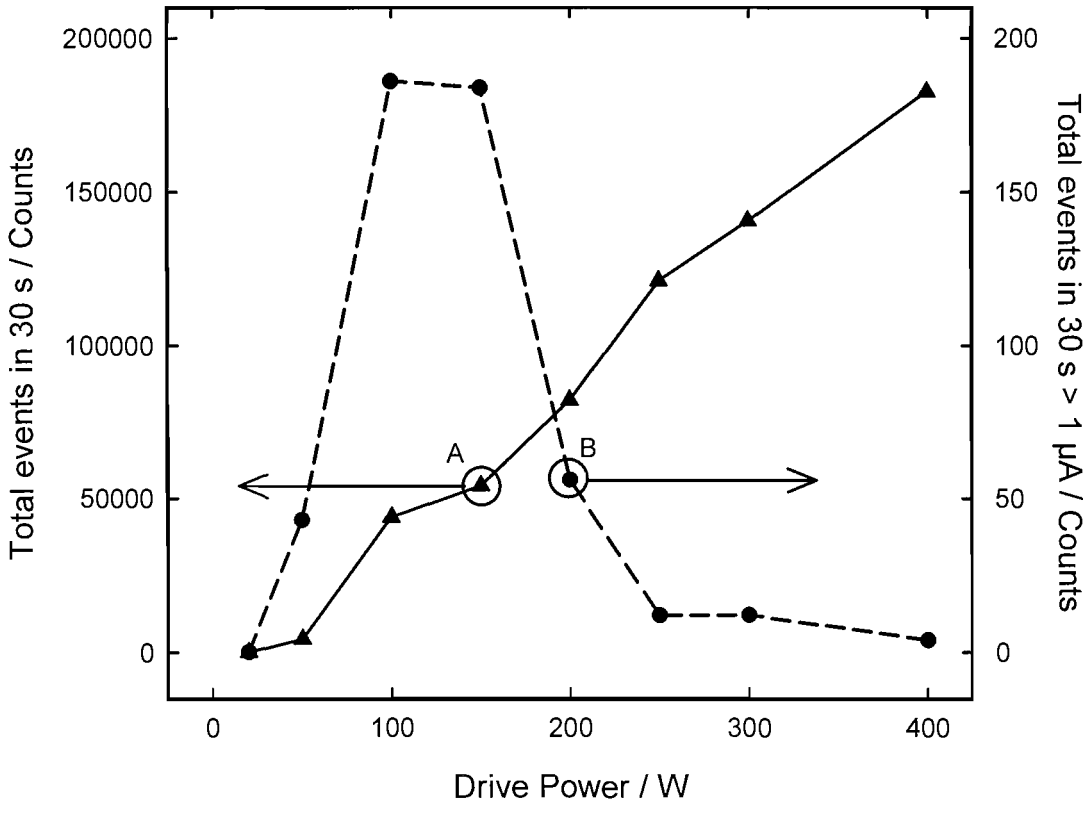

Figure 9.11: Plots showing the variation in the number of surface erosion/corrosion events recorded on an electrode at different drive powers. Plot a shows the number of events recorded greater than 0.18 μA and plot b shows the number of events greater than 1 μA. A 250 μm diameter titanium working electrode was held at 0 V vs. a silver wire counter/reference electrode. The vessel contained an aqueous solution of 0.1 M $NaNO_3$ at room temperature and was not degassed.

Figure 9.12 shows the maximum peak height recorded at each of the different drive powers along with the number of events with a magnitude >1 μA for the same powers. A clear relationship between the two can be seen with the maximum peak size reducing at higher drive powers in the same way that the number of events tails off. This supports the proposal that, although the number of events generally increases as the power increases, the magnitude of the events decreases.

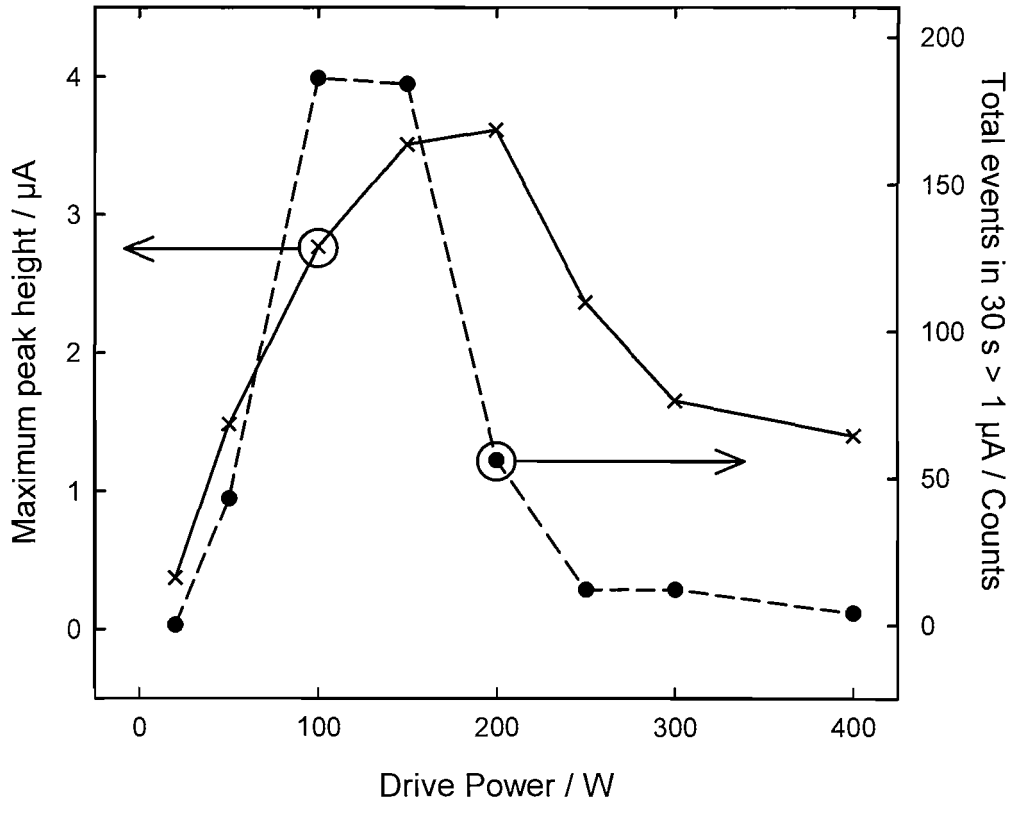

Figure 9.12: Plots showing the correlations between how the maximum peak height (——) and the number of events greater than 1 μA (- - - -) at the centre of the NPL reference vessel vary as a function of the drive power. Recorded on a 250 μm diameter titanium working electrode held at 0 V *vs.* a silver wire counter/reference electrode. The vessel contained an aqueous solution of 0.1 M Na_2NO_3 at room temperature and was not degassed.

9.2.2. Scans of the vessel

Each individual measurement within the vessel took approximately one minute; the images of the damaged working electrode in figure 9.9 have shown that prolonged exposure to the conditions within the reference vessel causes the deformation of the surface of the working electrode leading to degradation in the quality of the results recorded. Consequently it was felt to be impractical to conduct scans of the entire vessel, instead a series of line scans were conducted across the centre of the vessel (in the same plane as the drive transducers) at a number of different drive powers[§]. All the scans were conducted in the X axis of the positioning as marked on figure 9.7a.

[§] The number of scans that could be undertaken on the NPL reference vessel was constrained by the amount of time during which the reference vessel was available and by the logistics of transporting all the relevant equipment from Southampton in order to conduct the measurements. If the reference vessel was more easily accessed then the number and extent of the scans conducted could have been extended.

Scans of the vessel were conducted at five drive powers (20, 100, 200, 350 and 500 W). Figure 9.13 shows three successive scans across the reference vessels at a drive power of 100 W.

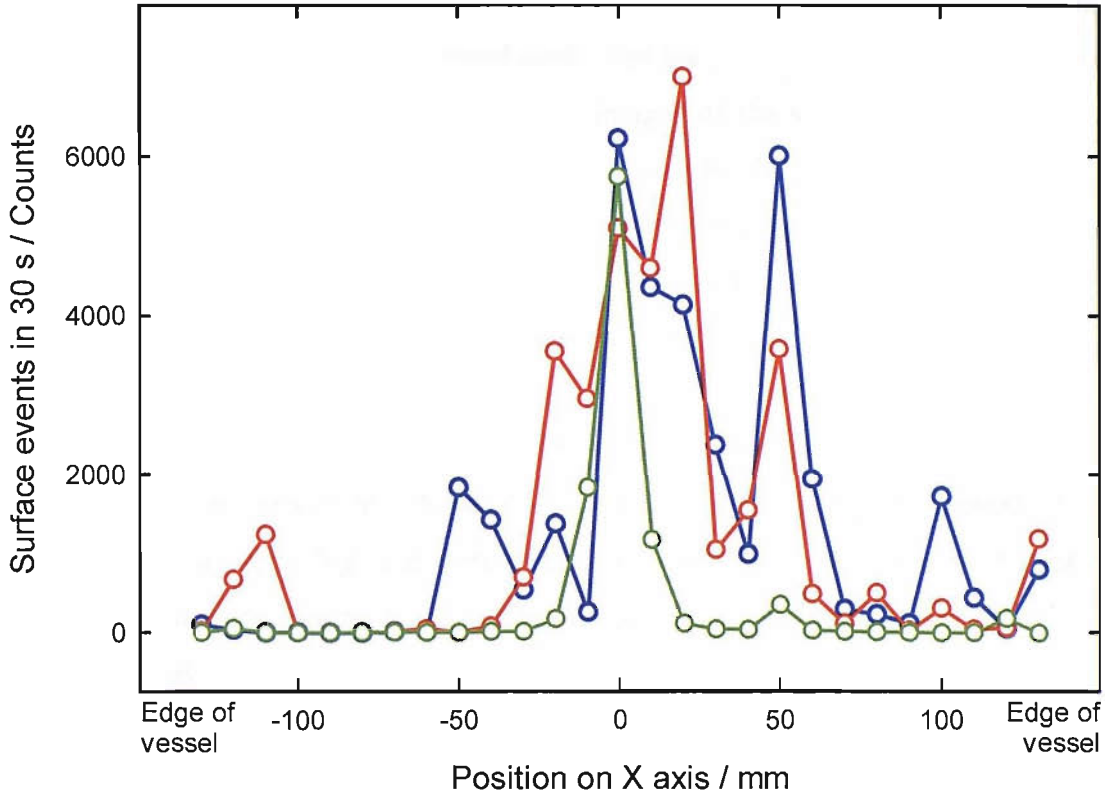

Figure 9.13: Plot showing three successive surface erosion/corrosion scans across the X axis of the NPL reference vessel at 100 W. The scans were conducted in the same plane as the transducers using a 250 μm diameter titanium working electrode held at 0 V *vs.* a silver wire counter/reference electrode and events with a magnitude greater than 0.6 μA were recorded using the MCA. The vessel contained an aqueous solution of 0.1 M Na_2NO_3 at room temperature and not degassed.

The three scans of the reference vessel presented in figure 9.13 all show the greatest level of activity to be located towards the centre of the vessel in correlation with the intensified images of the vessel (figure 9.7 image c). Events are also recorded at +50 and +100 mm from the centre on all of the scans indicating that the cavitation activity is not restricted to the centre of the vessel.

Figure 9.14 shows a series of scans conducted across the reference vessel at 20, 200, 350 and 500 W drive powers. As be expected from the light emission measurements in figure 9.2 and 9.3 only a small number of surface erosion/corrosion events were recorded at a drive power of 20 W. When the power was increased to powers at which significant light emission had been recorded (200-500 W) then a similar

distribution of surface activity is seen to that in figure 9.13 for a drive power of 100 W with a central maxima and limited number of events away from this. The scan conducted at 200 W shows the greatest activity away from the central maxima. In particular at the edge of the vessel there is a marked increase in the surface activity. At 350 and 500 W drive powers the scans are dominated by the central region of activity at the focal point of the transducers. For the 500 W drive power this would appear to be consistent with the intensified images of the vessel where the area of light emission is concentrated exclusively towards the centre of the reactor. Conversely the intensified image of the vessel being driven at 350 W shows significant areas of light emission away from the central area which are not mirrored by the presence of surface erosion/corrosion activity.

However the electrochemical and MBS(C)L measurements are broadly and encouragingly in agreement. Areas of high light emission (e.g. the centre of the reference vessel) show high numbers of erosion/corrosion events. Lastly it must be remembered that the electrochemical sensor is a point sensor while the MBS(C)L has a comparatively vast depth of field and hence large active sensing volume.

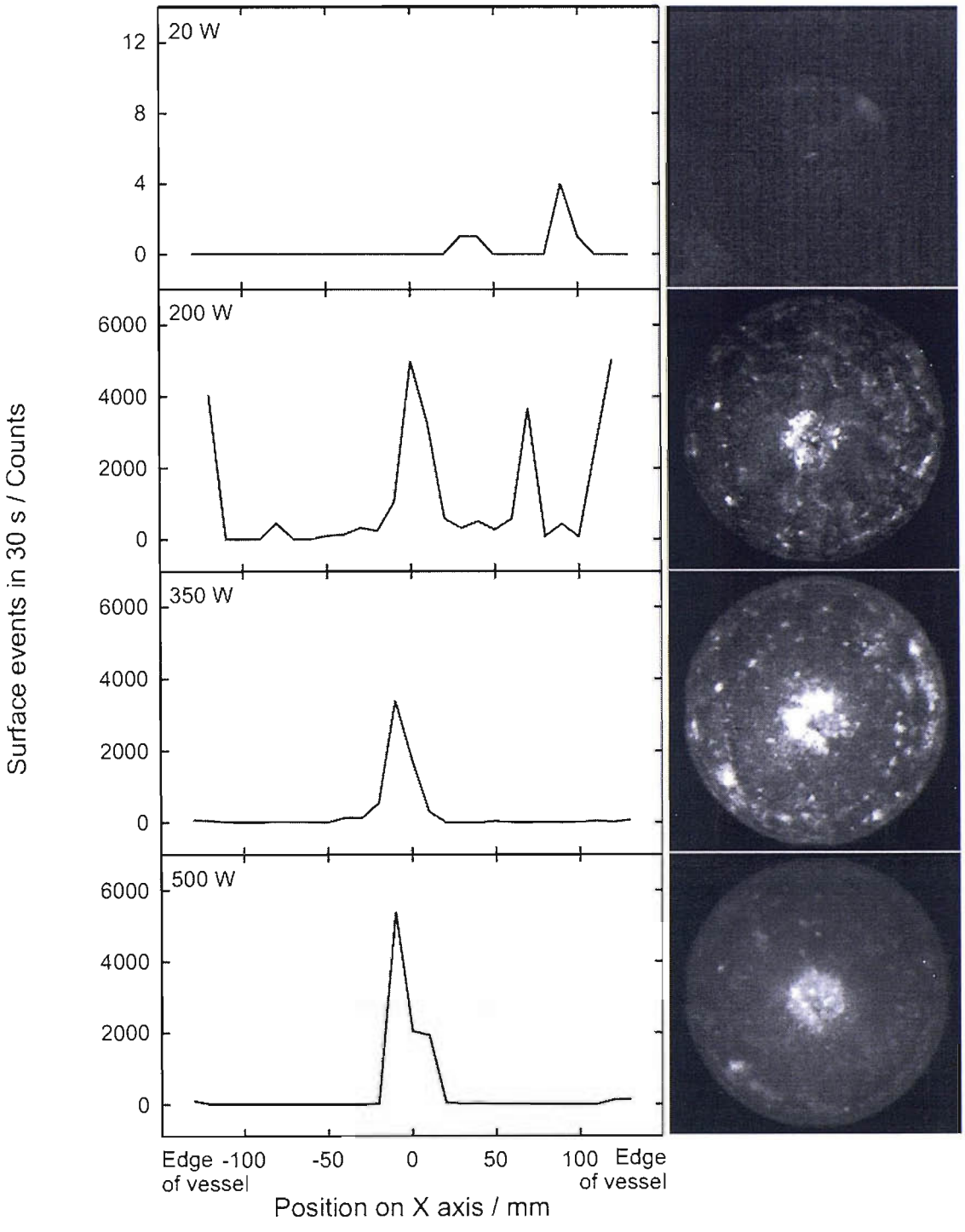

Figure 9.14: Plot showing surface erosion/corrosion scans across the X axis of the NPL reference vessel at 20, 200, 350 and 500 W. The scans were conducted in the same plane as the transducers using a 250 μm diameter titanium working electrode held at 0 V *vs.* a silver wire counter/reference electrode. For the 20, 350 and 500 W drive powers events with a magnitude greater than 0.6 μA were recorded and for 200 W events greater than 1 μA. The vessel contained an aqueous solution of 0.1 M $NaNO_3$ at room temperature and not degassed.

9.3. Chemical change measurements

To ascertain the rate of chemical change taking place within the reference vessel, during sonication, the production of I_3^- was monitored through two separate methods; electrochemical measurements and UV/Visible spectroscopy. Whilst at NPL electrochemical measurements were made using a three electrode flow cell and the slow bipolar optically isolated current follower. After a period of sonication an aliquot of solution was removed from the vessel and the concentration measured using UV/Vis spectroscopy on return to Southampton.

Due to technical problems associated with making measurements in the reference vessel no I_3^- was recorded using either UV/Visible or electrochemical methods. Contributing to this was the dilution of any localised formation of I_3^- through out the entire volume of the reference vessel through acoustic streaming and diffusion. The frequency at which the reference vessel operates is also not conducive to high rates of chemical change, previous studies (*62, 128*), as well as work reported earlier in this thesis (chapter 6) have shown that higher drive frequencies are more likely to generate chemical change. The results from the chemical measurements recorded have been included in appendix A for completeness.

9.4. Comparison of measurements

It is instructive to compare the results acquired using the various different methods to see if there is any correlation between the areas of increased activity. In addition to the light emission, surface erosion/corrosion activity and chemical measurements conducted in this chapter the author also had access to pressure and broadband emission measurements conducted by the NPL. It is obviously problematic to quantitatively compare the light emission results in the form of an intensified image with other results. This was overcome by taking the averaged intensified image of the reactor and manipulating it within MATLAB to elucidate the relative luminance across the vessel. For the purposes of this comparison the chemical measurements were ignored given the lack of spatial information and that the results were limited to only a single drive power.

The acoustic pressure measurements received from NPL were RMS (Root Mean Squared) values of the pressure signal. This makes relating the values recorded to the real pressures experienced difficult. From measurements seen in other environments it has been seen that in an active cavitating volume the recorded pressure trace is not sinusoidal. Therefore the actual pressure signal from the hydrophone is likely to differ from that which would be expected from the RMS output. The calculated pressure threshold for these comparisons is the RMS value of the sinusoidal wave with the same amplitude.

Figure 9.15 shows a comparison of the light emissive, acoustic pressure, broadband acoustic emission and surface erosive/corrosive measurements at a drive power of 100 W. There is a clear correlation between the measurements with the three measurements that rely on the effects of cavitation (surface erosion/corrosion activity and light and broadband acoustic emissions) all showing a concentration of activity towards the centre of the reference vessel quickly subsiding towards that edges of the reactor. The pressure measurement is more complicated with a series of maxima proceeding from the edge of the vessel with the greatest maxima falling at the centre of the vessel where the other measurements also reach their zenith. The acoustic pressure exceeds the calculated pressure threshold at a number of points away from the central maxima, clearly corresponding to increases in the cavimeter output but with ambiguous correlation to the surface erosion/corrosion and light emission measurements.

Figure 9.16 extends the comparison to a drive power of 200 W. Here the correlation between the different measurements is not as well defined. Whereas the pressure, broad band emission and surface erosion/corrosion activity all have a definite peak at the centre of the reference vessel the light emission would appear to reduce at the very centre of the reactor with peaks either side. Interestingly the pressure, broadband emission and surface erosion/corrosion activity all show an increase at the edges of the vessel (+/- 140 mm). Though the pressure at the centre of the bath is less than that seen at 100 W drive power, the calculated inertial pressure threshold is exceeded at more points across the scan; noticeably at the edges where the elevated activity is recorded.

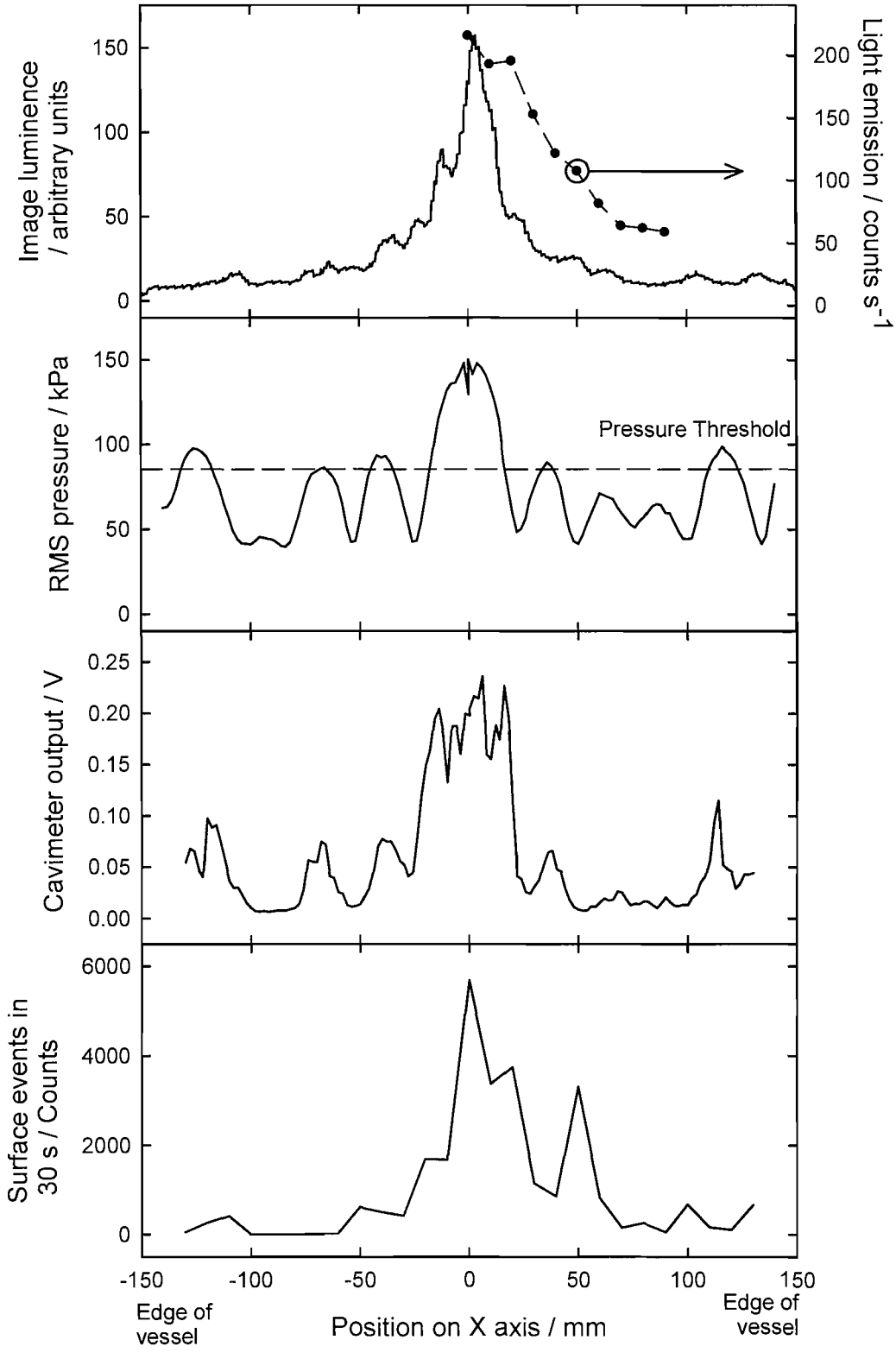

Figure 9.15: Plots comparing the light emission, pressure, cavitation sensor and surface erosion/corrosion measurements across the X axis of the NPL reference vessel at a drive power of 100 W. The luminance trace was calculated from an intensified image of the vessel containing a sonoluminescent solution using Matlab, the accompanying light emission trace (- - -) was collected using the photon counter mounted 25 cm above the reactor and collimated using a 7 cm tube. Pressure and cavitation traces produced by the NPL with a resolution of 2 mm; calculated expansive pressure threshold (- - -). The surface erosion/corrosion trace is the average of the three traces presented in figure 9.13.

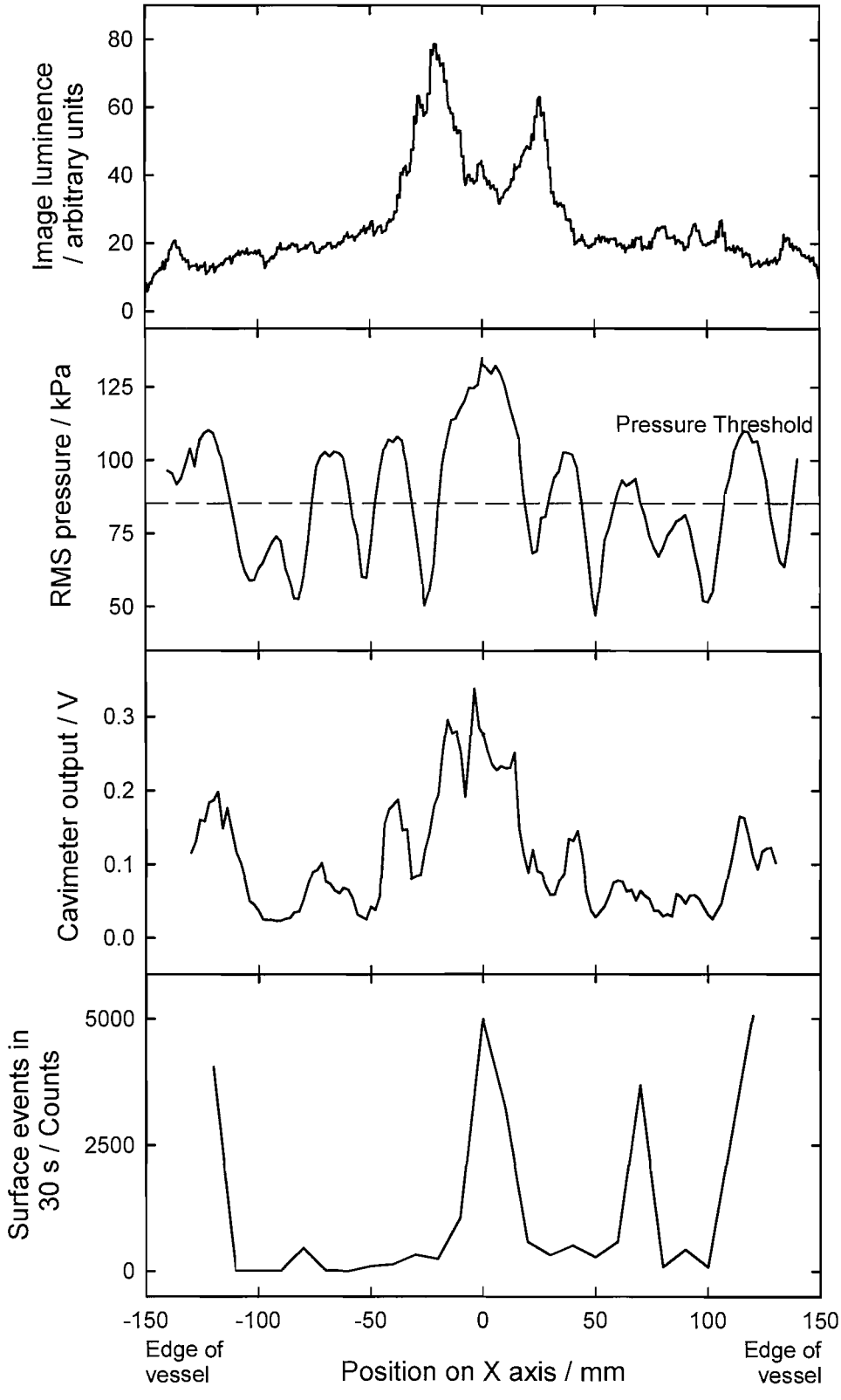

Figure 9.16: Plots comparing the light emission, pressure, cavitation sensor and surface erosion/corrosion measurements across the X axis of the NPL reference vessel at a drive power of 200 W. The luminance trace was calculated from an intensified image of the vessel containing a sonoluminescent solution using Matlab. Pressure and cavitation traces produced by the NPL with a resolution of 2 mm; calculated expansive pressure threshold (---). The surface erosion/corrosion trace is that in figure 9.14.

9.5. Effect of sensors on light emission

Imaging an ultrasonic reactor whilst a sensor is added or removed offers a quick and simple method for ascertaining whether the sensor is in any way effecting the cavitation within the reactor. Any alteration in the cavitation within the reactor will manifest itself as a change in the level of light emission recorded as well as the distribution of that emission. In this section we shall show the effect of the NPL broadband acoustic emission cavitation sensor on the light emission from a number of different cavitating cells. First, we shall see the effect of an unsoaked sensor on a single transducer ultrasonic reactor (the worst case scenario). Second, we shall see the effect of a soaked sensor on the light emission from a small ultrasonic cleaning containing both water and a solution containing the surfactant recommended by NPL. Finally we shall examine the effect of the NPL sensor on the light emission generated by the NPL reference vessel and at the same time consider the disruptive influence of an electrode.

9.5.1. In a single transducer reactor

An un-soaked NPL broadband acoustic cavitation sensor was lowered into a single transducer ultrasonic reactor (reactor 4) containing 1000 ml of water in 5 mm steps. At each point the reactor was imaged using the Photek intensifier based imaging system to ascertain the location of any light emission. The drive frequency of the reactor (23 kHz) was selected such that a stable mode was formed within the reactor, characterised by a series of parallel bands of luminescence as can be seen in figure 9.17 image a. Figure 9.17 shows both low light and ambient light images of the sensor as it just breaks the surface of the solution (images c and d for the low light and ambient light images respectively), with the sensor 5 mm into the solution (images e and f) and with the sensor fully submerged in the solution within the reactor (images g and h).

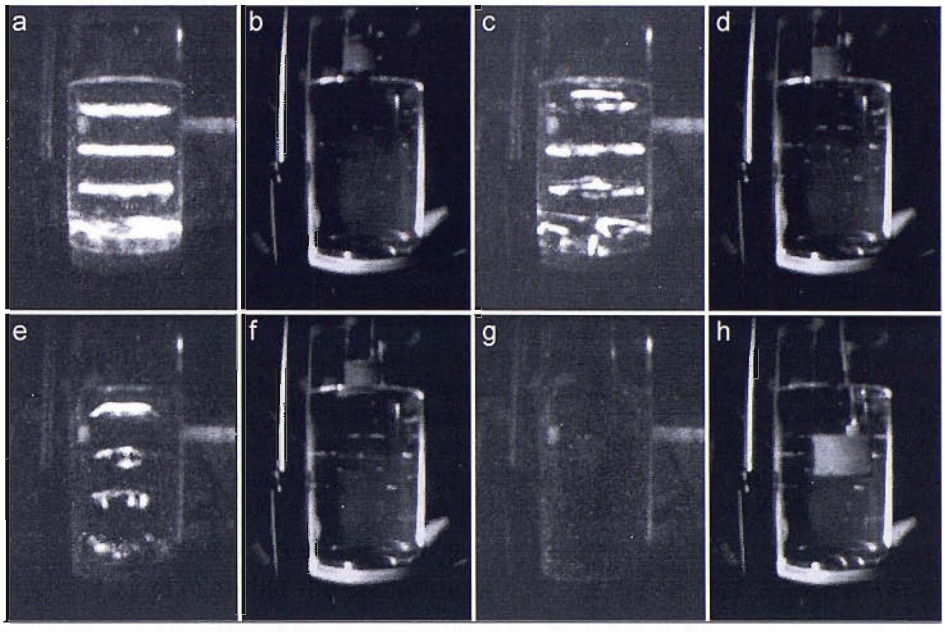

Figure 9.17: A series of images showing the effect that placing a non-soaked NPL cavitation sensor has on the light emission from reactor 4. The images show the reactor without sensor (a & b), with the sensor just touching the surface of solution (c & d), the sensor submerged 5 mm into the reactor (e & f) and with the sensor fully submerged within the reactor (g & h). The intensified images are an amalgamation of 100 individual images. Reactor 4 was driven at 150 V and contained 1 dm^3 of distilled water.

Figure 9.17 shows that the stable mode seen in the reactor before the sensor is added (image a) quickly changes as the sensor is introduced. When the NPL sensor is only just touching the surface the base of the sensor can be seen to be inducing a localised increase in cavitation (image c), characterised by the small area of luminescence at the top of the reactor. Further down the reactor the two bands corresponding to the first and second bands in image a can be seen to be somewhat deformed in comparison. When the sensor is lowered further into the reactor (image e) the effect on the luminescence is even greater with the banding seen in image a being replaced by three points of luminescence including the base of the sensor. Once the sensor has been fully lowered into the reactor (image g) no luminescence is seen; the mode within the reactor totally disrupted. This is not surprising given that the sound field within the reactor is going to be adversely affected by any change in volume or bubble population (*62, 155*), both of which are likely as a result of the insertion of sensor into the reactor.

9.5.2. In a small cleaning bath

The detrimental effect that the introduction of the NPL sensor had on the light emission from reactor 4 is not surprising; it is known that the sensor needs to have

been pre-soaked before use and the tuned mode seen in the reactor is not typical of the kind of conditions for which the sensor has been developed. To produce a more realistic scenario the effect of the presence of the sensor on the light emission from a small ultrasonic cleaning bath (bath A from chapter 8) was studied. In addition to studying the effect in pure water the sensor was also imaged as it was removed from a solution containing 0.2 % surfactant (Micro) to aid the wetting of the sensor.

The bath was imaged as the sensor was withdrawn from the bath and at the same time the overall level of light emission from the bath was recorded using the photon counter module. This gave a quantitative and qualitative measurement of the effect of the sensor on the light emission.

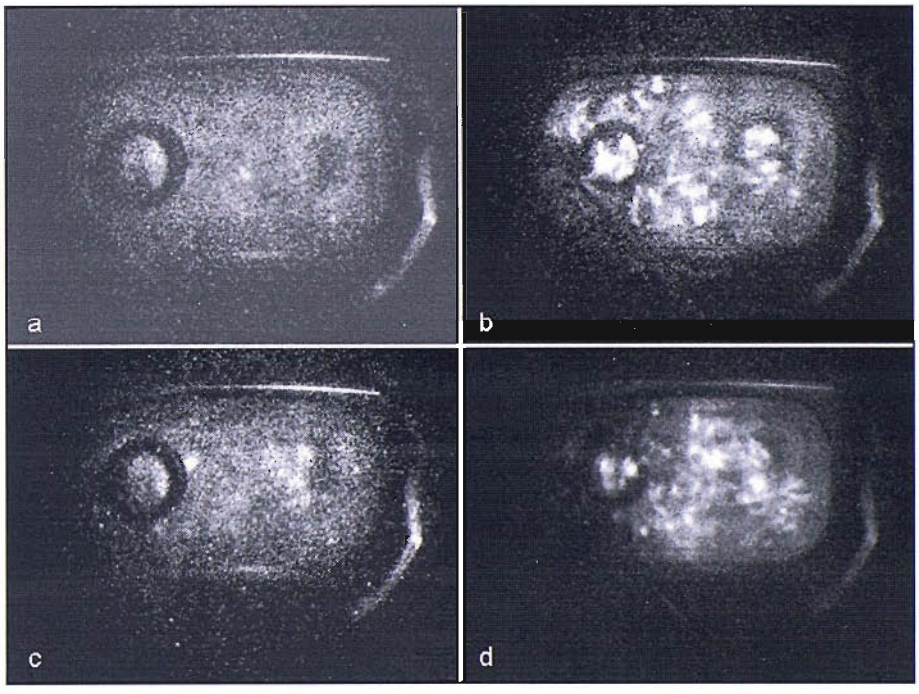

Figure 9.18: Intensified images showing the effect on the MBSL light emission from bath A of the addition of the NPL cavitation sensor with the bath containing water (a & b) and water with surfactant (c & d). Images a & c show the sensor above the level of solution within the bath and images b & d show the sensor fully submerged within the bath. Each intensified image is an amalgamation of 100 individual images. Bath A contained 500 ml distilled water at room temperature; for the measurements with surfactant 1 ml micro surfactant was added.

The images in figure 9.18 showing the sensor fully immersed (b and d) and fully removed (a and c) from the water (a and b) or water with surfactant (c and d) show that there is a limited effect on the distribution of the light emission within the cleaning bath. With the sensor fully immersed in the solution there appears to be a slight increase in the level of emission from the solution within the sensor. There would also appear to be a slight increase in the level of light emission across the bath,

though this is hard to discern purely from the low light images. If the measurements made from the photon counter in figure 9.19 are looked at it is possible to see that the overall level of light emission remains constant regardless of the position of the sensor in relation to the bath. This confirms that the sensor is not greatly affecting the overall light emission from the bath, though it may be affecting the area immediately surrounding it.

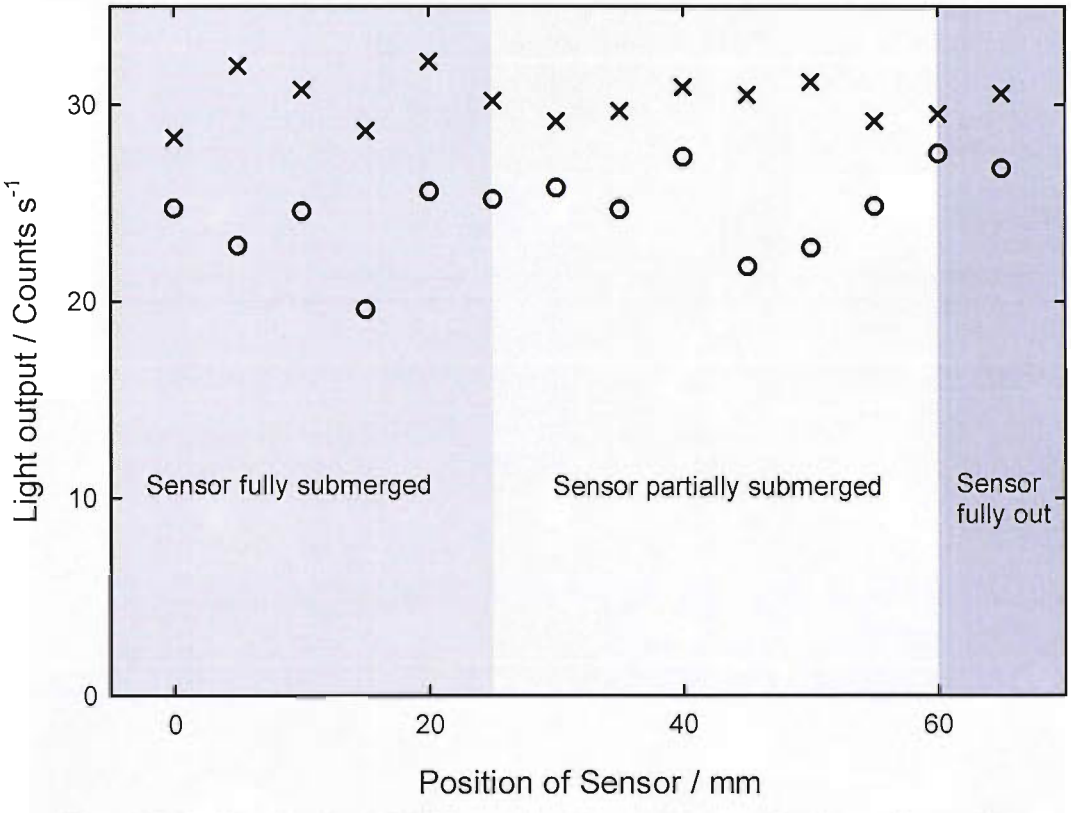

Figure 9.19: Plot showing the light emission from bath A as a function of the position of the NPL sensor in distilled water (o) and water with surfactant (X). Photon counter mounted 15 cm above the bath. Bath A contained 500 ml distilled water and for the surfactant measurements 1 ml of micro surfactant was added.

Interestingly the light level measurements in figure 9.19 show a general increase in the level of light emitted from the bath when the vessel contained surfactant rather than just water.

9.5.3. In the NPL reference vessel

Previously within this chapter we have seen that it is possible to image the NPL reference vessel with the aid of a solution containing luminol. The reference vessel is several times larger than either of the other two vessels so far looked at in this section. Therefore the introduction of the NPL broadband sensor would be expected to have even less of an effect than seen in the ultrasonic cleaning bath. To test this

hypothesis the experiment in figure 9.7 was repeated but with the sensor mounted centrally within the vessel; directly below the camera.

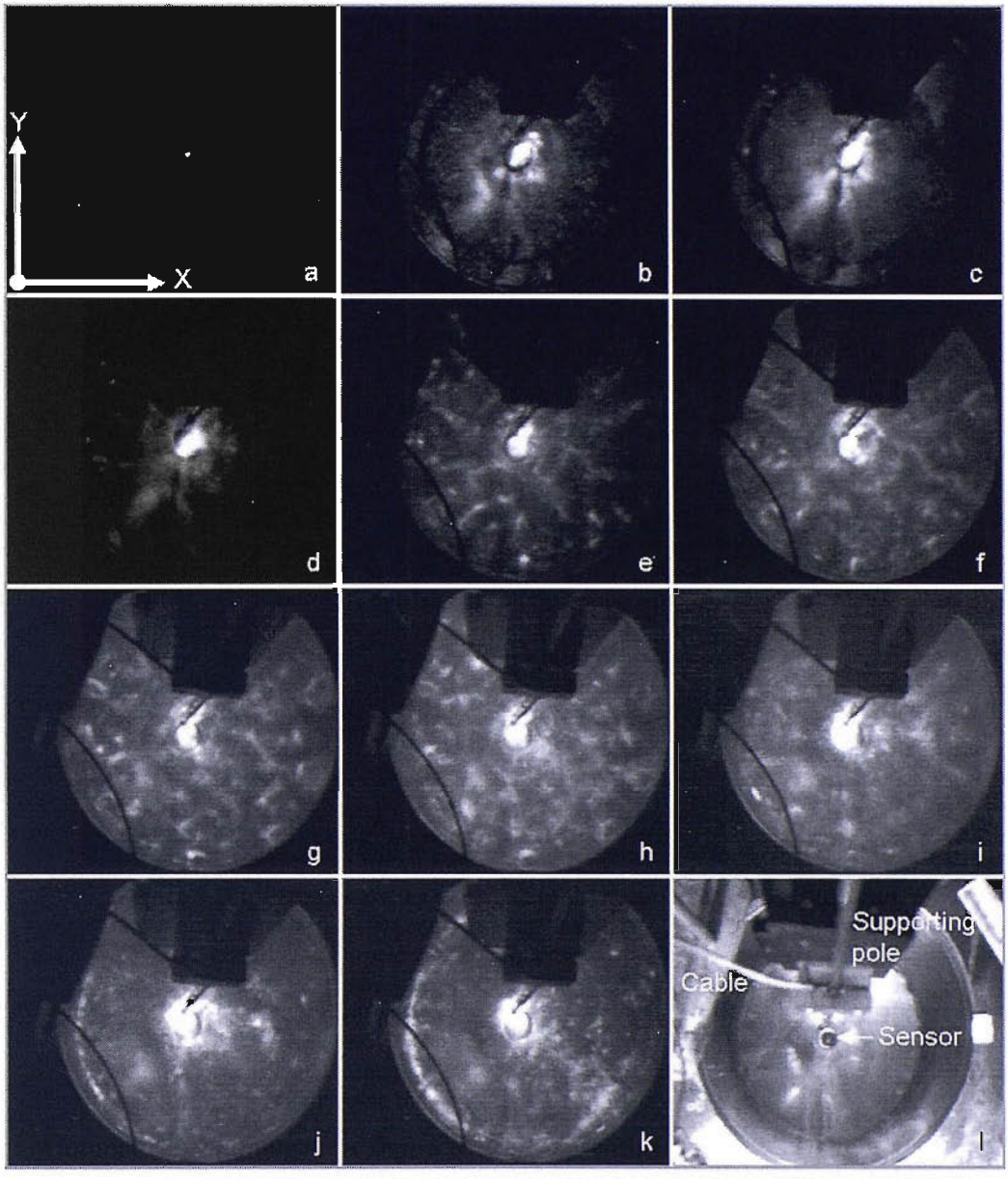

Figure 9.20: Images showing the effect of the presence of the NPL cavitation sensor at the centre of the NPL reference vessel on the MBS(C)L light emission at different drive powers. Images a–k correspond to drive powers of 20, 50, 100, 150, 200, 250, 300, 350, 400, 450 and 500 W respectively; image l shows the position of the sensor in an ambient light image. The sensor was placed centrally within the vessel in the same plane as the transducers. Each intensified image is an amalgamation of at least 10 individual images. The reference vessel contained an aqueous sonoluminescent solution of 5 μM luminol and 0.1 M Na_2CO_3 at room temperature (~25 °C) and was not degassed.

Comparing the images in figure 9.20 taken with the sensor in the centre of the tank with those in figure 9.7 without the sensor a clear difference can be seen. At all powers except 20 W (where no light emission is seen) there is a concentration of the luminescence around the sensor. In particular the concentration of light around the sensor required that a lower gain was used to capture the images between 50 and 300

W in figure 9.20 compared to that used in figure 9.7; acquired without the sensor present. At higher powers (>300 W) the concentration of the luminescence around the sensor enabled the detail in the rest of the bath to be viewed more easily.

To ascertain if the concentration of the luminescence around the sensor seen in figure 9.20 was restricted to the sensor being located in the centre of the bath; the bath was imaged whilst the sensor was scanned across the bath at 10 mm intervals with the vessel operating at a power of 100 W.

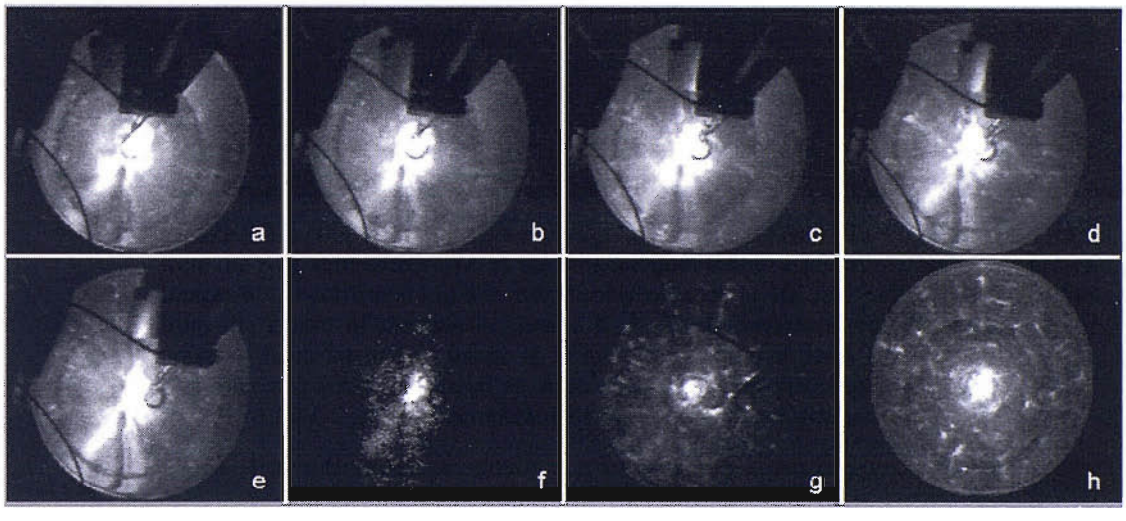

Figure 9.21: Intensified images showing the variation in the MBS(C)L light emission from the NPL reference vessel as the NPL cavitation sensor is scanned across the vessel. Images a – g correspond to a sensor displacement of 0, 10, 20,30, 40, 50 and 100 mm from the centre of the reactor; image h shows the reference vessel with no sensor present. Each intensified image is an amalgamation of at least 10 individual images. The reference vessel contained an aqueous sonoluminescent solution of 5 μM luminol and 0.1 M Na_2CO_3 at room temperature (~25 °C) and was not degassed.

Figure 9.21 shows that as the sensor is moved away from the central axis (images a-e) the area of increased light emission extends towards the sensor. When the sensor has been displaced 50 mm from the centre of the vessel the level of light emission decreases dramatically (image f) and by the time the sensor is at the edge of the bath (image g) the light emission is comparable to that seen when no sensor is present within the bath (image h). The same experiment was repeated with a photon counter positioned directly above the sensor. Simultaneous light emission measurements and broadband acoustic emission measurements were conducted and the resultant plots can be seen in figure 9.22.

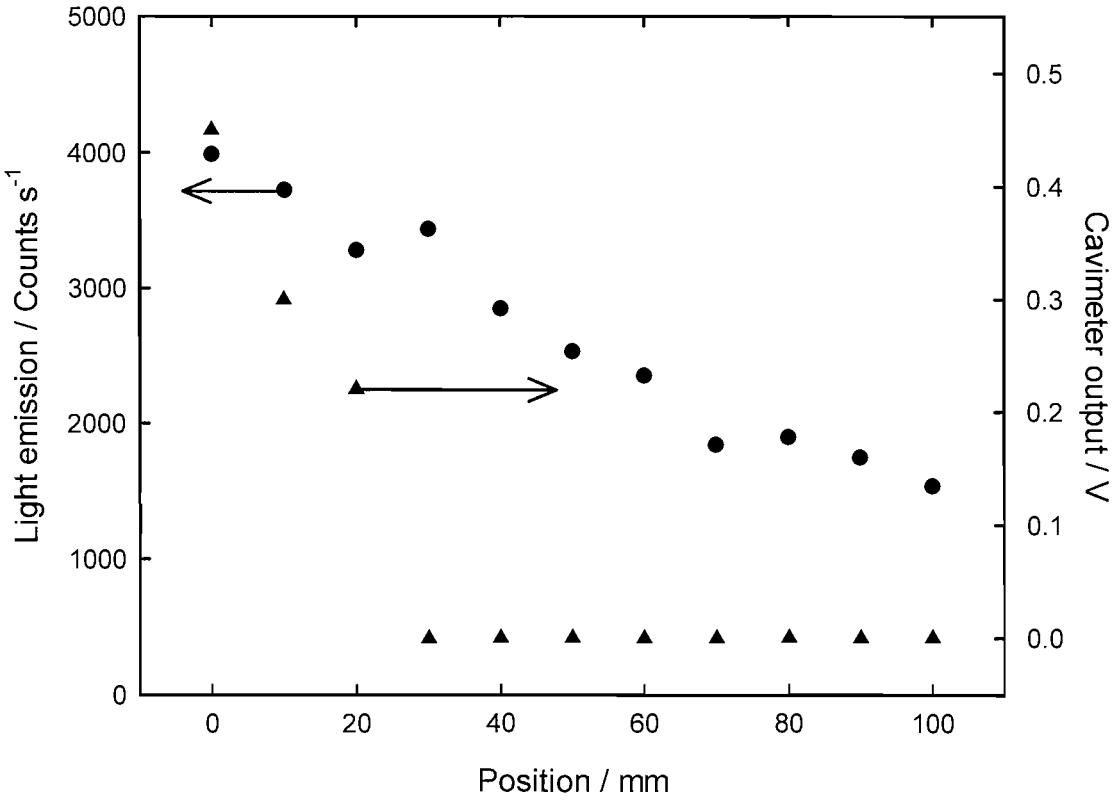

Figure 9.22: Plot comparing the MBS(C)L light emission (•) and NPL cavitation sensor out put (▲) as the sensor is moved away from the centre of the reactor. The photon counter was mounted 5 cm above the reference vessel directly above the cavitation sensor such that it moved with the sensor. The cavitation sensor was mounted so that it was in the same plane as the transducers. The reference vessel contained an aqueous sonoluminescent solution of 5 μM luminol and 0.1 M Na_2CO_3 at room temperature (~25 °C) and was not degassed.

Figure 9.22 shows that while there was a rapid reduction in the measured broadband emission from the sensor as it was removed from the centre of the reference vessel the light emission measurements reduced in a steady manner over the entire distance of the scan. The steady reduction in the light emission over the entire duration of the scan was thought to be as a result of the wide angle over which the photon counter was measuring. A 70 mm long, 14 mm diameter, black cardboard tube was placed over the end of the photon counter collimating the light entering the photon counter; making the measurement more specific to the region of the NPL sensor. Figure 9.23 shows that the simultaneous broadband sensor and collimated photon counter measurements now follow the same shape with a central peak decaying rapidly towards the edge of the vessel.

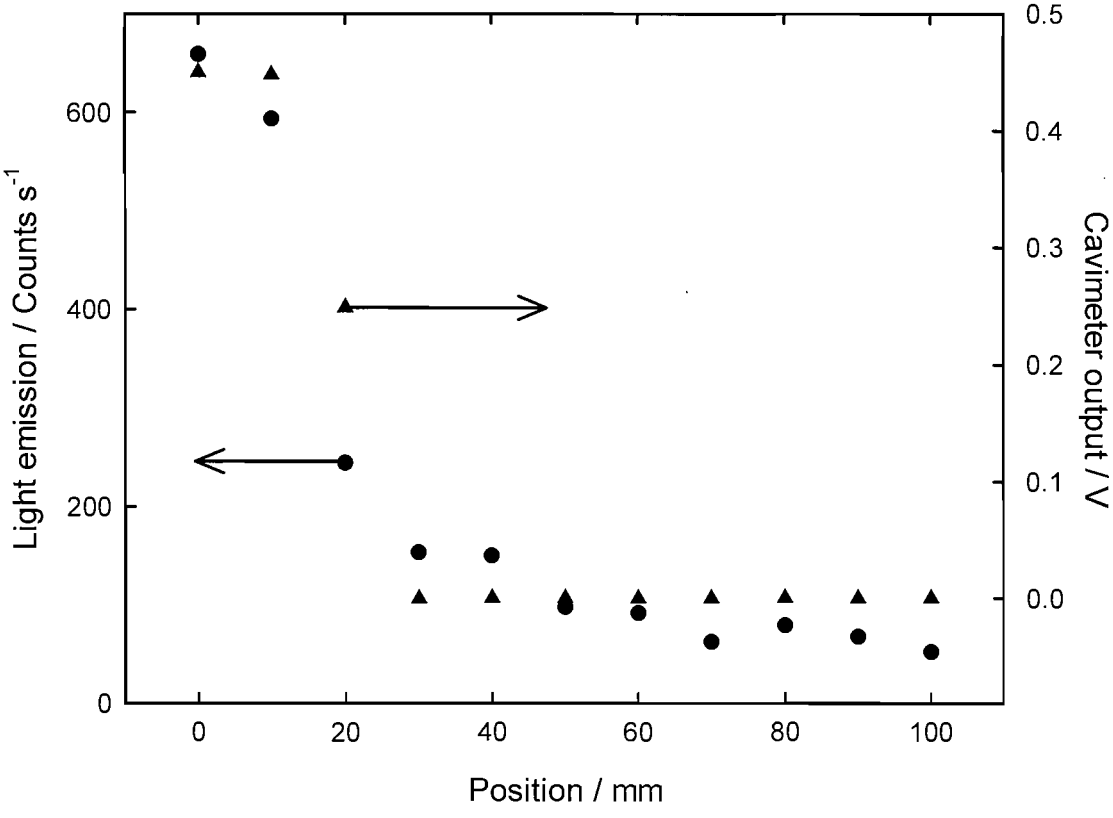

Figure 9.23: Plot comparing the MBS(C)L light emission (•) and NPL cavitation sensor output (▲) as the sensor is moved away from the centre of the reactor. The photon counter was mounted 5 cm above the reference vessel directly above the cavitation sensor such that it moved with the sensor; to increase the spatial specificity of the measurement a collimator was used. The cavitation sensor was mounted so that it was in the same plane as the transducers. The reference vessel contained an aqueous sonoluminescent solution of 5 μM luminol and 0.1 M Na_2CO_3 at room temperature (~25 °C) and was not degassed.

If we compare the level of light emission in figure 9.22 from the un-collimated photon counter to the emission in figure 9.23 from the collimated photon counter it can be seen that the level of emission recorded has dropped significantly from 4000 counts s^{-1} to 700 counts s^{-1}. To see the effect of the sensor on the level of light emission from the reference vessel the photon counter was scanned across the reference vessel without the sensor present. Figure 9.24 compares the light emission with (x) and without (o) the sensor present. At the centre of the vessel a significant (~500 counts s^{-1}) increase in the light emission is seen when the sensor is present. As the sensor is moved off axis the light emission returns to a similar level to that seen without the sensor. This is in agreement with the images in figure 9.21 where as the sensor is moved away from the centre the light emission reduces.

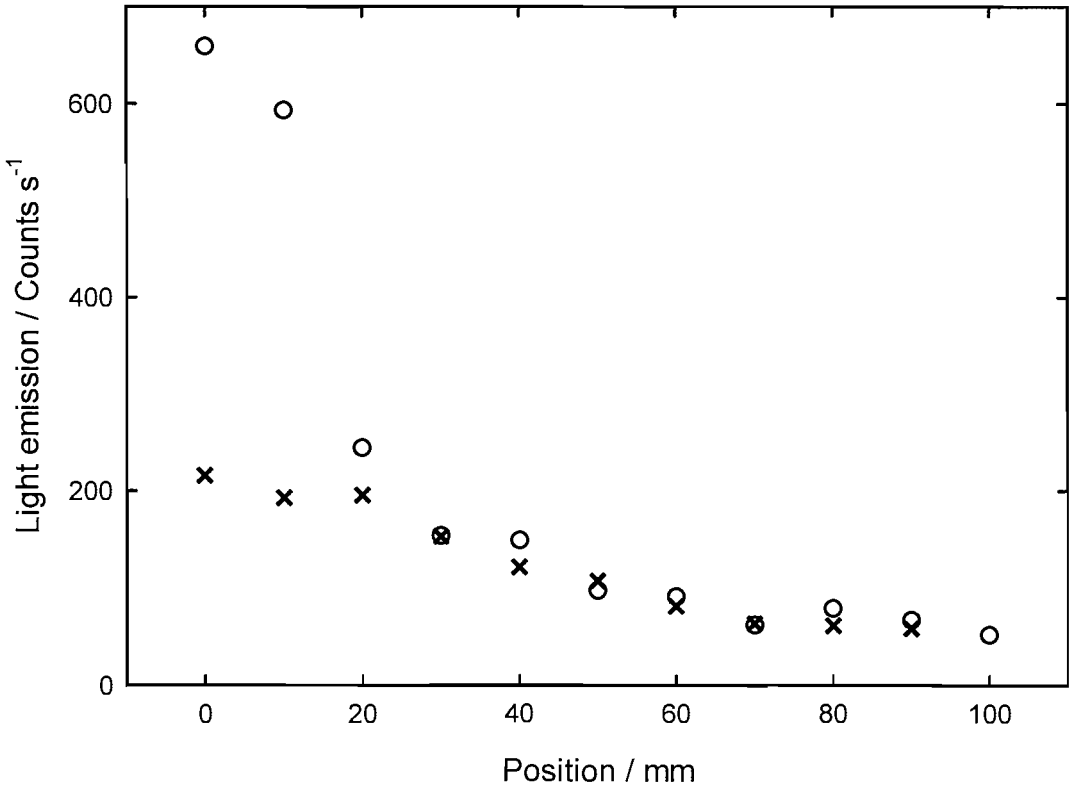

Figure 9.24: Plot comparing the level of MBS(C)L light emission form the NPL reference vessel with (o) and without (X) the NPL cavitation sensor. The sensor was mounted 5 cm above the top of the reference vessel and scanned along the X axis starting at the centre of the reactor. The spatial specificity of the measurements increased by means of a collimator. The reference vessel contained an aqueous sonoluminescent solution of 5 μM luminol and 0.1 M Na_2CO_3 at room temperature (~25 °C) and was not degassed.

From the measurements conducted in the NPL reference vessel it would appear that the broadband sensor was having a large effect on the localised level of cavitation within the bath. Specifically the images in figure 9.20 and 9.21 as well as the photon counter data in figure 9.24 would suggest that particularly at the centre of the bath the presence of the sensor is causing a three fold increase in the level of the light emission. However, care must be taken in analysing these effects. As was discussed in chapter 2 section 2.4.5 luminescence from a solution containing luminol persists beyond the period during which it is subjected to cavitation. The sensor having impermeable sides will also constrain the ability of the solution within it to flow away in a plane tangential to its major axis. Given that all of the intensified images of the vessel have to be conducted looking down the major axis of the sensor any flow in the solution would be along the axis of both the sensor and the camera/photon counter. This would increase the apparent level of light emission from the region in which the sensor sits. Without the sensor present flow caused by differences in the

pressure would be able to move in any direction, dissipating the prolonged luminol luminescence over a greater area and resulting in a lower level of light emission to be recorded. It was in fact possible to see the flow of the luminescing luminol solution through the sensor at higher powers with the naked eye.

The constriction of the flow of solution within the reactor does not account for the entire increase in the level of light emission seen but it certainly magnifies any effect. The results shown in this section have shown that the NPL broadband sensor does have an effect on the light emission from a cavitating solution into which it is placed. This effect is marginal when the sensor is well soaked and certainly considerably less than the effect on the light emission seen when sample items were introduced to a cleaning bath in chapter 8. The theoretical increase in the light emission as a result of the persistence of the luminescence from the luminol solution could be verified by recording images of the reference vessel from purely MBSL light emission. Due to the inability to move either the reference vessel or the high powered intensified cameras this was not possible.

In comparison the effect of the electrode used to conduct the surface erosion/corrosion measurements on the light emission was considerably less. Figure 9.25 shows the vessel that though a difference can be seen in the light emission between when no electrode is present (a) and when the electrode is position either at the centre of the bath (b) or off centre (c) the change is considerably less than that seen for the broadband sensor.

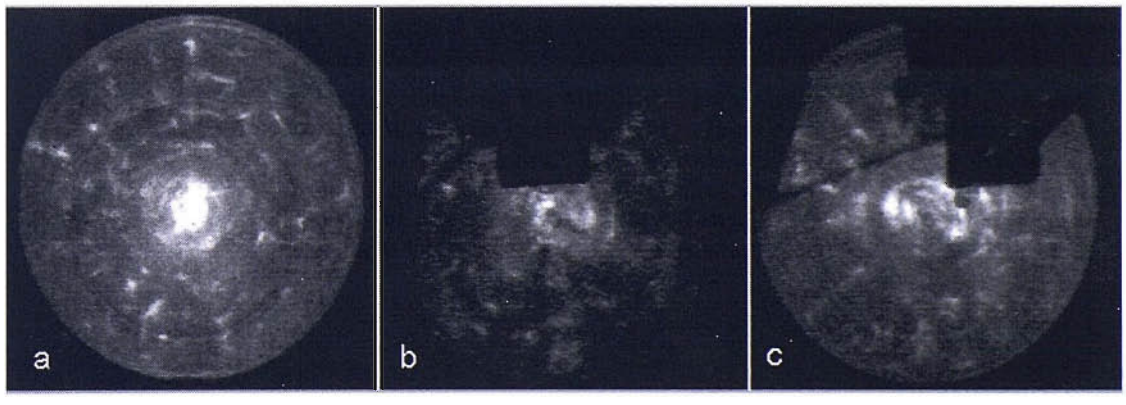

Figure 9.25: Images comparing the MBS(C)L light emission from the NPL reference vessel driven at 100 W with no interference (a), with an electrode at the centre (b) and displaced 50 mm from the centre(c). The electrode was positioned as for the surface erosion/corrosion measurements and each intensified image is an amalgamation of 10 individual images. The reference vessel contained an aqueous sonoluminescent solution of 5 μM luminol and 0.1 M Na_2CO_3 at room temperature (~25 °C) and was not degassed.

9.6. Conclusions

This chapter has shown that the methods developed in Southampton for the measurement of inertial cavitation can be transferred to the NPL reference vessel with varying degrees of success. In particular both methods used for the measurement of the formation of chemical bi-products of cavitation were found to not be sensitive enough to make credible measurements within the reference vessel. The other two methods employed looking at the light emission from the vessel; be it as a result of multi-bubble sonoluminescence or multi-bubble sonochemiluminescence; and the prevalence of surface erosion/corrosion on an electrode were shown to be successful and in figures 9.15 and 9.16 to be in general agreement with the pressure and acoustic broadband emission measurements conducted by the NPL.

Section 9.5 dealt with the effect that placing the NPL sensor within a cavitating environment had on the light emission. This showed that the sensor had a negligible effect in a small commercial bath but a more significant effect than expected on the reference vessel. The greater apparent influence on the reference vessel is thought to be a result of both the interference of the sensor on the cavitation occurring within the vessel but mainly as a result of the constraining of the ability of the solution within the sensor itself to flow. This constraint coupled with the persistence of the luminol solution required to magnify the luminescence from the solution to a level detectable is thought to have been responsible for some of the increase in light emission seen. In comparison the electrode used for the surface erosion/corrosion measurements was found to have less of an effect.

10. Conclusion

This thesis has developed and used electrochemical sensors, pressure measurements and intensified imaging techniques to examine the inertial cavitation taking place in several different ultrasonic systems. These were an ultrasonic horn (or piston like emitter), in a single transducer reactor, a series of ubiquitous cleaning baths and a standard reference vessel (*162*). The results from the different methods have then been compared and correlations noted.

10.1. Development of techniques

Changing the conformation of an existing flow cell and developing a stable pumping system enabled accurate sonochemical rate measurements to be made. It had been proposed that the new flow cell configuration would enable the sonochemical rate to be spatially resolved within a single transducer reactor. However, when the flow cell was scanned throughout a reactor little variation could be observed. The lack of spatial resolution seen was considered to be as a result of dispersion of locally generated sonochemical species; as a result of mass transfer within the vessel.

The presence of surface erosion/corrosion activity was studied using the reformation of passive oxide layers on aluminium and titanium electrodes. This was the first time that titanium electrodes had been used in this way. The use of titanium was necessitated due to the poor durability of aluminium electrodes. When subjected to inertial cavitation, the surface of aluminium electrodes would become prejudicially damaged leading to the presence of more rounded "secondary" peaks in addition to the sharper "primary" peaks seen for a freshly polished electrode. The relative damage done to the differing electrode materials was examined using microscopy which revealed that the titanium electrodes suffered considerably less damage compared to the aluminium ones. The processes which lead to the production of the surface/erosion transients were studied using simultaneous high-speed imagery and electrochemical measurements. This confirmed that both at the tip of an ultrasonic horn and in a single transducer ultrasonic reactor the damage done to the surface of the electrode was as a result of processes associated with the so called cluster collapse model. It was not possible to determine the difference between the processes that

lead to "primary" and "secondary" events. In both cases a clearing of the bubble cloud could be seen just prior to the point of maximum current. However, for "secondary" events, a bubble cloud could be seen on the surface at the point at which the current began to rise. Work conducted using laser induced cavitation and aluminium electrodes has suggested that the "primary" peak is a result of a pressure shock, whereas the "secondary" peak is as a result of bubble action on the surface (*37*). This area requires further investigation as it may reveal important insights into the processes that lead to cavitation induced erosion and its prevention/characterisation.

The deployment of the methods developed under "idealised" conditions (e.g. an ultrasonic horn or single transducer reactor) was extended to "real world" industrial type applications. This required the development of new electronic equipment as the level of electrical interference was limiting. Consequently two optocoupled current followers were developed that enabled suitable measurements to be made. One current follower was designed to be fast and unipolar; enabling the measurement of surface erosion/corrosion events. The second current follower was designed to be accurate and bi-polar; enabling electrochemical measurements of sonochemical change to be made. These two devices enabled the same measurements conducted in idealised conditions to be made in "real world" industrial applications and offer possibilities beyond the field of acoustoelectrochemistry.

10.2. Measurement of cavitation

Systematic scans of surface activity and pressure were made of a single transducer reactor, three ultrasonic cleaning baths and the NPL reference vessel in accompaniment to intensified imagery and some sonochemical measurements. These scans enabled a number of conclusions to be drawn.

The scanning of the single transducer reactor at a number of frequencies demonstrated that the different effects of inertial cavitation are prevalent at differing frequencies. As has been reported elsewhere (*62, 128*) increased light emission and sonochemical change are recorded at the higher ultrasonic drive frequencies tested. Conversely the level of surface erosion/corrosion activity is predominantly at lower

drive frequencies tested with little, if any, activity being recorded at the frequencies where light emission is more prevalent.

When the spatially resolved light emission, pressure and surface measurements were compared the correlation between them could clearly be seen. The comparison at higher frequencies was hampered by the relatively large active element of the hydrophone in comparison to the pitch of the modal banding of the sound field. However, at 23 kHz the correlation is startling with concurrent bands of light emission, high acoustic pressure amplitude and elevated surface erosion/corrosion activity being recorded. This is as expected given that the light emission and surface erosion/corrosion activity is dependent on the pressure amplitude exceeding the inertial cavitation threshold.

A similar agreement between the light emission, acoustic pressure amplitude and level of surface erosion/corrosion activity was recorded in the ultrasonic cleaning baths. For all three baths tested it was possible to see that the level of inertial cavitation activity was not homogenous with areas of elevated and reduced activity. The addition of items indicative of those which might be placed within such baths was shown to considerably reduce the level of activity recorded. However, despite a significant reduction in the acoustic pressure amplitude the recorded pressures (~200 kPa) were still in excess of the calculated inertial pressure threshold.

Finally the measurement techniques were transferred to the NPL reference vessel and compared to pressure measurements made with a hydrophone and the NPL broadband acoustic sensor. This again showed an excellent correlation between the different measurement techniques; at a drive power of 100 W all four measurement techniques showed the presence of the same central peak. The invasive nature of the different sensors was also investigated. This concluded that all sensors are to some extent invasive. From intensified images the NPL reference sensor was shown to have little effect on the light emission from a small cleaning bath, but a considerable effect in the NPL reference vessel. The effect in the reference vessel is thought, in part, to be as a result of the persistence of the MBS(C)L techniques used.

10.3. Concluding comments

The spatial correlation between the acoustic pressure amplitude, light emission (from either MBSL or MBS(C)L) and surface erosion/corrosion activity has been shown across a number of different conditions. The level of broadband acoustic emission has also been shown to be similar in the NPL reference vessel. Using the various techniques available it has been possible to build up a more complete picture as to the nature and distribution of inertial cavitation in a number of environments.

Principle to this thesis has been the development of aluminium and titanium electrodes for use in measuring the surface effects of cavitation. Although the electrochemical technique is simple, relatively accurate and portable, it would be wrong to say that it represents an 'ideal' inertial cavitation measurement technique. As with all localised measurement techniques (e.g. hydrophones), to map an entire vessel, a single electrode would have to scan all three dimensions of the cell, which is time-consuming (during which time the cavitation might change because of changes in the temperature, gas content etc.). Similarly a large array of electrodes capable of mapping large areas of the vessel would be prejudicially invasive. However, when used in conjunction with the other measurement techniques presented in this thesis, the electrode sensor represents a useful addition to inertial cavitation measurement.

The measurements conducted at various frequencies in chapter 6 make clear that using a single measurement for cavitation is unwise; if surface activity alone were to be used then it would appear that little or no inertial cavitation activity was taking place at higher frequencies. Instead it would seem more prudent if a number of measurements were presented to characterise the level of cavitation activity present. If in addition to regular acoustic pressure measurements, the NPL sensor, sonochemical reactions (such as the Weissler reaction) and surface activity measurement were made then comparison between experimental setups would be more valid.

10.4. Further work

Further work continuing from this project can be separated into two directions:

(A.) Further study of the processes taking place at the surface of an electrode during inertial cavitation damage

(B.) Further investigation into the use of electrochemical techniques to measure cavitation

Looking at (A) first, the work in this thesis and the work of Offin (*54*) and Hirsimaki (*37*) has suggested that the processes that lead to erosion by inertial cavitation is complex. There is great potential in a single project that would make use of both laser and acoustic cavitation to study these processes. The presence of "secondary" events on aluminium in both situations is intriguing; especially the suggestion from laser cavitation measurements that the process that leads to their genesis is different. A fuller understand of the mechanisms that lead to the damage of a surface by cavitation would enable its better exploitation.

If we turn now to area (B) and the further investigation of the measurement of cavitation through electrochemistry the obvious need is for a better spatially resolved sonochemical measurement system. The attempts in this thesis to produce such a system foundered on the movement of solution within the examined vessel. Therefore it is the authors' suggestion that a flow system using an acoustically transparent, but chemically isolated, volume within the vessel of interest is the best way to proceed. This would enable chemical change measurements to be made of a small specific area with great accuracy.

The further development of an electrochemical surface erosion/corrosion sensor would seem to be plausible. Currently the system only makes use of a single electrode; limiting the volume which can be studied. The use of a small array of electrodes would improve the volume that can be studied. If further work were to be carried out along the same lines as this project then the construction of a larger volume, highly controllable, ultrasonic vessel in Southampton would seem sensible. This project was impeded by the need to make measurements on a large, reproducible system at NPL. This delayed the development of the techniques as well as the number of measurements that could be made.

Appendix A: NPL Chemistry measurements

This appendix contains the chemical measurements conducted in the NPL reference vessel. Due to technical difficulties; primarily that any activity being spread out over the entire volume of the vessel and therefore hard to detect; these results were omitted from the main body of the thesis but were felt to be of enough interest to be included as an appendix for completeness.

Electrochemical measurements

The electrochemical measurements were conducted using the three electrode flow cell setup in a two electrode conformation with a 0.5 mm platinum diameter working electrode held at 0 V *vs.* a SCE counter/reference electrode. Because the NPL reference vessel was considerably larger than the other vessels used the needle inlet needle was extended to 40 cm allowing measurements to be made in the centre of the bath. By using the same pumping system as used for the measurements conducted in chapters 3, 6 and 8 (soft damping and a flow rate of 388 ml hr^{-1}) it was possible to ascertain the concentration of I_3^- in the solution directly from the current by using the conversion factor calculated from the calibration plot in figure 3.7. The flow cell was attached by means of a boss and clamp to a rod held by the XYZ positioning system such that the inlet to the needle could be placed at any point within the vessel.

Despite of the use of the use of the optically isolated current follower when the flow cell was positioned such that solution was being drawn from the vessel into the cell it became apparent that there was still a large amount of high frequency noise. This was overcome by the addition of a 330 Hz low pass filter the effect of which on the signal can be seen by comparing the current time traces in figure 0.1 where the unfiltered background signal ( ) can be seen to be 100 times greater than the filtered signal (—).

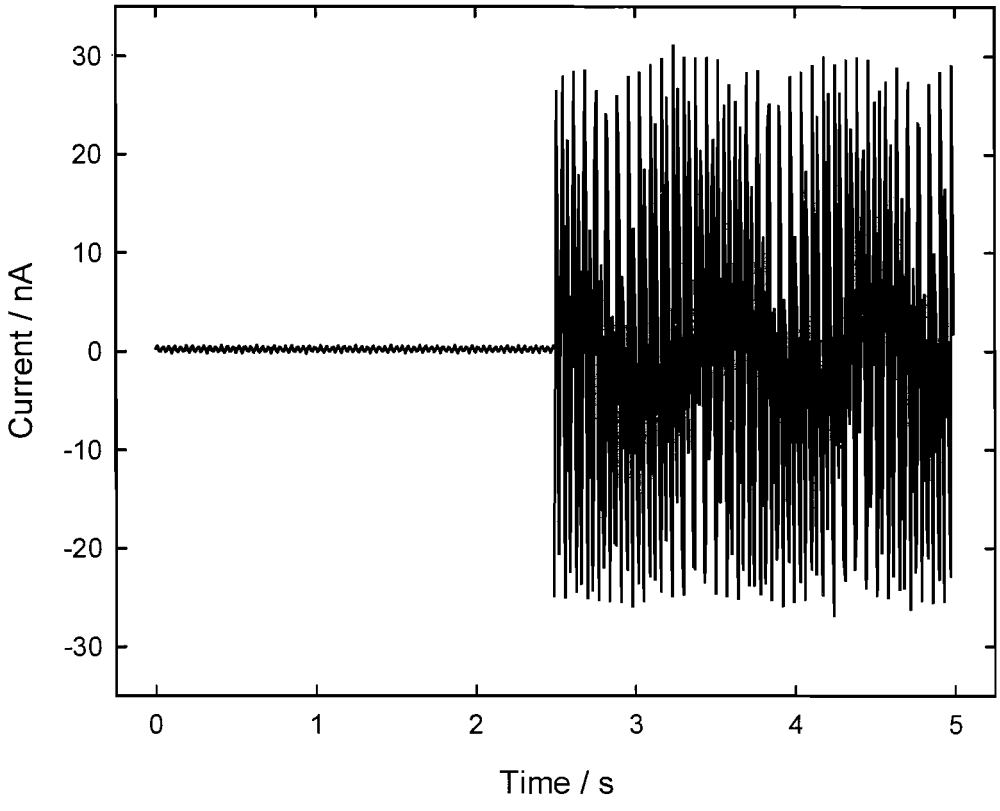

Figure 0.1: Plot showing the difference in the background signal from the electrochemical equipment with (——) and without ( ) a 330 Hz low pass filter.

To measure the rate at which the chemistry within the reference vessel was changing the steady state current was measured before and after a 180 s period during which the vessel was driven at maximum power (500 W). During the period of sonication the current was monitored for a period of 10 seconds to see if the real time change in current could be recorded. Figure 0.2 shows that little or no change in the current can be seen over this period of time.

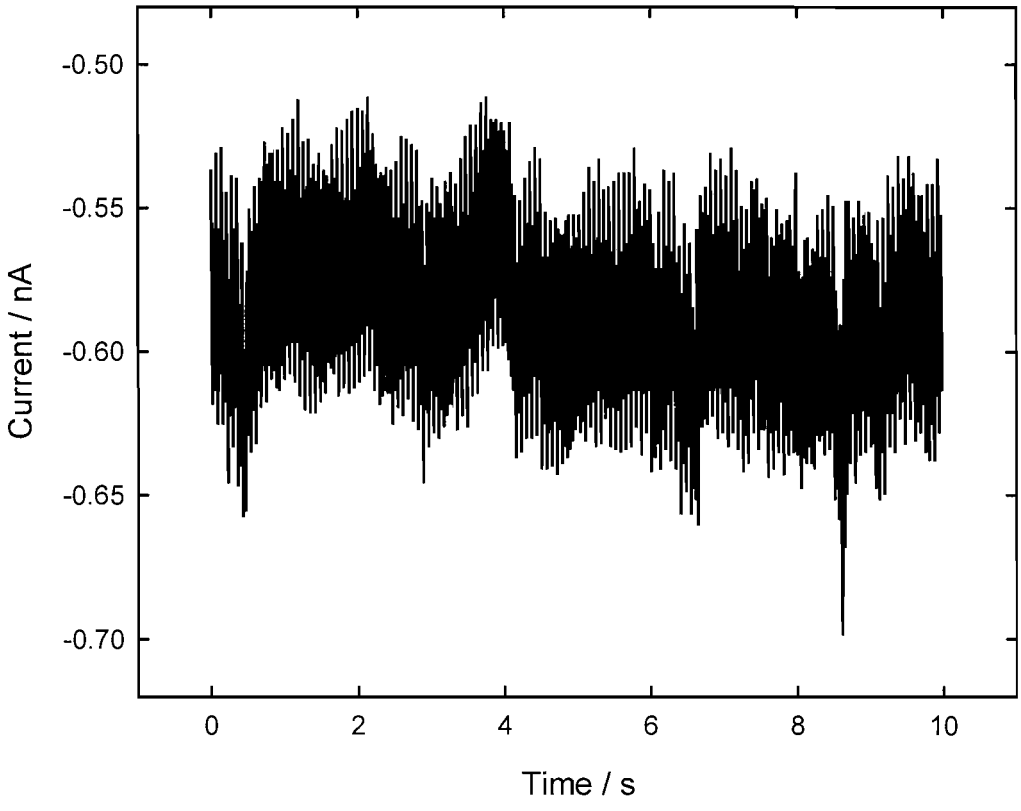

Figure 0.2: Plot showing the change in current at an electrode monitoring the formation of I_3^- whilst the NPL refence vessel was operating at a drive power of 500 W. The gradient of the trace was calculated to be -2.4 pA s^{-1} giving a rate of change of 0.2 nM s^{-1} though with a R^2 value of only 0.04. Recorded at the centre of the reference vessel with the needle fed three electrode flow cell with the soft damped peristaltic pump running at 388 ml hr^{-1}. A 0.5 mm diameter Pt electrode held at 0 V *vs.* a SCE counter/reference electrode was used to monitor the change in I_3^- concentration as a function of time. The reference vessel contained an aqueous solution of 90 mM KCl 10 mM KI solution at room temperature.

The rate of change of the current in figure 0.2 was calculated to be -2.4 pA s^{-1} but with an R^2 value of 0.04 demonstrating that it is a very poor fit. By considering the steady state currents recorded before and after the period of cavitation it is possible to calculate a more accurate figure for the rate of chemical change. The initial steady state current was found to be -0.4 +/- 0.03 nA and the final current -0.67 +/- 0.03 nA giving a rate of formation of I_3^- as 0.13 +/- 0.03 nM s^{-1}.

It was suggested that the variation in the chemistry seen in figure 0.2 could be as a result in changes in the mass transfer to the electrode. To ascertain whether this was taking place the potential between the working and counter/reference electrodes was changed to +0.9V so that instead of oxidising I_3^- at the working electrode I_2 was being plated. Given that the concentration of KI in the solution is not going to vary greatly as a function of time over the period of sonication any large variation in the current

recorded would be as a result in changes in the mass transfer of the analyte to the electrode. Figure 0.3 shows that during the period of time when the reference vessel was in operation (15 to 45 seconds, shaded grey) there is no discernable extra variation in the current beyond that seen whilst the vessel was not in operation.

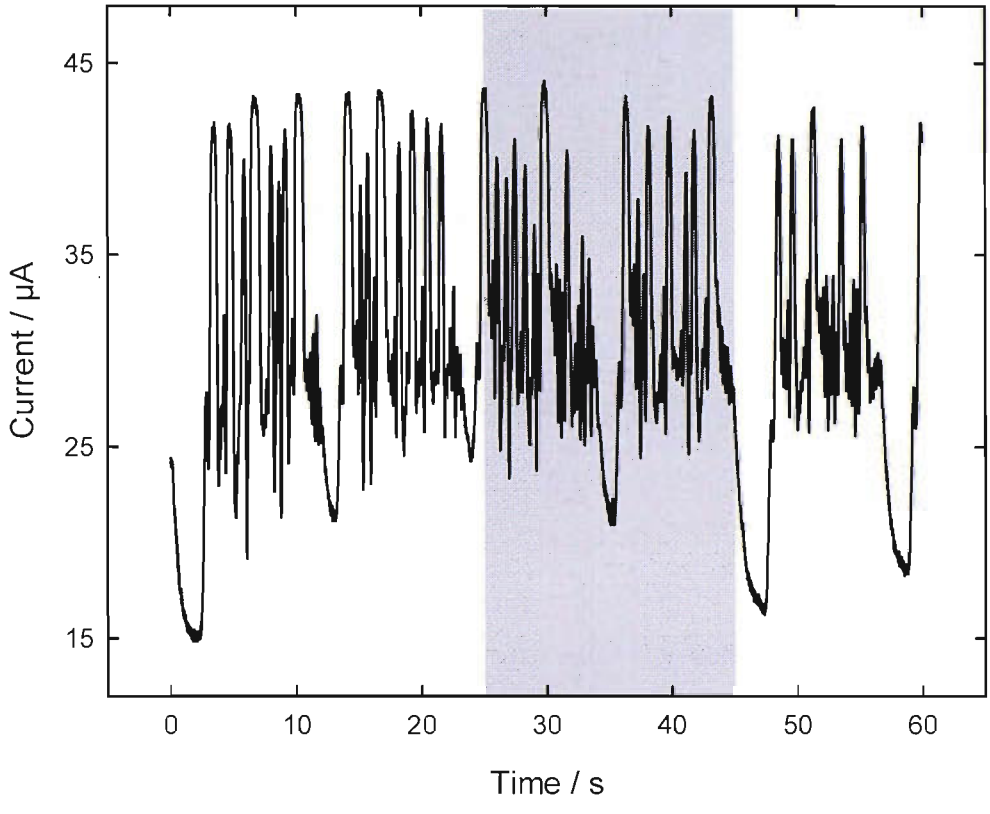

Figure 0.3: Plot showing the effect that turning on the ultrasound in the NPL reference vessel has on the current recorded at an electrode within the flow cell and therefore the effect it is having on the mass transfer. Recorded with the needle fed three electrode flow cell with the soft damped peristaltic pump running at 388 ml hr^{-1}. A 0.5 mm diameter Pt electrode was held at +0.9 V *vs.* a SCE counter/reference. The bath contained 500 ml 90 mM KCl 10 mM KI solution at ambient temperature.

UV/Visible spectroscopy

Two aliquots of the solution within the NPL reference vessel were taken. The first after a period of sonication of 180 seconds and the second after all the electrochemical chemical change measurements had be made (corresponding to a period of sonication in excess of 30 minutes). When the solution was tested using the spectrometer in Southampton no recordable level of chemical change could be found in comparison to a background sample. This is not entirely surprising given that the reference vessel operates at a lower ultrasonic frequency which has been seen to generate significantly lower rates of chemical change both in this study (chapter 6) and in other work (*62, 128*). In addition any chemical change taking place in the

reactor will be diluted throughout the entire 30 dm^3 volume severely reducing the chances of it being detected (for comparison bath A in chapter 8 has a volume of 500 ml, 60 times less than the reference vessel but has a drive power of 25 W meaning that there is a higher power density in bath A than the reference vessel).

Appendix B: Control circuit for remote switch

This appendix covers the control circuit used to operate a Brennen Stuhl FE433 remote switch.

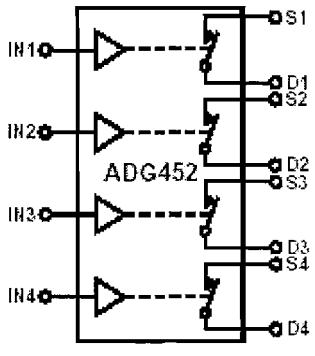

Diagram of ADG 452 chip switch circuit. Diode 1 was used.

Table 5. Truth Table (ADG451/ADG452)

ADG451 In	ADG452 In	Switch Condition
0	1	On
1	0	Off

Pin locations on chip

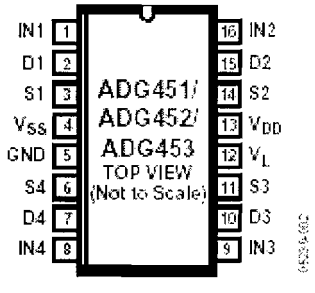

Figure 2. Pin Configuration (DIP, SOIC, TSSOP)

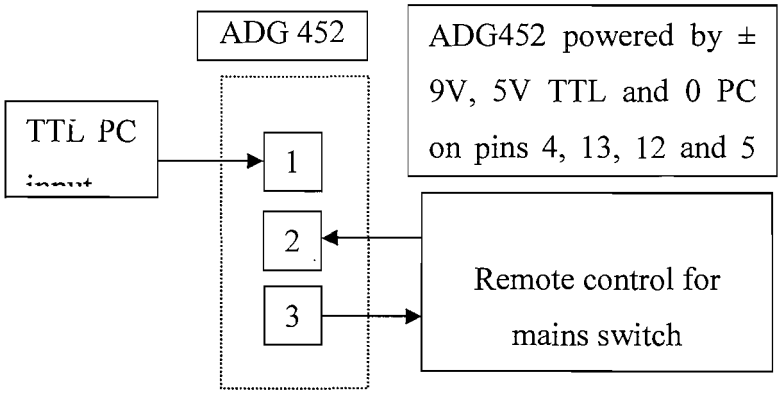

Appendix C: Data analysis programs

Peak Count (PeakcountA.vbp)

Used to determine the number of peaks in an ADC card time current trace

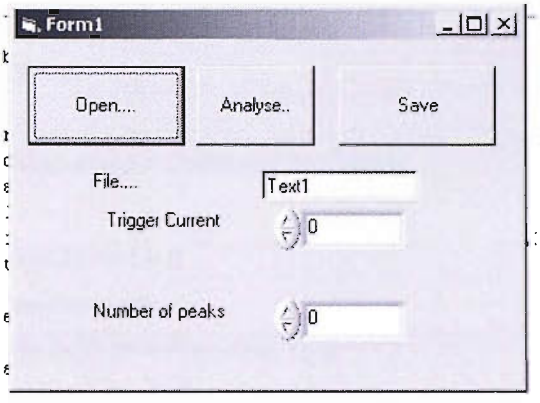

Code:

```
---------------------------------------------------------------------
Dim PeakAmp(1000000)
Dim Currentarr(15000000)
Dim Timearr(1000000)
Dim NoPeaks
Dim Current$
Dim x
Dim Trigcurrent
Dim TotCurrent

---------------------------------------------------------------------

Private Sub Command1_Click()
Filebox.CancelError = True
On Error GoTo ErrHandle2
Filebox.Filename = "*.dat"
Filebox.InitDir = "C:\Documents and Settings\Chris\My Documents"
Filebox.Action = 1

'put filename in textbox
Filename.Text = Filebox.Filename
```

```
ErrHandle2: Exit Sub

End Sub

---------------------------------------------------------------

Private Sub Command2_Click()
Dim no
Dim zz

Trigcurrent = CWNumEdit1.Value

'TotCurrent = 0
NoPeaks = 0
FiletoOpen = Filename.Text

Open FiletoOpen For Input As #1
   no = 0
   Do
     no = no + 1
     Input #1, Current$
     Currentarr(no) = Val(Current$)

   '   List1.AddItem Currentarr(no)
   Loop Until EOF(1)

For x = 3 To 14999995

If Currentarr(x) > Currentarr(x - 1) And Currentarr(x - 1) > Currentarr(x - 2) And Currentarr(x)
> Currentarr(x + 1) And Currentarr(x) > Currentarr(x + 2) And Currentarr(x) > Currentarr(x +
3) And Currentarr(x) > Currentarr(x + 4) And Currentarr(x) > Currentarr(x + 5) And
Currentarr(x) > Trigcurrent Then
      zz = zz + 1
      PeakAmp(zz) = Currentarr(x)
      Timearr(zz) = x

   End If

Next x
```

```
NoPeaks = zz

CWNumEdit2.Value = NoPeaks

Close #1

End Sub

---------------------------------------------------------------

Private Sub Command3_Click()
Dim g

Filebox.CancelError = True
On Error GoTo ErrHandle
Filebox.Flags = cdlOFNOverwritePrompt
Filebox.Filename = "*.txt"
Filebox.InitDir = "C:\Documents and Settings\Chris\My Documents"
Filebox.Action = 2

Filename.Text = Filebox.Filename

Open Filename.Text For Output As #1


'write to file
Print #1, "Peak Number"; ","; "Point"; ","; "Amplitude"
For g = 1 To NoPeaks

Print #1, g; ","; Timearr(g); ","; PeakAmp(g)

Next g
Close #1
List1.AddItem g
ErrHandle: Exit Sub

End Sub
---------------------------------------------------------------
```

Developed from a program by Offin (*54*)

Charge calculator (Peakcurrent.vbp)

Based upon the peak counting program and designed to calculate the charge passed in each peak.

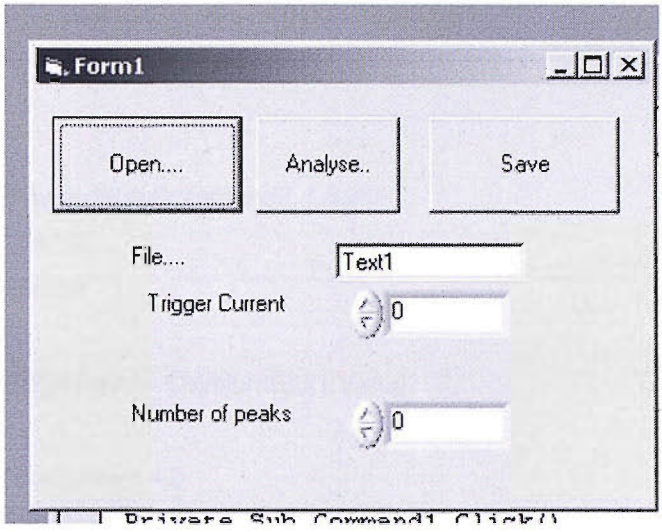

Code:

```
Dim PeakAmp(1000000)
Dim Currentarr(15000000)
Dim Timearr(1000000)
Dim NoPeaks
Dim Current$
Dim x
Dim Trigcurrent
Dim TotCurrent(1000000)
```

```
Private Sub Command1_Click()
Filebox.CancelError = True
On Error GoTo ErrHandle2
Filebox.Filename = "*.dat"
```

```
Filebox.InitDir = "C:\Documents and Settings\Chris\My Documents"
Filebox.Action = 1

'put filename in textbox
Filename.Text = Filebox.Filename

ErrHandle2: Exit Sub

End Sub
-----------------------------------------------------------------


Private Sub Command2_Click()
Dim no
Dim zz

Trigcurrent = CWNumEdit1.Value

'TotCurrent = 0
NoPeaks = 0
FiletoOpen = Filename.Text
zz = 0

Open FiletoOpen For Input As #1
   no = 0
   Do
     no = no + 1
     Input #1, Current$
     Currentarr(no) = Val(Current$)

   '   List1.AddItem Currentarr(no)
   Loop Until EOF(1)

For x = 3 To 14999995

If Currentarr(x) > Trigcurrent And Currentarr(x - 1) > Trigcurrent And Currentarr(x + 1) >
Trigcurrent Then
      TotCurrent(zz) = TotCurrent(zz) + (Currentarr(x) * (1 / 500000) * (10 ^ -5))
      PeakAmp(zz) = Currentarr(x)
      Timearr(zz) = x
```

```
 Else
    If Currentarr(x) < Trigcurrent And Currentarr(x - 1) > Trigcurrent And Currentarr(x - 2) >
Trigcurrent And Currentarr(x - 3) > Trigcurrent Then
  zz = zz + 1
  End If


    End If

Next x

NoPeaks = zz

CWNumEdit2.Value = NoPeaks

Close #1

End Sub
---------------------------------------------------------------

Private Sub Command3_Click()
Dim g

Filebox.CancelError = True
On Error GoTo ErrHandle
Filebox.Flags = cdlOFNOverwritePrompt
Filebox.Filename = "*.txt"
Filebox.InitDir = "C:\Documents and Settings\Chris\My Documents"
Filebox.Action = 2

Filename.Text = Filebox.Filename

Open Filename.Text For Output As #1


'write to file
Print #1, "Peak Number"; ","; "Point"; ","; "Amplitude"; ","; "Charge"
For g = 1 To NoPeaks
```

```
Print #1, g; ","; Timearr(g); ","; PeakAmp(g); ","; TotCurrent(g)

Next g
Close #1
List1.AddItem g
ErrHandle: Exit Sub

End Sub
```

Pressure calculator (pressure.vbp)

Used to analyse a string of pressure time waveforms recorded using the ADC card. The program calculates the zero to peak pressure amplitude by isolating the minimum and maximum voltage and halving the difference between them.

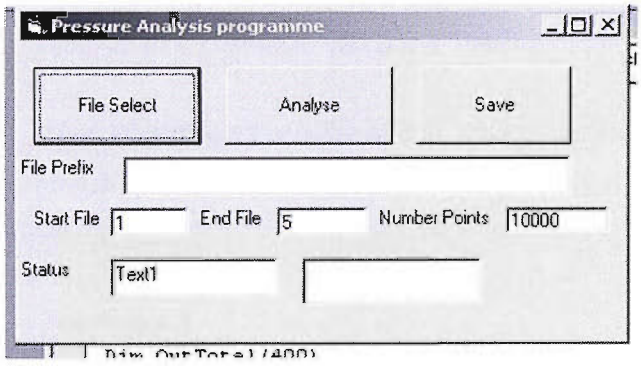

Code:

```
Dim no
Dim Pressure$
Dim Pressurearr(10005)
Dim N
Dim Max
Dim Min
Dim OutMax(400)
Dim OutMin(400)
Dim OutFile(400)
```

```
Dim OutAmp(400)
Dim OutTotal(400)
Dim z
Dim zz
Dim zzz
Dim k
Dim Total

---------------------------------------------------------------

Private Sub Analyse_Click()
N = StartNo.Text
k = StartNo.Text
z = 0

Check.Text = "Running....."


For k = StartNo.Text To Endno.Text

   FiletoOpen = Filename.Text & k & ".csv"

   Open FiletoOpen For Input As #1
   no = 0
   Do

      no = no + 1
      Input #1, Pressure$
      Pressurearr(no) = Val(Pressure$)
       List1.AddItem Pressurearr(no)
   Loop Until EOF(1)


   Max = -1
   Min = 1
   x = 1
   Total = 0

   For x = 1 To 10000
      If Pressurearr(x) > Max Then
```

```
        Max = Pressurearr(x)
        End If

        If Pressurearr(x) < Min Then
        Min = Pressurearr(x)
        End If
        Total = Total + Abs(Pressurearr(x))


    Next x

    z = z + 1
    OutFile(z) = k
    OutMax(z) = Max
    OutMin(z) = Min
    OutAmp(z) = (Max - Min) / 2
    OutTotal(z) = Total / CWNumEdit1.Value


    Close #1
Next k

  Check.Text = "Done"
End Sub

Private Sub Command1_Click()
Filebox.CancelError = True
On Error GoTo ErrHandle2
Filebox.Filename = "*.csv"
Filebox.InitDir = "C:\Documents and Settings\Chris\Desktop\Speedy Gonzalez\Pressure
experiments\"
Filebox.Action = 1

'put filename in textbox
Filename.Text = Filebox.Filename

ErrHandle2: Exit Sub

End Sub
```

```
Private Sub Save_Click()
Dim g

'Filebox.CancelError = True
'On Error GoTo ErrHandle
'Filebox.Flags = cdlOFNOverwritePrompt
'Filebox.Filename = "*.txt"
'Filebox.InitDir = "C:\"
'Filebox.Action = 2

Open Filename.Text & ".txt" For Output As #1

'write to file
Print #1, "File Number"; ","; "Max"; ","; "Min"; ","; "Amplitude"; ","; "Average"
For g = 1 To k

Print #1, OutFile(g); ","; OutMax(g); ","; OutMin(g); ","; OutAmp(g); ","; OutTotal(g)

Next g
Close #1
List1.AddItem g
ErrHandle: Exit Sub

End Sub
```

---

11. References

1. T. G. Leighton, *The Acoustic Bubble* (Academic Press Limited, London, 1994), pp. 613.
2. F. R. Young, *Cavitation* (McGraw-Hill, London, 1989), pp. 418.
3. B. Vyas, C. M. Preece, *Journal of Applied Physics* **47**, 5133 (1976).
4. I. Hansson, V. Kedrinskii, K. A. Morch, *Journal of Physics D-Applied Physics* **15**, 1725 (1982).
5. I. Hansson, K. A. Morch, *Journal of Applied Physics* **51**, 4651 (1980).
6. B. P. Barber, C. C. Wu, R. Lofsted, P. H. Roberts, S. J. Putterman, *Physical Review Letters* **72**, 1380 (1994).
7. L. A. Crum, G. T. Reynolds, *Journal of the Acoustics Society of America* **78**, 137 (1985).
8. C. Eberlein, *Physical Review Letters* **76**, 3842 (1996).
9. C. Eberlein, *Physical Review A* **53**, 2772 (1996).
10. E. B. Flint, K. S. Suslick, *Journal of the American Chemical Society* **111**, 6987 (1989).
11. D. F. Gaitan, L. A. Crum, C. C. Church, R. A. Roy, *Journal of the Acoustic Soiety of America* **91**, 3166 (1992).
12. B. Gompf, R. Gunther, G. Nick, R. Pecha, W. Eisenmenger, *Physical Review Letters* **79**, 1405 (Aug 18, 1997).
13. D. Hammer, L. Frommhold, *Journal of Modern Optics* **48**, 239 (2001).
14. E. N. Harvey, *Journal of the American Chemical Society* **61**, 2392 (1939).
15. T. G. Leighton, M. J. W. Pickworth, A. J. Walton, P. P. Dendy, *Physical Medical Biology* **33**, 1239 (1988).
16. T. J. Matula, R. A. Roy, P. D. Mourad, W. B. McNamara, K. S. Suslick, *Physical Review Letters* **75**, 2602 (1995).
17. K. Negishi, *Journal of the Physics Society of Japan* **16**, 1450 (1961).
18. R. Pecha, B. Gompf, G. Nick, Z. Q. Wang, W. Eisenmenger, *Physical Review Letters* **81**, 717 (Jul 20, 1998).
19. A. Prosperetti, *Journal of the Acoustics Society of America* **101**, 2003 (1997).
20. S. J. Putterman, *Scientific American* **272**, 32 (1995).
21. S. Putterman, P. G. Evans, G. Vazquez, K. Weninger, *Nature* **409**, 782 (Feb 15, 2001).

22. F. B. Seeley, C. K. Joens, *American Journal of Physics* **66**, 259 (Mar, 1998).
23. M. P. Brenner, S. Hilgenfeldt, D. Lohse, *Reviews Of Modern Physics* **74**, 425 (Apr, 2002).
24. W. Lauterborn, *Cavitation and Inhomogeneities in Underwater Acoustics* (Springer-Verlag, 1980), pp. 3.
25. K. S. Suslick, M. M. Ndleleni, J. T. Ries, *Journal of the American Chemical Society* **119**, 9303 (1997).
26. T. G. Leighton, M. Farhat, J. E. Field, F. Avellan, *Journal of Fluid Mechanics* **480**, 43 (Apr 10, 2003).
27. A. Philip, W. Lauterborn, *Journal of Fluid Mechanics* **361**, 75 (1998).
28. Y. Tomita, A. Shima, *Acustica* **71**, 161 (1990).
29. H. Hirsimäki, P. R. Birkin, J. G. Frey, T. G. Leighton, paper presented at the IOA Spring Conference, Southampton 2006.
30. O. Lindau, W. Lauterborn, *Journal of Fluid Mechanics* **479**, 327 (Mar 25, 2003).
31. S. J. Shaw, W. P. Schiffers, D. C. Emmony, *Journal Of The Acoustical Society Of America* **110**, 1822 (Oct, 2001).
32. E. A. Brujan, K. Nahen, P. Schmidt, A. Vogel, *Journal of Fluid Mechanics* **433**, 251 (Apr 25, 2001).
33. R. P. Tong, W. P. Schiffers, S. J. Shaw, J. R. Blake, D. C. Emmony, *Journal of Fluid Mechanics* **380**, 339 (Feb 10, 1999).
34. P. R. Birkin, H. M. Hirsimaki, J. G. Frey, T. G. Leighton, *Electrochemistry Communications* **8**, 1603 (Oct, 2006).
35. W. Lauterborn, C. D. Ohl, *Ultrasonics sonochemistry* **4**, 67 (1997).
36. B. Wolfrum, T. Kurz, R. Mettin, W. Lauterborn, *Physics Of Fluids* **15**, 2916 (Oct, 2003).
37. H. M. Hirsimaki, Phd, University of Southampton (2007).
38. J. R. Haines, *Journal of Nuclear Materials* **343**, 366 (Aug, 2005).
39. M. E. Abdelsalam, P. R. Birkin, *Physical Chemistry Chemical Physics* **4**, 5340 (2002).
40. K. M. Kalumuck, G. L. Chahine, *Journal of Fluids Engineering* **122**, 465 (2000).
41. P. R. Birkin, R. O'Connor, C. Rapple, S. Silva-Martinez, *Journal of the Chemical Society Faraday Transactions* **94**, 3365 (1998).

42. P. R. Birkin, D. G. Offin, T. G. Leighton, *Electrochemistry Communications* **6**, 1174 (2004).
43. S. G. Young, J. R. Johnson, *Accelerated cavitation Damage of Steels and Superalloys in Sodium and Mercury*, Erosion by Cavitation or Impingement (ASTM, Phildelphia, 1966), pp. 186-219.
44. R. Garcia, F. G. Hammitt, R. E. Nystrom, *Correlation of cavitation Damage with Other Material and Fluid Properties*, Erosion by Cavitation or Impingement (ASTM, Phildelphia, 1966), pp. 239-283.
45. S. G. Young, J. R. Johnson, *Effect of Temperature and Pressure on Cavitation Damage in Sodium*, Characterization and Determination of Erosion Resistance (ASTM, Phildelphia, 1969), pp. 67-108.
46. F. J. Heymann, *Towards Quantitative Prediction of Liquid impact Erosion*, Characterization and Determination of Erosion Resistance (ASTM, Phildelphia, 1969), pp. 212-243.
47. J. R. Haines, B. W. Riemer. D. K. Felde, J. D. Hunn, S. J. Pawel, C. C. Tsai, *Journal of Nuclear Materials* **343**, 58 (Aug, 2005).
48. F. Wu, Z. B. Wang, Y. D. Cao, W. Z. Chen, J. Bai, J. Z. Zou, *British Journal of Cancer* **89**, 2227 (Dec, 2003).
49. R. E. Apfel, C. K. Holland, *Ultrasound in Medicine and Biology* **17**, 179 (1991).
50. C. K. Holland, R. E. Apfel, *IEEE Transactions Ultrasonics Ferroelectrics and Frequency Control* **36**, 204 (1989).
51. H. G. Flynn, *Journal of the Acoustics Society of America* **58**, 1160 (1975).
52. H. G. Flynn, *Journal of the Acoustics Society of America* **57**, 1379 (1975).
53. T. G. Leighton, *The Acoustic Bubble* (Academic Press, London, 1994), pp.
54. D. G. Offin, PhD, University of Southampton (2006).
55. S. D. Hopkins, S. J. Putterman, B. A. Kappus, K. S. Suslick, C. G. Camara, *Physical Review Letters* **95** (Dec, 2005).
56. K. S. Suslick, *Scientific American* **260**, 80 (Feb, 1989).
57. G. Vazquez, C. Camara, S. Putterman, K. Weninger, *Optics Letters* **26**, 575 (May, 2001).
58. Y. T. Didenko, K. S. Suslick, *Nature* **418**, 394 (2002).
59. A. K. Jana, S. N. Chatterjee, *Ultrasonics sonochemistry* **2**, 87 (1995).
60. A. Weissler, *Journal of the American Chemical Society* **81**, 1077 (1959).

61. C. K. Holland, R. E. Apfel, *Ieee Transactions on Ultrasonics Ferroelectrics and Frequency Control* **36**, 204 (Mar, 1989).
62. J. Power, PhD, University of Southampton (2003).
63. P. R. Birkin, T. G. Leighton, Y. E. Watson, *Ultrasonics sonochemistry* **10**, 65 (2003).
64. P. R. Birkin, T. G. Leighton, Y. E. Watson, paper presented at the Applications of Power Ultrasound in Physical and Chemical Processing 4, Besançon 2003.
65. C. C. Church, *Journal of the Acoustics Society of America* **84**, 1758 (1988).
66. L. A. Crum, *Journal of the Acoustics Society of America* **68**, 203 (1980).
67. E. I. Eller, *Journal of the Acoustics Society of America* **46**, 1246 (1969).
68. P. R. Birkin, T. G. Leighton, Y. E. Watson, *Ultrasonics sonochemistry* **11**, 217 (May, 2004).
69. R. P. Taleyarkhan, J.S. Cho, C. D. West, R. T. Lahey, R. I. Nigmatulin, R. C. Block, *Physical Review E* **69** (Mar, 2004).
70. R. P. Taleyarkhan, C. D. West, J. S. Cho, R. T. Lahey, R. I. Nigmatulin, R. C. Block, *Science* **295**, 1868 (Mar, 2002).
71. R. P. Taleyarkhan C. D.West, R. T. Lahey, R. I. Nigmatulin, R. C. Block, Y. Xu, *Physical Review Letters* **96** (Jan, 2006).
72. T. J. Mason, *Sonochemistry: The Uses of Ultrsound in Chemistry.* T. J. Mason, Ed. (The Royal Society of Chemistry, Cambridge, 1990), pp.
73. I. Hansson, V. Kedrinskii, K. A. Morch, *Journal of Physics D: Applied Physics* **15**, 1725 (1982).
74. P. R. Birkin, D. G. Offin, T. G. Leighton, *Physical Chemistry Chemical Physics* **7**, 530 (2005).
75. H. C. Starritt, F. A. Duck, V. F. Humphrey, *Physics in Medicine and Biology* **36**, 1465 (1991).
76. F. J. Del-Campo, J. Melville, J. L. Hardcastle, R. G. Compton, *Journal of Physical Chemistry A* **105**, 666 (Feb 1, 2001).
77. F. Marken, R. P. Akkermans, R. G. Compton, *Journal of Electroanalytical Chemistry* **415**, 55 (Oct, 1996).
78. S. A. Elder, *Journal of the Acoustics Society of America* **31**, 54 (1958).
79. J. Kolb, *Journal of the Acoustics Society of America* **28**, 1237 (1956).
80. W. L. Nyborg, M.I.L.Seegall, paper presented at the Proceedings of the 3rd International Congress on Acoustics 1960.

81. W. E. Rowe, W.L.Nyborg, *Journal of the Acoustics Society of America* **39**, 965 (1966).
82. S. A. Elder, *Journal of the Acoustical Society of America* **31**, 54 (1958).
83. P. R. Birkin, T. G. Leighton, Y. E. Watson, J. F. Power, *Acoustics Bulletin* **Sept/Oct**, 24 (2001).
84. P. R. Birkin, Y. E. Watson, T. G. Leighton, *Journal of the Chemical Society Chemical Communications*, 2650 (2001).
85. P. R. Birkin, Y. E. Watson, T. G. Leighton, K. L. Smith, *Langmuir* **18**, 2135 (2002).
86. T. G. Leighton, P. R. Birkin, A. O. Maksimov, Y. E. Watson, P. R. White, paper presented at the BIFURCATIONS 2003.
87. Y. E. Watson, PhD, University of Southampton (2003).
88. Y. E. Watson, P. R. Birkin, T. G. Leighton, *Ultrasonics Sonochemistry* **10**, 65 (2003).
89. P. R. Birkin, J. M. Elliott, Y. E. Watson, *Journal of the Chemical Society Chemical Communications*, 1693 (2000).
90. T. G. Leighton, P. R. Birkin, A. O. Maksimov, Y. E. Watson, D. G. Offin, *In preparation for Proceedings of the Royal Society* (2005).
91. T. G. Leighton, P. R. Birkin, M. Hodnett, B. Zeqiri, J. F. Power, G. J. Price, T. Mason, M. Plattes, N. Dezhkunov, A. J. Coleman, *The Electrochemical measurement of mass flux in liquids associated with surface waves on the walls of acoustically excited gas bubbles*, Transworld Research Network: Recent Developments in Physical Chemistry (2005), pp.
92. G. Denuault, in *Chemistry in Industry*. (1996), vol. 18, pp. 678-680.
93. J. Kwak, A. J. Bard, *Analytical Chemistry* **61**, 1221 (1989).
94. J. L. Amphlett, G. Denuault, *Journal of Physical Chemistry B* **102**, 9946 (1998).
95. P. R. Birkin, T. G. Leighton, Y. E. Watson, J. F. Power, in *Acoustics Bulletin*. (2001), vol. Sept/Oct, pp. 24-37.
96. T. Okada, Y. Iwai, K. Awazu, *Wear* **133**, 219 (Oct, 1989).
97. Y. Iwai, T. Okada, S. Tanaka, *Wear* **133**, 233 (Oct, 1989).
98. Y. Tomita, A. Shima, *Journal of Fluid Mechanics* **169**, 535 (Aug, 1986).
99. A. Philipp, W. Lauterborn, *Journal of Fluid Mechanics* **361**, 75 (Apr, 1998).
100. E. A. Neppiras, *Physics Reports-Review Section of Physics Letters* **61**, 159 (1980).

101. W. Lauterborn, H. Bolle, *Journal of Fluid Mechanics* **72**, 391 (1975).
102. M. S. Plesset, R. B. Chapman, *Journal of Fluid Mechanics* **47**, 283 (1971).
103. A. Prosperetti, *Ultrasonics* **22**, 115 (1984).
104. T. G. Leighton, P.R. Birkin, M. Hodnett, B. Zeqiri, J.F. Power, G.J. Price, T. Mason, M. Plattes, N. Dezhkunov, A. Coleman, in *Bubble and Particle Dynamics in Acoustic Fields: Modern Trends and Applications* A. A. Doinikov, Ed. (Research Signpost, Kerala, 2005) pp. 37-94.
105. H. Frenzel, H. Schultes, *Z. Phys. Chem. B Lpz* **27**, 421 (1934).
106. S. J. Putterman, K. R. Weninger, *Annual Review of Fluid Mechanics* **32**, 445 (2000).
107. A. J. Walton, G. T. Reynolds, *Advances in Physics* **33**, 595 (1984).
108. V. Griffing, *Journal of Chemical Physics* **20**, 939 (1952).
109. K. S. Suslick, S. J. Doktycz, E. B. Flint, *Ultrasonics* **28**, 280 (Sep, 1990).
110. J. Frenkel, *Acta Physiochimica* **12**, 317 (1940).
111. T. Lepoint, D. DePauw, F. LepointMullie, M. Goldman, A. Goldman, *Journal of the Acoustical Society of America* **101**, 2012 (Apr, 1997).
112. P. D. Jarman, *Journal of the Acoustical Society of America* **32**, 1459 (1960).
113. B. P. Barber, S. J. Putterman, *Physical Review Letters* **69**, 3839 (Dec, 1992).
114. R. Lofstedt, B. P. Barber, S. J. Putterman, *Physics of Fluids a-Fluid Dynamics* **5**, 2911 (Nov, 1993).
115. C. Eberlein, *Physical Review Letters* **76**, 3842 (May, 1996).
116. C. Eberlein, *Physical Review A* **53**, 2772 (Apr, 1996).
117. J. Lind, G. Merenyi, T. E. Eriksen, *Journal of the American Chemical Society* **105**, 7655 (1983).
118. H. N. McMurray, B. P. Wilson, *Journal of Physical Chemistry A* **103**, 3955 (1999).
119. P. R. Birkin, T.G. Leighton, J.F. Power, M.D. Simpson, A.M.L. Vinçotte, P.F. Joseph, *Journal of Physical Chemistry A* **107**, 306 (2003).
120. P. R. Birkin, J. F. Power, M. E. Abdelsalam, T. G. Leighton, *Ultrasonics sonochemistry* **10**, 203 (2003).
121. P. R. Birkin, J. F. Power, A. M. L. Vinçotte, T. G. Leighton, *Physical Chemistry Chemical Physics* **5**, 4170 (2003).
122. A. M. L. Vinçotte, MPhil, University of Southampton (1999).

123. H. N. McMurray, B. P. Wilson, *Journal of Physical Chemistry A* **103**, 3955 (May, 1999).
124. G. Merenyi, J. S. Lind, *Journal of the American Chemical Society* **102**, 5830 (1980).
125. K. D. Gundermann, F. McCapra, *Chemiluminescence in Organic Chemistry* (Springer-Verlag, Berlin), pp.
126. V. Renaudin, N. Gondrexon, P. Boldo, C. Petrier, A. Bernis, Y. Gonthier, *Ultrasonics Sonochemistry* **1**, S81 (Sep, 1994).
127. G. Singh, MChem Project, University of Southampton (2000).
128. P. R. Birkin, J. F. Power, A. M. L. Vincotte, T. G. Leighton, *Physical Chemistry Chemical Physics* **5**, 4170 (Oct, 2003).
129. A. Henglein, *Ultrasonics sonochemistry* **2**, s115 (1995).
130. A. Henglein, D. Herburger, M. Gutierrez, *Journal of Physical Chemistry* **96**, 1126 (1992).
131. M. Gutierrez, A. Henglein, H. Moeckel, *Ultrasonics sonochemistry* **2**, 111 (1995).
132. A. Weissler, H. W. Cooper, S. Snyder, *Journal of the American Chemical Society* **72**, 1769 (1950).
133. G. Mark, A. Tauber, R.Laupert, H.P. Schuchmann, D. Schulz, A. Mues, C. von Sonntag, *Ultrasonics sonochemistry* **5**, 41 (1998).
134. X. Fang, G. Mark, C. v. Sonntag, *Ultrasonic Sonochemistry* **3**, 57 (1996).
135. C. von Sonntag, G. Mark, A. Tauber, H.-P. Schuchmann. (JAI Press, 1999), vol. Vol. 5, pp. 109-145.
136. P. R. Birkin, J. F. Power, T. G. Leighton, *Journal of the Chemical Society Chemical Communications*, 2230 (2001).
137. K. Makino, M. M. Mossoba, P. Riesz, *Journal of the American Chemical Society* **104**, 3537 (1982).
138. P. R. Birkin, J. F. Power, T. G. Leighton, A. M. L. Vinçotte, *Analytical Chemistry* **74**, 2584 (2002).
139. G. J. Price, E. J. Lenz, *Ultrasonics* **31**, 451 (1993).
140. A. Henglein, *Ultrasonics Sonochemistry* **2**, S115 (Oct, 1995).
141. G. Mark, A. Tauber, R.Laupert, H.P. Schuchmann, D. Schulz, A. Mues, C. von Sonntag, *Ultrasonics Sonochemistry* **5**, 41 (Jun, 1998).
142. E. J. Hart, A. Henglein, *Journal of Physical Chemistry* **91**, 3654 (Jun, 1987).

143. H. Fricke, E. J. Hart, in *Radiation Dosimetery* F. H. Attix, W. C. Roesch, Eds. (Academic Press, London, 1966), vol. 2.
144. G. J. Price, F. A. Duck, M. Digby, W. Holland, T. Berryman, *Ultrasonics Sonochemistry* **4**, 165 (Apr, 1997).
145. A. Weissler, *Journal of the American Chemical Society* **72**, 1769 (1950).
146. D. L. Goldfarb, H. R. Corti, F. Marken, R. G. Compton, *Journal of Physical Chemistry A* **102**, 8888 (Nov, 1998).
147. J. L. Hardcastle, J. C. Ball, Q. Hong, F. Marken, R. G. Compton, S. D. Bull, S. G. Davies, *Ultrasonics Sonochemistry* **7**, 7 (Jan, 2000).
148. P. R. Birkin, C. L. Delaplace, C. R. Bowen, *Journal of Physical Chemistry B* **102**, 10885 (1998).
149. S. Silva-Martinez, PhD, University of Southampton (1997).
150. G. T. Burstein, A. J. Davenport, *Journal of the Electrochemical Society* **136**, 936 (1989).
151. G. S. Frankel, B. M. Bush, C. V. Jahnes, C. E. Farrell, A. J. Davenport, H. S. Issacs, *Journal of the Electrochemical Society* **138**, 643 (1991).
152. G. S. Frankel, C. V. Jahnes, V. Brusic, A. J. Davenport, *Journal of the Electrochemical Society* **142**, 2290 (1995).
153. H. S. Isaacs, A. J. Davenport, *Journal of the Electrochemical Society* **137**, 2196 (1990).
154. J. C. Eklund, D. N. Waller, T. O. Rebbitt, F. Marken, R. G. Compton, *Journal of the Chemical Society-Perkin Transactions 2*, 1981 (Nov, 1995).
155. P. R. Birkin, T.G. Leighton, J.F. Power, M.D. Simpson, A.M.L. Vinçotte, P.F. Joseph, *Journal of Physical Chemistry A* **107**, 306 (Jan, 2003).
156. P. R. Birkin, J. F. Power, M. E. Abdelsalam, T. G. Leighton, *Ultrasonics Sonochemistry* **10**, 203 (Jul, 2003).
157. M. A. Beckett, I. Hua, *Journal of Physical Chemistry A* **105**, 3796 (2001).
158. P. R. Birkin, R. O'Connor, C. Rapple, S. S. Martinez, *Journal of the Chemical Society-Faraday Transactions* **94**, 3365 (Nov, 1998).
159. P. R. Birkin, T. G. Leighton, D. G. Offin, *Wear* **258**, 623 (2005).
160. T. G. Leighton, "A strategy for the development and standardisation of measurement methods for high power/cavitating ultrasonic fields: Review of Cavitation Monitoring Techniques" *Tech. Report No. 263* (ISVR, University of Southampton, 1997).

161. T. G. Leighton, *Journal of the Acoustical Society of America* **108**, 2516 (2000).
162. M. Hodnett, M. J. Choi, B. Zeqiri, *Ultrasonics Sonochemistry* **14**, 29 (Jan, 2007).
163. B. Zeqiri, P. N. Gelat, M. Hodnett, N. D. Lee, *IEEE Transactions on Ultrasonics Ferroelectrics and Frequency Control* **50**, 1342 (Oct, 2003).
164. B. Zeqiri, N. D. Lee, M. Hodnett, P. N. Gelat, *IEEE Transactions on Ultrasonics Ferroelectrics and Frequency Control* **50**, 1351 (Oct, 2003).
165. E. Neppiras, *IEEE Transactions on Sonics and Ultrasonics* **SU-15**, 81 (April 1968, 1968).
166. M. Hodnett, R. Chow, B. Zeqiri, *Ultrasonics Sonochemistry* **11**, 441 (Sep, 2004).
167. M. Ashokkumar, M. Hodnett, B. Zeqiri, F. Grieser, G. J. Price, *Journal of the American Chemical Society* **129**, 2250 (Feb, 2007).
168. B. Zeqiri, M. Hodnett, A. J. Carroll, *Ultrasonics* **44**, 73 (Jan, 2006).
169. G. J. Price, M. Ashokkumar, M. Hodnett, B. Zequiri, F. Grieser, *Journal of Physical Chemistry B* **109**, 17799 (Sep, 2005).
170. R. E. Apfel, *Journal of the Acoustical Society of America* **69**, 1624 (1981).
171. A. M. L. Vincotte, M Phil, University of Southampton (1999).
172. P. R. Birkin, D. G. Offin, P. F. Joseph, T. G. Leighton, *Journal of Physical Chemistry B* **109**, 16997 (Sep, 2005).
173. P. R. Birkin, J. F. Power, T. G. Leighton, A. M. L. Vincotte, *Analytical Chemistry* **74**, 2584 (Jun, 2002).
174. P. R. Birkin, J. F. Power, T. G. Leighton, *Chemical Communications*, 2230 (2001).
175. P. R. Birkin, S. Silva-Martinez, *Journal of Electroanalytical Chemistry* **416**, 127 (Nov 1, 1996).
176. D.-T. Chin, C.-H. Tsang, *Journal of the Electrochemical Society* **125**, 1461 (1978).
177. P. R. Birkin, J. F. Power, A. M. L. Vincotte, T. G. Leighton, *Physical Chemistry Chemical Physics* **5**, 4170 (Oct, 2003).
178. *Smithsonian Physical Tables*. W. E. Forsythe, Ed. (Knovel, ed. 9th Revised, 2003), pp. 837.
179. A. Shima, T. Tsujino, H. Nanjo, *Ultrasonics* **24**, 142 (May, 1986).

180. CRC, *Handbook of Chemistry and Physics 1913-1995*. D. R. Lide, Ed. (CRC Press, ed. 75th, 1995), pp.
181. G. W. C. Kaye, T. H. Laby, *Tables of Physical and Chemical Constants and some Mathematical Functions* (Longmans, Green and Co, London, ed. 12th, 1959), pp.
182. P. R. Birkin, J. F. Power, M. E. Abdelsalam, T. G. Leighton, *Ultrasonics Sonochemistry* **10**, 203 (Jul, 2003).
183. T. G. Leighton, P.R. Birkin, M. Hodnett, B. Zeqiri, J.F. Power, G.J. Price, T. Mason, M. Plattes, N. Dezhkunov, A. Coleman, in *Bubble and Particle Dynamics in Acoustic Fields: Modern Trends and Applications* A. A. Doinikov, Ed. (Research Signpost, Kerala, India, 2005) pp. 37-94.
184. Vishay, "Designing Linear Amplifiers Using the IL300 Optocoupler (Appnote 50)".
185. Siemens, "IL300 Linear Optocoupler".
186. Burr-Brown, "Precision Lowest Cost Isolation Amplifier - Application note".